The impact of respiratory motion on electromagnetic fields at ultra-high field cardiac Magnetic Resonance Imaging

Thesis
for the degree of

doctor rerum naturalium (Dr. rer. nat.)
approved by the Faculty of Natural Sciences of Otto von Guericke University Magdeburg

by M.Sc. Natalie Schön

born on 18th of June 1992 in Berlin

Examiner: Prof. Dr. Oliver Speck
Prof. Harald H. Quick

submitted on: 28th of November 2023, defended on: 12th of June 2024

Betreuer:

Dr. rer. nat. Sebastian Schmitter	Physikalisch-Technische Bundesanstalt (PTB), Braunschweig und Berlin
Dr. rer. nat. Frank Seifert	Physikalisch-Technische Bundesanstalt (PTB), Braunschweig und Berlin
Dr. rer. nat. habil. Bernd Ittermann	Physikalisch-Technische Bundesanstalt (PTB), Braunschweig und Berlin
Prof. Dr. rer. nat. habil. Oliver Speck	Otto-von-Guericke-Universität, Magdeburg

Contents

Abstract

While ultra high fields (UHF), field strength (B_0) above 7 T, offer numerous benefits, they also present challenges regarding the safety of electromagnetic (EM) fields.

The purpose of this thesis is to demonstrate and quantify the safety implications of respiratory motion for body MRI at UHF. First, a respiration-dependent simulation setup at 7 T is created, therefore, the XCAT body model is used. Previously measured respiration-induced changes in the transmitted RF field (B_1^+) are validated for static parallel transmission (pTx).
Second, due to the coupling of the magnetic and electric fields via Maxwell's equations, an impact of respiration on the electric field (E) is expected. The E-field within the human body cannot be measured directly and electromagnetic (EM) field simulations become relevant. As a risk-measure of RF induced temperature rise in human tissue, the specific absorption rate (SAR) is calculated. The impact of respiratory motion on local SAR is shown for the first time and is investigated for two different control modes: (i) The 'SAR-controlled mode' (SCM) utilizes complex RF shim vectors and (ii) the 'power-controlled mode' (PCM) limits the maximum amplitude of the shim vector per channel and is phase-independent. In the SCM, respiration may increase maximum local SAR values up to a factor of 2.5 for a 'Fixed' coil setup where the coil position is independent of the respiratory state. This means that worst-case SAR limits will be exceeded for the inhale respiratory state, if the safety assessment was performed for the exhale respiratory state. The PCM is less affected by respiratory motion than the SCM. Power limits calculated with the PCM for the exhale respiratory state are also safe for the inhale respiratory state, using a setup moving with the respiratory motion at 7 T.
Finally, higher field strengths (10.5 T) are examined for static and dynamic pTx, and stronger respiration-induced changes are observed for B_1^+ and local SAR_{10g} at 10.5 T compared to 7 T, and for dynamic pTx compared to static pTx.

For the first time, simulations confirmed the experimental findings of the respiratory impact on the B_1^+ distribution. Under certain conditions, respiration must be considered for safety assessment. Respiration could be considered by using multiple body models or by adding additional safety factors depending on the coil setup and field strength.

Zusammenfassung

'Ultrahohe' Magnetfelder (ultrahighfields, UHF), mit einem $B_0 \geq 7\,T$ eröffnen zahlreiche Vorteile in der Magnetresonanztomographie. Dennoch müssen Herausforderungen bezüglich starker elektromagnetischer (EM) Feldvariationen bewältigt werden.

Das Ziel dieser Arbeit besteht darin, die Sicherheitsrelevanz der Atembewegungen bei der UHF Magnetresonanzbildgebung des Körperstamms zu untersuchen. Dafür wurde ein simulationsbasiertes Modell erstellt, das die atemabhängigen Änderungen des Hochfrequenzfeldes (B_1^+) beim statischen parallelen Senden (pTx) validiert.

Durch die Kopplung von magnetischen und elektrischen Feldern in den Maxwell-Gleichungen wird eine Änderung des elektrischen Feldes (E) mit der Atmung erwartet. Da das E-Feld im menschlichen Körper nicht direkt gemessen werden kann, hat die EM Feldsimulationen eine wichtige Bedeutung. Die spezifische Absorptionsrate (SAR) wird als Gefährdungsmaß für die HF-induzierte Erwärmung des Körpers verwendet. Der Einfluss der Atembewegung auf die lokale SAR wird erstmalig gezeigt und für zwei verschiedene Kontrollmodi untersucht: Im SAR-kontrollierten Modus (SCM) wird die HF-Leistung so begrenzt, dass für einen spezifischen, komplexen Shim-Vektor die zulässigen SAR-Grenzwerte eingehalten werden. Im leistungskontrollierten Modus (PCM) hingegen wird die maximale HF-Leistung pro Spulenelement begrenzt, so dass alle Shim-Vektoren, welche dieses Leistungslimit für jedes Spulenelement einhalten, auch die zulässigen SAR-Grenzwerte einhalten. Im SCM kann die Atmung das maximale lokale SAR (psSAR) im Extremfall um den Faktor 2,5 erhöhen, wenn es sich um eine fest installierte, Atemzustand unabhängige Spulenanordnung bei 7 T handelt. Dies bedeutet, dass SAR-Grenzwerte für den eingeatmeten Zustand überschritten werden könnten, wenn SAR-Grenzwerte im ausgeatmeten Zustand berechnet wurden. Im PCM hat die Atembewegung im Vergleich zum SCM weniger Einfluss auf das psSAR. Es wurden Leistungsgrenzen für eine mit der Atmung mitbewegte Spule bei 7 T im ausgeatmeten Zustand berechnet, die auch im eingeatmeten Zustand sicher sind.

Schlussendlich wurden bei 10.5 T im Vergleich zu 7 T und bei dynamischen pTx im Vergleich zu statischem pTx stärkere durch die Atmung bedingte Veränderungen in B_1^+ und lokalem SAR beobachtet .

Zum ersten Mal bestätigen Simulationen das gemessene atemabhängige B_1^+. Unter bestimmten Bedingungen muss die Atmung bei der Sicherheitsbewertung im UHF-Bereich berücksichtigt werden. Die Atmung könnte durch die Verwendung mehrerer Körpermodelle oder das Hinzufügen von Sicherheitsfaktoren einbezogen werden.

Chapter

1 Introduction

1.1 State of research

Advantages and challenges of UHF MRI

UHF MRI ($B_0 \geq 7\,\mathrm{T}$) enables highly resolved images, revealing anatomical details not visible at 3 T or below [1]. Higher signal-to-noise ratio (SNR) at UHF allows for shorter acquisition times, enhancing the patient's comfort [2]. Those remarkable advantages of UHF MRI, come at the cost of several challenges.

Torso imaging at 7 T or above shows varying contrast, not feasible for diagnostic purposes. The shorter wavelength, below the dimension of the thorax, leads to propagation effects. Strong variations in the interference pattern of the radio frequency (RF) fields [3, 4], in detail the magnetic component of the excitation B_1^+ field are observed. These variations cause local dropouts in the flip angle (FA) distribution, resulting in variations in image contrast and compromised image quality.

Another challenge is the impact of strongly localized electric fields on patient safety. Constructive interference between the E-field of different transmit channels increases locally deposited power and forms hotspots. The specific absorption rate (SAR) is used as a risk-measure of RF-induced temperature rise inside the human body and SAR exposure is limited by international standards from organizations such as the International Electrotechnical Commission (IEC) and regulatory documents, e.g. from the U.S. Food and Drug Administration (FDA) [4–6]. According to the relevant IEC 60601-2-33 standard, the local SAR averaged over a volume containing 10 grams of tissue is considered. The standards restrict the maximum local SAR within the whole body, denoted as peak spatial SAR (psSAR). The global SAR is the SAR averaged over larger body regions, such as the head or the whole body [7]. For all field strengths $\geq 0.5\,\mathrm{T}$, local SAR limits are always reached before global SAR limits are reached [8–10]. The psSAR increases supralinear with increasing field strength [1, 11]. To assess the electric field and SAR exposure, finite difference time domain (FDTD) simulations are commonly used since direct measurements of the electric field are not possible in-vivo.

Solution approach: parallel transmission

Parallel transmission (pTx) in combination with multi-channel transmit (Tx) coils is an approach used to address the strong spatial FA variation in UHF MRI. By superimposing EM-fields from multiple transmit channels, a goal can be to homogenize the B_1^+ field within a region of interest (ROI), while inhomogeneities may persist outside the ROI.

Static pTx involves applying RF pulses with identical RF pulse shapes but different RF phases and amplitudes on the transmit channels to achieve homogeneous B_1^+ within small 2D ROIs [12, 13]. For static pTx a direct correlation between B_1^+ and FA exists for a known RF pulse shape. Dynamic pTx applies temporally varying complex weights to RF pulses in different k-space locations, resulting in changing B_1^+ over the RF pulses duration. The final FA at the end of the RF pulse train can then be optimized for large 3D ROIs [14, 15]. Due to the strong anatomical dependence of the EM-field distributions, individual patient-specific solutions of RF pulses for B_1^+ optimization are often necessary. So-called universal pulses have been pre-calculated for numerous B_1^+ maps and can be utilized for unseen subjects in the same target region without requiring additional calibration [16]. These universal pulses can provide a trade-off between homogeneity and applicability across various body shapes [16].

In addition, the local SAR distribution is influenced by the patient's anatomy and the characteristics of the applied RF pulses. This changes in SAR is a concern for parallel transmission applications. Safety estimations often involve multiple body models representing different anatomies [17]. The introduced degrees of freedom for B_1^+ optimization add complexity to local SAR calculations, considering the element-wise amplitude, phase and pulse duration of the RF pulses [4]. The increase in psSAR_{10g} is mitigated through the use of specialized coil designs [18] and modified RF pulses, such as the VERSE principle [19, 20]. Nevertheless, psSAR often imposes constraints on the allowed applicable RF pulse amplitudes.

The described inter-subject changes are observed for 7 T [21] and 10.5 T [22]. Utilizing pTx at 10.5 T for torso imaging with similar power efficiencies compared to 7 T, results in stronger interference pattern and higher psSAR for 10.5 T [22].

Open questions in UHF MRI using parallel transmission techniques

Parallel transmitted RF pulses enable highly optimized FA homogeneity at UHF for one specific subject in one specific anatomical state. The homogeneity is prone to inter-subject changes [17] and also intra-subject changes, for example, respiration. These changes can result in suboptimal FA distributions, which impact the MRI image quality.

The impact of respiration on the FA has been demonstrated in various studies [13, 23–25], where signal dropouts were observed for respiratory states in which the FA was not optimized. This can be addressed by respiration robust FA optimizations [26].
To the best of my knowledge, SAR calculations are currently performed on single respiratory states, for example, the virtual family [27] or segmented MRI scans [28]. The impact of respiration on local SAR has not been studied yet. Considering the coupling of the electric and magnetic fields through Maxwell's equations, it is expected that changes in local SAR can occur due to respiration. This can be particularly relevant for breath-hold scans performed in the respiratory state for which safety calculations were not conducted. For head motion, it was shown that intra-subject changes do not only lead to FA but also psSAR variations [29].
An open question in the current research is also whether respiration-induced changes in SAR become more pronounced with increasing field strength.

1.2 Aim of this work

This work presents a simulation setup aiming at investigating the impact of respiration on MR safety at 7 T and 10.5 T. The aim is to conclude the safety relevance of body models with different respiratory states and the correlation between field strength and respiratory changes in FA and SAR.

In chapter 4 the simulated coil is precisely validated by B_1^+ phantom measurements at a 7 T and 10.5 T MR scanner, as well as RF time domain field probe measurements at 7 T.

Power limit calculations are performed at 7 T as part of the coil array's safety assessment process for in-vivo measurements.
Simulated B_1^+ and S-Matrix changes induced by respiration at 7 T are shown in chapter 5. This was previously shown in similar setups by measurements. This thesis shows, for the first time, the impact of respiratory motion on local SAR. The used simulation environment allows for investigating the isolated impact of various parameters on the respiration-induced changes in the FA and SAR field maps: First, the breathing pattern which can change during measurements, second, the coil configuration used at different sites, third, the pTx pulse optimization on different respiratory states and fourth the used transmit element type.
In chapter 6 the field strength dependency of the changes in FA and SAR caused by respiration are investigated. Here, static and dynamic pTx is applied to 7 T and 10.5 T. Additionally, the simulated respiration-induced FA changes are qualitatively validated through in-vivo measurements.

It should be noted that parts of this work's introduction have been published in a similar manner in other articles, specifically referenced as [30–33].

Chapter

2 Background

The first effects of magnetic and electric fields on biological tissue date back to the late 19^{th} century [34, 35]. With the first MRI scans of a human, the effects of the electric field on biological-human tissue became evident for MRI safety. In 1977, Mansfield conducted an MRI scan of a finger at 0.35 T [36]. Shortly after whole body line scans of a human subjects were performed [37, 38]. The first MR safety standard by the FDA was published in 1982 [39]. This standard was setting global whole body SAR limits (0.4 W/kg), and local SAR limits over 1g tissue (2.0 W/kg) [39]. The same parameters are relevant for MRI safety today, although with different limits and different averaging volumes. The FDTD method, introduced by Yee in 1966 is often used to calculate the SAR. One of the first publications in the context of FDTD used for MRI is by Brown et al. in 1988 [40]. Ten years later MRI technology began to explore UHF. In 1998 the first 8 T was installed at Ohio State University, and shortly after (1999) the first 7 T scanner was built up at the University of Minnesota [1]. The first FDA-approved 7 T clinical system was cleared in 2017 [41]. Whereas global SAR is for some setups the limiting factor for low-field systems used at the early development of MRI [42], peak spatial SAR is the dominant constraint for UHF systems. UHF introduces many new challenges, as the shorter wavelength in and below the dimensions of the scanned subject leads to strong signal variations. Parallel transmission techniques allow to address those challenges and demand new safety estimations.

This section provides a brief overview of the fundamental MRI principles that are relevant to this thesis. The advantages and challenges of ultra-high field MRI are described in more detail and the concept of parallel transmission is introduced. Finally, the Finite Difference Time Domain method is explained in the context of EM-field simulations.

In the following, scalars and complex variables are denoted as italics, vectors are denoted as italics overlined with a vector arrow, and matrices are denoted as bold, underlined italics.

2.1 Magnetic resonance imaging

MRI is based on nuclear magnetic resonance, which is introduced here at the example of hydrogen, often used for MRI due to the high abundance of water in the human body (approximately 60-80%) [43]. This section focuses on the classical approach of MRI. A more detailed quantum mechanic explanation is given in [44, 45].

Water is built of oxygen and hydrogen atoms, containing protons, giving it a nuclear spin [43]. The z-direction of the used coordinate system is chosen to be parallel to an externally applied magnetic field ($\vec{B}_0$). The quantum mechanical spin of a proton aligns in two different energy states. The z-component of a single spin is either parallel (spin up) or anti-parallel (spin down) to $\vec{B}_0$. The spin-up state has the lower energy and therefore the majority of the protons align in the parallel state. This is described by the Boltzmann distribution. The resulting magnetic moment is denoted as the net macroscopic magnetization $\vec{M}$ and can be described by the classical equations of motion. The magnitude of $\vec{M}$ is characterized by the number of protons per unit volume. In addition, the magnetization vector $\vec{M}$ has a direction. In equilibrium $|\vec{M}|$ is proportional to the magnetic flux density $|\vec{B}_0|$, according to $|\vec{M}| = M_0 = \frac{\chi}{\mu_0 \cdot (1+\chi)} \cdot |\vec{B}_0|$ [43]. μ_0 is the magnetic permeability in free space and χ the magnetic susceptibility. The magnetization vector $\vec{M}$ is rotated away from the direction of $\vec{B}_0$, if an excitation RF pulse is applied [43]. If $\vec{M}$ is not aligned with $\vec{B}_0$, $\vec{M}$ is gaining a torque. The motion is described by :

$$\frac{\partial \vec{M}}{\partial t} = \vec{M} \times \gamma \vec{B}_0. \tag{2.1}$$

This leads to a precession with the Larmor frequency ω_0:

$$\omega_0 = \gamma |\vec{B}_0|, \tag{2.2}$$

γ is the gyromagnetic ratio, for protons this is $2\pi \times 42.58\text{MHz/T}$ [43]. Additionally to this equation of motion, longitudinal relaxation (eq. (2.5)) results in energy dissipation to the environment with the time constant T_1. Transversal magnetization disappears over time due to a lack of phase coherence among single spins, resulting in no change in energy in the system, with the time constant T_2 (eqs. (2.3) and (2.4)). Bloch's equations [46] describe the relaxation with the time constants T_1 and T_2:

$$\frac{\mathrm{d}M_x(t)}{\mathrm{d}t} = \gamma\left(\vec{M} \times \vec{B}\right)_x - \frac{M_x(t)}{T_2} \tag{2.3}$$

$$\frac{\mathrm{d}M_y(t)}{\mathrm{d}t} = \gamma\left(\vec{M} \times \vec{B}\right)_y - \frac{M_y(t)}{T_2} \tag{2.4}$$

$$\frac{\mathrm{d}M_z(t)}{\mathrm{d}t} = \gamma\left(\vec{M} \times \vec{B}\right)_z - \frac{M_z(t) - M_0}{T_1} \tag{2.5}$$

In addition to the transversal relaxation T_2, local magnetic field inhomogeneities ΔB_0 cause additional spin dephasing with the relaxation time T_2^*. The relaxation rate is given by

$$\frac{1}{T_2^*} = \frac{1}{T_2} + \frac{1}{\gamma \Delta B_0} \quad . \tag{2.6}$$

In MRI the concept of a rotating frame is used. $(x, y, z)^T$ from the laboratory frame are converted into a rotating reference frame $(x', y', z')^T$, to reduce complexity, leading to an effective magnetic field $\vec{B}_{eff}$. The rotating frame axis is parallel to the $\vec{B}_0$ axis, revolving with ω_0. If this resonance condition is full filled $\vec{B}_0$ is replaced by $\vec{B}_{eff} = 0$ in eq. (2.1) and the temporal derivative of $\vec{M}$ vanishes. Equations (2.3) to (2.5) are simplified for the rotating frame. The magnetization remains stationary within this rotating reference frame, provided that only the magnetic field $\vec{B}_0$ is present [43].

Applying an additional rectangular RF pulse is equivalent to applying a stationary magnetic field $\vec{B}_1 \perp \vec{B}_0$ [43]. In the rotating frame, application of a rectangular RF pulse induces rotation of the magnetization vector around $\vec{B}_1$ by the flip angle $\mathrm{FA} = \gamma \cdot |\vec{B}_1| \cdot \tau$, where τ is the pulse duration, as illustrated in fig. 2.1.1B-C [43]. After switching off the RF pulse (fig. 2.1.1D), the precession of $\vec{M}$ in the xy plane, denoted by the complex scalar $M_{xy} = M_x + i \cdot M_y$ as the transversal magnetization, is measured by receive coils. The precessing M_{xy} component induces a voltage in a nearby coil. The magnetization vector $\vec{M}$ is decaying back to $\vec{M}_0$ due to transversal relaxation in x'y'-direction (fig. 2.1.2A) and longitudinal relaxation in z'-direction (fig. 2.1.2B). Both relaxation processes are often investigated separately from each other since they often occur on different time scales. Solving Bloch's equations M_{xy} is proportional to e^{-t/T_2}. This decay is called the free induction decay.

The $\vec{B}_1$ field can be decomposed into two parts. A B_1^+ field rotates in the direction of the proton nuclear spins , while a B_1^- field rotates in the opposite direction of the proton

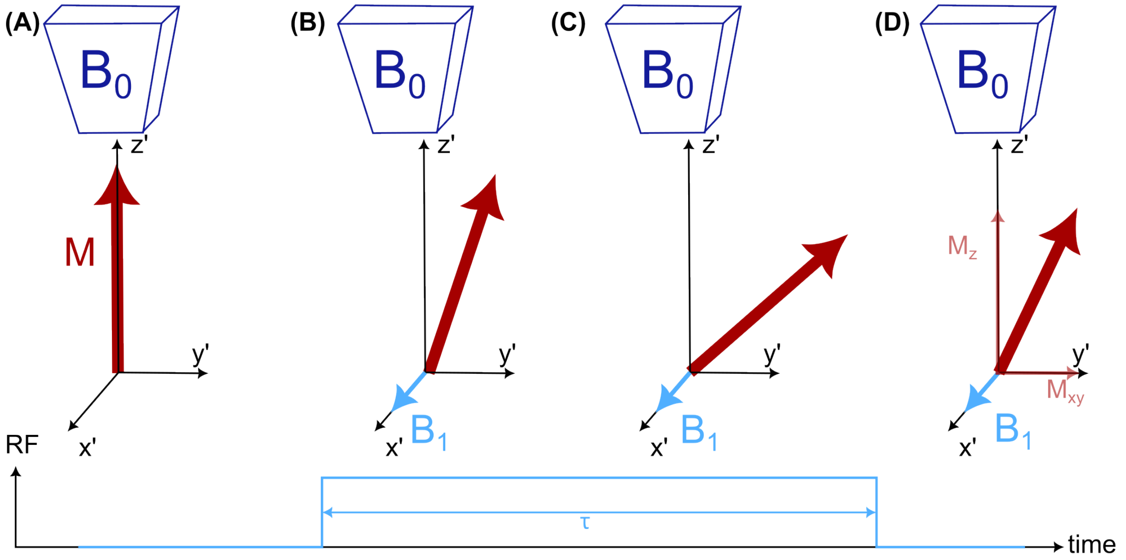

Figure 2.1.1: $\vec{B}_1$ in the rotating frame: In (A) the magnetization $\vec{M} = \vec{M}_0$ aligns with $\vec{B}_0$. Next, a rectangular RF pulse is applied (B), causing the magnetization to rotate around $\vec{B}_1$. As long as the RF pulse is applied, the magnetization continues to flip (C). The total FA is given by FA $= \gamma|B_1|\tau$. After a time τ has passed, the RF pulse is switched off and the magnetization vector $\vec{M}$ begins to decay back to $\vec{M}_0$, characterized by T_1, the longitudinal relaxation (decay in z'-direction) and T_2, the transversal relaxation (decay in x'y' direction) (D). T_2 and T_1 can happen on different time scales, and therefore the relaxation is investigated separately fig. 2.1.2.

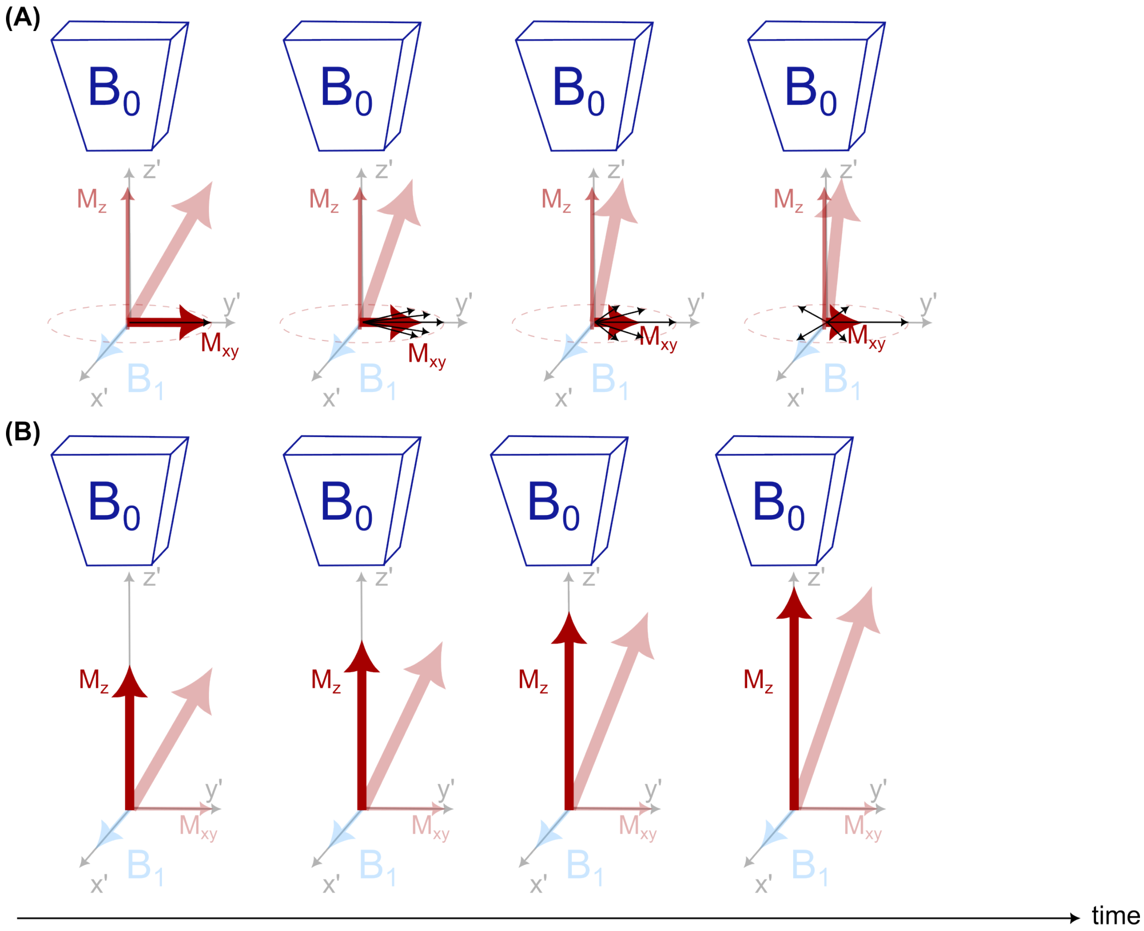

Figure 2.1.2: The decay of the magnetization vector $\vec{M}$ after the RF pulse is switched off, is characterized by T_2, the transversal relaxation (decay in x'y' direction) and T_1, the longitudinal relaxation (decay in z'-direction). Both relaxations are investigated separately from each other, since they can occur on different time scales. (A) illustrates the schematic dephasing of the spins, leading to the decay of M_{xy}. This is not a complete picture, as only a small fraction of the spins are in transverse phase coherence at the beginning. (B) illustrates the longitudinal relaxation, leading to the spin relaxation back to the lower energy state (spin-up).

nuclear spins. B_1^+ is the component flipping the magnetization $\vec{M}$ and B_1^- is determining the sensitivity of the receive coil. The complex values B_1^+ and B_1^- at the location vector $\vec{r}$ are described by [47]:

$$B_1^+(\vec{r}) = \frac{B_{1x}(\vec{r}) + i \cdot B_{1y}(\vec{r})}{2} \tag{2.7}$$

$$B_1^-(\vec{r}) = \frac{(B_{1x}(\vec{r}) - i \cdot B_{1y}(\vec{r}))^*}{2} \tag{2.8}$$

were B_{1x} and B_{1y} are the x and y component of the complex valued vector $\vec{B}_1$.
The applied RF magnetic fields are coupled to electric fields via Maxwell's equations, which is especially relevant for small wavelengths at UHF MRI (Farday law). The dependencies are described in detail in section 2.4. The spatial encoding magnetic field gradients used in MRI are not described in this thesis, as the results focus on the described RF pulses and corresponding electric and magnetic fields.

2.2 Ultra-high field MR

Improving body magnetic resonance imaging (MRI) envolves an increase in signal-to-noise ratio (SNR) to enhance image resolution and reduce acquisition time. This has been done by improving the hardware and acquiring more data. Noise induced by the sample, not the hardware, dominates the current measurement noise. To improve SNR, a stronger spin polarization in the sample can be achieved by using higher field strength since SNR increases as B_0 increases [1, 11]. The SNR increases linearly with the voxel volume [43]. As a result, if the SNR increases by raising $|\vec{B}_0|$, the voxel volume can be reduced. The smaller voxel volume reduces the partial volume effect, which averages the signal of the materials inside a voxel, enabling the resolution of smaller structures [1].

Therefore, UHFs such as 7 T are applied for head imaging, which results in high-resolution images [48]. So far, thorax imaging at 7 T emerged to be challenging for several reasons. One main issue is that standard circular polarized (cp) mode excitations, which to some degree can still be used in the brain, are not applicable without obtaining signal dropouts or massive signal variations [49].
Wavelength (approximately 12 cm at 7 T in water like tissue) below the dimensions of the scanned body leads to constructive and destructive interference of the EM fields. The B_1^+ fields of different transmit elements reach the body from different directions with different phases. Constructive and destructive interference potentially decreases the B_1^+

field uniformity and induces a varying FA over the field of view (FOV).

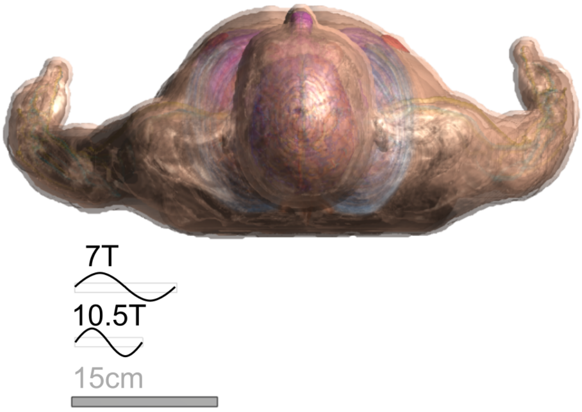

Figure 2.2.1: For UHF, the wavelength in water is below the dimensions of the human body. Body and wavelength are true to scale.

For sufficient low field strengths, a quasi-static approximation is made, which neglects displacement currents $\vec{D}$ in Amperes law eq. (2.9), as the impact of the electric field to RF-related problems is small [1]. Neglecting the temporal change of the displacement currents also ignores any phase variations, which is reasonable for low field strength. The long wavelength produces uniform phase distributions with only minor dielectric losses, and the time dependence of the source and the EM fields are in phase [1].

For higher field strength, the transition from quasi-static to electromagnetic field must be done to link electric and magnetic fields.

$$\nabla \times \vec{H} = \vec{J} + \frac{\partial \vec{D}}{\partial t} \tag{2.9}$$

The displacement current links the magnetic field $\vec{H}$ to the electric field $\vec{E}$ with $D = \varepsilon_0 \varepsilon_r \vec{E}$ for a linear isotropic medium, with ε_0 the permittivity of free space.

A second main issue for UHF cardiac MRI and the primary focus of this thesis is the impact of respiratory motion on EM-fields. Respiration impacts the FA and RF power deposition in human tissue. To avoid motion artifacts during free breathing, data acquisition can be performed with breath-hold scans. If long repetition times (TR) are required, the scans can not be performed during brath-hold, and the motion artifacts during free breathing data acquisition can create difficulties for image acquisition.

The described phase variations induce inhomogeneities not only in the B_1^+ field but also the severity of electric field hot spots increases. Constructive interference in the electric field can potentially cause high local SAR. Specific coil designs, the utilization of dielectric pads [50], or the application of adiabatic pulses [51] are employed to address B_1^+-field inhomogeneities and E-field hot spots. Moreover, parallel transmission offers additional flexibility by introducing extra degrees of freedom, allowing for the homogenization of the B_1^+ field and the mitigation of E-field hot spots.

2.3 Parallel transmission

UHFs come with shorter RF wavelengths and stronger constructive and destructive interference patterns of the resulting B_1^+ fields. In the worst case, strong interference patterns lead to local signal voids and vanishing excitation [3].

Various pTx RF pulses in combination with multi channel transmit coils can address subject-dependent [3] local inhomogeneities [49]. The basic principle of pTx was initially introduced by [52, 53] and has been summarized in a review by [3]. In the following, a brief summary is provided.

The main goal of pTx is to address the spatial inhomogeneous and temporal varying FA pattern of non-pTx applications, for example, standard circular polarized (cp)-mode or single channel applications [3]. A target FA pattern is pursued, for example, uniformity or large FAs inside an ROI [3], by individually adjusting amplitudes and phases of the applied RF pulses. pTx is also used for local excitations [54, 55], which is not part of this thesis. With pTx not only amplitudes and phases can be varied, but also temporally different RF pulses, can be applied for each channel [49].

pTx allows to shift B_1^+ inhomogeneities out of the ROI and locally increase B_1^+ [49].

These chances of pTx possibly come at the cost of increased local SAR compared to non-pTx applications. The local SAR of pTx applications is spatially and for some applications temporally variable compared to the local SAR using single-channel systems. The increased SAR should always be addressed by calculating and setting the safety limits for pTx RF coils.

In this work, static and dynamic pTx are applied. Generally, the B_1^+ of a multi-Tx channel RF coils is the complex sum of the element-wise produced $B_{1,i}^+$ fields [3] at the time t and N_{ch} the total number of transmit channels.

$$B_1^+(\vec{r},t) = \sum_{i=1}^{N_{\mathrm{ch}}} B_{1,i}^+(\vec{r},t) \tag{2.10}$$

Dynamic pTx uses different RF pulses $p_i(t)$ for each element i.

$$B_1^+(\vec{r},t) = \sum_{i=1}^{N_{\mathrm{ch}}} p_i(t)s_i(\vec{r}) \tag{2.11}$$

pTx requires prior knowledge of the spatial sensitivity $s_i(\vec{r})$ of each element. This can be gained by complex B_1^+ mapping. In contrast to dynamic pTx, where the superposed B_1^+ changes over time with the different RF pulses and the FA at the end of the RF pulse train is optimized, static pTx optimizes the B_1^+ field, which induces a certain FA. Static pTx applies the same RF pulse $p(t)$ for all channels but scales the pulses individually for each channel with the complex weight w_i.

$$B_1^+(\vec{r},t) = p(t)\sum_{i=1}^{N_{\mathrm{ch}}} w_i s_i(\vec{r}) \tag{2.12}$$

In this context, $|B_1^+|$ is in units μT, the sensitivity in μT/V, $p(t)$ and $p_i(t)$ in V and w_i has no units. In the following, we replaced B_1^+ with a B_1^+ normalized to the forward power. Therefore, $|B_1^+|$ is given in $\mu T/\sqrt{kW}$.

A more detailed description of static and dynamic pTx will be given in chapter 3.

2.4 Finite difference time domain simulations

The finite difference time domain (FDTD) method is a computational approach that discretely approximates spatial and temporal derivatives of the E- and H-field to solve the Maxwell equations in the temporal domain [56]. The use of finite differences to estimate partial derivatives allows for solving the complex Maxwell equations, making it especially useful for addressing computationally intensive challenges where object and wavelength are within a comparable range [56].

FDTD has various applications in the field of MRI. First, it is utilized for the design and testing of RF coils through simulations, eliminating the need for costly prototype production. Second, FDTD simulates the B_1 and E-field behavior for various setups, enabling the adaption of single parameters while keeping the remaining setup unchanged. Since the direct measurement of the E-field is in-vivo not possible, simulations provide valuable insights. Third, by simulating the E-field and calculating the specific absorption rate, power limits for MR applications can be calculated to ensure safety compliance with standards [57].

This section provides an overview of the Maxwell equations and the constitutive relations and their approximative representation of the FDTD method. Additionally, the section describes the boundary condition used in FDTD simulations of this thesis, the uniaxial perfectly matched layers. Finally, all the introduced methods are consolidated by summarizing the process of the FDTD algorithm.

The figures and text of this section are based on lecture notes by Raymond C. Rumpf [58].

Maxwell equations and constitutive relations

Maxwell's equations describe the propagation of EM fields in space and time: First, the Gauss law describes the divergence of the electric displacement field $\vec{D}$ (eq. (2.13)) and the magnetic flux density $\vec{B}$ (eq. (2.14)).

$$\nabla \cdot \vec{D} = \rho \tag{2.13}$$

$$\nabla \cdot \vec{B} = 0 \tag{2.14}$$

ρ is the charge density. Ampere's law defines the curl of the magnetic field strength $\vec{H}$ as the sum of the time derivative of the electric displacement field and the current density $\vec{J}$ (eq. (2.15)). Faraday's law describes the curl of the electric field $\vec{E}$ as the time derivative of the magnetic flux density $\vec{B}$. The curl equations define electromagnetic waves. The time-varying oscillating electric field induces a time-varying oscillating magnetic field, which induces again a time-varying oscillating electric field, and so on (fig. 2.4.1). This is described by Ampère's law (eq. (2.15)) and Faraday's law (eq. (2.16)).

$$\nabla \times \vec{H} = \vec{J} + \frac{\partial \vec{D}}{\partial t} \tag{2.15}$$

$$\nabla \times \vec{E} = -\frac{\partial \vec{B}}{\partial t} \tag{2.16}$$

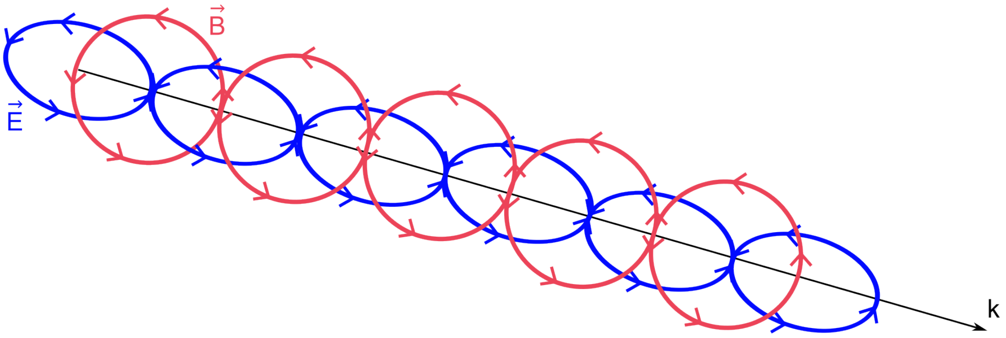

Figure 2.4.1: The time-varying oscillating electric field (eq. (2.15)) induces a time-varying oscillating magnetic field (eq. (2.16)), which induces a time-varying oscillating electric field again, and so on, after [58] lecture 1c.

The interaction of those fields with the material is defined by the constitutive relations. In this work, linear and isotropic material properties are considered: the effective permittivity ε describes the relation between the D-field and the E-field (eq. (2.17)). The magnetic permeability in free space μ_0 scales $\vec{H}$ to $\vec{B}$ (eq. (2.18))

$$\vec{D}(t) = \varepsilon \vec{E}(t) \tag{2.17}$$

$$\vec{B}(t) = \mu_0 \vec{H}(t). \tag{2.18}$$

FDTD describes Maxwell's equations as an approximation of the EM-fields in the cartesian space-time grid.

FDTD time component

Maxwell's equations can be solved by discrete approximations. This is done by finite difference time domain simulations. FDTD describes the coupling of Maxwell's equations as a sequence of discrete events. In reality, this happens all at the same time. If the time steps are sufficiently small, this approximation is reasonable. The derivatives are substituted in Maxwell's equations by finite difference approximation (use eqs. (2.15) to (2.18)). This section is limited to describing the approximation of the time component $\frac{\partial}{\partial t}$. For the full FDTD algorithm, this is done in analogy for the space component ∇, not shown here.

The finite difference approximation for Amperes law derivative of the magnetic field strength $\frac{\partial \vec{H}}{\partial t} \approx \frac{\vec{H}(t+\frac{\Delta t}{2})-\vec{H}(t-\frac{\Delta t}{2})}{\Delta t}$ exists at the midpoint t between $\vec{H}\left(t+\frac{\Delta t}{2}\right)$ and $\vec{H}\left(t-\frac{\Delta t}{2}\right)$. To obtain a stable FDTD equation, every term in the FDTD equation needs to be at the same time and space point. Therefore, $\nabla \times \vec{E}$ has to be defined at the same time point t as $\frac{\partial \vec{H}}{\partial t}$.

$$\frac{\partial \vec{H}}{\partial t} = -\frac{1}{\underline{\mathcal{M}}}\nabla \times \vec{E} \rightarrow \frac{\vec{H}\left(t+\frac{\Delta t}{2}\right)-\vec{H}\left(t-\frac{\Delta t}{2}\right)}{\Delta t} = -\frac{1}{\mu_0}\nabla \times \vec{E}(t) \tag{2.19}$$

Equation (2.19) is rearranged to the field at the future time step.

$$\vec{H}\left(t+\frac{\Delta t}{2}\right) = \vec{H}\left(t-\frac{\Delta t}{2}\right) - \frac{\Delta t}{\mu_0}\nabla \times \vec{E}(t) \tag{2.20}$$

The time point of Faraday's law is moved by $\frac{\Delta t}{2}$ compared to Ampere's law. $\frac{\partial \vec{E}}{\partial t}$ and $\nabla \times \vec{H}$ are obtained at $t+\frac{\Delta t}{2}$.

$$\frac{\partial \vec{E}}{\partial t} = \frac{1}{\underline{\mathcal{E}}}\nabla \times \vec{H} \rightarrow \frac{\vec{E}\,(t+\Delta t)-\vec{E}\,(t)}{\Delta t} = -\frac{1}{\varepsilon}\nabla \times \vec{H}\left(t+\frac{\Delta t}{2}\right) \tag{2.21}$$

The rearrangement to the field at the future time step is done in analogy to eq. (2.20) for eq. (2.21). The illustrated discrete approximation leads to a time shift of $\frac{\Delta t}{2}$ between E and H. This ensures that the time-wise derivative and the ∇ operator are defined at the same time within one equation, which is t for Ampere's law and $t+\frac{\Delta t}{2}$ for Faraday's law.

Yee Cell and FDTD space component

The approximation of the derivatives in Maxwell's equations discretizes continuous functions to discrete stored data points. The discrete points present values for a single unit cell (Yee cell) with dimensions $\Delta x, \Delta y, \Delta z$

The Yee cells are counted by indices l,m,n for x,y,z directions. The field components are not stored in the center of the Yee cell but are staggered on the boundaries of the Yee cell. The Yee grids of H and E are shifted by half a Yee cell in all three dimensions. This is an elegant way to approximate Maxwell's equations and obtain stable FDTD, with all values calculated at the same time and space within Faradays and within Amperes law.

To minimize rounding errors due to the different order of magnitudes between E and H, H is normalized by η_0 (free space impedance) $\tilde{\vec{H}} = \eta_0 \vec{H}$. After expanding the curl equations and simplifying to 1D in z-direction, the FDTD equations are summarized in table 2.4.1. For 1D, the derivatives in the x and y direction are zero ($\partial/\partial x = \partial/\partial y = 0$), and the Yee cell indices l and m are constant.

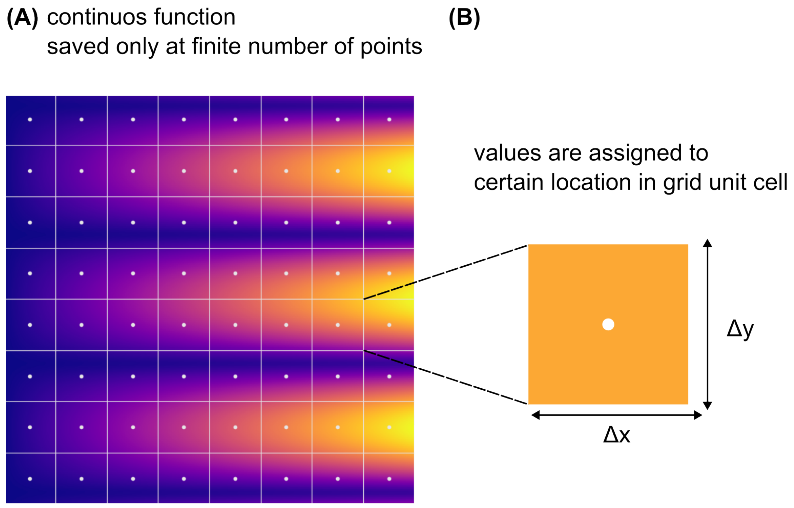

Figure 2.4.2: (A) A continuous 2D field is converted to (B) discrete points used for the unit cell (fig. 2.4.3), after [58] lecture 2a.

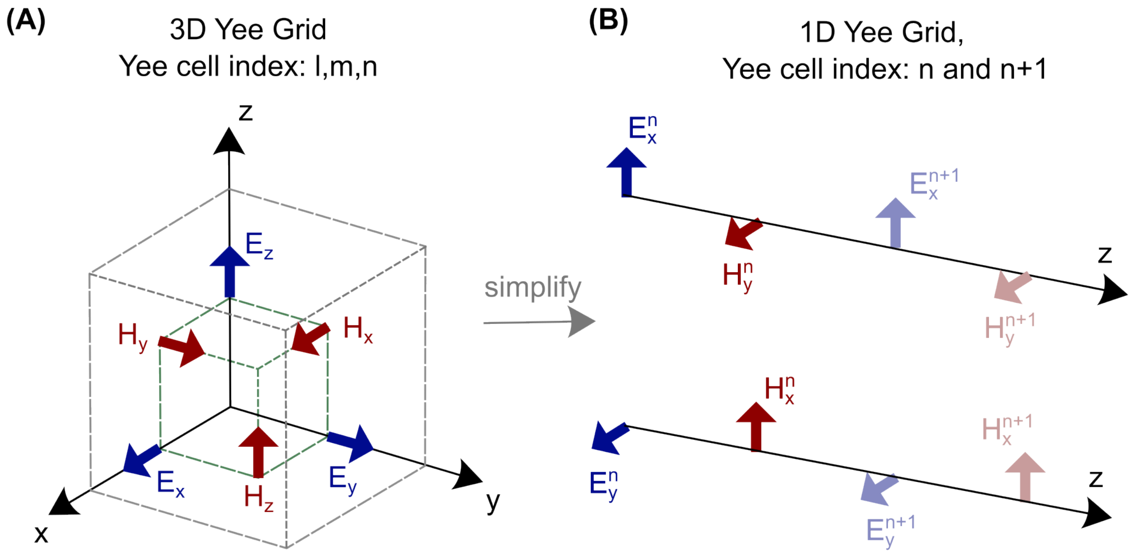

Figure 2.4.3: (A) illustrates a 3D Yee grid for one Yee cell with indices l,m,n. (B) shows two adjacent Yee cells. The indices l and m are kept constant, and the 3D Yee cell is simplified to 1D, with indices l,m,n and l,m,n+1. The 1D setup is utilized to investigate exemplary FDTD equations in table 2.4.1, after [58] lecture 2a.

Analytical equation	FDTD equation
E-update equation	
$\frac{\partial E_y}{\partial z} = \frac{\mu_{xx}}{c_0}\frac{\partial \tilde{H}_x}{\partial t}$	$-\frac{E_y^{n+1}\vert_t - E_y^n\vert_t}{\Delta z} = -\frac{\mu_{xx}^n}{c_0}\frac{\tilde{H}_x^n\vert_{t+\frac{\Delta t}{2}} - \tilde{H}_x^n\vert_{t-\frac{\Delta t}{2}}}{\Delta t}$
$\frac{\partial E_x}{\partial z} = \frac{\mu_{yy}}{c_0}\frac{\partial \tilde{H}_y}{\partial t}$	$-\frac{E_x^{n+1}\vert_t - E_x^n\vert_t}{\Delta z} = -\frac{\mu_{yy}^n}{c_0}\frac{\tilde{H}_y^n\vert_{t+\frac{\Delta t}{2}} - \tilde{H}_y^n\vert_{t-\frac{\Delta t}{2}}}{\Delta t}$
$0 = \frac{\mu_{zz}}{c_0}\frac{\partial \tilde{H}_z}{\partial t}$	$\tilde{H}_z^n = 0$
H-update equation	
$\frac{\partial \tilde{H}_y}{\partial z} = \frac{\varepsilon_{xx}}{c_0}\frac{\partial E_x}{\partial t}$	$-\frac{\tilde{H}_y^n\vert_{t+\frac{\Delta t}{2}} - \tilde{H}_y^{n-1}\vert_{t-\frac{\Delta t}{2}}}{\Delta z} = -\frac{\varepsilon_{xx}^n}{c_0}\frac{E_x^n\vert_{t+\Delta t} - E_x^n\vert_t}{\Delta t}$
$\frac{\partial \tilde{H}_x}{\partial z} = \frac{\varepsilon_{yy}}{c_0}\frac{\partial E_y}{\partial t}$	$-\frac{\tilde{H}_x^n\vert_{t+\frac{\Delta t}{2}} - \tilde{H}_x^{n-1}\vert_{t-\frac{\Delta t}{2}}}{\Delta z} = -\frac{\varepsilon_{yy}^n}{c_0}\frac{E_y^n\vert_{t+\Delta t} - E_y^n\vert_t}{\Delta t}$
$0 = \frac{\varepsilon_{zz}}{c_0}\frac{\partial E_z}{\partial t}$	$E_z^n = 0$

Table 2.4.1: 1D FDTD equations are derived from analytical equations. The initial fields are 0 and constant parameters are saved initially as update coefficients $\left(\frac{\mu_{xx}^n}{c_0 \cdot \Delta t}, \frac{\mu_{yy}^n}{c_0 \cdot \Delta t}, \frac{\varepsilon_{xx}^n}{c_0 \cdot \Delta t}, \frac{\varepsilon_{yy}^n}{c_0 \cdot \Delta t}\right)$ with c_0 the speed of light in vacuum.

Boundary condition: Uniaxial perfectly matched layers

The simulation domain is finite and uniaxial perfectly matched layers (UPML) are used for spatial boundaries of the domain, preventing the reflection of outgoing waves. Those UPMLs are a series of perfectly matched layers (PML) at the edge of the simulation domain, which absorbs outgoing waves with no reflection [59]. Gedney at al. [59] showed the computational advantages of UPML compared to PML, with the same absorbing efficiency. The wave experiences attenuation as it passes through successive lossy layers. The amplitude of the wave upon reaching the final PML layer decreases by several orders of magnitude when compared to the outgoing wave at the initial PML layer.

A PML uses anisotropic absorbing media that prevent outgoing waves' reflection in transverse direction [60]. Therefore, the transversal direction is defined by a layer with a gradually increasing imaginary part [60].

FDTD algorithm

This subsection summarizes the process of FDTD simulations after [58].

First of all, the model needs to be built, as illustrated in fig. 2.4.4A. Therefore, the grid resolution is set, the coil and phantom/body model are defined, and the source is implemented. Second, several parameters are precalculated. The update coefficients, described in table 2.4.1, are constant over the FDTD process, and time-wise, the fields and spatial boundary terms are initialized.

When running the FDTD algorithm, as illustrated in fig. 2.4.4B, first, a new H-field is calculated with the H update equation of table 2.4.1 by using the known E-field. This is done for all spatial positions, at the end, the new H-field numerical boundary terms are calculated. Second, the E-field is updated from the H-field (table 2.4.1) for all spatial positions and the new E-field boundary terms are calculated. Third, the voltage and current of the sinusoidal source are set.

This process is repeated over the time variable until a steady state is obtained. Details on the boundary term calculations and implementation of the source can be found in [56]. Finally, the field is visualized.

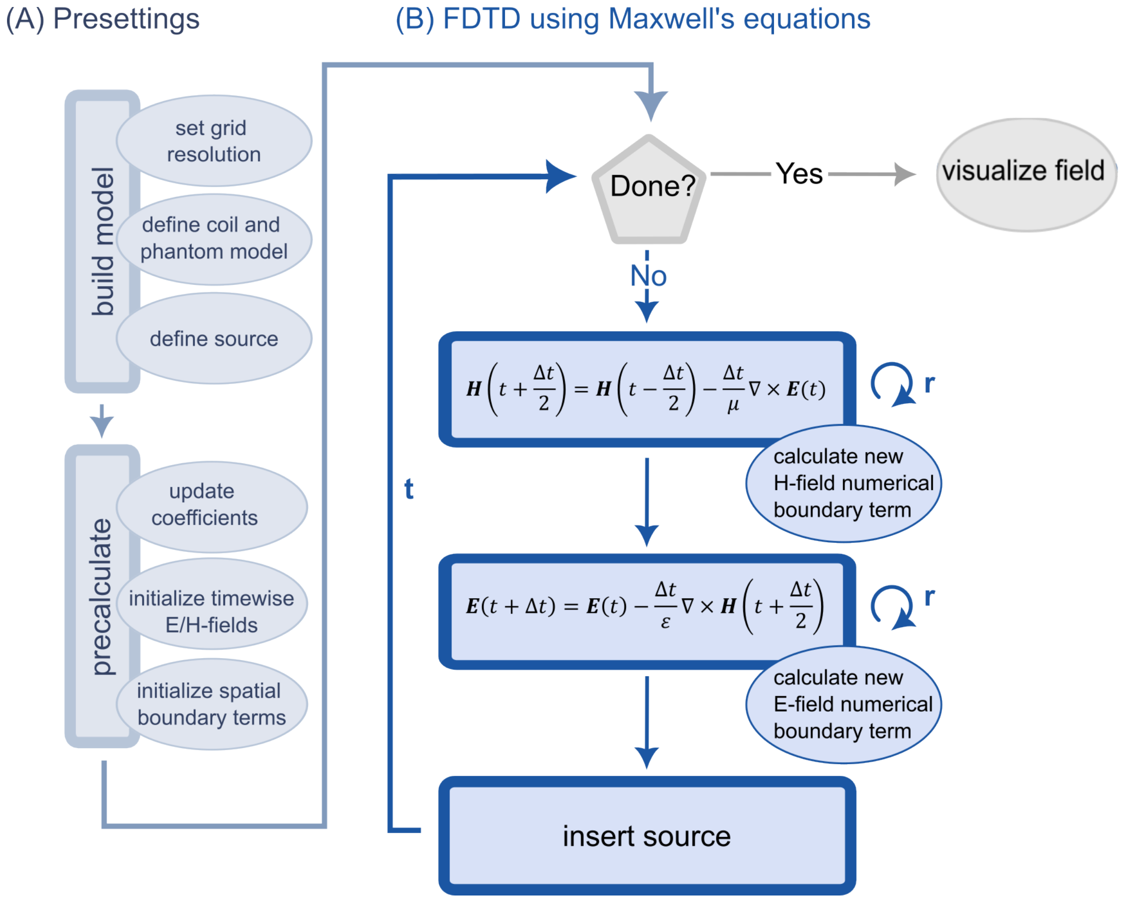

Figure 2.4.4: A schematic of the FDTD algorithm is presented. Prior to running the algorithm, the model is constructed and the necessary parameters are calculated (A). Once all settings are established, the FDTD algorithm (B) is initiated and repeated over time until a steady state is achieved. After [58] lecture 2d.

Chapter

3 Methods

This work compares measured and simulated B_1^+ maps to validate a novel EM-field simulation setup, which analyses respiration-induced changes in B_1^+ and local SAR. The simulated B_1^+, E-fields, and scattering matrices (S-matrices) were extracted from Sim4Life (v6.0, ZMT Zürich Med Tech AG) and post processed through a Python 3.9 [61] script similar to [62]. An RF time domain field probe is utilized at 7 T and MR scanner measurements at 7 T and 10.5 T are used for B_1^+ phantom measurements. In vivo measurements, which depend on the respiratory state, were conducted at both 7 T and 10.5 T.

3.1 Coil models

For a long time there existed no or only few commercially available UHF transmit and receive coils [63]. The classical body coil enclosing the bore liner from the outside and often used as the universal excitation coil at 1.5 T and 3 T, are challenging at 7 T and until now not provided by the vendors [63]. As a result, research sites had to acquire knowledge in RF coil design and construct their own transmit and receive coils [63]. The most relevant coil element for this work is the fractionated dipole antenna developed by Raaijmakers et al. [64] . This antenna reduced the SAR compared to single-side adapted dipole arrays. The combination of magnetic divergence free loops and curl-free electric fractionated dipole elements emerged to be advantageous regarding SNR and B_1^+ efficiency [65] compared to microstrip lines and fractionated dipole only arrays.

The 16 channel transmit receive (Tx/Rx) body array with 8 fractionated dipoles and 8 loops developed by Ertürk et al. [65] is used for 7 T simulations shown in this work. Dipole-only coils were utilized for 10.5 T as they have better performance outside the near field region compared to loops [22]. The near field region for 10.5 T is closer to the coil elements in contrast to 7 T, as detailed in [22]. In the following, the simulated and as well as the physically built coil models are described in detail.

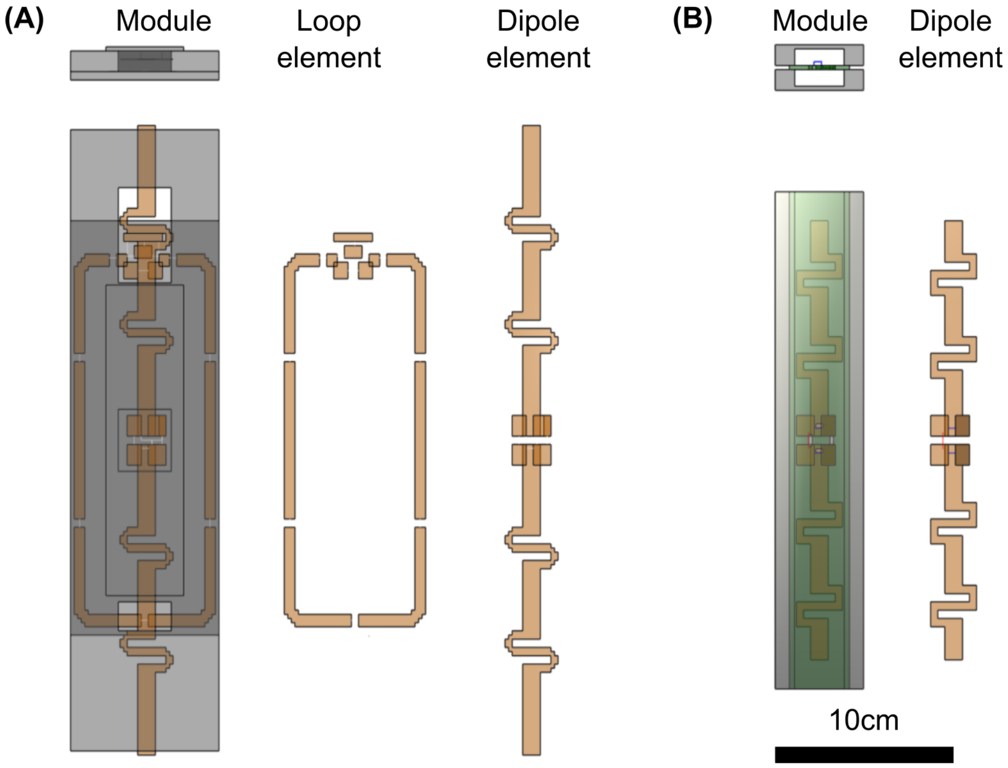

Figure 3.1.1: Tx/Rx coil modules: (A) shows a 7 T coil module from the front and the side, including a loop element and a dipole element, placed on top of each other with a distance of 6 mm. (B) shows a 10.5 T coil module, including only a dipole. For both field strengths the coil modules are tuned, matched and decoupled by a balun.

3.1.1 7 T Tx/Rx body coil array

For the 7 T measurements in this work, a duplicate of the loop-dipole coil by Ertürk et al. [65] is utilized. The array is separated into an anterior and a posterior panel, each containing 4 modules (fig. 3.2.1B). Each module contains one loop and one dipole element (fig. 3.1.1A). In the following the term ’element’ is used to describe the separate electric components of the module, either ’loop’ or ’dipole’. In contrast, the term ’channel’ is utilized for the driven elements on which different RF pulses are applied. In simulations or measurements, this can either be only dipole channels ’D’ (8Tx), only loop channels ’L’ (8Tx) or a combination of dipole and loop channels ’LD’ (16Tx).

For the loop elements, resistors with losses of 20 Ω were included in each simulated element. This resistor represents material losses, soldering losses, and lumped element losses in the coil. The losses were measured utilizing a single module and a pickup loop connected to an network analyzer. The module was not placed on a phantom to determine the losses independent of the loading of the coil element. The frequency was swept from 220 to 340 MHz, and the signal intensity of the pickup loop was evaluated. To calculate the loop losses (R_L), the Q-factor (Q) was determined using the full-width half maximum FWHM and the resonance frequency f_0 of the element. R_L is inversly proportional to Q and the capacitor C. The latter is the total capacitor of the series capacitors within the loop element (0.75 pF).

$$Q = \frac{f_0}{\mathrm{FWHM}} \tag{3.1}$$

$$R_L = \frac{1}{2 \cdot \pi \cdot f_0 \cdot C \cdot Q} \tag{3.2}$$

Including ohmic losses in the dipole element emerged to be challenging. Coupling between the dipole element and the coaxial cable connected to the loop, as well as skin effect losses, which are not equally distributed over the dipole element, need further investigations to be implemented correctly.

For this work, it was decided not to include dipole losses in the simulations. Safety-wise, this is a conservative approach.

Hardware limitations of the used scanner limit the number of transmit channels available to only eight. Dipole elements were utilized, and loop elements were terminated by 50 Ω resistors for in vivo transmission, while all 16 channels were used for reception. Either loop or dipole elements were terminated for phantom measurements. In this setup, transmission and reception were performed with 8 channels.

In comparison with [65], minor capacitance adjustments were made to the elements.

3.1.2 10.5 T Tx/Rx body coil array

A transmit-receive (Tx/Rx) body coil array with 16 coil modules, each containing a fractionated dipole element (fig. 3.1.1B), was used for 10.5 T. Ertürk et al. [65] originally described the element design used in a coil array with 10 modules. In [66] the used coil array with 16 coil modules is presented. To better compare 10.5 T and 7 T, simulation results for an 8-module setup at 10.5 T are also presented in this thesis.

3.2 EM simulation

Simulation can generate three-dimensional EM field data of the total human body, which is not possible in similar quality by in-vivo or phantom measurements [7]. Virtual body models are used in simulations to generate data about B_1^+ and E field distributions. EM-simulations are the only method to access highly spatially resolved local specific absorption rates in human bodies and therefore to verify the compliance with the safety limits [7].

This section gives an overview of the used body models, simulation parameters and post-processing methods. It introduces a simulation setup which is used to obtain respiration-resolved B_1^+ and SAR maps.

3.2.1 Duke body model

The male Duke standard body model [27] was used to calculate the maximum applicable power for the 7 T body array coil. B_1^+ maps, SAR maps and the maximum applicable power to stay below the IEC 60601-2-33 first-level controlled mode trunk SAR limit [5] of the 20 W/kg were extracted. The first level controlled mode includes all setups with field strengths equal or above 4 T and multi-channel transmit coils operated with varying RF shim settings are categorized as local transmit coils [5].
The body coil array was centered at three different locations of the Duke: (i) the center of the heart, (ii) the center of the liver and (iii) the center of the prostate (3.2.1A).

3.2.2 Respiration resolved body models

Respiration resolved body models were generated using a commercial software called XCAT [67–71], where user-defined parameters govern the respiratory and cardiac motion. Typical diaphragm displacements, denoted as d_d, and chest displacement d_c were measured in-vivo and implemented into the XCAT software.

Out of a total of 100 temporal equidistant respiratory states spanning a complete respiratory cycle of exhale-inhale-exhale lasting for 5 s, 5 respiratory states were chosen. The selection process involves obtaining equidistant d_d ranging from 0 mm (R1) to 40 mm (R5), which do not correspond to equidistant time steps. This diaphragm displacement in head-feet (HF)

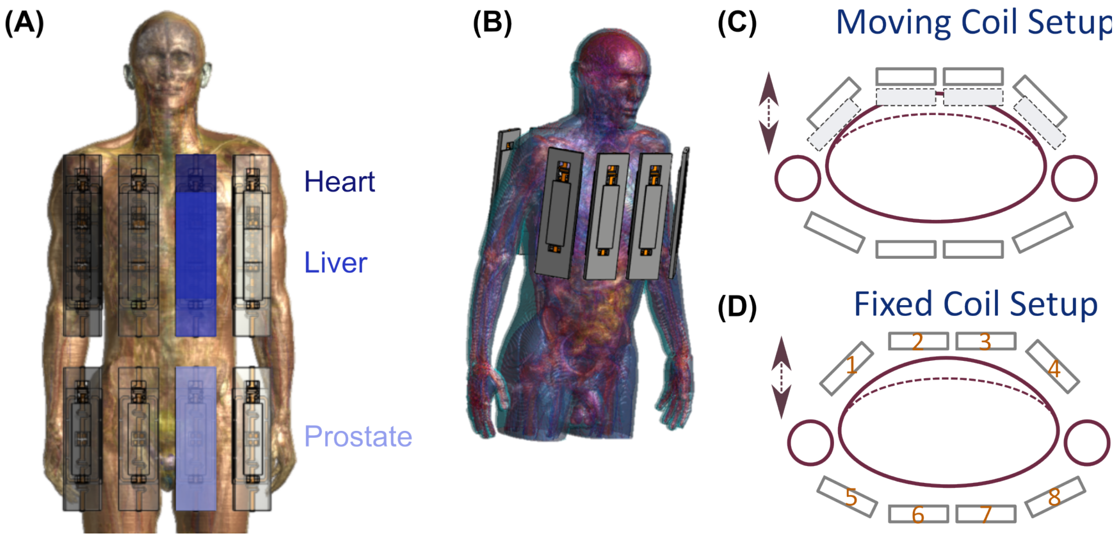

Figure 3.2.1: Body models and coil array setups utilized at 7 T are illustrated. (A) The Duke model simulation setup is investigated for three different coil positions: the center of the heart (dark blue), the center of the liver (blue) and the center of the prostate (light blue). For all positions, the power limits are determined to stay within the IEC 60601-2-33 first-level controlled mode trunk SAR limit [5]. The XCAT model (B) is investigated with two different coil array setups. The 'Moving' coil setup (C) has a constant minimum distance between the body and the coil. The 'Fixed' coil setup (D) stays rigid at one position and the coil moves under the body. In (D) the coil numeration is depicted.

direction results in a chest displacement in the anterior-posterior (AP) direction between 0 mm and 18 mm.

Out of the 5 different respiratory states generated, we designate 'R1' as exhale and 'R4' as inhale. 'R5' represents an additional scenario of increased inhalation depth, exceeding the typical measurements by 30%.

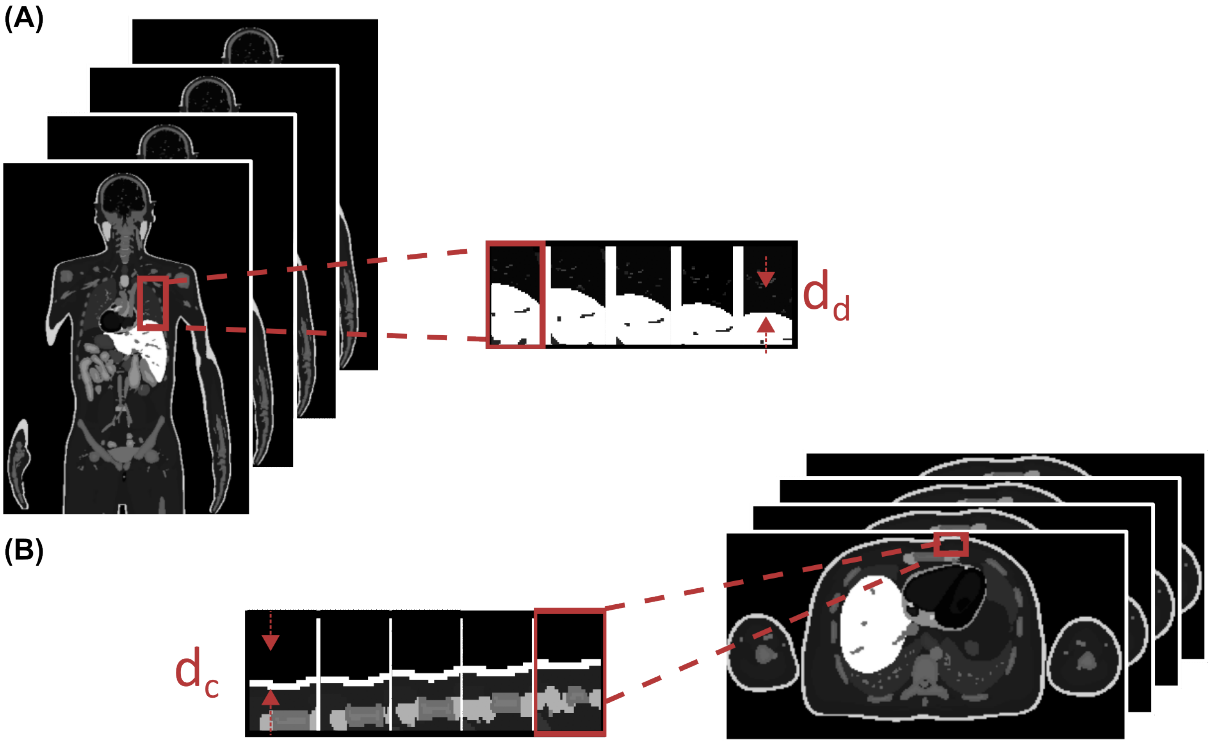

Figure 3.2.2: Investigation of the XCAT models diaphragm movement d_d (A) and chest movement d_c (B).

Breathing Pattern	**Conventional**		**Abdominal**	**Chest**
Coil Setup	**Fix**	**Moving**	**Fix**	**Moving**
d_d (mm)	[0,10,20,30]	[0,10,20,30,40]	[0,10,20,30,40]	[0,0,0,0,0]
d_c (mm)	[0,6,10,14,18]	[0,6,10,14,18]	[0,0,0,0,0,]	[0,6,10,14,18]

Table 3.2.1: XCAT parameters for different breathing patterns and coil setups. The coil setups are described in detail in the next paragraph. The diaphragm motion d_d in head-feet direction is set to be equidistant, resulting in a certain chest motion d_c in anterior-posterior direction.

The focus of this study does not involve investigating cardiac motion. The cardiac state is fixed to diastole as this is the most prevalent position of the heart. Three different breathing patterns for varying chest and diaphragm motion were modelled: ’Abdominal’ (d_c =0 mm), ’Chest’ ($d_d = 0$ mm) and conventional (’Conv’: abdominal and chest) breathing. The XCAT software generates models where distinct material types are assigned to individual voxels.

Coil Setup

Two different setups are considered in this study: First, a ’Moving’ setup: In this setup, the coil front modules moves along with respiration, ensuring a constant minimum distance between the chest and the elements. This setup was applied in our in-vivo measurements. Second, a ’Fixed’ setup: In this setup, the coil is spatially fixed at one position, with a varying minimum distance (ranging from 10 mm at inhale to 24 mm at exhale) between the chest and the elements. The simulation for R5 was not performed in this setup. It’s important to note that in both setups, the R4 respiratory state is identical, which allows further comparison of the two setups.

The coil was positioned at the central heart slice in HF direction of the XCAT model.

ROI

The region of interest (ROI) is the heart and was manually assigned.
ROI_1 represents the heart in a single transversal slice located at the iso-centre of the heart in the exhale respiratory state. The corresponding slice for the inhale respiratory state is shifted to the upper end of the heart. ROI_3 consists of three transversal slices with an equidistant spacing of 20 mm. The top slice corresponds to the slice labeled as ROI_1. ROI_H comprises 28 transversal slices with a 4 mm distance between each slice (as shown in fig. 3.2.3A). $\mathrm{ROI}_{\mathrm{SA3}}$ includes three slices along the short-axis view, spaced 20 mm apart (as shown in fig. 3.2.3B).

3.2.3 Simulation procedure

Sim4Life does not provide respiration-resolved body models. Therefore, the XCAT body models are manually implemented. The coil array is generated and EM material properties, such as electric conductivity and relative permittivity, are assigned to the respective materials by a python script.
For the XCAT model these properties are obtained from the ITIS database [72]. The ITIS database provides lung properties specifically for inhalation and exhalation. To account

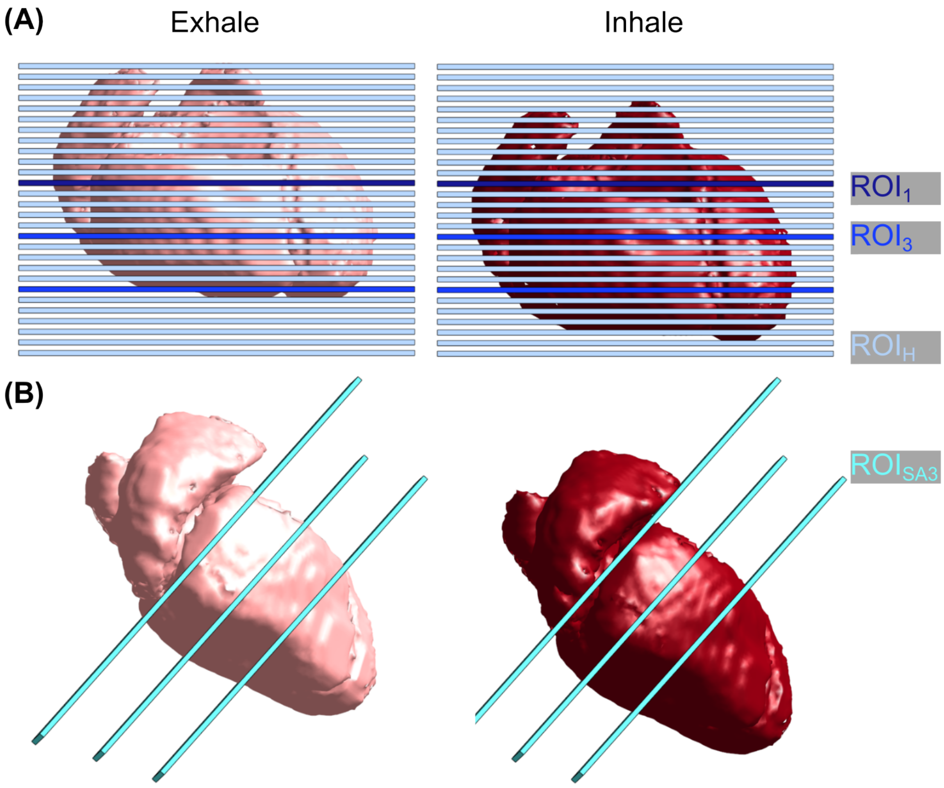

Figure 3.2.3: The heart of the XCAT model is investigated for different ROI's: In (A) transversal slices are illustrated. First, a single transversal slice ROI$_1$, located at the center of the heart during the exhale respiratory state, second, three transversal slices ROI$_3$ with an equidistant spacing of 20 mm, third, 28 transversal slices, with an equidistant spacing of 4 mm covering the full heart during the inhale and exhale respiratory state ROI$_H$. In addition, (B) shows 3 short axis view (SA) slices of the heart ROI$_{SA3}$, which are placed 20 mm apart.

for other respiratory states, the values are extrapolated linearly by considering the lung volume changes during respiration. The lung volume for the inhale respiratory state is $3.4 \cdot 10^6$ mm^3 and decreases by 30% for the exhale respiratory state.

A hexahedral FDTD mesh is generated and the voxeling is performed with a resolution of 2x2x2 mm^3 for further analysis and simulation. Finally, the EM-fields and the scattering matrix (S-Matrix) are extracted for subsequent investigations.

3.2.4 Post processing

In simulations, discrete voxels are used, rotated elements introduce staircasing artifacts that modify the length of conductors (as depicted in fig. 3.2.4A), resulting in differences in impedance and EM fields compared to non-rotated elements.

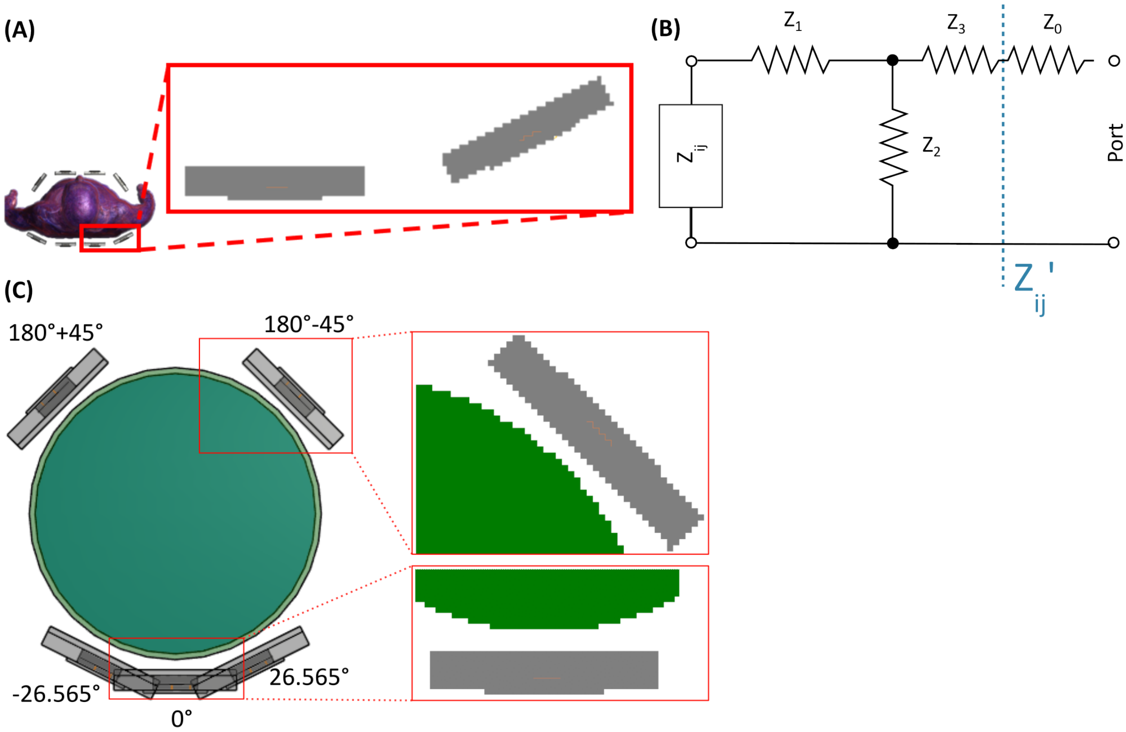

Figure 3.2.4: (A) Shows the XCAT setup, including staircaising artifacts for the rotated elements. (B) depicts the correction equivalent circuit and (C) the rotation symmetric phantom utelized to calculate the correction parameters.

Field strength	Setup	Rotation angles α_{rot} (°)
7 T	Phantom	0,26.6
7 T	XCAT	0,26.6,45
7 T	Duke	0,26.6
10.5 T	Phantom 16 modules	0,11.4,26.6
10.5 T	Phantom 8 modules	0,26.6
10.5 T	XCAT 16 modules	0,11.4,26.6,45
10.5 T	XCAT 8 modules	0,26.6,45

Table 3.2.2: Rotation angles of the coil modules for different simulation setups and field strength. The correction was done separately for α_{rot}, $-\alpha_{rot}$, $180° - \alpha_{rot}$, $180° + \alpha_{rot}$ if used in the setup.

The used rotation angles for different field strength and setups, including phantom, XCAT and Duke model simulations are given in table 3.2.2. Impedances, denoted as Z, for different rotation angles α_{rot} do not match.

$$Z_{ij}(0°) \neq Z_{ij}(11.4°) \neq Z_{ij}(26.6°) \neq Z_{ij}(45°) \tag{3.3}$$

Differences can be corrected through co-simulation in the post-processing stage. The goal is not to optimize tuning/matching or transmitted RF power, but rather to achieve the same Z-Matrix and EM fields for all rotation angles.

Impedances Z_1, Z_2, and Z_3 in a T-Type lumped element circuit (shown in fig. 3.2.4B) are adjusted for rotated elements to obtain the same impedance $Z'_{ij}(\alpha_{rot})$ as the default $Z_{ij}(0°)$ element. This adjustment is performed using a cylindrical-shaped phantom with rotation symmetric properties to ensure equal loading of each rotated element. The discrete rotation angles were chosen to ensure consistent voxeling on a 2 mm grid and realistic angulation. For example, a rotation angle of 26.6° corresponds to a voxeling of 4 mm to the right and 2 mm upward.

3.3 MR acquisitions

In-vivo and phantom MR measurements are used to validate the simulations and to establish confidence in the calculated safety limits. The phantoms are designed to result in similar EM-field distributions as the human torso in the MR scanner, which is achieved by comparing human body model simulations and phantom simulations with different material properties. After filling the phantom with a material, the conductivity σ and relative permittivity ε_r properties of the material are measured. These values are then used for the final simulations. One advantage of phantoms is that longer acquisition times are possible with the sequences, leading to higher precision than in vivo data acquisition. This allows for more accurate validation of simulation results.

In this thesis, polyvinylpyrrolidone (PVP) phantom measurements were performed at 7 T (Magnetom, Siemens Healthineers, Erlangen, Germany), to validate simulated B_1^+ maps. Saline phantom measurements were performed at a 10.5 T scanner (Magnetom, Siemens Healthineers, Erlangen, Germany). The measured slices were in the iso-center of the phantom along the long axis (HF direction).

In-vivo measurements are challenging due to the inter-subject variability, including different sizes, weights, and gender. Additionally, patient-specific intra-subject variability arising from respiratory and cardiac motion complicates the comparison to simulated models. Despite challenges in directly comparing measured in-vivo data to simulated body models, achieving a qualitative agreement between the two is often possible. While quantitative comparisons may be challenging due to inter-subject variability and other factors, qualitative assessments can still provide valuable insights and demonstrate a general agreement between the measured and simulated data.

In this thesis, in-vivo measurements were performed at the center of the heart. For all 7 T measurements -1.7 dB and for all 10.5 T measurements -3.4 dB losses were considered, including losses between the MR table coil plug and the module.
This section summarizes the used phantoms and B_1^+ mapping techniques.

3.3.1 Phantoms

For validation of the simulated coil model, single channel B_1^+ maps, simulation, and measurements were compared for a body phantom.

The PVP body phantoms utilized for measurements at 7 T are characterized by a σ of 0.586 S/m and an ε of 42.17. The dielectric properties were determined by a network analyzer using a home-built coaxial sensor. The setup is described in detail in [73].
A closed phantom was utilized for scanner measurements (fig. 3.3.1A). In contrast, H-field probe measurements were performed using an additional open body phantom, featuring a lid for inserting a H-Field probe, which is depicted in fig. 3.3.1C.

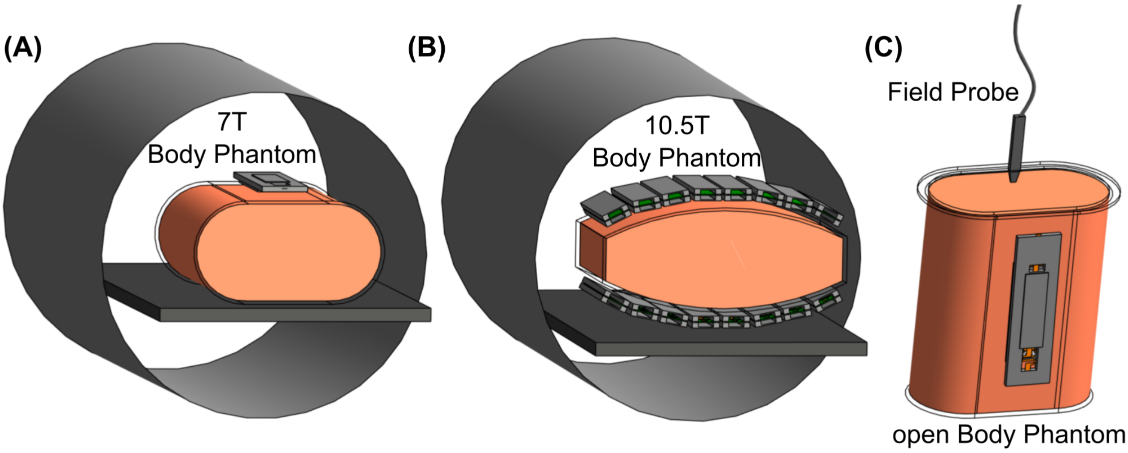

Figure 3.3.1: Schematic phantom setups are illustrated in the 7 T MR scanner with a single module placed on top of the body phantom (A). For 10.5 T the body phantom is shown inside the MR scanner with the full body coil array (B). The H-field probe setup with the upright standing open body phantom is shown with a single 7 T module (C). The field probe position is controlled by a robot, which scans the phantom with a resolution of 1cm and measures at each position B_{1x} and B_{1y}.

For 10.5 T scanner measurements a saline phantom with $\sigma = 0.5\,\mathrm{S/m}$ and $\varepsilon = 80$ was used (fig. 3.3.1B). Those dielectric properties obtained a good homogeneity and mean(B_1^+) in a central ROI of initial simulations.

3.3.2 Relative B_1^+ mapping

In-vivo data acquisition, as well as channel-wise phantom measurements at 7 T and 10.5 T, were conducted using a Gradient Echo (GRE) based sequence [74]. GRE-based sequences offer fast data acquisition, which is important for cardiac imaging under breath hold.

For in-vivo measurements at 7 T and 10.5 T the same parameters were used, summarized in table 3.3.1.

3.3.3 Absolute B_1^+ mapping

Preparation pulse sequence

For phantom data acquisition at 7 T, a saturation-based preparation pulse sequence was utilized [8].

This sequence consists of two parts: a preparation block and a readout block. The preparation block is adjusted during the measurement, while the readout block remains unchanged. The preparation voltage that needs to be set at the scanner to achieve a residual 90° flip angle is determined, and the corresponding B_1^+ value is calculated.

Therefore the signal S is measured at a location $\vec{r}$ for various preparation pulses with voltages U ranging from 150 V to 0 V in 10 V steps (fig. 3.3.2 top two rows, B_1^+ sensitive preparation) for a duration τ of 1 ms, resulting in an unknown flip angle of α at a given spatial location. The signal is normalized by S_0, which is the signal for no applied preparation pulse voltage (U = 0 V). The normalized signal $\frac{S(\vec{r})}{S_0(\vec{r})}$ is described by eq. (3.4) and fig. 3.3.3B. 1.7dB losses between the table coil plug and the cables of the modules decrease the preparation pulse voltages.

The signal of a single 2D slice is received by a GRE sequence with the readout pulse β. For a certain voltage, denoted as U_{90°, the unknown flip angle will match 90° resulting in no signal $\left(\frac{S}{S_0} = 0\right)$. The B_1^+ can be calculated pixel-wise based on U_{90°.
As determined in fig. 3.3.3C, at 55 V, the marked voxel shows no signal. The detailed equations to calculate B_1^+ from this signal are given in section A.1.1.

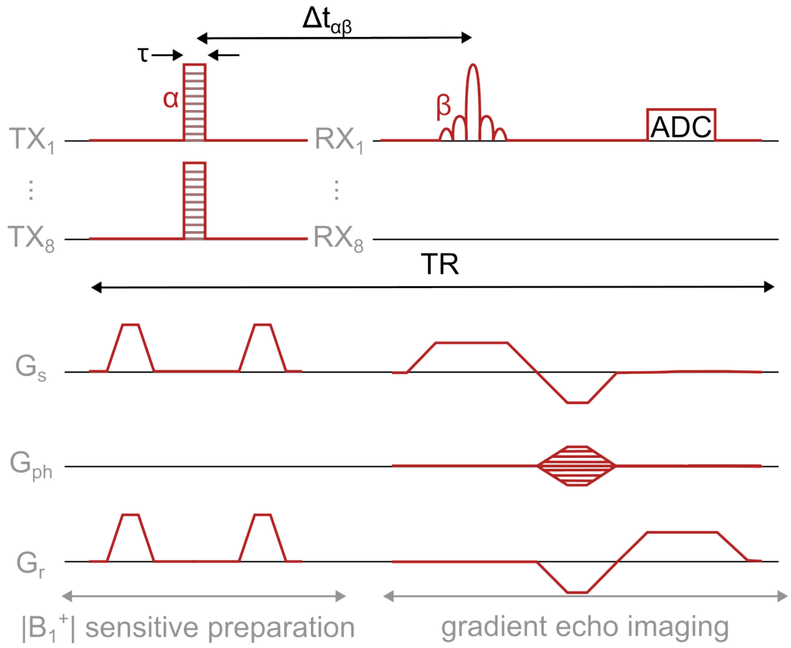

Figure 3.3.2: A sequence diagram is illustrated for the preparation pulse sequence: The top two rows show exemplary the B_1^+ sensitive preparation for the transmit channels TX_1 and TX_8. The bottom three rows illustrate the applied gradients: G_s - slice selective gradient, G_{ph} - phase encoding gradient, G_r - read out direction gradient.

$$\frac{S(\vec{r})}{S_0(\vec{r})} = \frac{1 - e^{-\frac{\Delta t_{\alpha\beta}}{T_1}}(1 - cos\alpha(\vec{r})(1 - e^{-\frac{\mathrm{TR}-\Delta t_{\alpha\beta}}{T_1}}))}{1 - e^{-\frac{\mathrm{TR}}{T_1}} cos\beta(\vec{r}) cos\alpha(\vec{r})} \tag{3.4}$$

The parameters involved in the preparation pulse sequence can be categorized into phantom-dependent and sequence-dependent parameters. The relaxation time T_1 is phantom dependent and represents the relaxation time of the longitudinal magnetization. Sequence-dependent parameters are: $\Delta t_{\alpha\beta}$, the time interval between the center of the preparation pulse and the center of the readout pulse. TR, the repetition time, refers to the duration from the start of one preparation pulse until the beginning of the subsequent preparation pulse. β, the flip angle of the readout pulse. α, the flip angle achieved by the preparation pulse applied for a duration of $\tau = 1$ ms, using different voltages U.

Actual flip angle (AFI) sequence

For 10.5 T an actual flip angle (AFI) sequence was used for 3D data acquisition with an applied shim vector [75]. The AFI applies two identical RF pulses, separated by delay times TR_1 and TR_2. The resulting fast induction decay signals S_1 and S_2 after TR_1 and

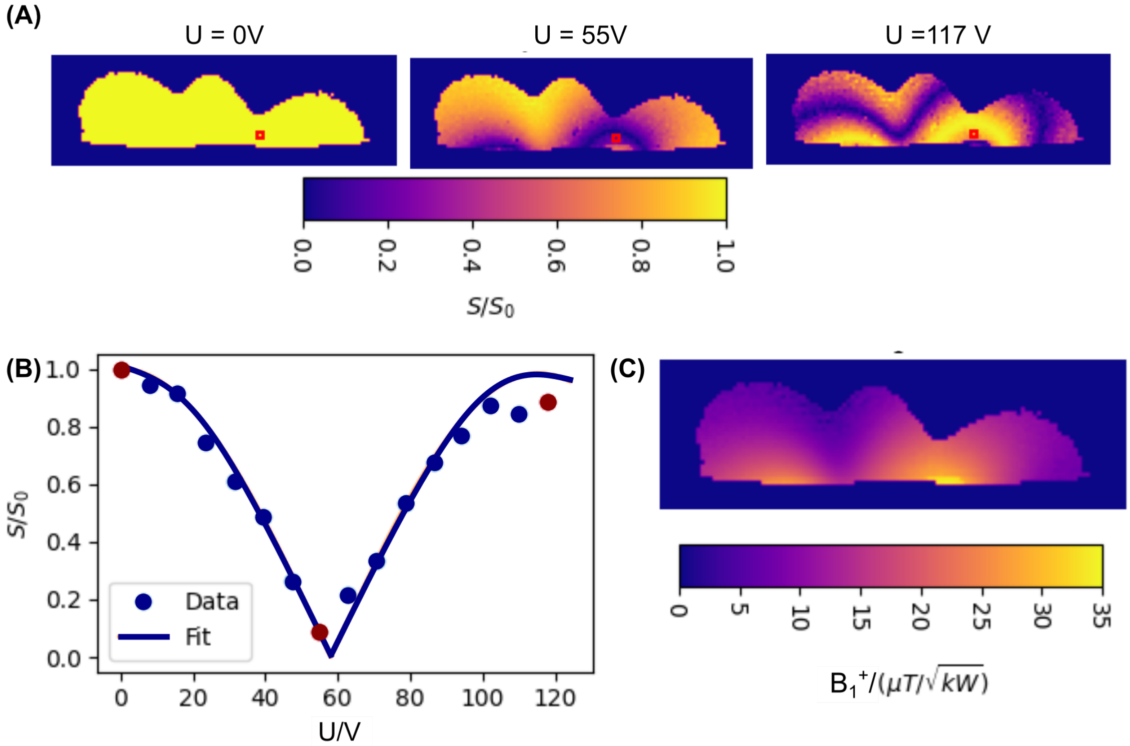

Figure 3.3.3: The preparation pulse sequence workflow is illustrated. The applied voltages are between 0 V and 150 V in 10 V steps. 1.7dB losses between the MR table coil plug and the switch box downscale the applied voltages. (A) shows the measured signal maps for three different example voltages, (B) illustrates the fitted signal for a single voxel (marked in red in (A)) and all applied downscaled voltages. The data points marked in dark red correspond to the voltages illustrated in (A). $U_{90^\circ} = 59\,\mathrm{V}$ is determined by the fit to calculate B_1^+ for the single voxel. This is repeated for all voxels in the signal maps shown in (A). In (C), the resulting B_1^+ map is shown

TR_2 are observed by a GRE sequence. The ratio $r = \frac{S_2}{S_1}$ is proportional to the FA, which is computed by:

$$FA \approx arccos\left(\frac{rn-1}{n-r}\right) \tag{3.5}$$

$n = \frac{TR_2}{TR_1}$ is the ratio of the delay times. A detailed sequence description is given in [75]. Within the flip angle ranging from 10° to 60° the AFI method exhibits high precision with errors below 2° [75].

sequence	B_0 (T) (ms)	TR (ms)	TE (mm)	FOV read	FOV phase (%)	spatial resolution (mm)	FA (°)
GRE (in-vivo)	7 , 10.5	10	1.52	384	78.1	3x3x5	5
GRE (phantom)	7	285.5	3.14	384	52.1	4x4x4	15
GRE (phantom)	10.5	50	2.19	480	41.7	2x2x5	15
prep. pulse (phantom)	7	5000	3	384	75	2x2x4	-
AFI (phantom)	10.5	60	1.8	480	41.7	2x2x2	45

Table 3.3.1: Summary of the utilized sequence parameters. For the preparation pulse sequence voltages between 0-150V in 10V steps were used.

3.4 H-Field probe

A second validation method of simulated B_1^+ maps are RF time domain field probe measurements, which determine the H-field (fig. 3.3.1). The phantom and body coil array setup is located outside an MR scanner room. An H-field probe determines the B_1^+ field generated by a 7 T body coil channel.

The body coil channel is driven by two 16-bit 4-channel arbitrary waveform generators (M4i,6622-x8, Spectrum Instrumentation GmbH, Grosshansdorf, Germany), with a sampling frequency of 400 MHz. This results in a target frequency of 297 MHz and a sideband signal of 103 MHz suppressed by a high pass filter [76]. The signal is amplified by eight broadband power amplifiers (RFPA) (ZHL-20W-13SWX+, Minicircuits, New York, USA).

The H-field probe is an optical field probe [77], which is a time domain H-field sensor (H1TDSx, Speag, Zurich, Switzerland). Typically, the signal transmission is performed by a laser (fig. 3.4.1D) transmitted over an optical fiber (fig. 3.4.1C).

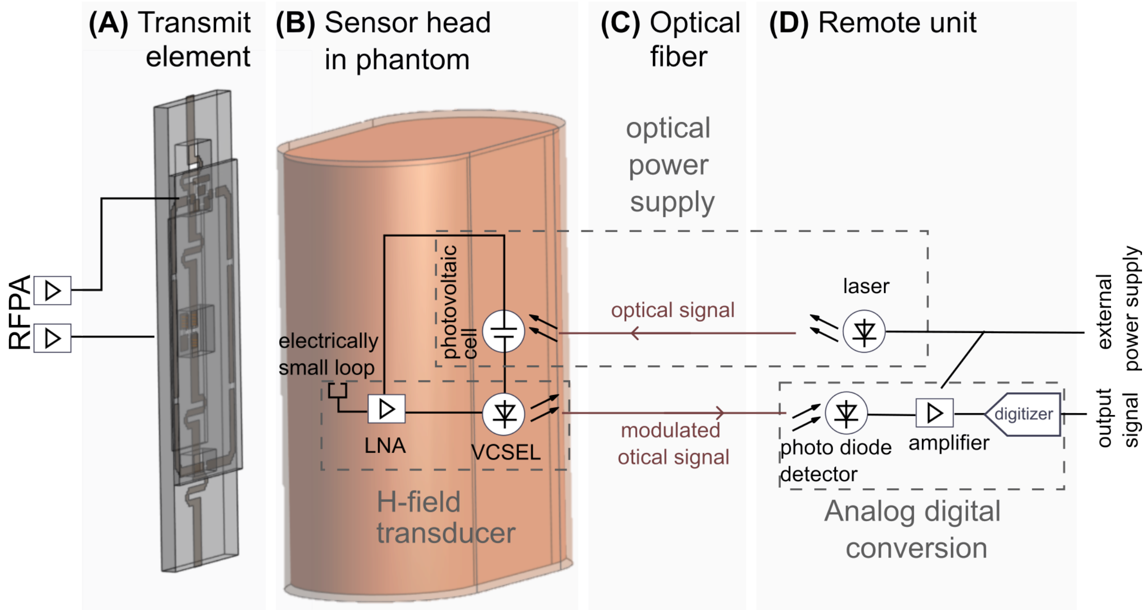

Figure 3.4.1: Schematic setup of the H-field probe measurement: In (A) the transmit channel of the 7 T body coil array is illustrated. The power supply of the transmit channel is provided by RFPAs. (B-D) illustrate a symbolic drawing of the H-field probe [77] (B) illustrates the sensor head inside the phantom, (C) depicts the optical fiber transmitting the laser signal and (D) shows the remote unit, including a laser and an analog-digital conversion setup.

The laser illuminates a photovoltaic cell inside a sensor head (fig. 3.4.1B), which is placed inside the phantom. The photovoltaic cell provides power for a low noise amplifier (LNA) and a vertical cavity surface emitting laser (VCSEL) inside the sensor head. The H-field generated by the transmitting channel (fig. 3.4.1A) induces a current in an electrically small loop antenna located in the sensor head. The current is proportional to the H-field component radial to the probe axis. To measure H_x and H_y, the antenna needs to be rotated by 90°. The received signal of the loop antenna gets amplified by the LNA and modulates the current provided for the VCSEL.

The signal is transmitted back over the optical fiber and fed into the remote unit [78]. The optical signal modulated by the H-field is used to illuminate a photodiode, and the generated voltage is fed into two 14-bit 4-channel digitizers (M4i,4451-x8, Spectrum Instrumentation GmbH, Grosshansdorf, Germany). This results in a signal intensity for the H_x and H_y components [76].

So far, the obtained signal intensity is in arbitrary units. To obtain absolute B_1^+, the signal is calibrated using a transverse electromagnetic (TEM) cell described in [79]. The TEM cell

is an open double-stripline design and the accuracy of field probe measurements strongly depends on the calibration of the field probes.
Before each H-field probe measurement in the phantom, the signal intensity of the H-field probe is measured in the TEM cell, as described in detail in [80]. Combining the known B_1 inside the TEM cell from MR scanner measurements [79] and the signal intensity of the H-field probe inside the TEM cell, leads to a scaling factor to convert the signal intensity of the H-field probe to B_{1x} and B_{1y} of which B_1^+ is calculated. The TEM cell used in this work is calibrated with an accuracy of 5% [79].

3.5 FA optimization

The non-uniformity of the transmit field in UHF MRI is addressed by the additional degrees of freedom gained by the separate control of the RF pulse phases and amplitudes (static pTx) or the application of different RF pulses (dynamic pTx) on multiple transmit channels [81].
Static pTx uses temporal constant B_1^+ fields. A direct correlation between B_1^+ and FA exists for a known RF pulse shape. In dynamic pTx, the complex weights that are applied to the RF pulses change over time, and with this, the resulting B_1^+. The final FA at the end of the RF pulse train is optimized.
This section gives an overview on static and dynamic pTx used in this work.

3.5.1 Static pTx using phase and amplitude shimming for FA optimization

Static pTx adjusts B_1^+ through the optimization of complex weights, called shim vectors, within a ROI [3]. The optimization can pursue different purposes inside a defined ROI: Such as generating uniformity, aligning the averaged phases to obtain constructive interference (efficient shim) or obtaining a homogeneous magnitude (homogeneous shim) or maximizing the minimum [3].

To determine the desired shim vectors, the approach involves solving optimization problems that aim to minimize a cost function. This cost function takes into account factors such as the spatial distribution of B_1^+ [3].
The channel-wise B_1^+ maps are imported into Matlab (Version R2020b, The Mathworks, Natick, MA, USA) and the fmincon function is used to find the minimum of a nonlinear

multivariable function, obtaining a shim vector, denoted as $\vec{u} = (u_1 \cdot e^{i\varphi_1} ... u_{N_{\mathrm{ch}}} \cdot e^{i\varphi_{N_{\mathrm{ch}}}})^T$ which minimizes the CV. u_n and φ_n are the amplitude and phase of channel n, with N_{ch} total number of channels.

To achieve a homogeneous $|B_1^+|$ inside the ROI, the coefficient of variation (CV) can be minimized [82].

$$\mathrm{CV} = \frac{\mathrm{std}(|B_1^+(\vec{r}, \vec{u})|}{\mathrm{mean}(|B_1^+(\vec{r}, \vec{u})|)} \tag{3.6}$$

In addition, shim vectors maximizing the transmit efficiency η are used.

$$\eta(\vec{r}) = \frac{\left|\sum_{\mathrm{ch}=1}^{N_{\mathrm{ch}}} B_{1,\mathrm{ch}}^+(\vec{r}, \vec{u})\right|}{\sum_{\mathrm{ch}=1}^{N_{\mathrm{ch}}} |B_{1,\mathrm{ch}}^+(\vec{r}, \vec{u})|} \tag{3.7}$$

In this thesis, the optimization process involves evaluating 1000 different initial phase sets to minimize the risk of obtaining a local minimum, which differs greatly from the global minimum. It is important to note that different starting phase sets might lead to the same local minimum of the CV or η, resulting in the same shim vector $\vec{u}$. For each local minimum the CV and the minimum B_1^+ $(\min(|B_1^+(\vec{r}, \vec{u})|))$ are recorded.
The optimization is done for 'phase shimming' with a constant amplitude of 1 and 'phase and amplitude shimming'.
The homogeneous optimization of $\vec{u}$ is performed on simulation data. The CV is optimized for the ROI during the respiratory states 'R1' (exhale only), 'R4' (inhale only), and for 'R1&R4' simultaneously.

Comparing 7 T phantom measurements and simulation was done with shim vectors maximizing the efficiency on measured data $\vec{u}_\eta^{\mathrm{meas}}$. For 10.5 T phantom measurements and simulations, a circular polarized (cp) shim vector is applied with a phase offset of 22.5° between the neighboring channels of the 16-channel coil.
Static phase shimming with $u_1 = ... = u_{N_{\mathrm{ch}}} = 1$ is mostly used in our 7 T 2D slice selective in-vivo cardiac measurements.

3.5.2 Dynamic pTx using kT points for FA optimization

In situations where static pTx proves insufficient for achieving a homogeneous FA distribution, the utilization of dynamic pTx provides enhanced degrees of freedom [3]. Dynamic pTx includes slice-selective (spokes) and non-selective (kT points and SPINS) variants, which optimize the time-variant RF pulses to obtain the desired actual flip angle distribution. The following section focuses on kT points, an excitation module consisting of a train of short, complex weighted shim vectors and gradient blips. This applies shim vectors at different excitation k-space locations [15] and goes beyond considering only time-invariant B_1^+ [3].

In this work, the optimization problem considers a root mean squared error (RMSE) term, aiming to minimize the differences between the desired target pattern m_d and the FA maps by using the magnitude least-squares solution. The small-tip-angle approximation and an interleaved greedy and local optimization are applied [83, 84]. For each kT point, the following optimization is performed to obtain the shim vectors $\vec{u}_{kT}$:

$$\vec{u}_{kT} = \arg\min_{\vec{u}_{kT}} \left(\left\| |m_d| - \left| \underline{A}(kT) \cdot \vec{u}_{kT} \right| \right\|^2 + b \|\vec{u}_{kT}\|^2 \right) \tag{3.8}$$

The accuracy of the FA within the ROI to the desired target pattern is given by the difference of m_d and the matrix-vector product of the excitation system matrix $\underline{A}(kT)$ for one kT point and $\vec{u}_{kT}$. Additionally, a regularisation parameter b is included to balance FA and RF power [15].

The optimization is done for regularisation parameters $b = b_1 \cdot 10^{b_2}$ with b_1 in range [1,9] and b_2 in range [0,6], with 5 starting sets of phase shim vectors. As the regularization parameter varies, it provides FA distribution solutions with the trade-off between the regularized solution's magnitude (RF power root mean square (RMS)) and its alignment with the provided data (FA RMSE) [85]. The obtained data set has the shape of the letter 'L' and is therefore called 'L-Curve'.

Once the L-Curve is obtained, a regularisation parameter with a trade-off between small FA RMSE and small RF power RMS is selected and with this fixed regularisation parameter, the optimization is repeated with 200 starting sets of phase shim vectors. Different starting sets can lead to the same optimized RF pulse and kT-point location. The FA maps shown in this thesis use the ideal regularisation parameter, while for safety estimations, a wider spread of possible RF pulses is used. Therefore, for each resulting RF pulse of the 200 starting phase shim vectors with a fixed regularisation parameter, the CV and mean(FA) are determined. The $\text{psSAR}_{10\text{g}}$ is calculated for each RF pulse of the full L-curve.

This work investigates a train of 2 or 4 kT-points with $kT_1, ..., kT_4$, optimizing the kT-points locations and the shim vectors $\vec{u}_{kT1}, ..., \vec{u}_{kT4}$. The kT-point location optimization always begins at the origin (0,0,0), while the shim vector amplitude always starts at $\gamma \cdot \tau$, where τ

represents the RF pulse length. kT-points are optimized on the exhale respiratory state to a desired target FA of 10°.

3.6 FA analysis

The quantification of respiration-induced changes is done by analyzing the FA for dynamic pTx and B_1^+ for static pTx. For static-pTx the FA is proportional to B_1^+. This correlation is used in the thesis for a direct comparison of static and dynamic pTx. The parameters in this section are explained using B_1^+ but are also valid for the FA.

The CV (eq. (3.6)), the $\min(B_1^+)$ and the $\mathrm{mean}(B_1^+)$ inside the ROI investigate the magnitude of B_1^+.

The coefficient of variation CV is a measure of the homogeneity. $\min(|B_1^+|)$ is an important measure for in-vivo measurements, as single $|B_1^+|$ dropouts in the ROI can lead to contrast variation in an MR image.

Channel-wise respiration-induced B_1^+ phase changes give information about possible changes in the B_1^+ interference pattern and, therefore, changes in destructive and constructive interference in the absolute superimposed channel-wise B_1^+ values obtained from parallel transmission. The phase is denoted as $\varphi(\mathrm{Ri}, \vec{r}_{center})$ at the respiratory state Ri, at the center of the heart in all three dimensions. Additionally, the mean phase and the mean gradient along the AP direction $\frac{\partial}{\partial \vec{r}_{AP}}\varphi(\mathrm{Ri}, x)$ over the full ROI are analyzed.

The respiration-induced changes are given in absolute values ΔCV:

$$\Delta\mathrm{CV} = \mathrm{CV}(\mathrm{R4}) - \mathrm{CV}(\mathrm{R1}) \tag{3.9}$$

In analogy, this is done for $\Delta\min(B_1^+)$, $\Delta\mathrm{mean}(B_1^+)$ and $\frac{\partial}{\partial \vec{r}_{AP}}\Delta\varphi(x)$.

In the results section, minimum and maximum values of CV and $\min(B_1^+)$ are stated in square brackets [min,max].

3.7 SAR analysis

The specific absorption rate is used as a risk-measure of RF induced temperature rise in biological tissue, proportional to E^2 and used by the IEC to set safety limits. The E-field cannot be directly measured and therefore, EM simulations become relevant. EM simulations and the calculation of spatial SAR distributions are presently the only practical possibility to confirm the safety compliance of a setup. SAR is a limiting factor for most UHF MR applications [86].

To ensure adherence to safety limits, different control modes can be used. This work investigates two different modes, which are applied at different sites. A SAR-controlled mode (SCM) calculates the SAR directly. To this end, precalculated Q-matrices [86] of so-called virtual observation points (VOP) [87, 88] are utilized. The power-controlled mode (PCM) calculates an upper limit of the SAR by using the triangle inequality equation. For scanner SAR supervision, the SCM needs the complex shim vectors and the PCM needs the maximum applied power of all channels.

This section introduces the correlation between E-field and SAR calculation and the concept of the two control modes. At the location $\vec{r}$ and during a sampling time period t_s, the electric field $\vec{E}(\vec{r}, t_s)$ induces a current $\vec{J}$ in the material [89].

$$\vec{J}(\vec{r}, t_s) = \sigma \cdot \vec{E}(\vec{r}, t_s) \tag{3.10}$$

The current inside the material leads to a power deposition $P(\vec{r}, t_s)$, which causes a temperature increase in the human body.

$$P(\vec{r}, t_s) = \sigma \cdot ||\vec{E}(\vec{r}, t_s)||^2 \tag{3.11}$$

This temperature increase can be controlled if SAR is controlled. The relationship between temperature increase and SAR is under certain approximative assumptions given by Pennes' bioheat equation [89]. The SAR is the power deposited per mass density in a specific averaging Volume V [86].

$$\mathrm{SAR}(\vec{r}, t_s) = \frac{1}{V} \int_V \frac{\sigma \cdot ||\vec{E}(\vec{r}, t_s)||^2}{\rho \cdot 2} dV \tag{3.12}$$

The total E-field is the sum of the single channel E_{ch} fields and can be expressed by

$$\vec{E}(\vec{r}, t_s) = \sum_{\text{ch}=1}^{N_{\text{ch}}} \vec{E}_{ch}(\vec{r}, t_s) = \underline{E}(\vec{r}) \cdot \vec{u}(t_s) \ , \tag{3.13}$$

where N_{ch} is the total number of pTx channels. Using eq. (3.12) the $\text{SAR}(\vec{r}, t_s)$ can be expressed as

$$\text{SAR}(\vec{r}, t_s) = \frac{1}{V} \int_V \frac{\sigma}{2\rho} \cdot ||\underline{E}(\vec{r}) \cdot \vec{u}(t_s)||^2 dV \tag{3.14}$$

$$\text{SAR}(\vec{r}, t_s) = u^{\dagger}(t_s) \cdot \frac{1}{V} \int_V \frac{\sigma}{\rho \cdot 2} \cdot \underline{E}^{\dagger}(\vec{r}) \cdot \underline{E}(\vec{r}) dV \cdot \vec{u}(t_s) \tag{3.15}$$

at this point Graesselin et al. [86] introduces the Q-matrix $\underline{Q}(\vec{r}) = \frac{1}{V} \int_V \frac{\sigma}{\rho \cdot 2} \cdot \underline{E}^{\dagger}(\vec{r}) \cdot \underline{E}(\vec{r}) dV$. This simplifies eq. (3.15) to:

$$\text{SAR}(\vec{r}, \vec{u}) = \vec{u}^{\dagger}(t_s) \cdot \underline{Q}(\vec{r}) \cdot \vec{u}(t_s) \tag{3.16}$$

The SAR is evaluated voxelwise at each position $\vec{r}$ for the full body. As an averaging volume, the IEC standards use the volume of a 10g mass. The averaged quantities are called $\underline{Q}_{\text{10g}}$ and $\text{SAR}_{\text{10g}}(\vec{r}, \text{Ri}, \vec{u})$.

To minimize the computational effort, virtual observation points (VOPs) were calculated [87, 88]. VOPs typically reduce the number of Q-matrices from millions to several hundred. Similar Q-matrices are represented in one VOP Q-matrix, which slightly overestimates local SAR for all considered matrices. One VOP Q-Matrix stands for multiple locations of all original Q-Matrices.

To calculate SAR_{10g} for RF pulses using dynamic pTx with four kT points and four RF pulses of the same pulse length, the SAR values of the RF pulses at each kT point are summed.

$$\text{SAR}_{\text{10g}}(Q_{\text{10g}}, \vec{r}, \vec{u}_{kT_1}, ...\vec{u}_{kT_4}) = \sum_{kT_j = kT_1}^{kT_4} \text{SAR}_{\text{10g}}(Q_{\text{10g}}, \vec{r}, \vec{u}_{kT_j}) \tag{3.17}$$

The peak spatial SAR $\text{psSAR}_{\text{10g}}(Q_{\text{10g}}, \vec{r}, \vec{u}_{kT_1}, ...\vec{u}_{kT_4})$ represents the maximum value of $\text{SAR}_{\text{10g}}(Q_{\text{10g}}, \vec{r}, \vec{u}_{kT_1}, ...\vec{u}_{kT_4})$ across all locations $\vec{r}$.

The volume of the unit mass can be approximated by a unit volume (10cm^3) [90], this is applied in this thesis. In this work, different Q-matrices ($\underline{Q}(\vec{r}, \text{Ri})$) are used for different respiratory states Ri. In images the SAR is visualized as maximum intensity projections (MIP) in HF direction.

For VOP calculation, an overestimation of 1% is used, which results to 250-300 VOPs. Independent VOP sets are calculated for five respiratory states and two coil setups. The respiratory impact on SAR is evaluated by two different supervision modes. The SCM uses the VOPs and applies individual shim vectors on the VOPs to calculate shim vector-dependent SAR. The PCM calculates a maximum permitted RF amplitude per channel. The SAR of all shim vectors with equal or smaller amplitudes is then ensured to keep the local and global IEC SAR limits. Notably, this calculation is independent of the channel phases. For both control modes, the respiration-induced changes are expressed by a normalisation on the first level controlled IEC SAR limits:

$$\Delta \mathrm{psSAR}_{10\mathrm{g}} = \frac{\mathrm{psSAR}_{10\mathrm{g}}(\mathrm{R4}) - 20\,\mathrm{W/kg}}{20\,\mathrm{W/kg}} \tag{3.18}$$

3.7.1 SAR controlled mode

This SAR-controlled mode allows to calculate the shim vector dependent $\mathrm{psSAR}_{10\mathrm{g}}$ on the fly at the scanner. Several VOP Q-matrices often of multiple body shapes are stored and the required shim vector is applied to all VOP Q-matrices (eq. (3.16)). This method is used by various sites [91–96].

In this thesis the shim vectors are afterwards scaled by a factor c_{SCM}. Including this scaling factor a $\mathrm{psSAR}_{10\mathrm{g}}$ value matching a pre set limit is obtained, e.g. IEC 60601-2-33 first level controlled mode trunk SAR limit for 6 min [5]. The new shim vector is denoted as $\vec{u}_{\mathrm{SCM}} = c_{\mathrm{SCM}} \cdot \vec{u}$ and the new $\mathrm{psSAR}_{10\mathrm{g}}$ is notated as $\mathrm{psSAR}_{10\mathrm{g}}(\vec{u}_{\mathrm{SCM}})$. In this thesis c_{SCM} is selected to scale the exhale respiratory state $\mathrm{psSAR}_{10\mathrm{g}}(\vec{u}_{\mathrm{SCM}}, \mathrm{R1})$ to 20 W/kg. The same $\vec{u}_{\mathrm{SCM}}$ is applied to the inhale respiratory state $\mathrm{psSAR}_{10\mathrm{g}}$. $\mathrm{psSAR}_{10\mathrm{g}}(\vec{u}_{\mathrm{SCM}}, \mathrm{R4})$ unequal to 20 W/kg are expected. For static pTx at 7 T, calculations are performed for $2 \cdot 10^6$ random shim vectors, including 10^6 random phase shim vectors and 10^6 random phase and amplitude shim vectors. Figure A.2.1 shows the uniform distribution of the amplitude and phase of the random shim vectors. Additionally, $\mathrm{psSAR}_{10\mathrm{g}}(\vec{u}_{\mathrm{SCM}})$ is calculated for a set of RF pulses that are optimized to obtain low CV for static pTX and a mean(FA) of 10° for dynamic pTx. Therefore, 200 starting sets of different phase vectors are used for the optimization process.

According to eq. (3.18) the respiratory changes $\Delta\mathrm{psSAR}_{10\mathrm{g}}(\vec{u}_{\mathrm{SCM}})$ are calculated.

3.7.2 Power controlled mode

Another more conservative approach is a pre calculated power limit per channel [10, 13, 97–100]. This mode controls only the maximum channel-wise amplitude $\vec{u}_{\mathrm{PCM}}^{\max}$ applied during the scan and is phase independent. The upper SAR boundary for each location is given by the triangle inequality equation using the supremum norm $||\ ||_\infty$.

$$\mathrm{SAR}_{10\mathrm{g}}(\vec{r}, \mathrm{R1}, \vec{u}) \leq ||\vec{u}||_\infty^2 \sum_{i,j=1}^{N_{\mathrm{ch}},N_{\mathrm{ch}}} \left| Q_{10\mathrm{g}}^{i,j}(\vec{r}, \mathrm{R1}) \right| \tag{3.19}$$

Using eq. (3.19), the maximum amplitude, $u_{\mathrm{PCM}}^{\max}$, can be computed in a way that ensures compliance with the IEC standard limit of 20 W/kg for the exhale respiratory state, all spatial locations $\vec{r}$ and for any shim vector $\vec{u}_{\mathrm{PCM}}$ with a maximum norm $||\vec{u}_{\mathrm{PCM}}||_\infty \leq u_{\mathrm{PCM}}^{\max}$:

$$\mathrm{psSAR}_{10\mathrm{g}}(\mathrm{R1}, u_{\mathrm{PCM}}^{\max}) = \max_{\vec{r}} \left((u_{\mathrm{PCM}}^{\max})^2 \sum_{i,j=1}^{N_{\mathrm{ch}},N_{\mathrm{ch}}} \left| Q_{10\mathrm{g}}^{i,j}(\vec{r}, \mathrm{R1}) \right| \right) = 20\,\mathrm{W/kg} \tag{3.20}$$

The amplitude $u_{\mathrm{PCM}}^{\max}$ is the same for all channels. $u_{\mathrm{PCM}}^{\max}$ is applied to calculate $\mathrm{psSAR}_{10\mathrm{g}}(\mathrm{Ri}, u_{\mathrm{PCM}}^{\max})$ for the other respiratory states. $\mathrm{psSAR}_{10\mathrm{g}}(\mathrm{Ri}, u_{\mathrm{PCM}}^{\max})$ is an upper limit for the $\mathrm{psSAR}_{10\mathrm{g}}(\mathrm{Ri}, \vec{u}_{\mathrm{PCM}})$ considering shim vectors $\vec{u}_{\mathrm{PCM}}$ with all possible combinations of amplitudes and phases, that do not exceed the channel amplitude of $u_{\mathrm{PCM}}^{\max}$.

In summary:

$$\mathrm{psSAR}_{10\mathrm{g}}(\mathrm{R1}, \vec{u}_{\mathrm{SCM}}) = \mathrm{psSAR}_{10\mathrm{g}}(\mathrm{R1}, u_{\mathrm{PCM}}^{\max}) = 20\,\mathrm{W/kg} > \mathrm{psSAR}_{10\mathrm{g}}(\mathrm{R1}, \vec{u}_{\mathrm{PCM}}). \tag{3.21}$$

According to eq. (3.18) the $\Delta psSAR_{10\mathrm{g}}(\vec{u}_{\mathrm{PCM}})$ and $\Delta psSAR_{10\mathrm{g}}(u_{\mathrm{PCM}}^{\max})$ are calculated. Please note $\Delta\mathrm{psSAR}_{10\mathrm{g}}(\vec{u}_{\mathrm{SCM}})$ and $\Delta\mathrm{psSAR}_{10\mathrm{g}}(\vec{u}_{\mathrm{PCM}})$ are calculated for a range of $2 \cdot 10^6$ shim vectors, while $\mathrm{psSAR}_{10\mathrm{g}}(\mathrm{R1}, u_{\mathrm{PCM}}^{\max})$ is a single value giving the upper boundary for $\Delta\mathrm{psSAR}_{10\mathrm{g}}(\vec{u}_{\mathrm{PCM}})$. A summary of the most important variables is given in table 3.9.1.

3.7.3 Power limit calculation

For power limit calculation, the PCM was used. The upper SAR limit, which holds for any conceivable shim vector with a given maximum channel amplitude, was calculated.

The parameter $P_{\text{fwd}}^{\max} = \left(u_{\text{PCM}}^{\max}\right)^2$ is the maximum allowed upper forward power to stay below 20 W/kg. This calculation was done independent of respiration with the Duke model and was used for the safety assessment process of the 7 T body array coil for in-vivo measurements.

As an additional measure, the whole body SAR ($\text{wbSAR}_{10\text{g}}(P_{\text{fwd}}^{\max})$) was determined for safety estimations, using the voxel volume V_{voxel} and the mass of the simulated body m.

$$\text{wbSAR}_{10\text{g}}(P_{\text{fwd}}^{\max}) \leq \frac{V_{\text{voxel}}}{m} \cdot P_{\text{fwd}}^{\max} \sum_{i,j} \sum_{\vec{r}} Q_{10\text{g}}^{i,j}(\vec{r}) \cdot \rho(\vec{r}) \tag{3.22}$$

This thesis uses the conservative PCM, which calculates an upper SAR boundary, of which an upper channel-wise power limit is calculated for the coil array safety assessment. Other sites use approaches such as the SCM, which are shim-dependent SAR calculations on VOPs.

3.8 Scattering matrix

The Scattering matrix (S-matrix) is related to the forward voltage and reflected voltage of the coil array channels. Coupling between channels and variations in the reflected port voltages are indicated.

1988 Buikmann et al. [101] showed the possibility of using the S-Matrix of RF coils as respiratory and cardiac motion detectors and performing respiratory gating with this method at 2 T. 30 years later in 2018 Hess et al. [102] used the same principle for 7 T measurements.

The coupling between different coil element as well as the power reflected by each element depend on the loading of theses elements by the subject's body and therefore on the material conductivities of the body. Changes, for example, due to respiratory motion, induce changes in the reflected voltages in the RF coil channels and thus the S-Matrix [102]. In a multichannel transmit array, the relations between forward and reflected voltages for each channel while applying an RF pulse at a specific channel are saved in an S-matrix . The S-matrix can be monitored by the directional couplers (DICOs), as the reflected RF power is used for intrinsic safety supervision during RF pulse application [102].

This section describes the concept of the scattering matrix and its correlation with the material conductivity and with this respiration-dependency. The S-Matrix is related to the forward $\vec{v}_{\mathrm{fwd}}$ and return $\vec{v}_{\mathrm{ret}}$ voltage of the coil array, which are measured by the DICOs at an MR scanner [102]. The used coil array is an N_{ch} port network.

$$\vec{v}_{\mathrm{ret}} = \underline{S}\,\vec{v}_{\mathrm{fwd}} \tag{3.23}$$

The impedance matrix $\underline{Z}$ characterizes the load of the network and depends on the tissue properties near the channel of the body-coil. The relation between $\underline{Z}$ and $\underline{S}$ is described by eq. (3.24) with a characteristic impedance Z_0 ($= 50\,\Omega$) and the identity matrix $\mathbb{1}$ [102, 103].

$$\underline{Z}(t) = Z_0 \cdot (\mathbb{1} + \underline{S}) \cdot (\mathbb{1} - \underline{S})^{-1} \tag{3.24}$$

The Z-Matrix element m,l is proportional to the dot product of the current density vector (a vector in the x,y,z space) per unit input current at the channel m ($\vec{J}_m(\vec{r}, \mathrm{Ri})$) and channel l ($\vec{J}_l(\vec{r}, \mathrm{Ri})$)), in the measurement volume V. Changes in current density at location $\vec{r}$ resulting from the varying respiratory states Ri's deforming effect on the human body are taken into account. Additionally, changes in the lung volume's complex conductivity $\sigma(\vec{r}, \mathrm{Ri})$ resulting from respiration are also considered [102, 104].

$$Z_{m,l} = \int_V \frac{1}{\sigma(\vec{r}, \mathrm{Ri})} \vec{J}_m(\vec{r}, \mathrm{Ri}) \cdot \vec{J}_l(\vec{r}, \mathrm{Ri}) dV \tag{3.25}$$

The S-Matrix function comprises of a temporal invariant $\underline{S}_0$, and a respiration state dependent $\Delta\underline{S}_{\mathrm{motion}}(\mathrm{Ri})$. In this work, $\underline{S}_0$ is considered to be the S-matrix for the respiratory exhale state.

$$\underline{S}(\mathrm{Ri}) = \underline{S}_0 + \Delta\underline{S}_{\mathrm{motion}}(\mathrm{Ri}) \tag{3.26}$$

3.9 Overview important variables

EM-field	Derived Quantity	Description	Phase dependence
$\lvert B_1^+\rvert$-field	CV	Homogeneity	Yes
	$\min(B_1^+)$	Minimum value of B_1^+	Yes
	$\mathrm{mean}(B_1^+)$	Mean value of B_1^+	Yes
E-field	$\mathrm{psSAR}_{10\mathrm{g}}(\mathrm{Ri}, \vec{u}_{\mathrm{SCM}})$	Peak spatial SAR, with individual shim vector normalization to 20 W/kg for exhale	Yes
	$\mathrm{psSAR}_{10\mathrm{g}}(\mathrm{Ri}, \vec{u}_{\mathrm{PCM}})$	Peak spatial SAR, with individual shim vector normalization by the amplitude $u_{\mathrm{PCM}}^{\mathrm{max}}$, leading to a maximum exhale $\mathrm{psSAR}_{10\mathrm{g}}$ of 20 W/kg for all shim vectors $\vec{u}_{\mathrm{PCM}}$	Yes
	$\mathrm{psSAR}_{10\mathrm{g}}(\mathrm{Ri}, u_{\mathrm{PCM}}^{\mathrm{max}})$	Upper peak spatial SAR boundary value for all shim vectors $\vec{u}_{\mathrm{PCM}}$ is normalized to 20 W/kg for exhale with the maximum applicable amplitude $u_{\mathrm{PCM}}^{\mathrm{max}}$	No
	$\mathrm{wbSAR}(P_{\mathrm{fwd}}^{\mathrm{max}})$	whole body SAR	No
Power	$P_{\mathrm{fwd}}^{\mathrm{max}}$	maximum allowed applicable power to stay within IEC 60601-2-33 first level controlled mode trunk SAR limit[5] for the 7 T body coil array.	No
S-Matrix	$\underline{S}(\mathrm{Ri}) = \underline{S}_0 + \Delta\underline{S}_{\mathrm{motion}}(\mathrm{Ri})$	The scattering matrix is the sum of a respiration-independent part and a respiration-dependent part. In this work the respiration-independent part is considered to be the S-matrix of the exhale respiratory state.	No

Table 3.9.1: This table shows a summary of all relevant derived quantities for the result and discussion sections.

Chapter

4 Coil validation and calculation of power limits

The value of a simulation study is enhanced when the coil model can be validated through phantom measurements. This validation process increases the confidence in the simulations and the corresponding calculated safety limits.

This section shows element-wise B_1^+ comparison of simulations and MR scanner measurements for 7 T and 10.5 T. For 7 T additional element-wise H-field probe measurements are shown, and power limit calculations are performed for safety compliance with the IEC60601-2-33 first level controlled mode SAR limit for the trunk.

4.1 Single-channel B_1^+ map validation at 7 T

This section compares simulated and measured B_1^+ maps for 'L' and 'D' channels at 7T. To obtain single-channel B_1^+ measurements, a preparation pulse sequence (section 3.3.3) was used at the MR scanner, and additional H-field probe measurements (section 3.4) were conducted. Parts of the results displayed in this section were introduced in a recent Master thesis [80], which I co-supervised.

The AFI sequence was utilized for absolute B_1^+ mapping and a GRE-based sequence (section 3.3.2) was used for relative B_1^+ mapping in the measurements with 8 Tx channels.

Dipole channel B_1^+ map validation at 7 T

The single-channel dipole B_1^+ maps depicted in fig. 4.1.1A show a good qualitative agreement between field probe and scanner measurement. The field probe is capable of determining $|B_1^+|$ for low field regions but is constrained by the setup to obtain values close to the phantom border. The right-left (RL) line plot indicates a higher signal at the right-hand side in the plot of the scanner measurement in comparison to the H-field probe measurement. In the AP line plot, deviations below 10% are observed above $6.2\,\mu\mathrm{T}/\sqrt{\mathrm{kW}}$ between the B_1^+ magnitude of the H-field probe and the MR-scanner measurement. Comparing the measurements to the simulation, quantitative differences are observed.
At a central RL position and with 28 mm distance in AP direction to the phantom border the simulation has a $|B_1^+|$ of $18.5\,\mu\mathrm{T}/\sqrt{\mathrm{kW}}$, while scanner/H-field probe show smaller values of $12.5\,\mu\mathrm{T}/\sqrt{\mathrm{kW}}/12.7\,\mu\mathrm{T}/\sqrt{\mathrm{kW}}$. The simulation shows approximately 46% higher signal.

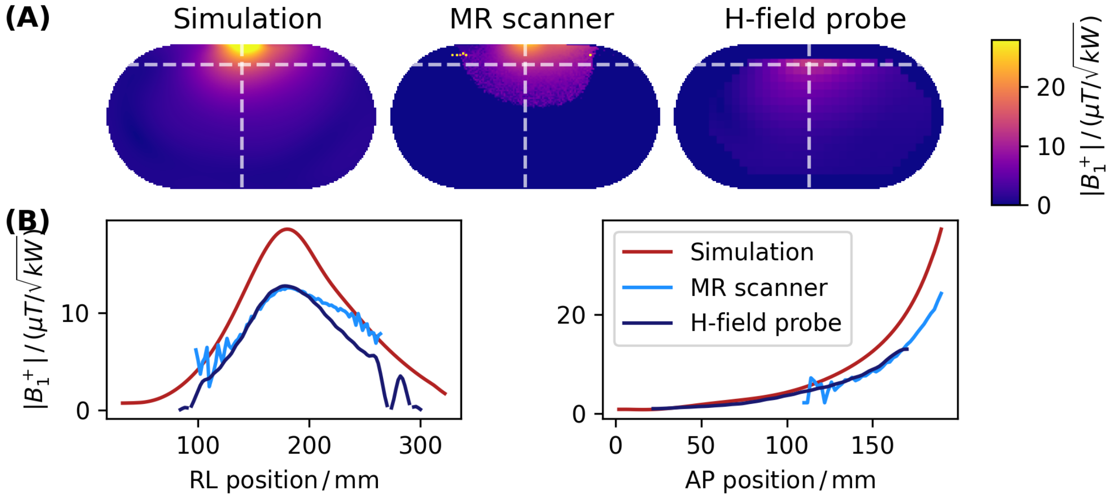

Figure 4.1.1: A single 'D' element was measured at a body phantom, the channel-wise $|B_1^+|$ data is investigated: Simulated, MR scanner preparation pulse sequence measured and H-field probe measured $|B_1^+|$ maps are compared in (A) and line plots along RL and AP direction of the maps are compared in (B). The locations of the line plots are illustrated by white dashed lines in (A).

Loop channel B_1^+ map validation at 7 T

To achieve good agreement between simulation and measurement for the loop, element losses were evaluated in advance. The loop element's ohmic losses are determined by

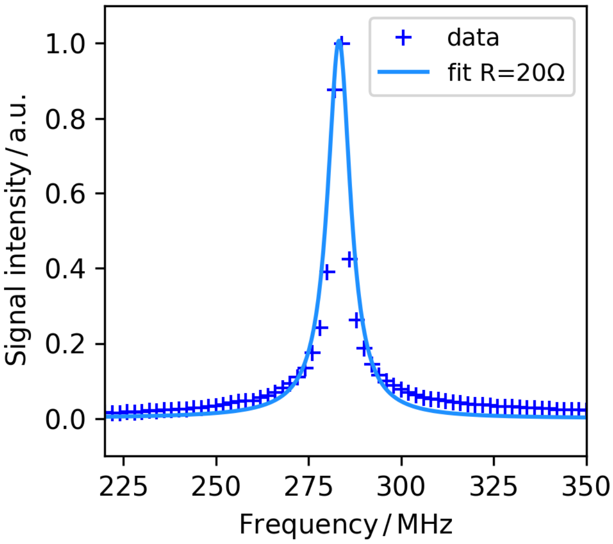

Figure 4.1.2: Measurement of the Q-factor of the ’L’ element. The total ohmic losses in the ’L’ (material losses, soldering losses, lumped element losses) were determined by using a pickup coil. The best fit was obtained by ohmic losses of 20 Ω. An off-resonance of 7.6 MHz for 7 T applications is observed.

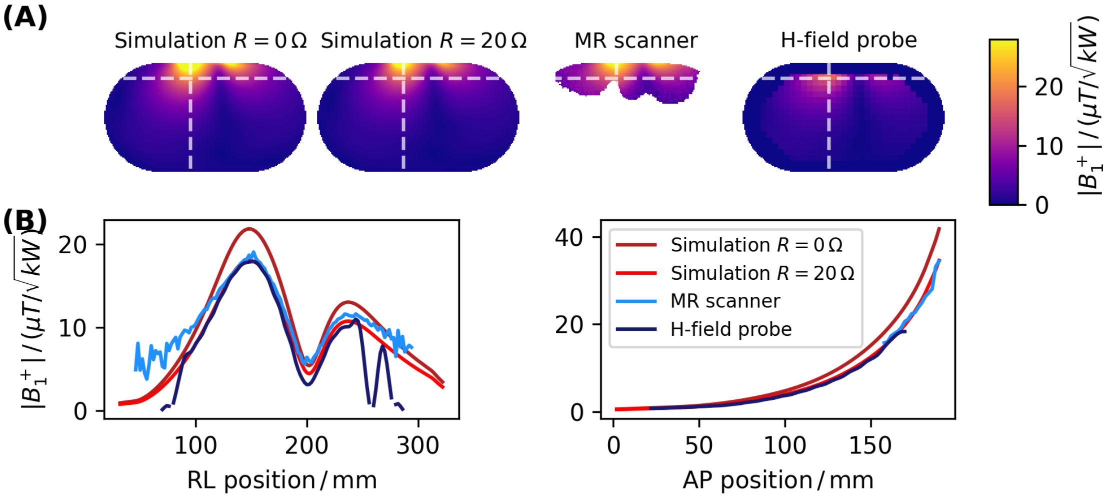

Figure 4.1.3: A single ’L’ element was measured at a body phantom, the channel-wise $|B_1^+|$ data is investigated: Simulated, MR scanner preparation pulse sequence measured and H-field probe measured $|B_1^+|$ maps are compared in (A) and line plots along RL and AP direction of the maps are compared in (B). The locations of the line plots are illustrated by white dashed lines in (A).

fitting a Lorentz function to its resonance peak, which is measured through a pickup coil. This results in a Q-factor of $Q = f_0/\mathrm{FWHM} = 37.6$. The full width at half maximum (FWHM) of the resonance peak, which is proportional to the ohmic losses, is 7.6 MHz as described in section 3.1.1. This indicates ohmic losses of 20 Ω (fig. 4.1.2), which are implemented symmetrically to the lattice balun, 10 Ω right of lattice balun, 10 Ω left of lattice balun. The measurement showed that the resonance frequency of the 'L' is 13.8 MHz off the resonance frequency of 7 T.

The single-channel loop measurements show a good agreement with the simulation in field pattern and $|B_1^+|$ values when a 20 Ω resistor is added to the simulations. In the left column of fig. 4.1.3B, the left maxima in the RL line plots (distance to phantom boundary 28 mm) show $|B_1^+|$ values of 18.0 $\frac{\mu\mathrm{T}}{\sqrt{\mathrm{kW}}}$ for the simulation and 18.4 $\frac{\mu\mathrm{T}}{\sqrt{\mathrm{kW}}}$/17.9 $\frac{\mu\mathrm{T}}{\sqrt{\mathrm{kW}}}$ for the scanner/H-field probe measurement.

4.2 Eight modules setup: B_1^+ map validation at 7 T

For a qualitative comparison of an 8Tx-channel setup, absolute B_1^+ maps and relative phase B_1^+ maps with respect to channel 3 are acquired using a preparation pulse (section 3.3.3) and GRE-based sequence (section 3.3.2). B_1^+ magnitude and relative phase maps are illustrated for two example channels, one central channel (D2 & L2) and one outer channel (D4 & L4), in figs. 4.2.1 and 4.2.2. The B_1^+ maps for all elements are shown in figs. A.1.1 and A.1.2.

In principle, a qualitative agreement of the B_1^+ channel-wise magnitude maps is observed, while qualitative differences are seen in the channel-wise B_1^+ phase maps. Channel-wise B_1^+ magnitude maps show quantitative variations with larger simulated values than measured values for the central 'D' elements (fig. 4.2.2) and smaller simulated than measured values for the rotated 'L' elements (fig. 4.2.1). In addition, the phase maps relative to channel 3 of both element types have regions with qualitative deviations between measurement and simulation. For instance, the line plot for the relative phase of 'L2' (fig. 4.2.1) indicates a minimum at 150 mm, which is not observed in the simulations. Additionally, the relative phase map of channel D4 indicates a discrepancy between measured and simulated relative B_1^+ phase data in the left region of the phantom.

So far, channel-wise maps have been investigated. As a next step, an efficient shim vector was applied to the eight transmit channels. A comparison was made between simulated data and measured data through an absolute measurement utilizing the preparation pulse sequence explained in section 3.3.3. An efficient shim vector, optimized for the center of the phantom in the measured data $\vec{u}_\eta^{\mathrm{meas}}$, was applied during both the preparation pulse

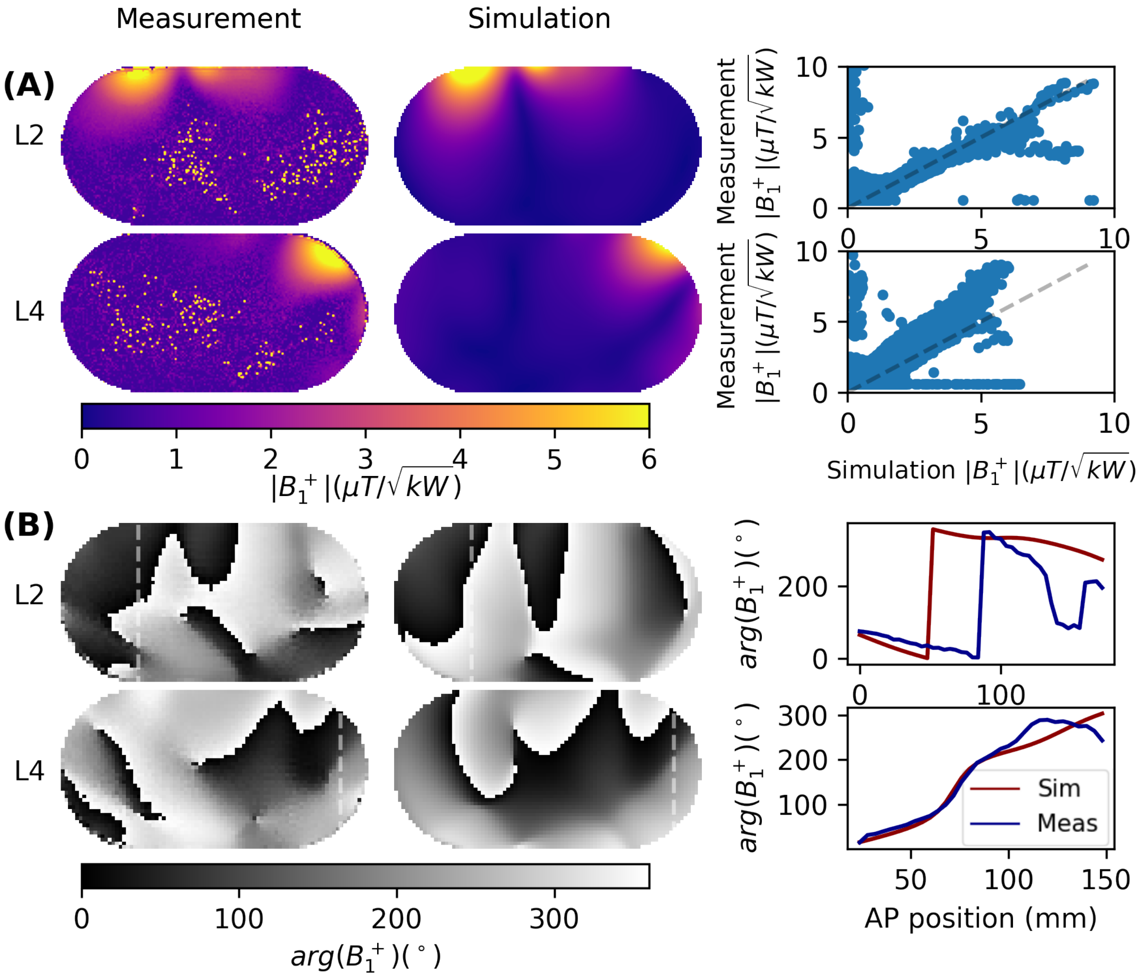

Figure 4.2.1: Channel-wise B_1^+ for an inner 'L' channel (L2) and an outer 'L' channel (L4): A setup with a phantom and eight modules was used to compare absolute B_1^+ maps (A) and phase B_1^+ maps (B) of measurements (left column) and simulations (central column). The right column shows correlation plots between measured and simulated data in (A) and phase line plots for measured (dark blue) and simulated data (dark red) in (B). The line plot positions are indicated by white dashed lines in the phase maps and are located at the RL position of the $|B_1^+|$ maxima. The measured $|B_1^+|$ data is acquired with the preparation pulse method and the measured phase data is acquired with a GRE sequence.

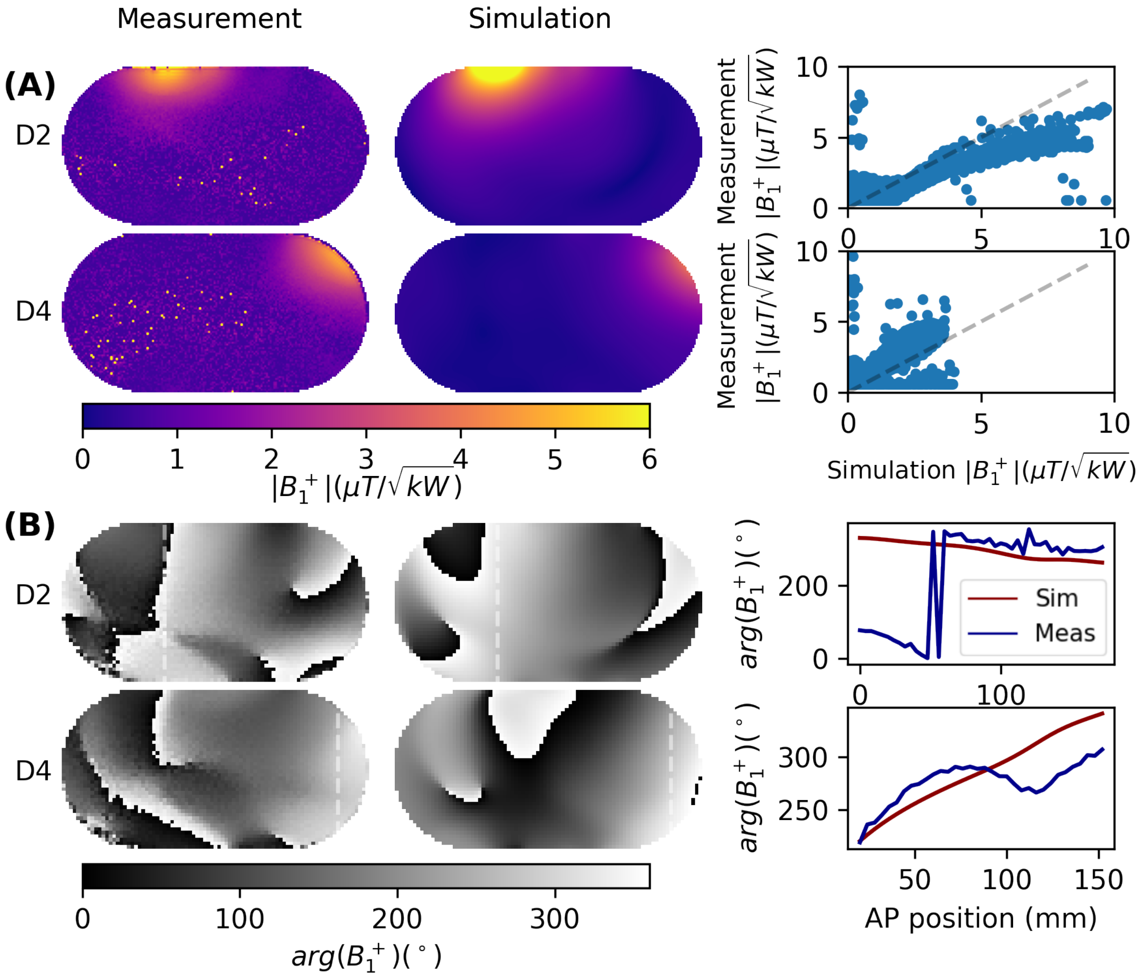

Figure 4.2.2: Channel-wise B_1^+ for an inner 'D' channel (D2) and an outer 'D' channel (D4): A setup with a phantom and eight modules was used to compare absolute B_1^+ maps (A) and phase B_1^+ maps (B) of measurements (left column) and simulations (central column). The right column shows correlation plots between measured and simulated data in (A) and phase line plots for measured (dark blue) and simulated (dark red) data in (B). The line plot positions are indicated by white dashed lines in the phase maps and are located at the RL position of the $|B_1^+|$ maxima. The measured $|B_1^+|$ data is acquired with the preparation pulse method and the measured phase data is acquired with a GRE sequence.

measurement and for the simulated channel-wise data (figs. 4.2.3 to 4.2.5). Additionally, the SOM was calculated for the simulated data. On the simulated $|B_1^+|$ maps 1.7 dB losses were applied.

In general, there is a good qualitative agreement in the $|B_1^+|$ pattern achieved by the efficient shim vector applied to Tx-channels in measurements and the channel-wise B_1^+ maps in simulations.

Quantitatively, the $|B_1^+|$ values achieved by the efficient shim vector using the 'L' channels are larger for the measured data compared to the simulated data. Additionally the sum of magnitudes (SOM) of the simulated $|B_1^+|$ is smaller compared to the measured $|B_1^+|$ using the efficient shim vector $\vec{u}_\eta^{\text{meas}}$. This is an unexpected finding. Therefore, an additional simulation investigates the impact of possibly reduced loop losses and possibly reduced dielectric property values on the B_1^+ magnitude in fig. 4.2.4. A decrease in the electric conductivity (9.3% over two years and 4 month) and relative permittivity (9% over 2 years and 4 month) of the PVP solution was observed in measurements over time of the open body phantom (fig. 3.3.1 C). The non-decreased dielectric properties used for initial simulations were measured in the same month as the B_1^+ measurements were performed. The dielectric properties were reduced from $\sigma = 0.586\,\text{S/m}$ to $\sigma = 0.58\,\text{S/m}$ and $\varepsilon = 42.17$ to $\varepsilon = 40.8$ and the loop element losses (R) were set to $0\,\Omega$. Qualitatively, an overall higher B_1^+ magnitude is observed, and quantitatively, the B_1^+ magnitude in the central position is 24% higher for the simulation with no ohmic losses and reduced dielectric properties compared to the simulation with $20\,\Omega$ ohmic losses and the initial dielectric properties.

For the 'D' channels, an accordance between measured and simulated central $|B_1^+|$ values is observed. Whereas the channel-wise measured data is 30% smaller compared to the simulated data, at a distance of 28 mm from the phantom boundary in AP direction. The central $|B_1^+|$ values for both element types for an efficient shim vector are summarized in table 4.2.1.

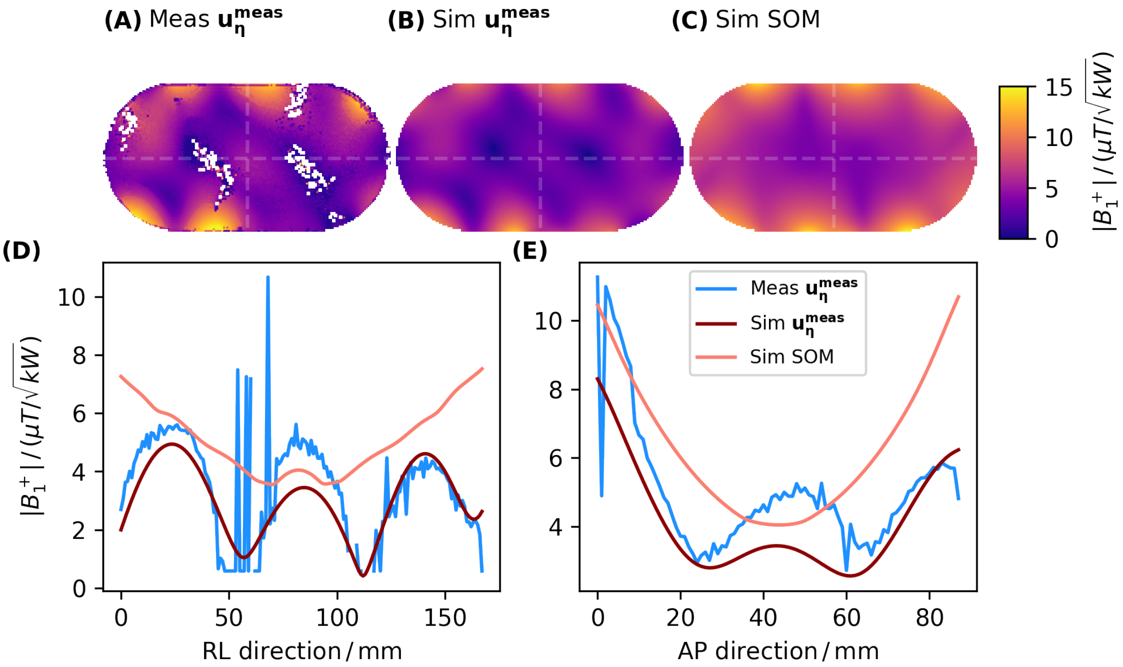

Figure 4.2.3: Phantom setup, using 8 'L' channels with an efficient shim vector: A preparation pulse sequence measurement (A) with an optimized efficient shim vector $\vec{u}_\eta^{\text{meas}}$ is shown and compared to simulations where the same $\vec{u}_\eta^{\text{meas}}$ was applied to the simulated channel-wise B_1^+ maps (B) and the SOM of the simulated channel-wise B_1^+ maps (C). (D) shows line plots at the central location of the phantom, indicated by white dashed lines in (A-C). The electric conductivity for the simulated setup is $\sigma = 0.586\,\text{S/m}$ and the relative permittivity is $\varepsilon = 42.17$. 'L' element losses (R) of 20 Ω were included.

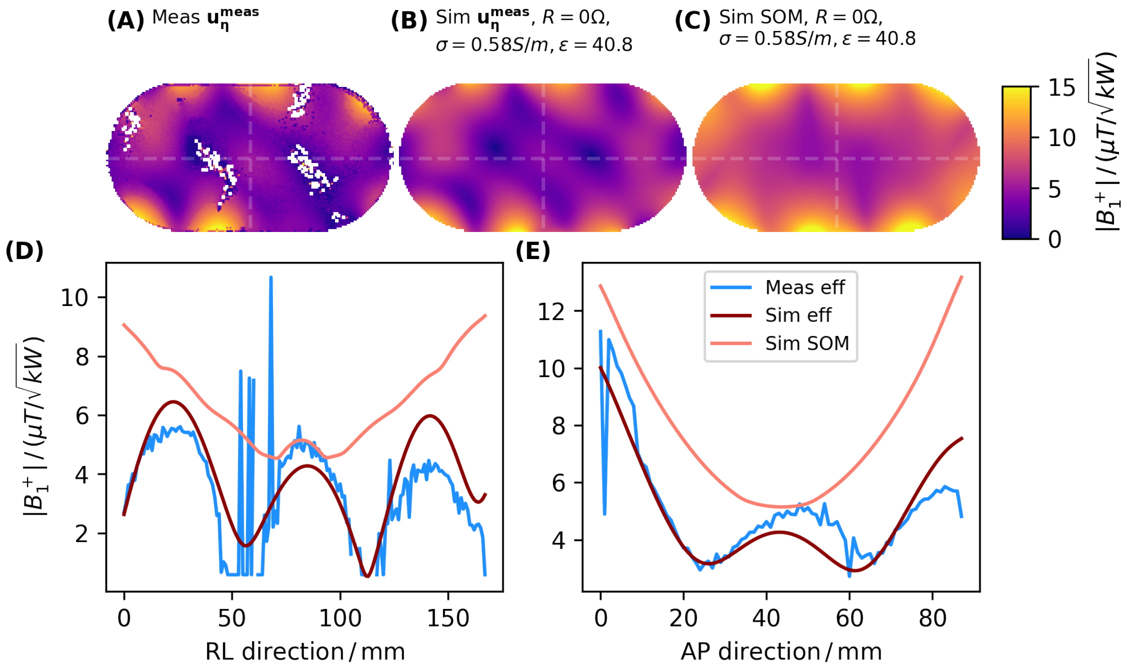

Figure 4.2.4: Phantom setup, using 8 'L' channels with an efficient shim vector and adjusted dielectric properties and losses: A preparation pulse sequence measurement (A) with an optimized efficient shim vector $\vec{u}_\eta^{\text{meas}}$ is shown and compared to simulations where the same $\vec{u}_\eta^{\text{meas}}$ was applied to the simulated channel-wise B_1^+ maps (B) and the SOM of the simulated channel-wise B_1^+ maps (C). (D) shows line plots at the central location of the phantom, indicated by white dashed lines in (A-C). The dielectric properties were reduced from $\sigma = 0.586\,\text{S/m}$ to $\sigma = 0.58\,\text{S/m}$ and $\varepsilon = 42.17$ to $\varepsilon = 40.8$ and the 'L' element losses (R) were set to $0\,\Omega$.

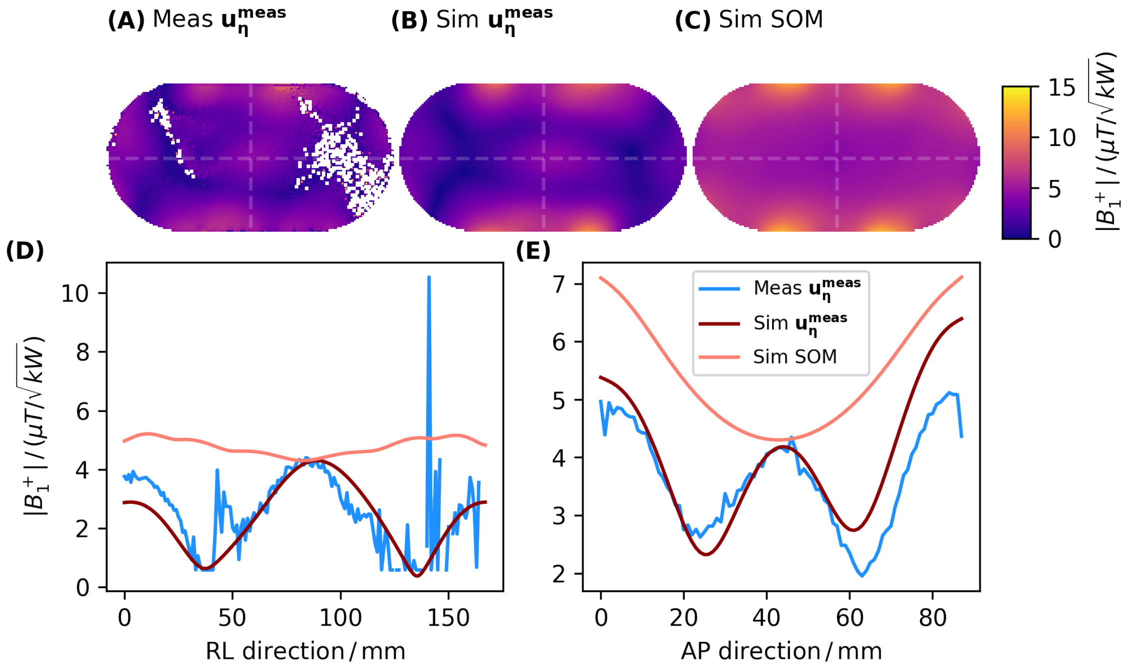

Figure 4.2.5: Phantom setup, using 8 'D' channels with an efficient shim vector: A preparation pulse sequence measurement (A) with an optimized efficient shim vector $\vec{u}_\eta^{\text{meas}}$ is shown and compared to simulations where the same $\vec{u}_\eta^{\text{meas}}$ was applied to the simulated channel-wise B_1^+ maps (B) and the SOM of the simulated channel-wise B_1^+ maps (C). (D) shows line plots at the central location of the phantom, indicated by white dashed lines in (A-C). The electric conductivity for the simulated setup is $\sigma = 0.586\,\text{S/m}$ and the relative permittivity is $\varepsilon = 42.17$.

	$\lvert B_1^+\rvert / \left(\frac{\mu\mathrm{T}}{\sqrt{\mathrm{kW}}}\right)$			
element type	Measurement $\vec{u}_\eta^{\mathrm{meas}}$	Simulation $\vec{u}_\eta^{\mathrm{meas}}$ ($\sigma = 0.586\,\mathrm{S/m}$, $\varepsilon = 42.17$, $R_L = 20\,\Omega$)	Simulation SOM ($\sigma = 0.586\,\mathrm{S/m}$ $\varepsilon = 42.17$, $R_L = 20\,\Omega$)	Simulation $\vec{u}_\eta^{\mathrm{meas}}$, ($\sigma = 0.58\,\mathrm{S/m}$, $\varepsilon = 40.8$, $R_L = 0\,\Omega$)
'L'	4.8	3.4	4.0	4.26
'D'	4.2	4.2	4.3	4.4

Table 4.2.1: Central B_1^+ for absolute phantom B_1^+ maps using 8 channels ('L' or 'D'): The values of a preparation pulse sequence measurement with an applied efficient shim, optimized on the measurement $\vec{u}_\eta^{\mathrm{meas}}$ are compared to channel-wise B_1^+ simulations with the applied shim vector $\vec{u}_\eta^{\mathrm{meas}}$ and the SOM of simulated channel-wise B_1^+ maps. The simulation data with the applied efficient shim is given for 2 different sets of dielectric properties (σ, ε) of the PVP and losses for the loop element (R_L).

4.3 B_1^+ map validation at 10.5 T

This section shows results for a higher field strength 10.5T setup. We compared channel-wise simulations and GRE-based relative B_1^+ measurements, which provided a quick overview for low flip angle regions. Due to time constraints, additional quantitative channel-wise measurements were not performed on 10.5T. In favor, 16-channel simulation and AFI measurement with an applied CP shim vector were compared. This allowed us to make a qualitative and quantitative comparison between the measured and simulated full coil array setup.

There is a qualitative agreement between the data obtained from simulation and measurement for the channel-wise relative $\lvert B_1^+\rvert$ map in areas of low flip angle. In such regions, the simulation and GRE-based measurement indicate a wave-like pattern (fig. 4.3.1A).
Between 10 mm and 70 mm a lower slope is observed compared to the 70 mm to 180 mm region in the measurement line plot shown in fig. 4.3.1A. Near the border of the phantom, the measured signal intensity is lower when compared to the maximum measured at 10 mm. The simulated data does not present this variation in the slope of $\lvert B_1^+\rvert$ nor the shift of the maximum $\lvert B_1^+\rvert$ away from the phantom border.

Figure 4.3.1B shows a qualitatively good agreement between measured and simulated $|B_1^+|$ maps, when applying a cp shim vector to the 16 channels. Quantitative, a median scaling factor of 1.8 is observed for the cp shim vector $|B_1^+|$ maps between simulation and measurement across all voxels.

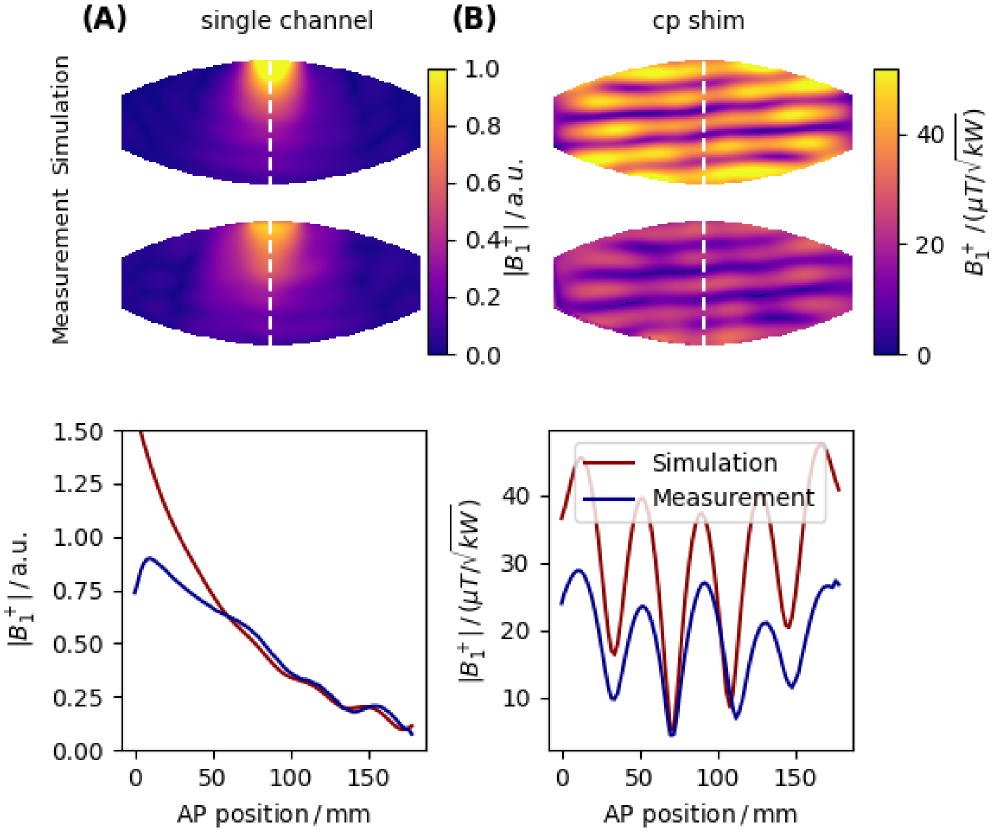

Figure 4.3.1: Comparison 10.5 T B_1^+ simulation (first row) and measurement (second row). (A) shows single channel B_1^+ data, with the module placed on top of the phantom. The channel-wise map was measured by a relative GRE-based sequence. Simulation and measurement are scaled manually, to fit for low FA regions. For high FA regions close to the Ernst angle, deviations are observed. In (B) 16 channels were driven in a circular polarized (CP) mode, and an absolute B_1^+ measurement with an AFI was done. The third row shows a line plot along the AP direction. The position of the line plots is indicated by the dashed lines in the maps.

4.4 Power limit calculation at 7T

This section presents the power limit results of the 7T 16ch Tx/Rx body coil array safety assessment for cardiac usage and goes beyond by showing the power limits for liver and

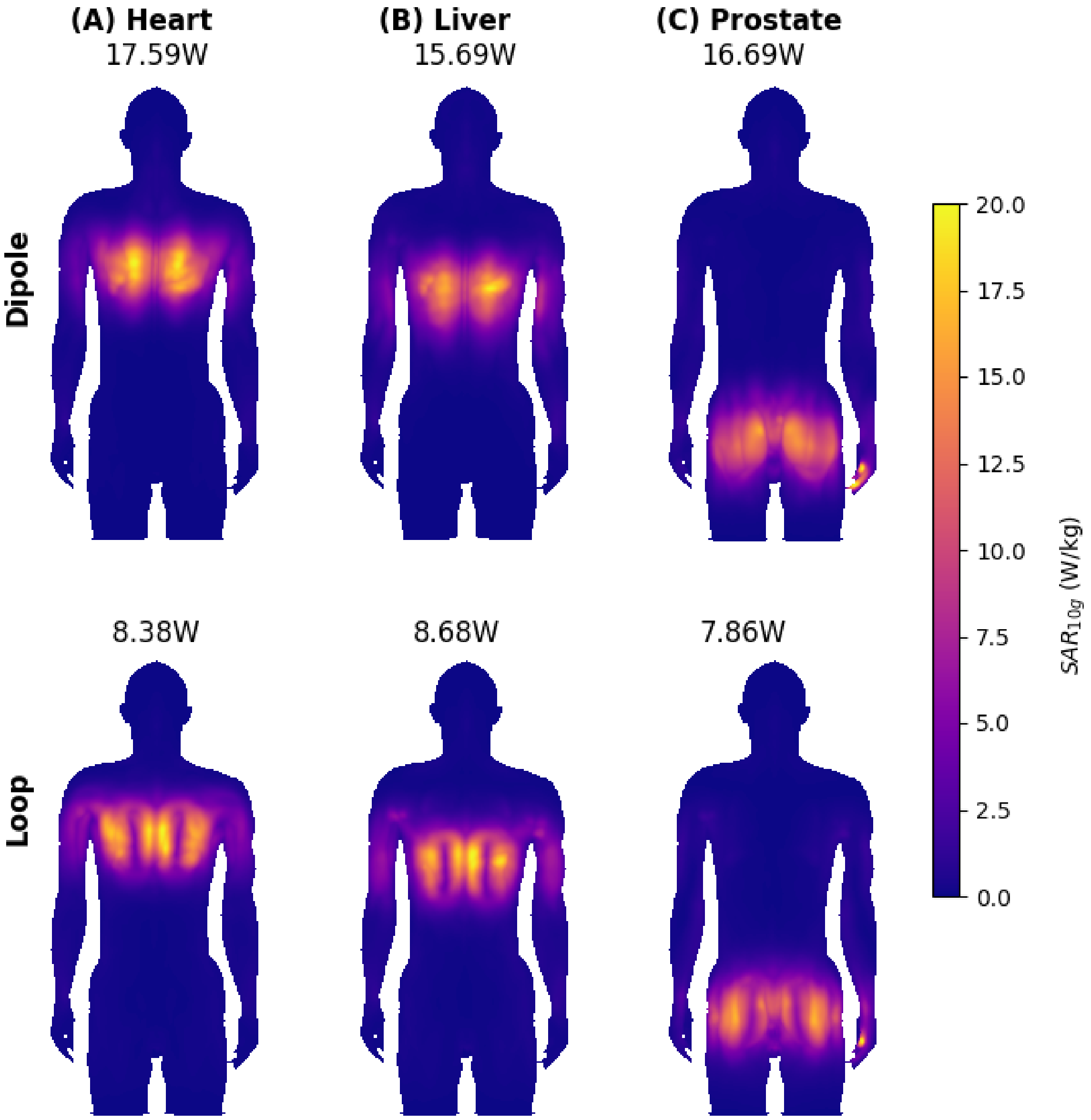

Figure 4.4.1: The SAR_{10g} distribution is shown for a setup utilizing the Duke body model with the 7 T body coil array. The input power stated on top of each MIP is scaled to achieve a psSAR_{10g} of 20 W/kg. The distribution is shown for three different coil-array locations: (A) heart, (B) liver and (C) prostate for the 'D' (top row) and the 'L' (bottom row) channels

	Maximum input power per Tx channel / W		
	Heart	**Liver**	**Prostate**
’D’	17.59	15.69	16.69
’L’	8.38	8.68	7.86

Table 4.4.1: Maximum allowed input power per Tx channel for heart, liver, and prostate coil-array positions, using ’L’ or ’D’ channels.

prostate applications.

Figure 4.4.1 illustrates the MIP of the local SAR_{10g} for the three coil-array positions: (A) heart, (B) liver and (C) prostate for the ’D’ channels (top row) and the ’L’ channels (bottom row), the maximum applicable input power is summarized in table 4.4.1. The dipoles located for cardiac imaging allow the highest $P_{\mathrm{fwd}}^{\mathrm{max}}$ of 17.59 W, the loops located for prostate imaging allow the lowest $P_{\mathrm{fwd}}^{\mathrm{max}}$ of 7.86 W.
The coil location dependence of $P_{\mathrm{fwd}}^{\mathrm{max}}$ is below 11%.

In the safety assessment of the coil array for cardiac imaging -1.7 dB losses of the scanner from the table coil plug to the Tx/Rx switch box are considered as a safety factor. The -1.7 dB was determined by applying 100 V at the table coil plug and measuring 4.82 V behind the Tx/Rx switch box. 35.27 dB were determined of which 33.57 dB are the attenuator connected to the oscilloscope and 1.7 dB are losses between the table coil plug and the Tx/Rx switch box. This damps the voltage by a factor of 0.82 and the power by a factor of 0.68.

4.5 Summary

In summary, at 7 T simulated B_1^+ maps are qualitatively validated for dipole and loop elements of the 16-channel Tx/Rx body coil array. The field patterns of measured and simulated B_1^+ magnitude maps are in accordance. A quantitative agreement between measured H-field probe B_1^+ magnitude maps and MR scanner B_1^+ magnitude maps is achieved for single-channel measurements. The quantitative validation of MR scanner measurements by simulations of single dipole channel (simulation locally 46% higher $|B_1^+|$ compared to measurement) and 8-channel loop setups (measurement locally 41% higher $|B_1^+|$ compared to simulation) emerged to be challenging. Additional simulations with decreased dielectric properties (σ, ε) and decreased ohmic losses in the loop element indicate higher $|B_1^+|$ values compared to the initial simulations. A quantitative agreement between MR scanner measurements and simulations is achieved for single-channel loop and 8-channel dipole setups.

For the 16-channel 10.5 T coil array setup, MR scanner measurements are compared to simulations. Qualitative agreement between measurement and simulation is observed for single-channel low FA regions and the full phantom region for cp-mode measurements. Quantitatively, a factor of 1.8 is observed in the cp-mode between measurement and simulation.

The safety assessment of the 16-channel 7 T body coil array allows a maximum applicable channel-wise forward power of 17.59 W for dipole channels and 7.86 W for loop channels when the coil array is positioned at a central heart position. Placing the coil array at a central liver or prostate position reduces the maximum allowable forward power by less than 11%. Loss mechanisms exist between the MR table coil plug and the coil element that are not accounted for in the simulations and add an additional safety factor.

Finally, this chapter establishes the basis for a coil setup that is relied on qualitatively. The qualitative agreement is essential to evaluate the impact of relative respiration-induced changes in B_1^+ and $\mathrm{psSAR}_{10\mathrm{g}}$ and to describe the observed trend. The quantitative variations suggest that the absolute B_1^+ values for particular respiratory states in the measurements may deviate from the simulations. $\mathrm{psSAR}_{10\mathrm{g}}$ values are calculated based on the exhalation respiratory state and scaled to the IEC limit, with the same scaling factor applied to other respiratory states. It is expected that the scaling factor will differ between measurements and simulations, but the observed changes between respiratory states should indicate the correct trend.
The safety assessment was performed using the conservative power-controlled mode and included safety factors. This allows in-vivo measurements to validate the observed simulated respiration-induced B_1^+ changes with this specific coil setup.

Chapter 5

The impact of respiratory motion on EM-fields in FDTD simulations

Previous studies showed respiration-induced FA changes for thorax MRI at 3 T [23, 24] and 7 T [13]. But not only the B_1^+ and, therefore, the FA is affected by field inhomogeneities at UHF MRI, also the E-field is expected to be influenced due to coupling of the B and E-field via Maxwell's equations. Maxima in the electric field can induce hot spots, causing a rise in local temperature. The SAR is used as a surrogate for the associated patient hazard. SAR simulations indicate strong SAR changes induced by inter-subject changes. Additionally, physiological motion, for example, induced by respiration, is expected to impact SAR values.

Most previous simulations have been based on the virtual family which are segmented breath-hold scans [27] or segmented MR images imported into the software iSeg (ZMT, Zürich, Switzerland) which use averaged free breathing scans [28]. Those models do not reflect different respiratory states.

The aim of this work is first to investigate respiration-induced changes in the B_1^+ field for different coil setups and breathing patterns at 7 T. The results are compared to previous measurement studies. Second, this work motivates a discussion about the safety relevance of respiration at 7 T. For different coil setups and breathing patterns the safety compliance with the IEC60601-2-33 first-level controlled mode SAR limit for the trunk is evaluated.

The results of this section have been published in [30–32, 105].

5.1 Respiration induced B_1^+ changes at 7 T

In this section, respiration-induced B_1^+ changes are first examined channel-wise to investigate the individual contributions of anterior and posterior elements (fig. 5.1.1). Second, an example homogeneous shim is shown to investigate possible B_1^+ dropouts in the ROI (fig. 5.1.2). Third, a larger variety of homogeneous shim vectors is used to investigate the impact of respiration on the CV and the $\min(|B_1^+|)$. Therefore, several optimized shim vectors are analyzed for the 'Fixed' and 'Moving' coil setup. The shim vectors are optimized for the ROI and for different shimmed respiratory states (fig. 5.1.3).

5.1.1 Channel-wise - respiration-induced B_1^+ changes

Channel-wise respiration induced B_1^+ magnitude and phase changes are shown for an anterior dipole element close to the heart (D2) and a posterior dipole element diagonally mirrored (D7) in fig. 5.1.1. The used coil setup is the 'Moving' coil. The shown B_1^+ maps are for a single transversal slice, with a highlighted ROI_1 at the center of the heart.
In quantitative terms, the magnitude of B_1^+ is larger for anterior elements ranging from 0.21 to $8.13\,\mu\mathrm{T}/\sqrt{\mathrm{kW}}$ compared to posterior elements with a range of 0.08 – $2.79\,\mu\mathrm{T}/\sqrt{\mathrm{kW}}$. Also the $\min(|B_1^+|)$ varies stronger during inhalation for the anterior element D2 ($\Delta\min(|B_1^+|) = -0.29\,\mu\mathrm{T}/\sqrt{\mathrm{kW}}$) compared to the posterior element D7 ($\Delta\min(|B_1^+|) = +0.14\,\mu\mathrm{T}/\sqrt{\mathrm{kW}}$). For D2 the channel-wise mean B_1^+ magnitude within ROI_1 decreases by $0.87\,\mu\mathrm{T}/\sqrt{\mathrm{kW}}$ (equivalent to 32% decrease) from exhale to inhale, while the channel-wise mean B_1^+ magnitude of the posterior element increases by 28%.
Outside the region of interest, closer to the chest wall, the observed changes are larger. The phase at the central location in ROI_1 varies by $+1°(-56°)$ for D2 (D7). Table 5.1.1 summarizes all values for all dipole channels.

5.1.2 Example shim - Respiration-induced B_1^+ changes

Figure 5.1.2 investigates all five respiratory states for an example homogeneous shim vector that has been optimized with respect to R1 with a CV of 16% for R1. The respiration-induced changes of the CV is below 7% from R1 to R4, whereas a strong increase from R1 to R5 of 17% is observed. 'R5' represents an additional scenario of increased inhalation depth. The $\mathrm{mean}(|B_1^+|)$ decreases by 12% from R1 to R4. The $\min(|B_1^+|)$ decreases with inhalation from $3.03\,\mu\mathrm{T}/\sqrt{\mathrm{kW}}$ (exhale) to $2.26\,\mu\mathrm{T}/\sqrt{\mathrm{kW}}$

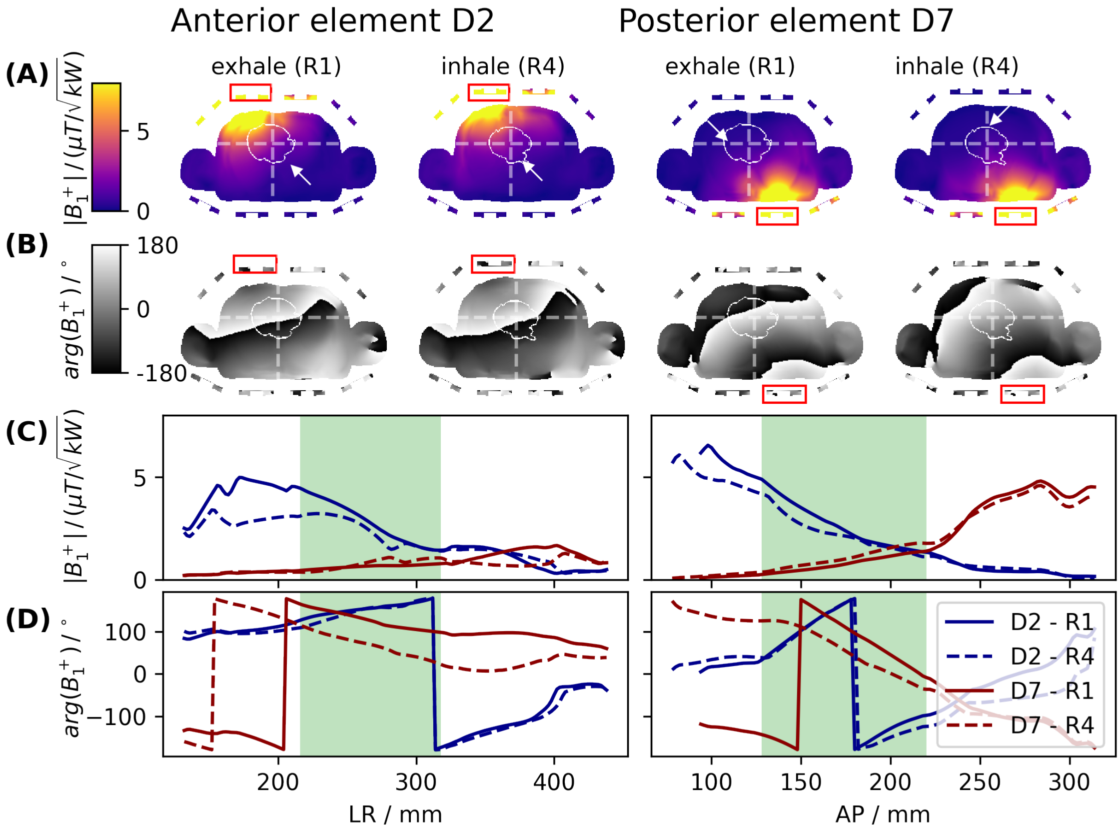

Figure 5.1.1: Respiration induced channel-wise B_1^+ changes: Channel-wise respiration-induced B_1^+ changes during transmission on a single channel are investigated for the 'Moving' setup, for two example dipole elements. The left-side columns show channel-wise B_1^+ data of the anterior element D2 located above the heart, the right-side columns depict the diagonally opposite posterior element D7. The respiratory states R1 and R4 are represented. In (A) and (C), the B_1^+ magnitude, and in (B) and (D), the B_1^+ phase is investigated. In (C-D), line plots along the dashed lines illustrated in (A-B) are presented for both respiratory states in a central anterior-posterior (AP) and left-right (LR) direction. The heart's location is indicated by a mask in (A-B) and a green range in (C-D). The arrows in (A-B) indicate the location of the min($|B_1^+|$) inside the ROI.

(inhale), much smaller values are observed outside the ROI (exhale: $0.03\,\mu\text{T}/\sqrt{\text{kW}}$). The phase change at a central location in ROI_1 is -19° from exhale to inhale.

This is only one example shim, to generalize findings 1000 different starting phases were used in the following section. An additional example case is shown in fig. A.2.3 illustrating a shim optimized on ROI_3 covering three transversal slices. The impact of static pTx on slices not considered for the optimization process is shown for three short-axis view slices.

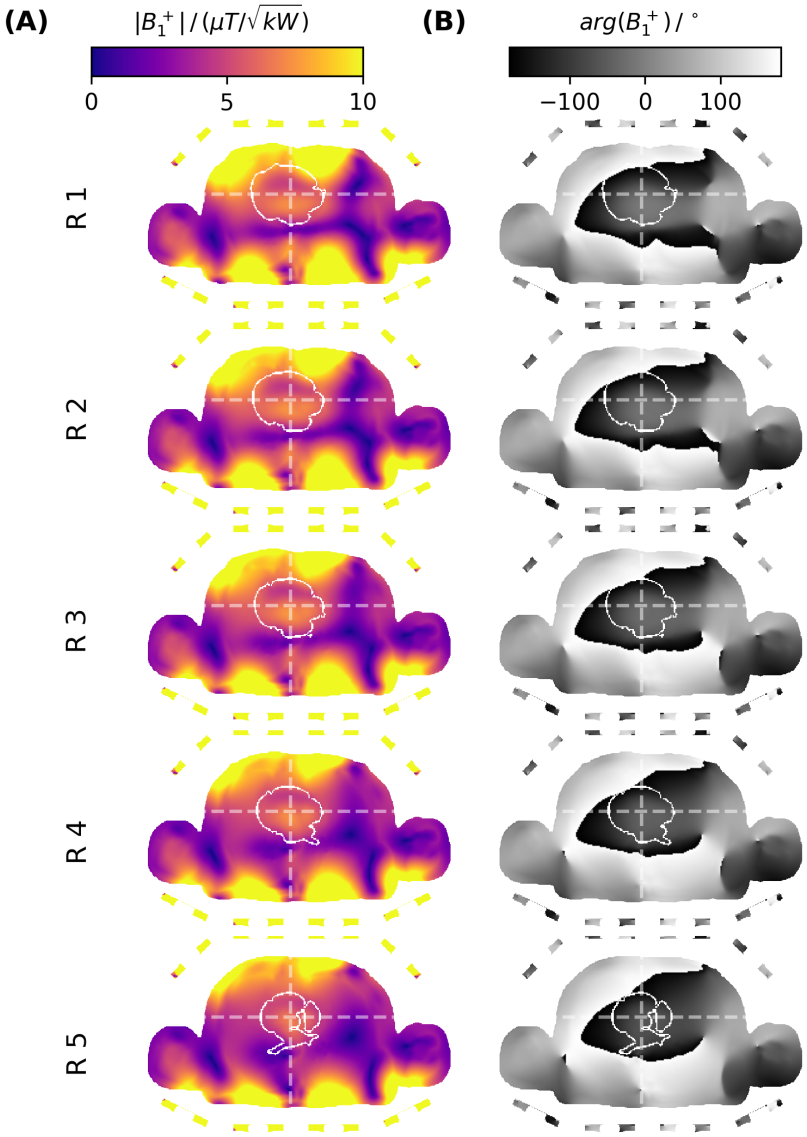

Figure 5.1.2: Example $|B_1^+|$ maps of a homogeneous shim vector: The magnitude (A) and phase (B) maps of B_1^+ are shown for the 'Moving' setup and five respiratory states. The crossing of the dashed lines indicates the location of the phase changes given in table 5.1.2. The heart's location is indicated by a mask.

	Anterior				Posterior			
	D1	D2	D3	D4	D5	D6	D7	D8
$\overline{\lvert B_1^+(\text{R1})\rvert}$ / (μT/ $\sqrt{\text{kW}}$)	1.38	3.16	2.47	0.72	0.62	1.17	0.72	0.34
$\Delta\overline{\lvert B_1^+\rvert}$ / %	-22	-32	-27	-25	-5	-7	+28	+9
min($\lvert B_1^+(\text{R1})\rvert$) / ($\mu$T/ $\sqrt{\text{kW}}$)	0.41	0.96	0.62	0.21	0.22	0.38	0.23	0.08
$\Delta\varphi$ / °	-29	+1	-3	-61	- 63	-58	-56	-83

Table 5.1.1: Summary of channel-wise B_1^+ and channel-wise respiration-induced B_1^+ changes: The mean value of the exhale channel-wise $|B_1^+|$ inside the ROI, the respiratory changes of the channel-wise mean $|B_1^+|$, the minimum value of the exhale channel-wise $|B_1^+|$ in the ROI and the channel-wise phase changes at a central location in the heart are given for the four anterior dipole elements (D1-D4) and the four posterior dipole elements (D5-D8). The B_1^+ maps of D2 and D7 are shown in fig. 5.1.1.

		R5	R4 (inhale)	R3	R2	R1 (exhale)
in ROI$_\text{I}$	$\overline{\lvert B_1^+(\text{R1})\rvert}$ / (μT/ $\sqrt{\text{kW}}$)	5.14	5.55	5.80	5.97	6.23
	min($\lvert B_1^+\rvert$) / (μT/ $\sqrt{\text{kW}}$)	1.40	2.26	2.52	2.95	3.03
	$\Delta\overline{\lvert B_1^+\rvert}$ / %	-19	-12	-7	-4	0
	ΔCV / %	17	1	-2	-7	0
	$\varphi(\text{Ri}) - \varphi(\text{R1})$ / °	-36	-19	-7	-2	0
Full slice	min($\lvert B_1^+\rvert$) / (μT/ $\sqrt{\text{kW}}$)	0.05	0.02	0.05	0.07	0.03

Table 5.1.2: Quantitative summary of respiration-state resolved B_1^+ values, an example homogeneous shim vector was applied to channel-wise B_1^+ maps: Absolute and phase B_1^+ values are summarized for the 'Moving' setup and the five respiratory states, considering only the 'dipole' channels with one example optimized homogeneous shim vector. The mean value of $|B_1^+|$, the minimum $|B_1^+|$, the respiration-induced changes of the mean $|B_1^+|$ and the CV in reference to R1 are listed for the ROI. In addition, the phase changes at a central location in the heart and the minimum $|B_1^+|$ over the full slice are given. The corresponding B_1^+ maps are shown in fig. 5.1.2.

5.1.3 Coil setup and shimmed breathing state - Respiration-induced B_1^+ changes

Figure 5.1.3 and table 5.1.3 depict the homogeneity CV and min($|B_1^+|$) for an optimization process utilizing 1000 different starting phase vectors for a 'Moving' and a 'Fixed' coil setup and different shimmed breathing states as described in the method section. It is important to note that different starting phase vectors can yield the same solution, only unique solutions are illustrated in fig. 5.1.3A,C&D. All solution sets have low CV values (<27%) for the optimized case but lead to different respiration-induced changes in dependence on the exact shim-vector.

Overall, CV values in the range of 9% to 26% are observed for the optimized respiratory state. In the majority of cases, the CV decreases from exhale to inhale. Figure 5.1.3A shows only one solution with increasing CV during inhalation when shimming is performed on R1. Shimming the B_1^+ on 'R4' (see fig. 5.1.3B) results in more optimized solutions with larger respiration-induced changes ($[\min(\Delta\mathrm{CV}), \max(\Delta\mathrm{CV})] = [-93.2, -14.3]\%$) compared to shimming on 'R1' only ([24.7,50.4]) or 'R1 & R4' ([-28.6,15.6]).

The $\min(|B_1^+|)$ is in all optimizations ('R1&R4','R1','R4') for some solutions below $0.4\,\frac{\mu\mathrm{T}}{\sqrt{\mathrm{kW}}}$. Many solutions with high exhale $\min(|B_1^+|)$ show a strong decrease during inhalation. For example the solution with the largest $\min(|B_1^+(\mathrm{R1})|) = 3.3\,\frac{\mu\mathrm{T}}{\sqrt{\mathrm{kW}}}$ decreases by 27% for the optimization 'R1&R4'. Increased $\min(|B_1^+|)$ during inhalation is mainly observed for small exhale $\min(|B_1^+|)$ values.

For the Fixed setup, more solutions are found compared to the Moving setup (see $\min(|B_1^+|)$ in fig. 5.1.3C&D). Similar observations are made for the 'L' channels and the combination of 'LD' channels (figs. A.2.4 and A.2.5).

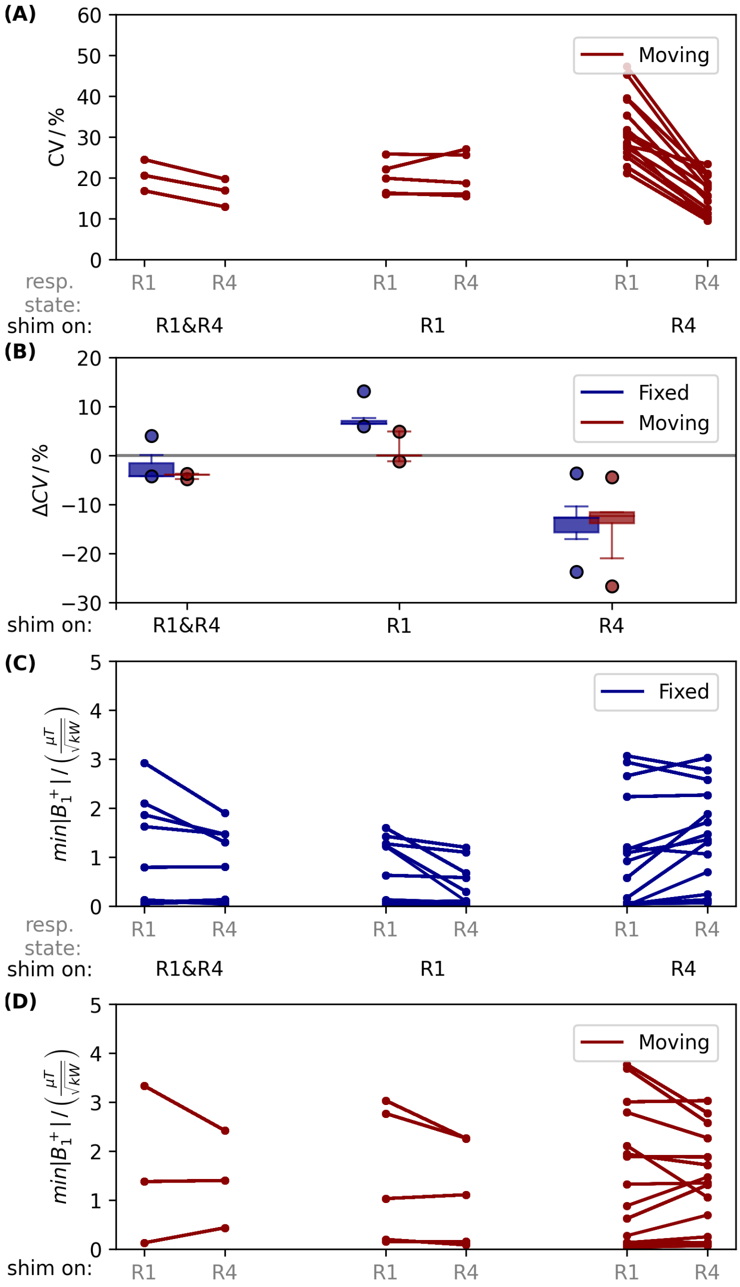

Figure 5.1.3: Respiration-induced B_1^+ changes in dependence of the coil setup and the shimmed breathing state: A set of 1000 starting phase shim vectors was utilized to optimize the B_1^+ homogeneity (CV) for a 'Fixed' and 'Moving' coil setup using 'D' channels. Multiple initial phase vectors for the optimization can result in the same optimized shim vector. The optimization was performed on 'R1&R4' simultaneously (left column), 'R1' only (centre column) and 'R4' only (right column). For this setup the CV values (A), the ΔCV values (B) and the min($|B_1^+|$) (C&D) are evaluated. The CV values are only shown for the 'Moving' setup, while all other values are shown for the 'Moving' and 'Fixed' setup.

Shim on	**’R1 & R4’**		**’R1’**		**’R4’**	
Respiratory state	R1	R4	R1	R4	R1	R4
CV / % Moving	[16.8,24.5]	[12.9,19.7]	[16.1,25.8]	[15.6,27.0]	[21.1,47.3]	[9.5,23.4]
ΔCV / % Fixed	[-28.6,15.6]		[24.7,50.4]		[-93.2,-14.3]	
ΔCV / % Moving	[-26.3,-19.7]		[-6.0,19.8]		[-97.9,-17.3]	
min($\vert B_1^+\vert$) / $\left(\frac{\mu\mathrm{T}}{\sqrt{\mathrm{kW}}}\right)$ Fixed	[0.0,2.9]	[0.0,1.9]	[0.0,1.6]	[0.0,1.2]	[0.0,3.1]	[0.1,3.0]
min($\vert B_1^+\vert$) / $\left(\frac{\mu\mathrm{T}}{\sqrt{\mathrm{kW}}}\right)$ Moving	[0.1,3.3]	[0.4,2.4]	[0.2,3.0]	[0.1,2.3]	[0.0,3.8]	[0.1,3.0]

Table 5.1.3: Respiration-induced B_1^+ changes in dependence of the coil setup and the shimmed breathing state: A set of 1000 starting phase shim vectors was utilized to optimize the B_1^+ homogeneity (CV) for a ’Fixed’ and ’Moving’ coil setup using ’D’ channels. Multiple initial phase vectors for the optimization can result in the same optimized shim vector. The starting phase vectors give a range of CV, ΔCV and min($|B_1^+|$) values. The extrema are summarized in this table by [min,max] values for optimizations performed on ’R1&R4’ simultaneously, ’R1’ only and ’R4’ only as investigated in fig. 5.1.3.

5.2 Respiration induced SAR changes 7 T

In the following, the respiration impact on the local specific absorption rate averaged over 10g (SAR_{10g}) is investigated. First, three different example shim vectors (fig. 5.2.1)) illustrate the main findings and challenges at UHF MRI concerning respiration-induced changes in local SAR_{10g}. Second, in order to generalize these findings, fig. 5.2.2 assesses the respiration-induced changes of peak spatial SAR_{10g} ($psSAR_{10g}$) for 10^6 random phase and 10^6 random phase and amplitude shim vectors applied to both the SAR-controled mode (SCM, described in section 3.7.1) and the power-controled mode (PCM, described in section 3.7.2), along with the maximum applicable amplitude using the PCM. Lastly, the maximum changes are visualized in fig. 5.2.3 for the entire respiratory cycle.

5.2.1 Example shim vector - respiration induced local SAR_{10g} changes

Figure 5.2.1 investigates maximum intensity projections of local SAR_{10g} for the 'Fixed' setup. Three main observations were made:

For the shown homogeneous shim vector optimized on the respiratory state 'R1' (fig. 5.2.1A, Shim vector 1) the $psSAR_{10g}$ location (posterior left) does not change during breathing and the $psSAR_{10g}$ value decreases from 20 W/kg to 19.34 W/kg during the respiratory cycle.

When applying the shim vector optimized on 3 transversal slices ROI_3 for the respiratory states 'R1&R4' (fig. 5.2.1B, Shim vector 2), it results in larger respiration-induced $psSAR_{10g}$ changes of up to 42%. Additionally, a $psSAR_{10g}$ location shift from posterior left to anterior left is observed.

The third shim vector gives the worst case $psSAR_{10g}$ changes between exhale and inhale (150%, factor 2.5) of 10^6 random amplitude and phases shim vectors. For all respiratory states the $psSAR_{10g}$ is located anterior right for this shim vector.

Please note, those large changes are only seen for the 'Fixed' setup, due to large distance changes (10-24mm) between the coil modules and the chest. Location changes of the $psSAR_{10g}$ during respiration occur more often for the 'Fixed' setup ('D' 26%) compared to the 'Moving' setup ('D' 4%). A graphical representation can be found in fig. 5.2.4.

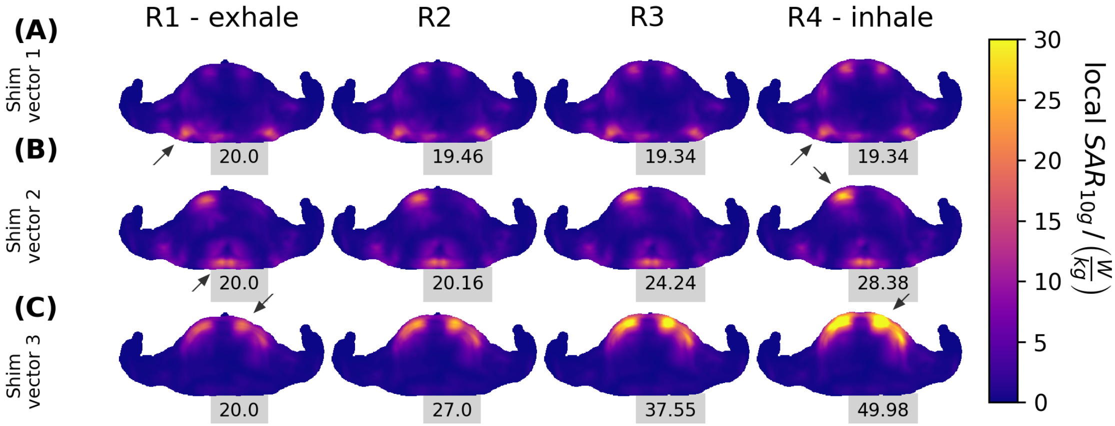

Figure 5.2.1: Local SAR$_{10g}$ maps for three example shim vectors: The maximum intensity projection (MIP) along head feet direction of the local SAR$_{10g}$ is shown for the 'Fixed' setup and four respiratory states. First, a homogeneous shim vector optimized on ROI$_1$ of the respiratory state 'R1' was applied (A). Second, a homogeneous shim vector optimized on ROI$_3$ of the respiratory states 'R1&R4' is applied, inducing a location change of the psSAR$_{10g}$ from a posterior location at the exhale respiratory state to an anterior location for the inhale state (B). Lastly, the shim vector is selected, which induces the largest respiration-induced psSAR$_{10g}$ changes between exhale and inhale of the random 10^6 amplitude and phases shim vectors (C). The psSAR$_{10g}$ values are given in gray boxes, and the locations are marked by arrows.

Shim case	psSAR$_{10g}$(Ri, $\vec{u}_{\text{SCM}}$) / (W/kg)				$\lvert\Delta$psSAR$_{10g}$($\vec{u}_{\text{SCM}}$)$\rvert$ / %
	R1 - exhale	R2	R3	R4 -inhale	
Shim vector 1 $\vec{u}_{hom}$ on 'R1', ROI$_1$	20	19.46	19.34	19.34	3.4
Shim vector 2 $\vec{u}_{hom}$ on 'R1&R4', ROI$_3$	20	20.16	24.24	28.38	42
Shim vector 3 maximum ΔpsSAR$_{10g}$($\vec{u}_{\text{SCM}}$)	20	27.0	37.55	49.98	149.9

Table 5.2.1: psSAR$_{10g}$ for the example shims shown in fig. 5.2.1: psSAR$_{10g}$ values are given for four respiratory states using a 'Fixed' coil setup. Shim vector 1 is a homogeneous shim vector optimized on ROI$_1$ of the respiratory state 'R1'. Shim vector 2 is a homogeneous shim vector optimized on ROI$_3$ of the respiratory state 'R1&R4'. Lastly, shim vector 3 is the shim vector of 10^6 random amplitude and phases shim vectors, which induces the largest ΔpsSAR$_{10g}$.

5.2.2 Coil setup and control mode - respiration induced $\mathrm{psSAR}_{10\mathrm{g}}$ changes

The impact of example shim vectors on the local $\mathrm{SAR}_{10\mathrm{g}}$ and the potential increases in $\mathrm{psSAR}_{10\mathrm{g}}$ during respiration was demonstrated in fig. 5.2.1. To generalize these findings, fig. 5.2.2 examines a larger set of $2 \cdot 10^6$ random shim vectors, which included both phase-only shim vectors and amplitude and phase shim vectors. The shim vectors cover a broad range of $\mathrm{psSAR}_{10\mathrm{g}}$ values, which is shown for the $\vec{u}_{\mathrm{PCM}}$ shim vectors in fig. A.2.2.

Figure 5.2.2 investigates $\mathrm{psSAR}_{10\mathrm{g}}(\mathrm{R4})$ values with respect to a possible violation of the IEC 60601-2-33 first-level controlled mode torso SAR limit. Compliance with the IEC limit during the exhale state is ensured by scaling the shim vectors magnitude $|\vec{u}(\mathrm{R1})|$ for the different control modes $(\vec{u}_{\mathrm{SCM}}, \vec{u}_{\mathrm{PCM}})$ to achieve $\mathrm{psSAR}_{10\mathrm{g}}(\mathrm{R1}, \vec{u}_{\mathrm{SCM}}) = \mathrm{psSAR}_{10\mathrm{g}}(\mathrm{R1}, \vec{u}_{\mathrm{PCM}}) = 20\,\mathrm{W/kg}$. In addition, the upper amplitude $(u_{\mathrm{PCM}}^{\max})$ is calculated to obtain an amplitude limit for the shim vectors which ensures $\mathrm{psSAR}_{10\mathrm{g}}(\mathrm{R1}, u_{\mathrm{PCM}}^{\max}) = 20\,\mathrm{W/kg}$. Those shim vectors and the upper amplitudes are applied to the inhale state (fig. 5.2.2) and the resulting respiration-induced changes of the $\mathrm{psSAR}_{10\mathrm{g}}$ between R4 and R1 are evaluated in Table 5.2.2. VOP Q-Matrix sets have been used for $\mathrm{psSAR}_{10\mathrm{g}}$ calculations.

Across all cases the following relation is valid:

$$\max(\Delta\mathrm{psSAR}_{10\mathrm{g}}(\vec{u}_{\mathrm{SCM}})) > \Delta\mathrm{psSAR}_{10\mathrm{g}}(u_{\mathrm{PCM}}^{\max}) > \Delta\mathrm{psSAR}_{10\mathrm{g}}(\vec{u}_{\mathrm{PCM}}). \tag{5.1}$$

Generally, the ’Fixed’ setup leads to larger changes compared to the ’Moving’ setup.

For instance, with amplitude and phase shim vectors for the SCM, the ’Fixed’ setup has maximum $\Delta\mathrm{psSAR}_{10\mathrm{g}}(\vec{u}_{\mathrm{SCM}})$ of 151 % while the ’Moving’ setup shows $\Delta\mathrm{psSAR}_{10\mathrm{g}}$ values below (27 %), see fig. 5.2.2. Similar behavior is observed for ’L’ channels (fig. A.2.6) and the combination of ’LD’ channels (fig. A.2.7). The $\Delta\mathrm{psSAR}_{10\mathrm{g}}(u_{\mathrm{PCM}}^{\max})$ is a factor of 3.5 smaller compared to the maximum SCM changes for the ’Fixed’ setup.

The decreased respiration-induced $\mathrm{psSAR}_{10\mathrm{g}}$ changes for the PCM come at the cost of generally smaller applicable amplitudes (fig. A.2.8) compared to the SCM. Furthermore, phase and amplitude shimming result in larger respiration-induced $\mathrm{psSAR}_{10\mathrm{g}}$ changes compared to phase-only shimming.

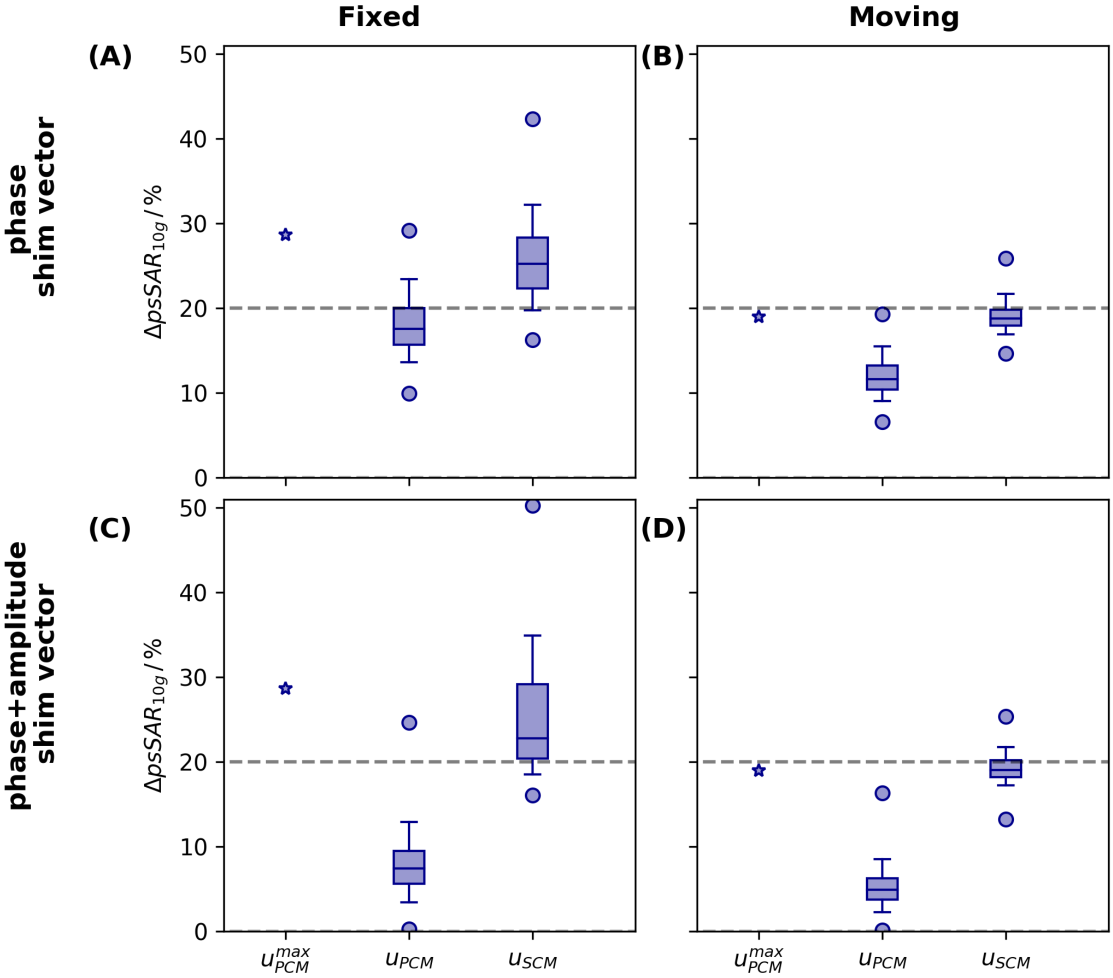

Figure 5.2.2: $\mathrm{psSAR_{10g}}$(R4) in dependence of the coil setup and the control mode: The $\mathrm{psSAR_{10g}}$(R4) values are investigated with respect to a possible violation of the IEC 60601-2-33 first-level controlled mode trunk SAR limit (20 W/kg), indicated by the dashed line. Compliance with the IEC limit during the exhale state is ensured by scaling the shim vector magnitude to obtain $\mathrm{psSAR_{10g}}$(R1) = 20 W/kg. The same scaled shim vector is applied to Q_{10g}(R4) to calculate $\mathrm{psSAR_{10g}}$(R4).
$\mathrm{psSAR_{10g}}$(R4) values are investigated for (i) a 'Fixed' (left column) and a 'Moving' (right column) setup, for (ii) a set of 10^6 random phase shim vectors (top row) and 10^6 amplitude and phase shim vectors (bottom row) and for (iii) shim vectors of the SAR-controlled mode ($\vec{u}_{\mathrm{SCM}}$), the power-controlled mode ($\vec{u}_{\mathrm{PCM}}$) and in addition, the upper amplitude of the power controlled mode ($u_{\mathrm{PCM}}^{\mathrm{max}}$). The SCM uses the VOP Q-matrix set with an overestimation of 1%, while the PCM uses the complete Q-matrix set.
The shown results include only 'D' channels. The box plots display whiskers representing the 5th and 95th percentiles, boxes marking the first and third quartiles with the median value, and circles indicating the extrema.

Coil setup	**Element type**	**ΔpsSAR$_{10g}$ $(u^{\max}_{\mathrm{PCM}})$ / %**	**ΔpsSAR$_{10g}(u_{\mathrm{SCM}})$ / %**		**ΔpsSAR$_{10g}(u_{\mathrm{PCM}})$ / %**	
			phase shim vectors	amplitude & phase shim vectors	phase shim vectors	amplitude & phase shim vectors
Fixed	D	43	[-18,112]	[-20,151]	[-50,45]	[-99,23]
	L	2	[-15,106]	[-16,116]	[-73,7]	[-99,-8]
	LD	12	[-18,150]	[-17,160]	[-83,10]	[-98,-32]
Moving	D	-5	[-27,29]	[-34,27]	[-67,-3]	[-99,-18]
	L	-2	[-18,25]	[-30,29]	[-74,3]	[-99,-13]
	LD	-2	[-23,28]	[-31,31]	[-85,-4]	[-98,-32]

Table 5.2.2: ΔpsSAR$_{10g}$ in dependence of the coil setup and the control mode: The extrema values [min,max] of ΔpsSAR$_{10g}$ are summarized. The corresponding psSAR$_{10g}$(R4) values are investigated in fig. 5.2.2. ΔpsSAR$_{10g}$ values are investigated for (i) a 'Fixed' and a 'Moving' coil setup, for (ii) a set of 10^6 random phase shim vectors and 10^6 amplitude and phase shim vectors and for (iii) shim vectors of the SAR-controlled mode ($\vec{u}_{\mathrm{SCM}}$), the power-controlled mode ($\vec{u}_{\mathrm{PCM}}$) and in addition, the upper amplitude of the power controlled mode ($u^{\max}_{\mathrm{PCM}}$).

5.2.3 Control mode - respiration-induced psSAR changes over a full respiration cycle

While the last section investigated in detail respiration-induced changes of psSAR$_{10g}$ between 'R1' and 'R4', fig. 5.2.3 shows for the full respiratory cycle the extrema of the absolute psSAR$_{10g}$ values for the SCM and PCM. The psSAR$_{10g}$(R1) is normalized to 20 W/kg.

In general, with increasing chest and diaphragm motion, the range of psSAR$_{10g}(\vec{u}_{\mathrm{SCM}})$ increases. psSAR$_{10g}(\vec{u}_{\mathrm{SCM}})$ provides the actual SAR values for a given complex shim vector $\vec{u}_{\mathrm{SCM}}$, showing a maximum of 26 W/kg (R5, t=2 s). In contrast psSAR$_{10g}(u^{\max}_{\mathrm{PCM}})$, that denotes an upper boundary of psSAR$_{10g}(\vec{u}_{\mathrm{PCM}})$, and the range of psSAR$_{10g}(\vec{u}_{\mathrm{PCM}})$ is less impacted. psSAR$_{10g}(u^{\max}_{\mathrm{PCM}})$ is always below the IEC limit 20 W/kg for 'D' channels, for 'LD' channel combinations also changes above the IEC limit are observed (fig. A.2.9).

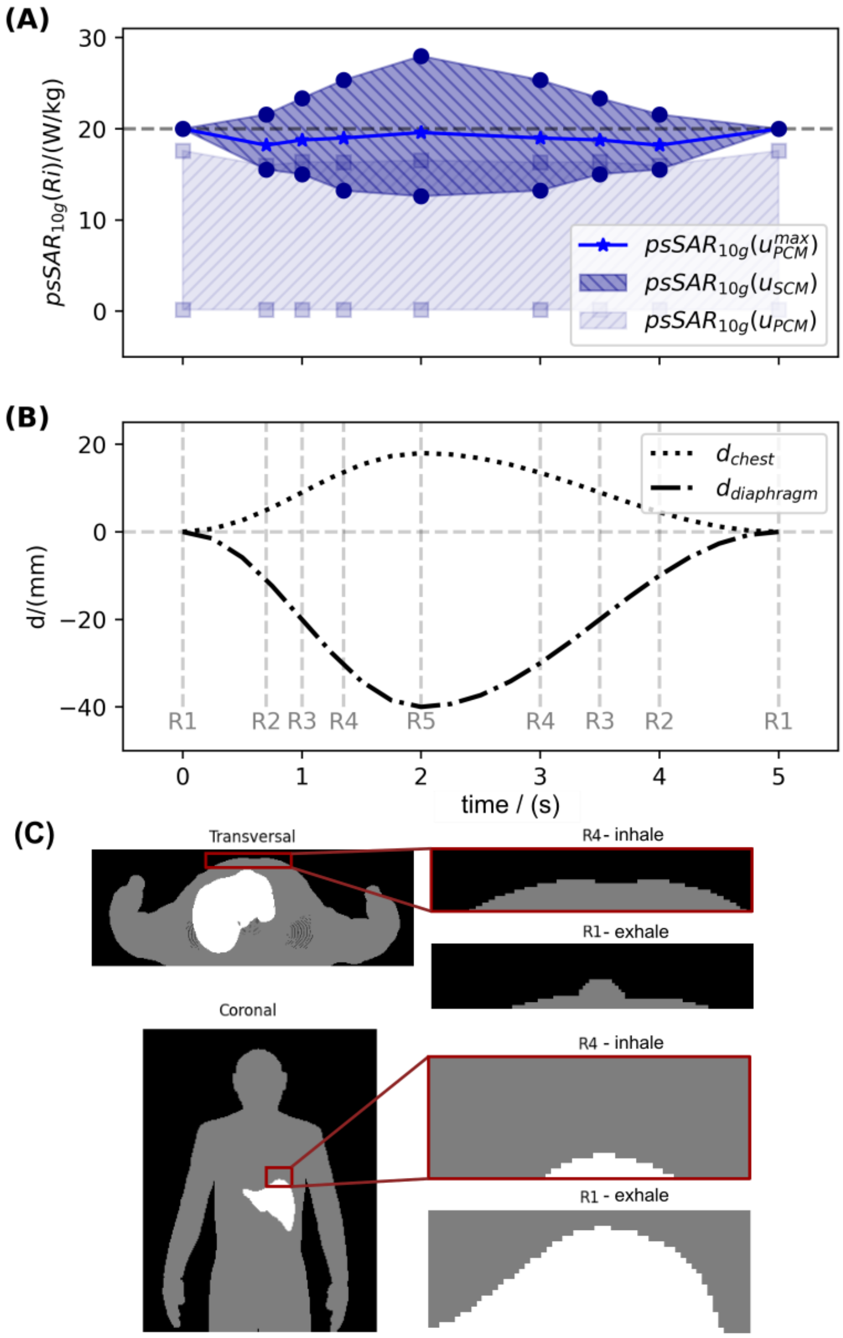

Figure 5.2.3: $\mathrm{psSAR}_{10\mathrm{g}}$ for a full respiratory cycle in dependence of the control modes: (A) shows the $\mathrm{psSAR}_{10\mathrm{g}}$ values for the ’Moving’ setup utilizing ’D’ channels. The SCM ($\mathrm{psSAR}_{10\mathrm{g}}(\vec{u}_{\mathrm{SCM}})$ dark blue circles) and the PCM ($\mathrm{psSAR}_{10\mathrm{g}}(\vec{u}_{\mathrm{PCM}})$ light blue squares) use 10^6 random amplitude and phase shim vectors. The shaded area represents the range of all possible values. The values are compared to $\mathrm{psSAR}_{10\mathrm{g}}(u^{\mathrm{max}}_{\mathrm{PCM}})$ (blue stars), which is an upper boundary for the $\mathrm{psSAR}_{10\mathrm{g}}(\vec{u}_{\mathrm{PCM}})$. Compliance with the IEC limit during the exhale state is ensured by scaling the shim vector magnitude to obtain $\mathrm{psSAR}_{10\mathrm{g}}(\mathrm{R1}) = 20\,\mathrm{W/kg}$, the same scaled shim vector is applied to $Q_{10\mathrm{g}}(\mathrm{Ri})$ to calculate $\mathrm{psSAR}_{10\mathrm{g}}(\mathrm{Ri})$.(B) quantitatively illustrates the variation of the chest d_{chest} and diaphragm $d_{\mathrm{diaphragm}}$ position, while (C) shows the qualitative variations. The liver is marked in white to highlight the diaphragm position.

5.2.4 Correlation of $\mathrm{psSAR}_{10\mathrm{g}}$ location and value

So far, respiration-induced changes in the $\mathrm{psSAR}_{10\mathrm{g}}$ values have been investigated. This section expands the analysis from respiration-induced $\mathrm{psSAR}_{10\mathrm{g}}$ value changes to respiration-induced $\mathrm{psSAR}_{10\mathrm{g}}$ location changes and the correlation between $\Delta\mathrm{psSAR}_{10\mathrm{g}}$ and $\mathrm{psSAR}_{10\mathrm{g}}$ location.

100 random example shim vectors were selected to illustrate possible location changes of the $\mathrm{psSAR}_{10\mathrm{g}}$ from the exhale to the inhale respiratory state (fig. 5.2.4A). For the selected shim vectors, the $\mathrm{SAR}_{10\mathrm{g}}$ was calculated for each voxel. Therefore, the Q-matrices were not reduced to the VOP Q-matrices. In general, the 'Fix' setup shows more changes of the $\mathrm{psSAR}_{10\mathrm{g}}(\vec{u}_{\mathrm{SCM}})$ location during respiration compared to the 'Moving' setup. Quantitatively 26%/20% of the shim vectors investigated for the 'D'/'L' channels show location changes during respiration for the 'Fixed setup and 4%/5% of the 'Moving' setup.

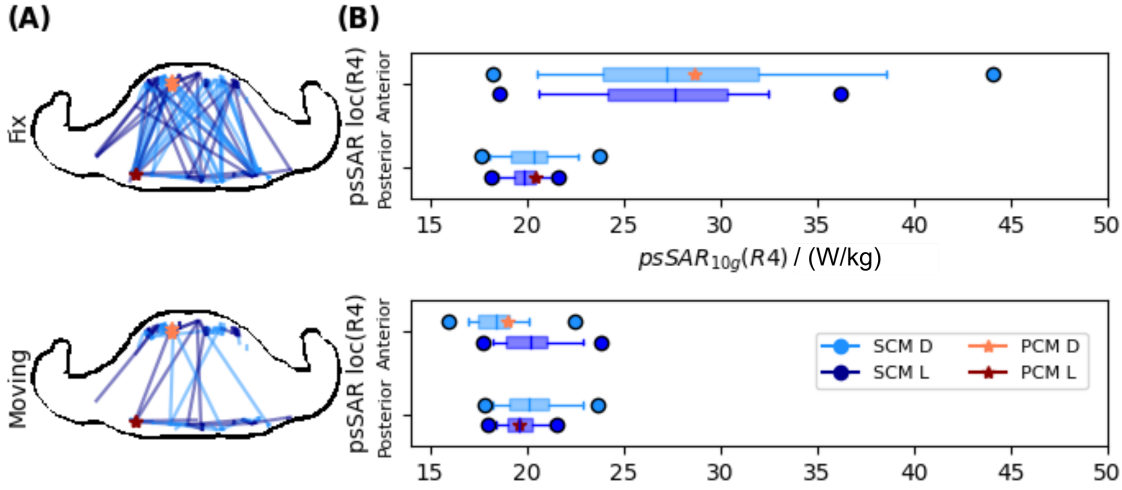

Figure 5.2.4: Respiration induced location changes of $\mathrm{psSAR}_{10\mathrm{g}}$ are shown for different coil setups ('Fixed' and 'Moving') using the SCM and PCM, with 'L' and 'D' channels in (A). The value changes of $\mathrm{psSAR}_{10\mathrm{g}}$ in dependence of the $\mathrm{psSAR}_{10\mathrm{g}}$ location for the inhale state are illustrated in (B).

For the 'Fixed' setup, anteriorly located $\mathrm{psSAR}_{10\mathrm{g}}$ values in the inhale state show larger $\mathrm{psSAR}_{10\mathrm{g}}(\mathrm{R4})$ values compared to posteriorly located $\mathrm{psSAR}_{10\mathrm{g}}(\mathrm{R4})$ (fig. 5.2.4B). This is not observed for the 'Moving' setup.

The PCM calculates a single upper boundary $\mathrm{psSAR}_{10\mathrm{g}}$ value for which no location changes are observed during respiration. For the 'D' channel setup, the $\mathrm{psSAR}_{10\mathrm{g}}$ is located anterior, and for the ’L’ channel setup, it is located posterior. $\mathrm{psSAR}_{10\mathrm{g}}(u_{\mathrm{PCM}}^{\mathrm{max}}, \mathrm{R4})$ is larger for the ’D’ channel setup compared to the ’L’ channel setup. The results of this section have been published in [105].

5.3 Breathing pattern dependent respiration-induced B_1^+ and local $\mathrm{SAR}_{10\mathrm{g}}$ changes

Conventional (’Conv’) breathing, a combination of ’Abd’ and ’Chest’ breathing, was investigated for the ’Moving’ and ’Fixed’ coil setup in the previous data analysis. This section investigates, additionally, the impact of only ’Chest’ breathing and only abdominal (’Abd’) breathing on B_1^+ and $\mathrm{psSAR}_{10\mathrm{g}}$. In this subsection, ’Conv’ breathing refers to the usage of the ’Moving’ setup.

The respiration-induced body model changes of all three breathing patterns are illustrated in fig. 5.3.1. The impact of the respiratory motion on the chest, heart and liver position is investigated for 3 orientations and all respiratory states. The position of the liver, the heart and the chest are highlighted. ’Conv’ breathing results in motion along both the head-feet (HF) direction with maximum displacement for R4 of 20/40mm for the heart/liver and the anterior-posterior (AP) direction with maximum displacement of 4, 20, and 16 mm for chest, liver, and heart, respectively. The chest breathing pattern yields no displacement for the liver along HF, all other values are kept unchanged with respect to ’Conv’ breathing pattern. In contrast, abdominal breathing reflects a pure motion along HF for the liver and no chest motion. For comparison, the last column in fig. 5.3.1 highlights the EM body models combined for all three breathing patterns for the R5 state only.

The enumerated displacements for the different breathing types imply the same coil displacements for ’Conv’ and ’Chest’ breathing, the ’Moving’ coil setup. In contrast, for ’Abd’ breathing, no movement of the chest was observed and the coil remained rigid in one position, a ’Fixed’ setup corresponding to the coil position for ’R1’ in the ’Moving’ setup. Note the difference to the ’Fixed’ setup of the ’Conv’ breathing pattern, here the rigid coil position is equal to ’R4’ in the ’Moving’ setup.

Figure 5.3.2 compares the respiration induced changes of B_1^+ and $\mathrm{psSAR}_{10\mathrm{g}}$ in dependence of the different breathing patterns. ΔCV, $\min|B_1^+|$ and $\mathrm{psSAR}_{10\mathrm{g}}(\mathrm{R4})$ are in the same range for all three breathing patterns (fig. 5.3.2). The ’Abd’ breathing pattern reflects slightly smaller changes in CV [-4.7%,14.4%] and smaller changes in $\mathrm{psSAR_{10g}}$ [-27%,9%] compared to the other setups ('Conv': CV = [-6.0%,19.8%], $\mathrm{psSAR_{10g}}(\vec{u}_{\mathrm{SCM}}) = [-34\%, 27\%]$).

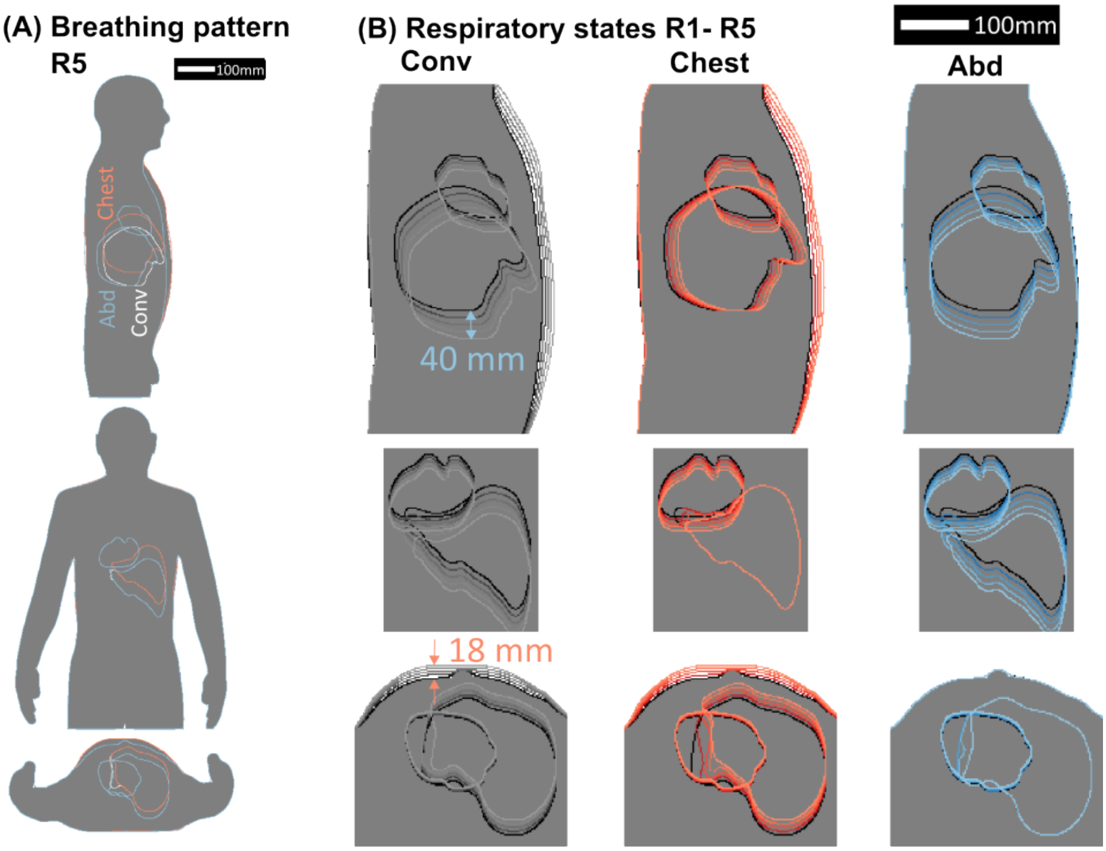

Figure 5.3.1: Analysis of respiration-induced anatomical variations of the XCAT body model for different breathing patterns. (B) shows five respiratory states from exhale-R1 (black contour) to R5. A grey contour is used for 'Conv' breathing as applied for the 'Moving and 'Fixed setup, light red is used for 'Chest' breathing and light blue for 'Abd' breathing. The contours illustrate the heart, liver and chest movements. For each breathing pattern, a sagittal, coronal and transversal projection is shown. (A) reduces the movements shown in (B) on the R5 state and illustrates a direct comparison of the three breathing patterns.

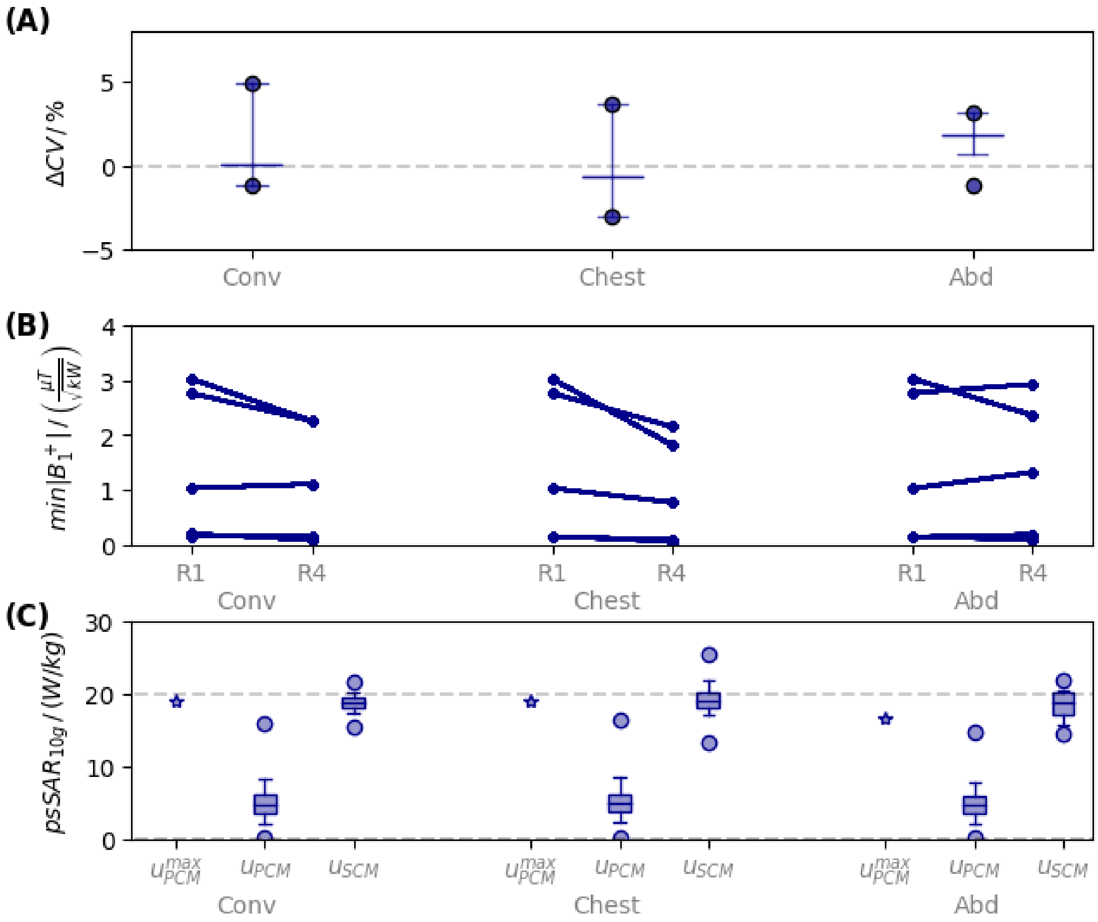

Figure 5.3.2: Respiration induced B_1^+ and $\mathrm{psSAR}_{10\mathrm{g}}$ changes in dependence of the breathing pattern: (A-B) In analogy to fig. 5.1.3 ΔCV values (A) and the $\min(|B_1^+|)$ (B) are evaluated for a set of homogeneous shim vectors. 'D' channels and an optimization performed on 'R1' were utilized. (C) $\mathrm{psSAR}_{10\mathrm{g}}(\mathrm{R4})$ values are illustrated in analogy to fig. 5.2.2 for 10^6 random amplitude and phase shim vectors . $\mathrm{psSAR}_{10\mathrm{g}}(\vec{u}_{\mathrm{SCM}})$, $\mathrm{psSAR}_{10\mathrm{g}}(\vec{u}_{\mathrm{PCM}})$ and $\mathrm{psSAR}_{10\mathrm{g}}(u_{\mathrm{PCM}}^{\mathrm{max}})$ are evaluated. Compliance with the IEC limit during the exhale state is ensured by scaling the shim vector magnitude to obtain $\mathrm{psSAR}_{10\mathrm{g}}(\mathrm{R1}) = 20\,\mathrm{W/kg}$, the same scaled shim vector is applied to $Q_{10\mathrm{g}}(\mathrm{R4})$ to calculate $\mathrm{psSAR}_{10\mathrm{g}}(\mathrm{R4})$. The respiration-induced changes are calculated for the breathing patterns illustrated in fig. 5.3.1. The box-plots display whiskers representing the 5th and 95th percentiles, boxes marking the first and third quartiles with the median value, and circles indicating the extrema.

5.4 Element type dependent respiration-induced B_1^+ and local SAR_{10g} changes

Each module of the body coil array used contains a loop ’L’ and a dipole ’D’ element. In the previous sections, respiration-induced B_1^+ and psSAR_{10g} of the ’D’ channels were investigated. Figure 5.4.1 additionally shows the respiration-induced changes in B_1^+ and psSAR_{10g} for the ’L’ and the combination of both element types, the ’LD’ setup. The ’Moving’ setup with the ’Conv’ breathing pattern is used.

In general, the largest respiration-induced B_1^+ changes and most solution sets of the B_1^+ optimization are observed for the ’LD’ setup. ΔCV is larger for the ’L’ and ’LD’ combination compared to ’D’ (’D’: [-1.2,4.9], ’L’: [-4.1,15.6], ’LD’: [2.0,30.5]).
In contrast to the larger respiration-induced B_1^+ changes for the ’LD’ setup compared to the ’D’ setup, $\Delta\mathrm{psSAR}_{10g}$ of the ’L’ and ’LD’ combination shows similar values compared to ’D’, for all control-modes.

Element type		**’D’**				**’L’**	**’LD’**
Breathing pattern		**Conv**	**Conv**	**Chest**	**Abdominal**	**Conv**	**Conv**
Coil setup		**Fixed**	**Moving**	**Moving**	**Fixed**	**Moving**	**Moving**
ΔCV / %		[6.0,13.1]	[-1.2,4.9]	[-3.1,3.6]	[-1.2,3.1]	[-4.1,15.6]	[2.0,30.5]
$\min(\lvert B_1^+\rvert)$ / $\left(\frac{\mu\mathrm{T}}{\sqrt{\mathrm{kW}}}\right)$	R1	[0.0,1.6]	[0.1,3.0]	[0.1,3.0]	[0.1,3.0]	[0.0,2.8]	[0.1,4.9]
	R4	[0.0,1.2]	[0.1,2.3]	[0.1,2.2]	[0.1,2.9]	[0.0,1.4]	[0.0,3.4]
$\mathrm{psSAR}_{10\mathrm{g}}(\mathrm{R4})$/ $\left(\frac{\mathrm{W}}{\mathrm{kg}}\right)$	$u_{\mathrm{PCM}}^{\max}$	28.7	19.0	19.1	16.7	19.6	19.7
	$\vec{u}_{\mathrm{PCM}}$	[0.2,24.7]	[0.2,16.3]	[0.2,16.7]	[0.2,14.7]	[0.1,17.4]	[0.3,13.5]
	$\vec{u}_{\mathrm{SCM}}$	[16.1,50.3]	[13.2,25.3]	[13.7,24.0]	[14.5,21.8]	[14.0,25.8]	[13.8,26.2]

Table 5.4.1: Respiration-induced B_1^+ and $\mathrm{psSAR}_{10\mathrm{g}}$ changes in dependence of the element type, breathing pattern and coil setup: In analogy to fig. 5.1.3 ΔCV values and the $\min(\lvert B_1^+\rvert)$ are evaluated for a set of homogeneous shim vectors. The $\mathrm{psSAR}_{10\mathrm{g}}(\mathrm{R4})$ is listed in analogy to fig. 5.2.2. Compliance with the IEC limit during the exhale state is ensured by scaling the shim vector magnitude to obtain $\mathrm{psSAR}_{10\mathrm{g}}(\mathrm{R1}) = 20\,\mathrm{W/kg}$, the same scaled shim vector is applied to $Q_{10\mathrm{g}}(\mathrm{R4})$ to calculate $\mathrm{psSAR}_{10\mathrm{g}}(\mathrm{R4})$. $\mathrm{psSAR}_{10\mathrm{g}}(\vec{u}_{\mathrm{SCM}})$, $\mathrm{psSAR}_{10\mathrm{g}}(\vec{u}_{\mathrm{PCM}})$ and $\mathrm{psSAR}_{10\mathrm{g}}(u_{\mathrm{PCM}}^{\max})$ are evaluated. The extrema are labeled as [min,max].

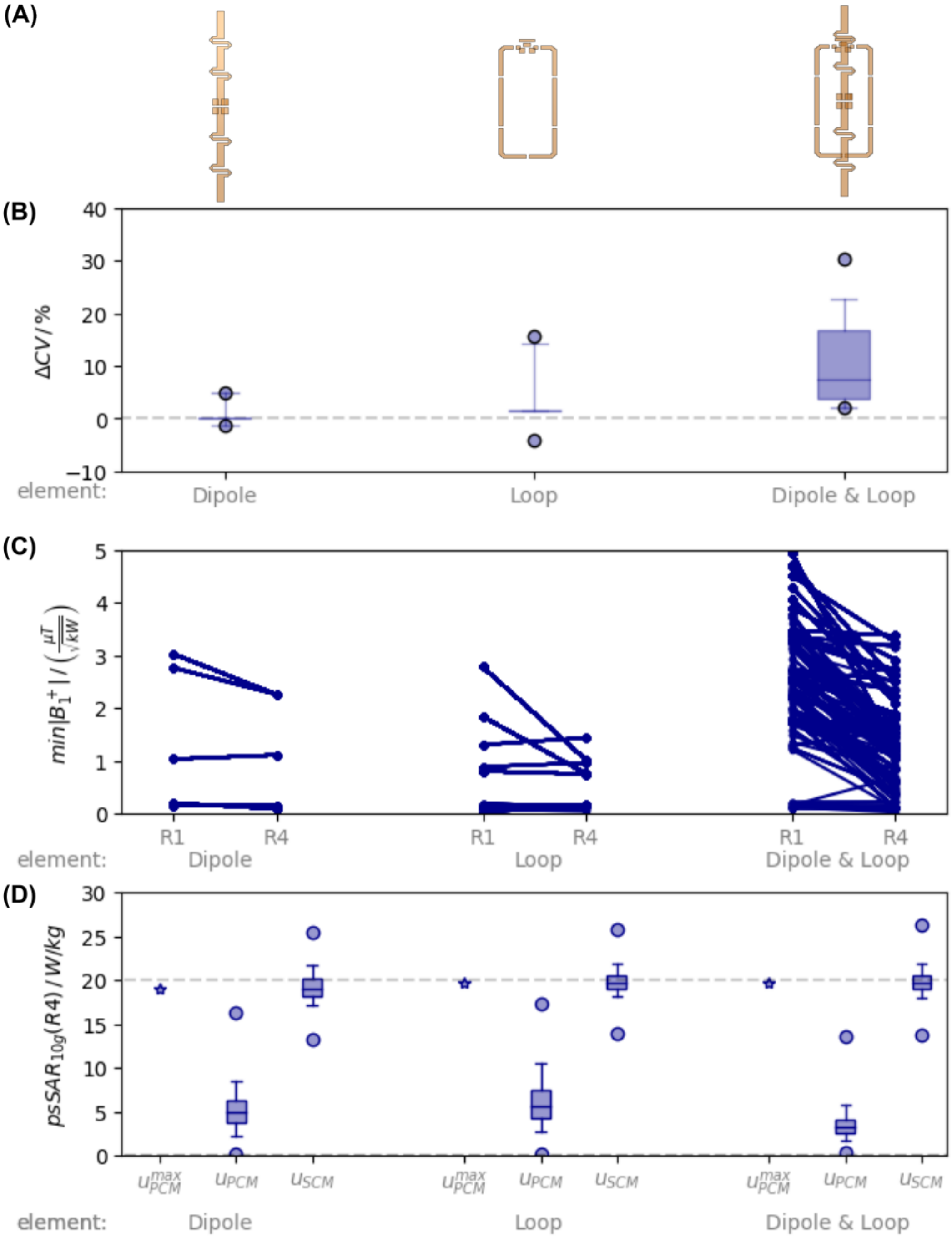

Figure 5.4.1: Respiration-induced B_1^+ and $\mathrm{psSAR}_{10\mathrm{g}}$ changes in dependence of the element type, using the 'Moving' setup and 'Conv' breathing: (A) shows an overview of the FDTD models of the simulated element types. In (B-C) the respiration-induced ΔCV and the $\min(|B_1^+|)$ are quantified in analogy to fig. 5.1.3 for a set of homogeneous shim vectors optimized on 'R1'. In (D) the $\mathrm{psSAR}_{10\mathrm{g}}(\mathrm{R4})$ is compared in analogy to fig. 5.2.2 for 10^6 random amplitude and phase shim vectors. $\mathrm{psSAR}_{10\mathrm{g}}(\vec{u}_{\mathrm{SCM}})$, $\mathrm{psSAR}_{10\mathrm{g}}(\vec{u}_{\mathrm{PCM}})$ and $\mathrm{psSAR}_{10\mathrm{g}}(u_{\mathrm{PCM}}^{\max})$ are evaluated. Compliance with the IEC limit during the exhale state is ensured by scaling the shim vector magnitude to obtain $\mathrm{psSAR}_{10\mathrm{g}}(\mathrm{R1}) = 20\,\mathrm{W/kg}$, the same scaled shim vector is applied to $Q_{10\mathrm{g}}(\mathrm{R4})$ to calculate $\mathrm{psSAR}_{10\mathrm{g}}(\mathrm{R4})$. The box-plots display whiskers representing the 5th and 95th percentiles, boxes marking the first and third quartiles with the median value, and circles indicating the extrema.

5.5 Respiration-induced S-matrix changes

The primary objective of this work was to investigate the impact of respiratory motion on FA and psSAR_{10g}. One main finding is that respiration-induced FA changes are smaller for FA optimization performed on the exhalation respiratory state compared to the inhalation respiratory state. Another solution for decreasing respiration-induced changes in the FA is to use respiration gating during the measurement.

The S-Matrix is measured by directional couplers of the MR scanner, which enables respiration gating without increasing the measurement time or additional hardware and sequence design.

The S-Matrix respiration-induced changes are shown in fig. 5.5.1 for the ’Moving’ and ’Fixed’ setup. The absolute S-Matrix values for the exhale (R1) respiratory state are summarized for all setups and element types in table 5.5.1.

The largest $|\Delta S_{m,l}^{(motion)}|$ of 0.103/0.056 is observed for the channel m=l=L2/D2 with the ’Fixed’ setup. This corresponds to 50%/6% respiration-induced changes of the absolute $S_{\mathrm{L2,L2}}/S_{\mathrm{D2,D2}}$ of 0.204/0.848 for the exhale respiratory state.

The inner anterior elements (elements 2,3) show larger changes compared to the outer anterior (elements 1,4) and posterior (elements 5,6,7,8) elements. Analysing a full respiratory cycle of inner anterior elements L2/D2 (fig. 5.5.1E/F) shows an increasing $|\Delta S_{m,l}^{(motion)}|$ with inspiration.

Coil setup	**Fixed**		**Moving**	
Element type	**’D’**	**’L’**	**’D’**	**’L’**
Max(S_{ml})	0.9398 = -0.54dB	0.4322 = -7.29dB	0.9312 = -0.6dB	0.4051 = -7.85dB
Min(S_{ml})	0.0004 = -67.31dB	0.001 = -59.77dB	0.0005 = -65.5dB	0.0016 = -55.71dB

Table 5.5.1: The S-Matrix entries $S_{m,l}$ with maximum and minimum values for the respiratory state R1 are summarized for the ’Fixed’ and ’Moving’ coil setup, and the element types ’D’ and ’L’. The values are given as absolute and db values. The maximum values are observed for all element types and coil setups in $S_{3,3}$. The minimum values are observed for ’D’ channels in $S_{3,5}$ and for ’L’ channels in $S_{3,4}$ for ’Fixed’ and ’Moving’.

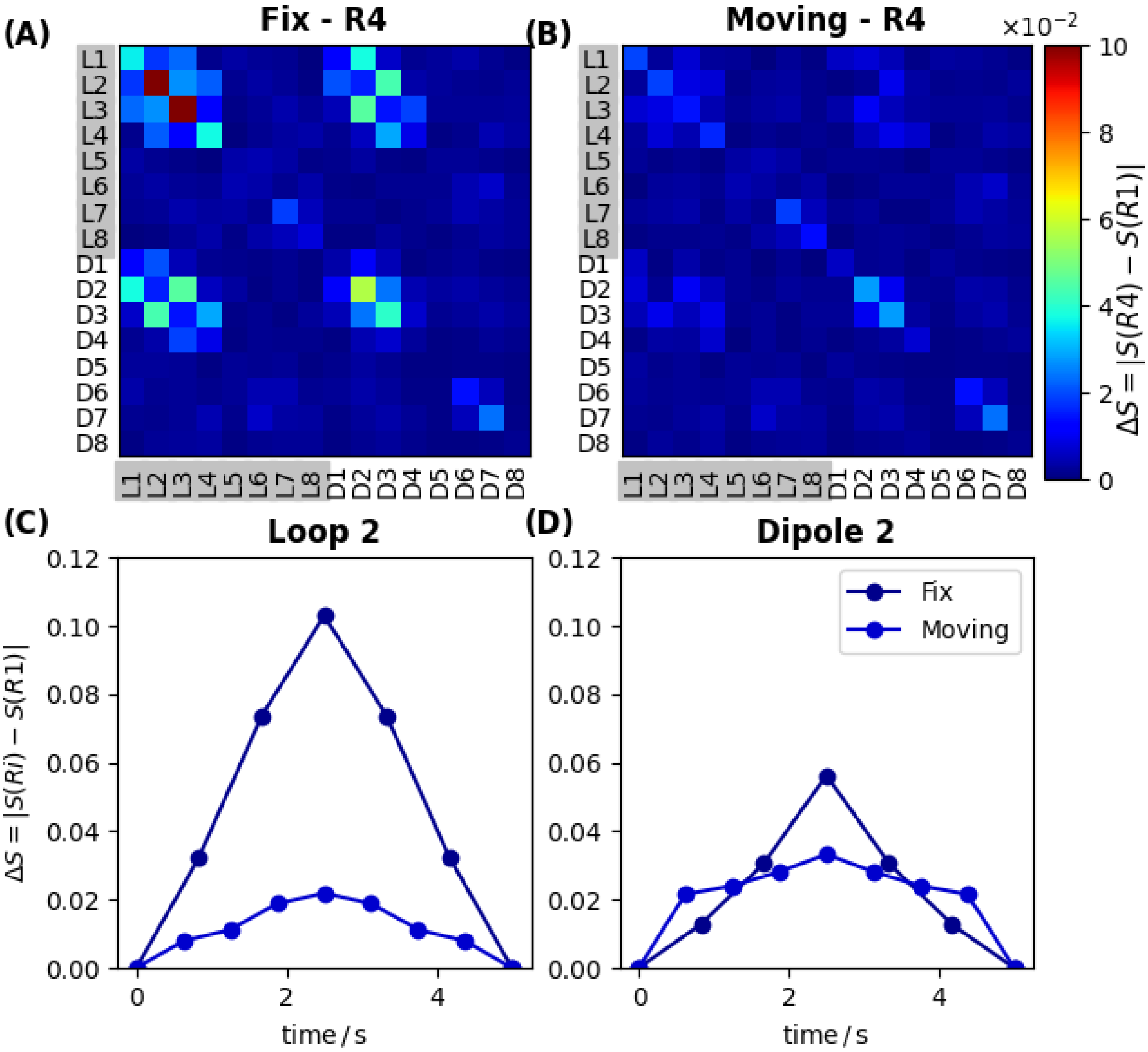

Figure 5.5.1: Respiration-induced S-Matrix changes: (A-B) coil setup dependent respiration-induced changes between R4 and R1 for the full S-Matrix (including loop (L_m) and dipole (D_m) channels, with m = 1...8), (C-D) element type dependent respiratory changes of $\Delta S_{m,l}$ for m=l=2 channel for a full respiratory cycle. The exhale respiratory state is used for reference.

5.6 Summary

First, the results show an impact of respiratory motion on the B_1^+ field for a 'Moving' and a 'Fixed' coil setups with a 'Conv' breathing pattern at 7 T.

The channel-wise $\Delta|B_1^+|$ is larger for anterior elements compared to posterior elements, while the phase B_1^+ changes are larger for posterior elements using the 'Moving' setup.

The investigation of 1000 starting phase sets, for static B_1^+ optimizations using the 7 T 8Tx 'D' setup, was done for optimizations on different respiratory states ('R1&R4','R1' and 'R4'). CV(R1) ranges from 16% to 26% for optimizing on 'R1' with the 'Moving' setup. In general the largest ΔCV and $\Delta \min|B_1^+|$ are observed for optimizing on 'R4', here a similar range for the 'Fixed' and 'Moving' setup was observed. Optimizations performed on 'R1&R4' or 'R1' data yielded larger ΔCV for the 'Fixed' setup compared to the 'Moving' setup.

Second, larger respiration-induced $\mathrm{psSAR}_{10\mathrm{g}}$ changes are observed for the SCM compared to the PCM. Amplitude and phase shim vectors imply larger $\Delta\mathrm{psSAR}_{10\mathrm{g}}$ than only phase shim vectors. Quantitatively, the worst case $\Delta\mathrm{psSAR}_{10\mathrm{g}}$ of the SCM is 151% for the 'Fixed' setup and 29% for the 'Moving' setup. In addition to the respiration-induced $\mathrm{psSAR}_{10\mathrm{g}}$ value changes, also $\mathrm{psSAR}_{10\mathrm{g}}$ location changes and thus changes of the hot spot's from anterior to posterior are observed.

Third, the results show similar ΔCV, $\Delta \min|B_1^+|$ and $\Delta\mathrm{psSAR}_{10\mathrm{g}}$ for different breathing patterns, as 'Conv','Chest' and 'Abd'. The element type impacts ΔCV, the dipoles showed the smallest CV changes, while the loop-dipole combination showed the largest CV changes. In contrast, within each control mode similar $\Delta\mathrm{psSAR}_{10\mathrm{g}}$ values are observed for all element types.

Last, the matrix entries ΔS_{mm} are larger for inner anterior elements compared to all other elements and are larger for the 'Fixed' setup compared to the 'Moving' setup.

In conclusion, this chapter has confirmed the experimentally observed respiration-induced B_1^+ changes through simulations and illustrated the impact of respiratory motion on $\mathrm{psSAR}_{10\mathrm{g}}$ for the first time. This work has demonstrated the trends of respiration-induced B_1^+ and $\mathrm{psSAR}_{10\mathrm{g}}$ changes for a specific body model, and a specific coil model, under static pTx at 7 T. In the next chapter, it will be investigated how these changes are affected by an increase in field strength and the transition from static pTx to dynamic pTx.

Chapter

6 The impact of the field strength on respiration-induced EM field changes

It is crucial to recognize that while higher field strengths offer numerous benefits, they also present challenges in relation to the E- and B-fields. The wavelength is below the range of the human thorax, leading to stronger interference patterns and signal dropouts. This does not only increase the FA inhomogeneity but also results in more localized hot spots and, therefore, higher peak spatial SAR values for 7 T [21] and 10.5 T [22]. FA variations at 7 T can be addressed by static pTx [12, 13] for small ROIs and dynamic pTx (e.g. kT points) for larger 3D ROIs [13–15]. For static pTx the last chapter illustrated the impact of respiration-induced motion on CV, min($|B_1^+|$) and $\text{psSAR}_{10\text{g}}$.

So far, the combination of increasing the field strength and considering the respiration has not been published yet.

This work investigates: first, the safety relevance and respiration-induced FA changes for field strengths of 7 T and 10.5 T, Second, the respiration-induced FA and SAR changes with increasing number of kT points, third, the qualitative validation of respiration-induced B_1^+ changes at 7 T and 10.5 T.

The results of this section are currently under internal revision for submission in the journal 'Magnetic Reconance in Medicine' [106].

6.1 Respiration-induced FA changes

Respiration-induced changes in the FA are compared for $B_0 = 7\,\mathrm{T}$ and $B_0 = 10.5\,\mathrm{T}$. The changes are evaluated channel-wise, for static and for dynamic pTx (2kT points and 4kT points). The dynamic pTX optimization is first performed with a wide range of regularisation parameters, from which a fixed regularisation parameter is selected in a second run. The second run utilizes 200 starting sets of phase vectors to obtain the ideal FA optimizations. In the last chapter, the respiratory states exhale (R1), intermediate respiratory states (R2,R3), inhale respiratory state (R4) and an additional scenario of increased inhalation depth (R5) were investigated. In this chapter, only inhale and exhale respiratory states are investigates, for consistency reasons, the nomenclature of R1 and R4 is maintained.

6.1.1 Channel-wise - respiration induced B_1^+ changes

In general, comparing the mean magnitude of channel-wise B_1^+ maps for 7 T and 10.5 T at the exhale respiratory state inside the ROI, larger $|B_1^+|$ values are observed for 10.5 T for all channels. $|B_1^+|$ values are normalized by the same forward power (25 mW) for 7 T and 10.5 T, while the input power, which is the forward power minus the reflected power, differs between 7 T and 10.5 T. The anterior elements D1-D4 have mean $|B_1^+(\mathrm{R1})|$ values inside the ROI, ranging from 0.7 to $3.3\frac{\mu\mathrm{T}}{\sqrt{\mathrm{kW}}}$ at 7 T, and from 1.7 to 5.2 $\frac{\mu\mathrm{T}}{\sqrt{\mathrm{kW}}}$ at 10.5 T (table A.3.1). For the posterior elements, the mean $|B_1^+(\mathrm{R1})|$ values inside the ROI, are smaller compared to the anterior elements, and in addition, smaller differences in mean $|B_1^+(\mathrm{R1})|$ between 7 T and 10.5 T are observed. The minimum $|B_1^+|$ values are for all channels smaller for 10.5 T compared to 7 T. Investigating the mean B_1^+ phase gradient in AP direction (table A.3.3), for non-angulated elements (D2,D3,D6,D7), larger gradients are observed for 7 T compared to 10.5 T (7 T: 2.4-$2.7\frac{\circ}{\mathrm{mm}}$, 10.5 T: 3.9-$4.1\frac{\circ}{\mathrm{mm}}$).

Investigating respiration-induced B_1^+ changes channel-wise, it was observed that $\Delta\min(|B_1^+|)$ remains below 0.33 $\frac{\mu\mathrm{T}}{\sqrt{\mathrm{kW}}}$ for both 7 T and 10.5 T and all channels. Moreover, the channel-wise respiration-induced changes in the mean$|B_1^+|$ either remain within a similar range or slightly expand for 10.5 T when compared with 7 T. The root sum of squares of Δmean$|B_1^+|$ over all channels is 1.3 times larger at 10.5 T than at 7 T. Comparing the mean $\Delta\varphi$ within the ROI, larger phase changes are observed for non-angulated posterior elements, compared to non-agulated anterior elements, for both 7 T and 10.5 T.

Respiration-induced changes in the B_1^+ field for all individual channels are summarized in tables A.3.1 to A.3.3.

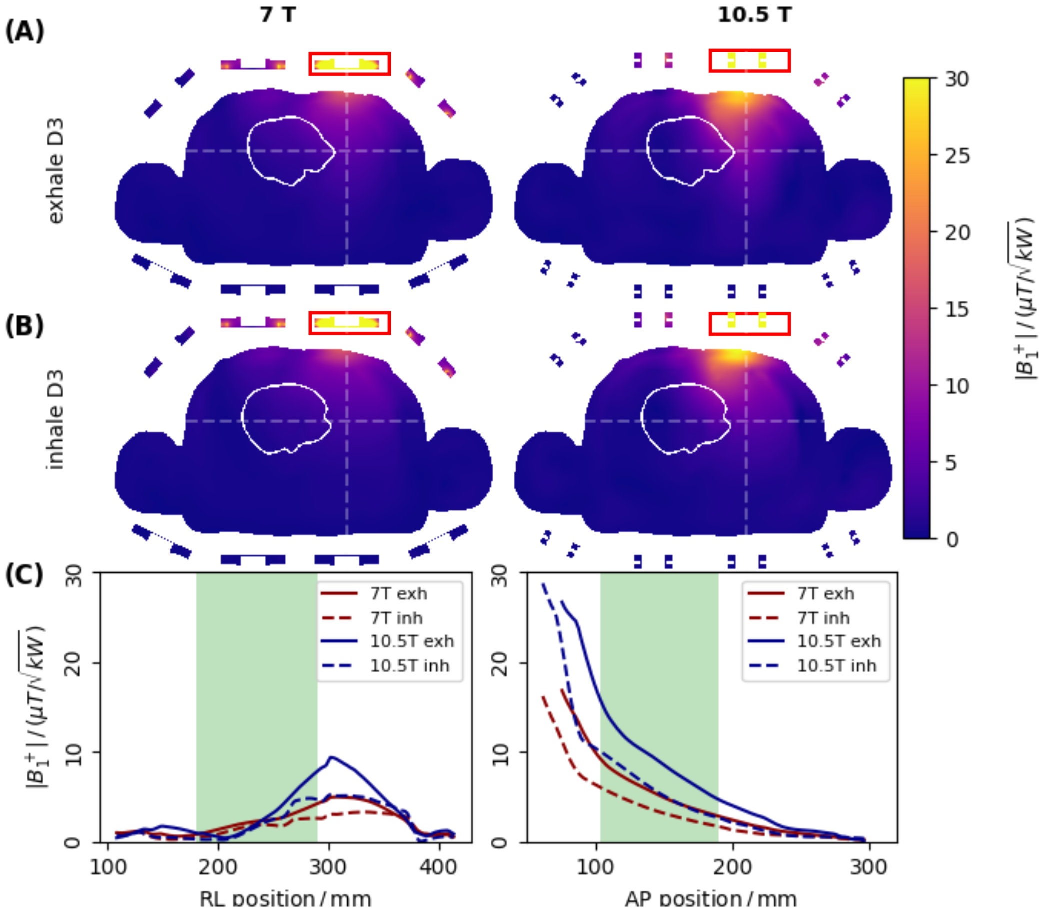

Figure 6.1.1: The channel-wise B_1^+ magnitude maps are shown for the inner anterior element D3. The active channels are marked by a red box. (A) corresponds to the respiratory state exhale (R1), while (B) represents the respiratory state inhale (R4). Furthermore, the first column corresponds to the 7 T field strength, while the second column pertains to the 10.5 T field strength. The shown slices are central heart slices. (C) illustrates line plots in RL and AP directions for $|B_1^+|$. The ROI is marked by the white line in the maps and the green region in the line plots.

Figure 6.1.1 depicts respiration state-dependent B_1^+ amplitude values for both 7 T and 10.5 T for the anterior element D3. In this context, the min $|B_1^+(\text{R1})|$ is found to be two-fold greater at 7 T than at 10.5 T, while the mean$|B_1^+|$ registers a 23% increase at 10.5 T in comparison to 7 T. For this channel, the input power is 36% for 7 T and 80% for 10.5 T of the forward power. The forward power was chosen, as $|B_1^+|$ measurements are normalized

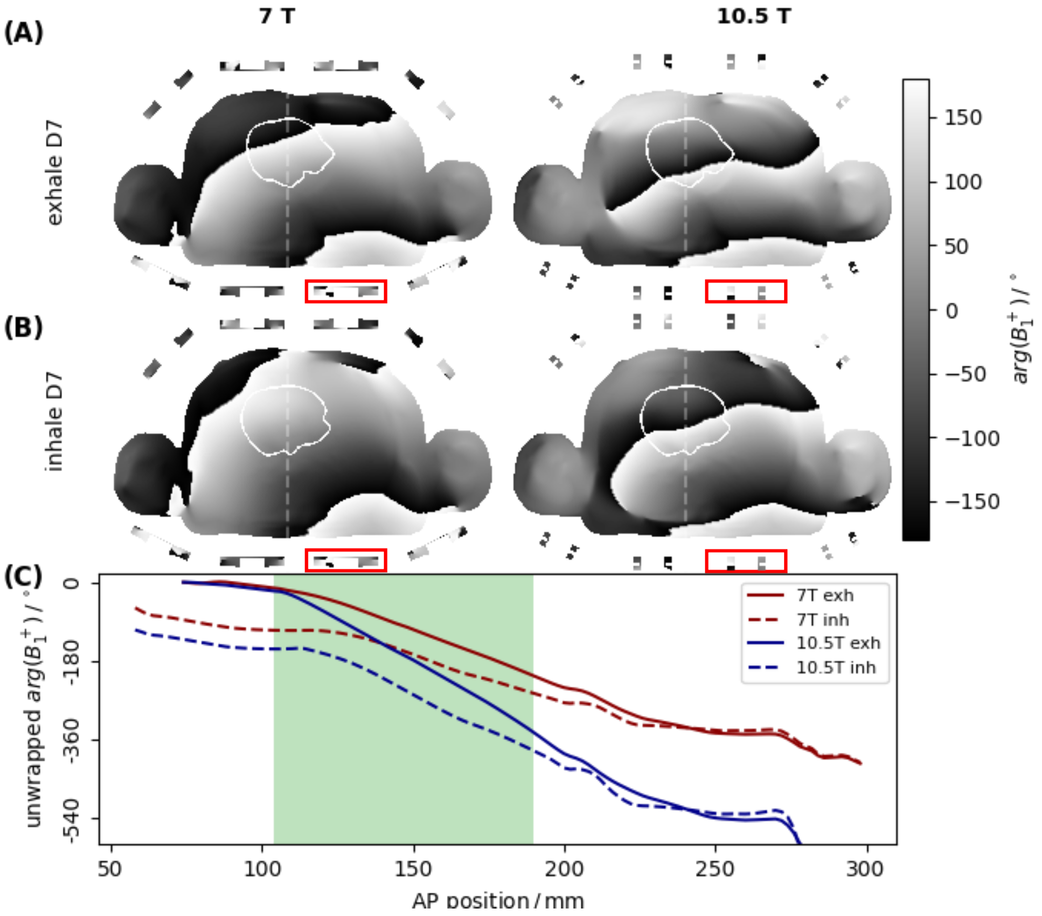

Figure 6.1.2: The channel-wise B_1^+ phase maps are shown for the inner posterior element D7. The active channels are marked by a red box. (A) corresponds to the respiratory state exhale (R1), while (B) represents the respiratory state inhale (R4). Furthermore, the first column corresponds to the 7 T field strength, while the second column pertains to the 10.5 T field strength. The shown slices are central heart slices. (C) illustrates line plots in AP directions for the unwrapped B_1^+ phase. The ROI is marked by the white line in the maps and the green region in the line plots.

to the forward power, often also termed the power efficiency.

Furthermore, channel-wise respiration-induced phase changes are more pronounced in the central posterior elements when compared to their central anterior counterparts (table A.3.1). As such, fig. 6.1.2 pertains to the central posterior element D7. The channel-wise phase changes induced by respiration for element D7 are greater at 10.5 T than at 7 T, both at a central cardiac location and in terms of the mean phase changes over the ROI within the central heart slice. The mean phase undergoes a 1.6-fold faster change at 10.5 T compared to 7 T for the exhale respiratory state $\left(\text{mean}\left(\frac{\partial}{\partial r_{\text{AP}}}\varphi(\text{R1}, x)\right)\right)$, and the mean respiration-induced phase changes $\left(\text{mean}\left(\frac{\partial}{\partial r_{\text{AP}}}(\varphi(\text{R4}, x) - \varphi(\text{R1}, x))\right)\right)$ exhibit a 1.4-fold faster rate of change for 10.5 T compared to 7 T.

6.1.2 Static and dynamic pTx - respiration induced FA changes

The application of different RF pulses during parallel transmission leads to a FA pattern resulting from the interference of the eight channel-wise B_1^+ maps. In dynamic pTx, the complex weights that are applied to the RF pulses change over time, and with this, the resulting B_1^+. The final FA at the end of the RF pulse train is optimized. For static pTx the B_1^+ is optimized, here the B_1^+ is proportional to the FA. In the following subsection, FA changes for static and dynamic pTx at 7 T and 10.5 T are illustrated (figs. 6.1.3 and 6.1.4). For dynamic pTx 2kT and 4kT points are used, with a fixed regularisation parameter β and 200 starting phase vector sets. The FA is homogenized inside the ROI for the respiratory state 'R1' to a mean(FA) of approximately 10°. The obtained pulses were applied to the inhale state. All solutions have a mean(FA) of approximately 10° but in dependence on the exact RF pulse train, they lead to different respiration-induced changes.

Figure 6.1.3 illustrates the distribution of the CV values and mean(FA) values for the inhale and exhale respiratory states. This is shown for 7 T and 10.5 T, as well as for static and dynamic pTx.

In general, fig. 6.1.3A illustrates larger ΔCV values for 7 T compared to 10.5 T. Quantitatively, a maximum ΔCV of 18%/24.7% is observed for 7 T/10.5 T with 2kT points. For static pTx the maximum Δmean(FA) increased from 1.3° (7 T) to 1.7° (10.5 T) with increasing field strength. In contrast, 2kT points showed a decrease in the maximum Δmean(FA) from 2.5° (7 T) to 2.2° (10.5 T) with increasing field strength.

Increasing the number of kT points decreases CV(R1) and increases the respiration-induced changes ΔCV and Δmean(FA). Quantitatively, a maximum CV(R1) of 21.7%/7.1%/3.6%

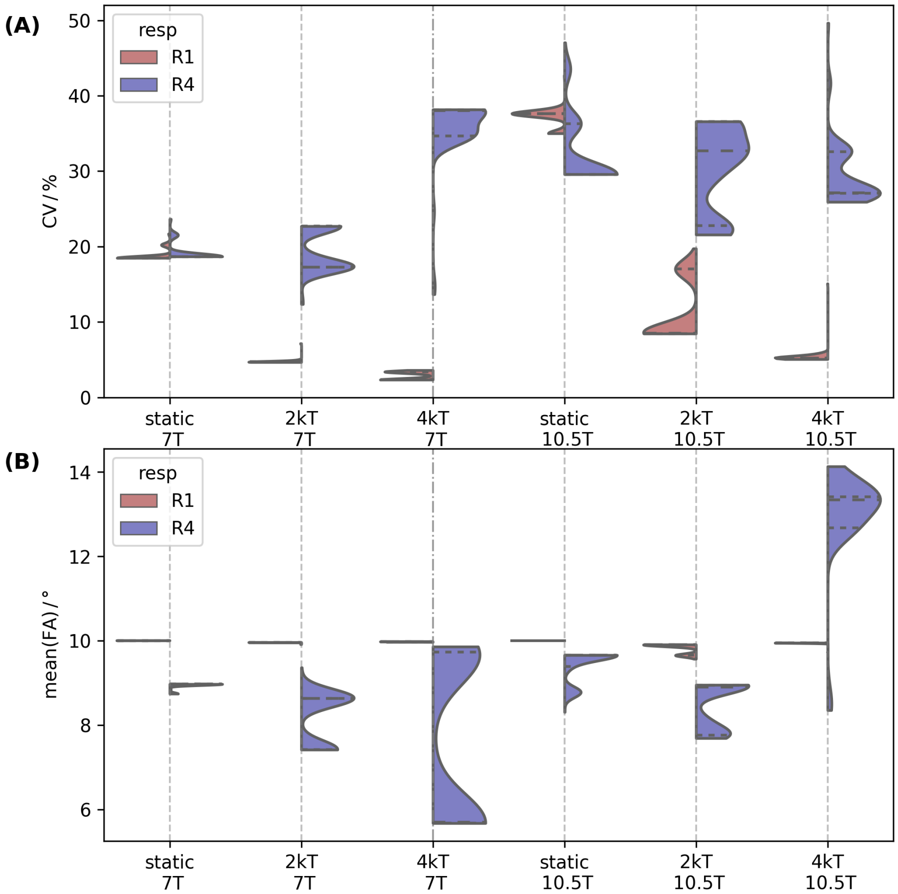

Figure 6.1.3: Quantitative FA analysis, comparing static and dynamic (2kT, 4kT) pTx at 7 T and 10.5 T. 200 starting sets of phase vectors were applied to a FA optimization for the 3D heart in the respiratory exhale state. In (A) the CV values and in (B) the mean(FA) of the solution sets were evaluated. For dynamic pTx, a fixed regularisation parameter was used for all 200 starting sets of phase vectors. The generated RF pulses are assessed both for exhale (red) and inhale (blue), using violin plots. The dashed lines represent the first, second, and third quartiles.

and a maximum ΔCV of 1.9%/18%/35.8% is observed for static pTx / 2kTpoints / 4kT points at 7 T.

Figure 6.1.4 investigates the dependency between ΔCV and CV(R1) for 7 T and 10.5 T, for static and dynamic pTx. Qualitatively, an increase in the field strength increases the range of CV(R1) and ΔCV, which highlights the observations made in fig. 6.1.3A. Quantitatively, the maximum obsreved CV(R1) was 21.7%/42.7% for 7 T/10.5 T using static pTx. The largest observed ΔCV was 35.8%/44.1% for 7 T/10.5 T using 4kT points, with CV(R1) below 10%.

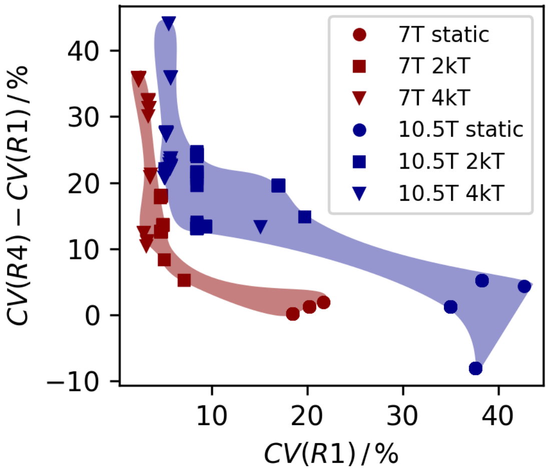

Figure 6.1.4: Respiration induced CV changes in dependence of CV(R1), were compared for static and dynamic (2kT, 4kT) pTx at 7 T (red) and 10.5 T (blue). 200 starting sets of phase vectors were applied to a FA optimization for the 3D heart in the respiratory exhale state, the CV values of the solution sets were evaluated. For dynamic pTx, a fixed regularisation parameter was used for all 200 starting sets.

6.2 Respiration-induced psSAR changes

psSAR_{10g} values for the inhale respiratory state are illustrated for 7 T and 10.5 T utilizing the SAR-controlled mode (SCM) in fig. 6.2.1 and utilizing the power-controlled mode (PCM) in fig. 6.2.2.

For the SCM, individual shim vectors $\vec{u}$ are scaled by c_{SCM} to u_{SCM} to obtain $\mathrm{psSAR}_{10g}(\mathrm{R1}, \vec{u}_{\mathrm{SCM}}) = 20\,\frac{W}{kg}$ matching the IEC first level controlled SAR limit. The same shim vector $\vec{u}_{\mathrm{SCM}}$ is applied to the inhale respiratory state, and fig. 6.2.1 shows the distribution of $\mathrm{psSAR}_{10g}(\mathrm{R4}, \vec{u}_{\mathrm{SCM}})$ for static and dynamic pTx at 7 T and 10.5 T. Dynamic pTx uses 2kT and 4kT points with 63 different regularisation parameter values b using 5 starting sets of phase vectors for each regularisation parameter (section 3.5.2) to cover a broad range of possible RF pulses for estimating the impact of respiration on psSAR_{10g}.

In general, an increase of the maximum $\mathrm{psSAR}_{10g}(\mathrm{R4}, \vec{u}_{\mathrm{SCM}})$, for all regularisation parameters and starting phase vector sets, is observed from 7 T to 10.5 T by 10%. $\Delta\mathrm{psSAR}_{10g}(\vec{u}_{\mathrm{SCM}})$ is below 14%/26% for 7 T/10.5 T for static and dynamic pTx. An increase of the number of kT points, from one (static pTx) to four (dynamic pTx), implies an increase of the maximum $\mathrm{psSAR}_{10g}(\mathrm{R4}, \vec{u}_{\mathrm{SCM}})$, for all regularisation parameters and starting phase vector sets, by 4%/5% for 7 T/10.5 T.

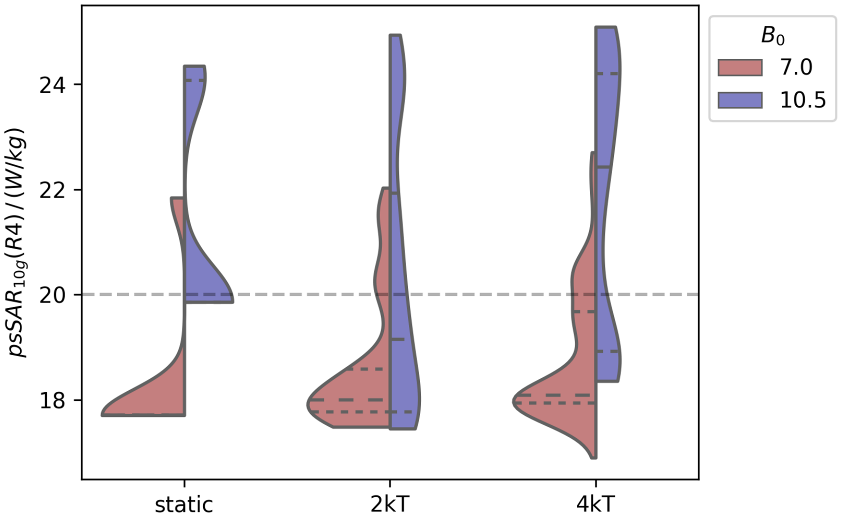

Figure 6.2.1: Quantitative $\mathrm{psSAR}_{10\mathrm{g}}$(R4) analysis using the SCM, comparing static and dynamic (2kT, 4kT) pTx at 7 T (red) and 10.5 T (blue). The FA in the 3D heart ROI was optimized using 200 starting sets of phase shim vectors for static pTx and 5 starting sets of phase shim vectors for each of 63 different regularisation parameters for dynamic pTx. For the resulting RF pulses the local $\mathrm{SAR}_{10\mathrm{g}}$ distributions were calculated and $\mathrm{psSAR}_{10\mathrm{g}}$ determined. $\mathrm{psSAR}_{10\mathrm{g}}(\mathrm{R1}, \vec{u}_{\mathrm{SCM}})$ is scaled to 20 W/kg and the same scaling factor is applied to the inhale $\mathrm{psSAR}_{10\mathrm{g}}$. The graph shows possible IEC first level controlled SAR limit violations for the inhale state if safety assessment is performed on the exhale state and $\mathrm{psSAR}_{10\mathrm{g}}(\mathrm{R4}, \vec{u}_{\mathrm{SCM}}) > 20$ W/kg.

The PCM calculates an upper channel-wise RF pulse amplitude ($u^{\mathrm{max}}_{\mathrm{PCM}}$), which ensures to obtain exhale $\mathrm{psSAR}_{10\mathrm{g}}$(R1) values below 20 W/kg for all shim vectors with channel-wise amplitudes, below $u^{\mathrm{max}}_{\mathrm{PCM}}$. $u^{\mathrm{max}}_{\mathrm{PCM}}$ is applied to the inhale SAR-matricies and the corresponding $\mathrm{psSAR}_{10\mathrm{g}}(u^{\mathrm{max}}_{\mathrm{PCM}}, \mathrm{R4})$ is calculated. The PCM was investigated for coil setups with 16 and 8 channels. Please note 16 channels for 7 T include a ’LD’ combination of 8 ’L’ and 8 ’D’ channels, while the 10.5 T setup utilizes 16 ’D’ channels.

In general, for both setups, 10.5 T has higher $\mathrm{psSAR}_{10\mathrm{g}}(\mathrm{R4}, u^{\mathrm{max}}_{\mathrm{PCM}})$ compared to 7 T. This is in agreement with the findings of the SCM. For 7 T $\mathrm{psSAR}_{10\mathrm{g}}(\mathrm{R4}, u^{\mathrm{max}}_{\mathrm{PCM}})$ values are below the $\mathrm{psSAR}_{10\mathrm{g}}(\mathrm{R1}, u^{\mathrm{max}}_{\mathrm{PCM}})$ values and with this below the IEC-limit. For 10.5 T an exceedance of the IEC-SAR limit by 30%/19% is observed for the $\mathrm{psSAR}_{10\mathrm{g}}(\mathrm{R4}, u^{\mathrm{max}}_{\mathrm{PCM}})$ for 8/16 Tx channel-coil setups.

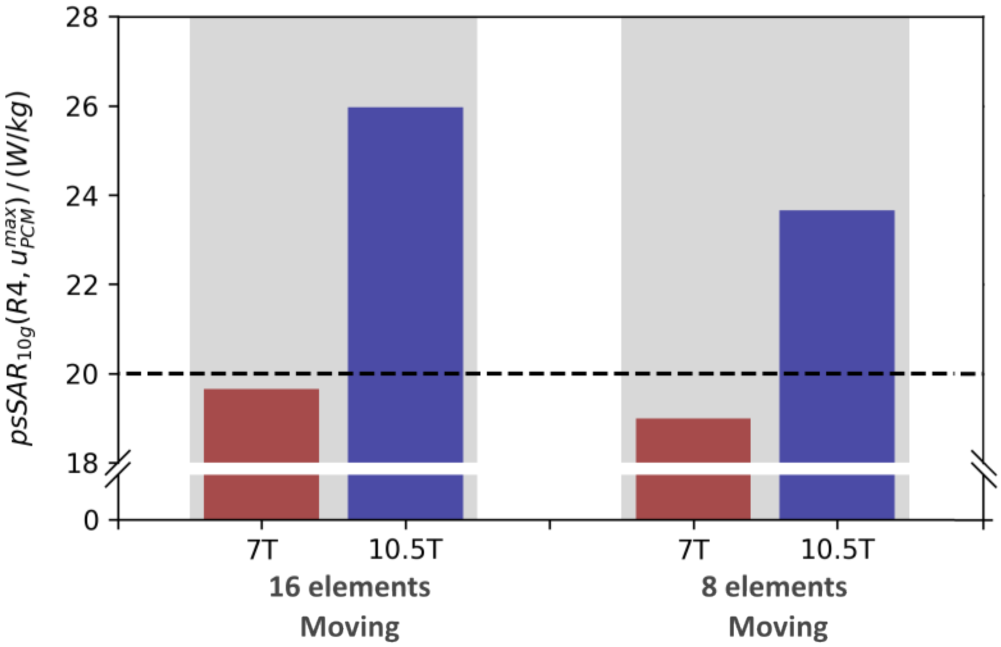

Figure 6.2.2: Quantitative $\mathrm{psSAR}_{10\mathrm{g}}$(R4) analysis using the PCM, comparing 7 T (red) and 10.5 T (blue) with 16- and 8-channel 'Moving' coil arrays. $\mathrm{psSAR}_{10\mathrm{g}}(\mathrm{R1}, u_{max}^{PCM})$ is scaled to 20 W/kg and the same scaling factor is applied to the inhale $\mathrm{psSAR}_{10\mathrm{g}}$. The graph shows possible IEC first-level controlled SAR limit violations for the inhale state if safety assessment is performed on the exhale state and $\mathrm{psSAR}_{10\mathrm{g}}(\mathrm{R4}, u_{max}^{PCM}) > 20\,\mathrm{W/kg}$.

control mode	number of elements	pTx	$\mathrm{psSAR_{10g}}$(R4) / (W/kg) **7 T**	 **10.5 T**
$\vec{u}_{\mathrm{SCM}}$	8	static	[17.7,21.8]	[19.9,24.3]
$\vec{u}_{\mathrm{SCM}}$	8	2kT points	[17.5,22.0]	[17.5,24.9]
$\vec{u}_{\mathrm{SCM}}$	8	4kT points	[16.9,22.7]	[18.4,25.1]
$u^{\mathrm{max}}_{\mathrm{PCM}}$	8	static & dynamic	19.0	23.7
$u^{\mathrm{max}}_{\mathrm{PCM}}$	16	static & dynamic	19.7	26.0

Table 6.2.1: Summary of the $\mathrm{psSAR_{10g}}$(R4) values for the evaluated RF pulses using the SCM with an 8-channel 'Moving' coil array for 7 T and 10.5 T. 200 starting sets of phase vectors were used for static pTx and 5 starting sets of phase vectors for each of 63 different regularisation parameters for dynamic pTx. The minimum and maximum values are given in [min,max]. In addition, the upper boundary $\mathrm{psSAR_{10g}}$(R4) using the PCM is given for 8 and 16-channel 'Moving' coil arrays.

6.3 Example FA and local $\mathrm{SAR_{10g}}$ maps at 7 T and 10.5 T

Example RF pulses of the 2kT point FA optimization were selected separately for 7 T and 10.5 T. The selected RF pulses are solutions of the FA homogenization in the 3D heart ROI (ROI_H) for the exhale respiratory state using different starting phase vector sets, yielding several solution sets. Different starting sets can lead to the same optimized shim vector and kT-point location.

The selected RF pulses illustrate the solution of the FA optimization with minimum ΔCV ('RF pulse 1'), worst-case ΔCV ('RF pulse 2'), and the worst-case $\Delta\mathrm{psSAR_{10g}}$ ('RF pulse 3') within the solution sets of dynamic pTx. 'RF pulse 1' and 'RF pulse 2' were selected from the solution sets of the 2kT point FA optimization, using the fixed regularisation parameter and 200 starting sets of phase vectors. In contrast, 'RF pulse 3' was selected from the solution sets of the 2kT point FA optimization, using 63 different regularisation parameters and 5 starting sets of phase vectors. Please note, 'RF pulse 1' for 7 T is not the same RF pulse as RF pulse 1' for 10.5 T, as individual FA optimizations were performed for 7 T and 10.5 T (in analogy for 'RF pulse 2' and 'RF pulse 3').

Figure 6.3.1 illustrates the FA maps and fig. 6.3.2 illustrates the maximum intensity projection (MIP) along the head-feet direction of the $\mathrm{SAR}_{10\mathrm{g}}$ maps, for the example RF pulses. Sagittal and coronal slices of the FA maps are shown in fig. A.3.1.

In general, for all shown FA maps, the ΔCV is larger for 10.5 T compared to 7 T. In contrast, only 2 selected RF pulses show a larger $\Delta\mathrm{psSAR}_{10\mathrm{g}}$ for 10.5 T compared to 7 T.

The FA maps of 'RF pulse 1' have the smallest ΔCV of all solution sets with ΔCV = 5.2%/13.1% for 7 T/10.5 T of all solution sets. The Δmean(FA) is 1.1°/1.0° for 7/10.5 T. Despite larger ΔCV for 10.5 T compared to 7 T, the $\Delta\mathrm{psSAR}_{10\mathrm{g}}$ is larger for 7 T compared to 10.5 T.

The FA maps of 'RF pulse 2' have the largest ΔCV of all solution sets with ΔCV = 18.0%/24.7% for 7 T/10.5 T. Although the ΔCV is large, small $\mathrm{psSAR}_{10\mathrm{g}}$ respiration induced changes of 0.16/0.01 W/kg are observed for 7 T/10.5 T.

The bottom row maps of 'RF pulse 3' have the maximum $\Delta\mathrm{psSAR}_{10\mathrm{g}}$ of all solution sets with $\Delta\mathrm{psSAR}_{10\mathrm{g}}$ = 2.0/4.9 W/kg for 7 T/10.5 T. For 10.5 T ΔCV of 'RF pulse 3' is similar to ΔCV of 'RF pulse 2', in contrast the $\Delta\mathrm{psSAR}_{10\mathrm{g}}$ of 'RF pulse 3' is 25% higher compared to $\Delta\mathrm{psSAR}_{10\mathrm{g}}$ of 'RF pulse 2'. The $\mathrm{psSAR}_{10\mathrm{g}}$ location for 10.5 T is anterior, while all other shown RF pulses in fig. 6.3.2 have posterior $\mathrm{psSAR}_{10\mathrm{g}}$ locations. Please note the difference of randomly selected shim vectors for fig. 5.2.1 'shim vector 3' and 2kT point RF pulses which were optimized for a mean(FA(R1)) of 10° in fig. 6.3.2 'RF pulse 3'.
All values are summarized in table A.3.5.

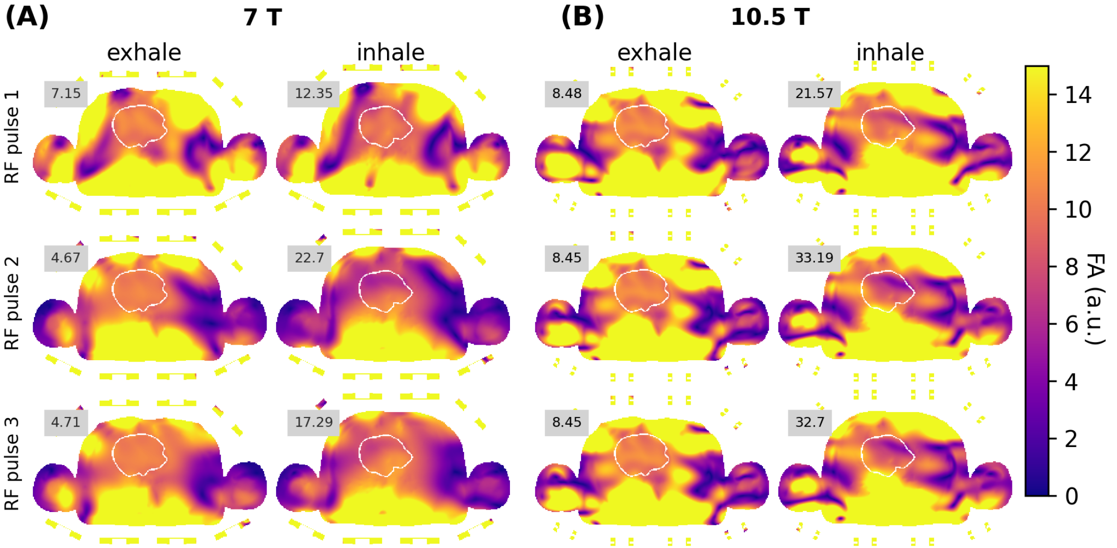

Figure 6.3.1: Example transversal FA maps are shown for 3 different RF pulses at 7 T and 10.5 T. Dynamic pTx using 2kT points was utilized to optimize the FA in the 3D heart ROI for the exhale respiratory state using different starting sets of phase vectors. Coronal and sagittal slices are shown in fig. A.3.1. ('RF pulse 1') shows the solution with min(CV(R4) – CV(R1)) and ('RF pulse 2') with max(CV(R4) – CV(R1)) of the 2kT point cases shown in figs. 6.1.3 and 6.1.4, while ('RF pulse 3') is the solution with the largest psSAR_{10g}(R4) of the 2kT point cases shown in fig. 6.2.1. The CV values of the entire 3D ROI are denoted inside the gray boxes.

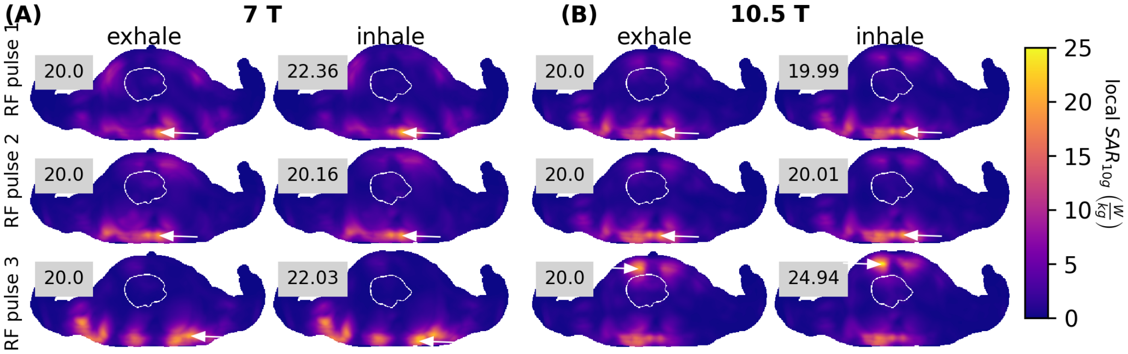

Figure 6.3.2: Maximum intensity projections of example SAR_{10g} maps are shown for 3 different RF pulses at 7 T and 10.5 T. Dynamic pTx using 2kT points was utilized to optimize the FA in the 3D heart ROI for the exhale respiratory state using different starting settings of phase vectors. ('RF pulse 1') shows the solution with min(CV(R4) – CV(R1)) and ('RF pulse 2') with max(CV(R4) – CV(R1)) of the 2kT point cases shown in figs. 6.1.3 and 6.1.4, while ('RF pulse 3') is the solution with the largest psSAR_{10g}(R4) of the 2kT point cases shown in fig. 6.2.1. The psSAR_{10g} values of the entire 3D ROI are denoted inside the gray boxes.

6.4 Qualitative validation of respiration-induced B_1^+ changes - simulation and measurement

The aim of this section is to compare respiration-induced changes of simulated and measured SOM $|B_1^+|$ maps and channel-wise phase maps for one posterior element at 7 T and 10.5 T. The choice of the posterior module was made to demonstrate spatial phase changes, ensuring good signal quality across both field strengths during the measurement. Additionally, larger respiration-induced channel-wise phase changes have been observed in simulations for posterior elements compared to anterior elements. All channel-wise phase maps for simulations and measurements are shown in figs. A.3.2 to A.3.5. At 10.5 T, measurements are conducted with a coil array consisting of 16 dipole channels. Hence, for the 10.5 T measurements and simulations, 16 dipole channels are utilized in this section. Please note that the 7 T coil array uses only 8 dipole channels, which implies different locations of the coil elements on the human torso for 7 T and 10.5 T.

The SOM for the simulated $|B_1^+|$ maps are shown in fig. 6.4.1A,C. Comparing 10.5 T to 7 T, a more continuous $|B_1^+|$ enhancement close to the skin is observed at 10.5 T compared to 7 T, which is likely linked to the number and location of the transmit elements. Due to a stronger gradient in AP direction of the SOM $|B_1^+|$ for 10.5 T compared to 7 T, in the center of the heart, smaller values for 10.5 T are observed compared to 7 T at the exhale respiratory state.

In the ROI, respiration-induced relative differences of the SOM $|B_1^+|$ are larger for 10.5 T compared to 7 T (fig. 6.4.1A third row), the maximum $\frac{|B_1^+(\mathrm{R4})|-|B_1^+(\mathrm{R1})|}{|B_1^+(\mathrm{R1})|}$ is 18%/69% for 7 T/10.5 T.

Comparing the exhale respiratory state to the inhale respiratory state for both field strengths, the same trend is observed: The signal shifts towards the anterior direction with inhalation, therefore at a fixed anterior position close to the skin (e.g. 45 mm) the $|B_1^+|$ is larger for the exhale respiratory state with 0.6/0.8 $\frac{\mu\mathrm{T}}{\sqrt{\mathrm{kW}}}$ (7 T/10.5 T), compared to the inhale respiratory state with 0.52/0.65 $\frac{\mu\mathrm{T}}{\sqrt{\mathrm{kW}}}$ (7 T/10.5 T). Going towards the posterior direction the spatial gradient of SOM $|B_1^+|$ is larger for the exhale respiratory state compared to the inhale respiratory state until a minimum is reached, after the minimum similar gradients are observed for inhale and exhale respiratory states (fig. 6.4.1C).

The phase of an inner posterior element is displayed in fig. 6.4.1B,D. As anticipated, faster phase variations are observed at 10.5 T compared to 7 T. This is quantified by the gradients along the line plots shown in fig. 6.4.1D. For the exhale respiratory state the gradient is

-3.0/-5.8 $\frac{\circ}{\text{mm}}$ for 7 T/10.5 T.

Qualitative measurements demonstrate results that are comparable to those obtained from the simulations (fig. 6.4.2)). The amplitude changes of the SOM $|B_1^+|$ at a central heart location induced by respiration are 15% for 7 T and 25% for 10.5 T. The linear fit of the exhale phase gradient in the measured data along the shown line plot in fig. 6.4.2D is 2.3/3.3 $\frac{\circ}{\text{mm}}$ for 7 T/10.5 T. Because of strong noise, the quantitative phase difference between the respiratory states, inhale and exhale, could not be determined.
Please note that different subjects were measured at the two different field strengths due to the scanners being located at different sites. Additionally, the measured subjects are not identical to the simulated model.

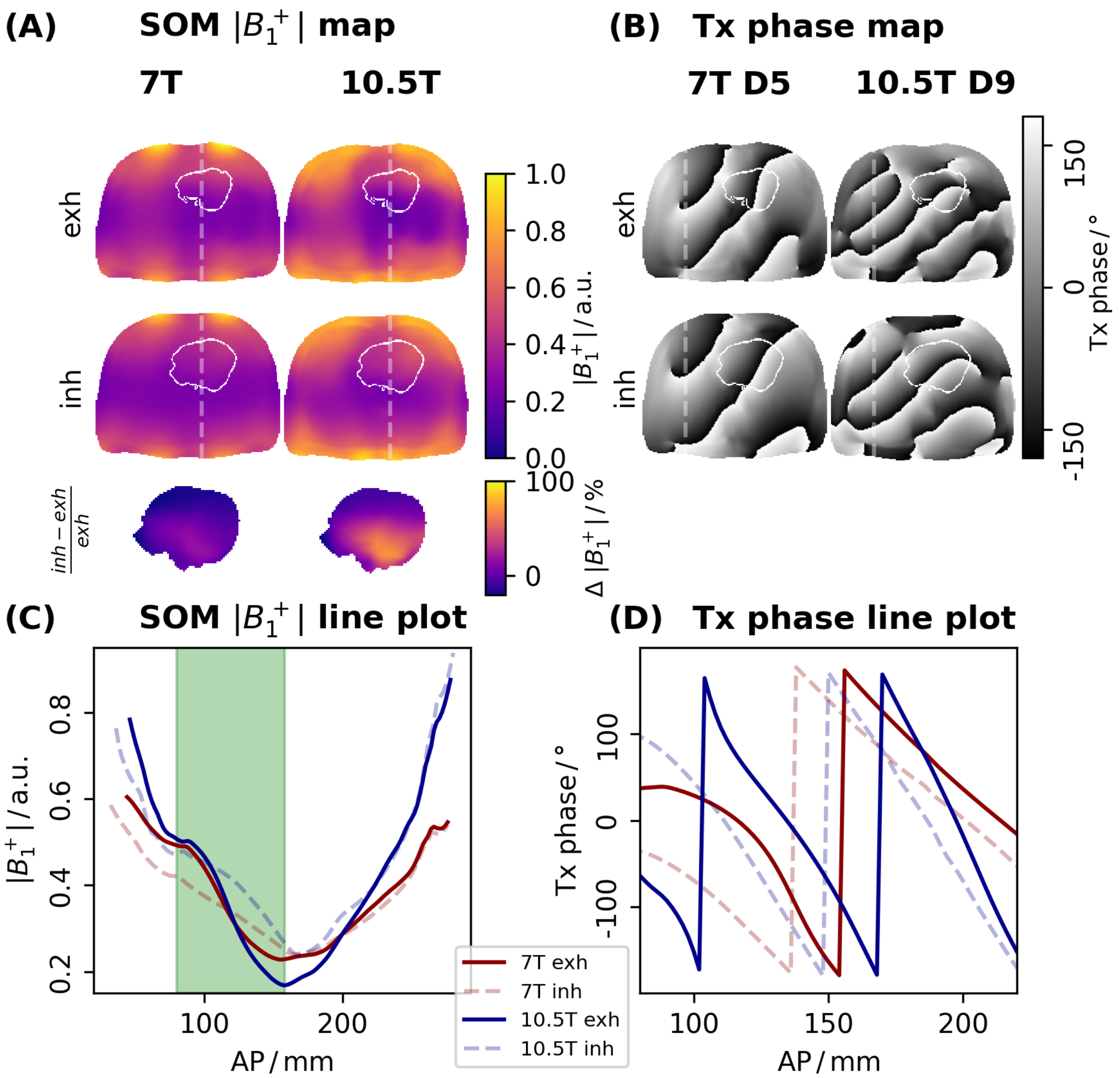

Figure 6.4.1: B_1^+ of the simulated respiration resolved XCAT body model for comparison with in-vivo measurements (fig. 6.4.2): B_1^+ SOM maps (A) and line plots (C) are investigated. The SOM is normalized to the maximum of the SOM |B_1^+| of the inhale respiratory state. The ROI is marked by a white line in the maps and the green region in the line polts. Additionally, channel-wise B_1^+ phase maps (B) and line plots (D) of a central posterior element are investigated. This element was chosen to obtain the best signal in measurements. All maps and line plots are shown for the respiratory states exhale, inhale at 7 T and 10.5 T. An additional third row shows the relative respiration-induced differences of the SOM. The presented line plots correspond to the white dashed lines shown in the maps.

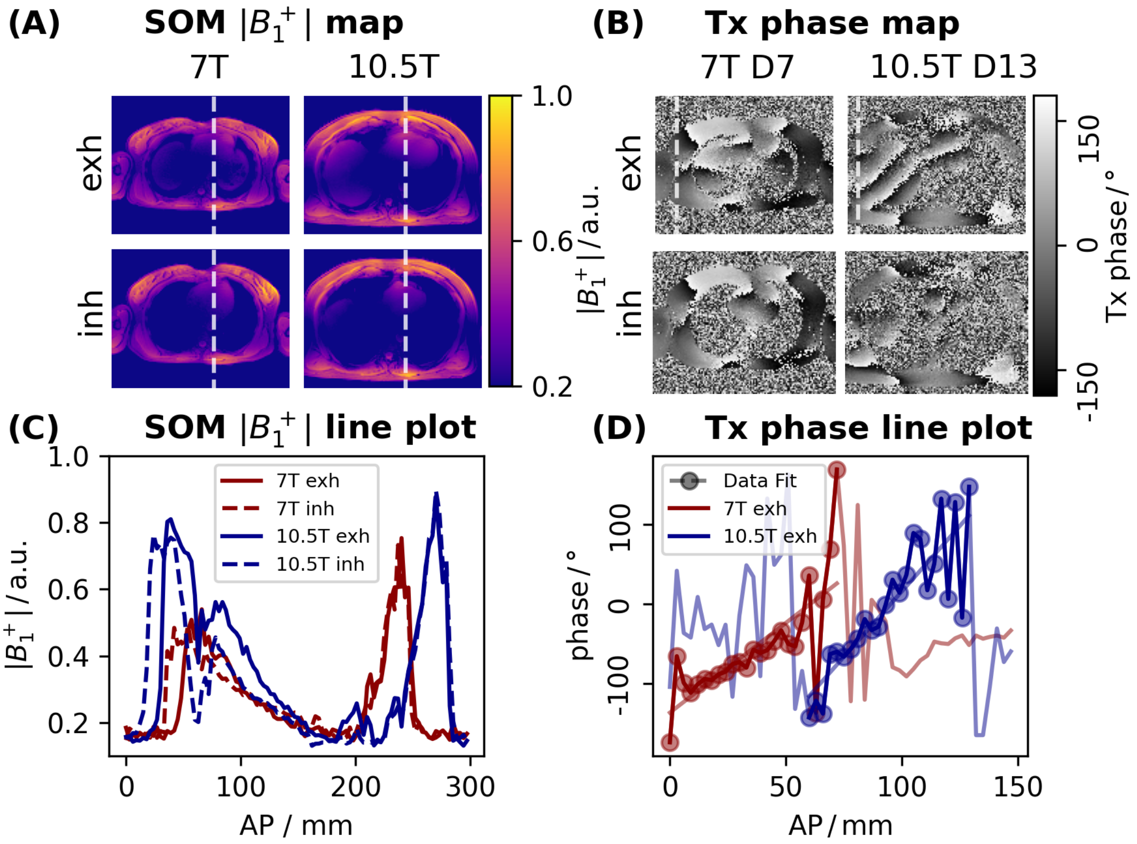

Figure 6.4.2: B_1^+ in-vivo measurements for comparison with XCAT body model simulations (fig. 6.4.1): B_1^+ SOM maps (A) and line plots (C) are investigated. The SOM is normalized to the maximum of the SOM $|B_1^+|$ of the inhale respiratory state. Additionally, channel-wise phase maps (B) and line plots (D) of a central posterior element are shown. This element was chosen to obtain the best signal in measurements. All maps and line plots are shown for exhale, inhale at 7 T and 10.5 T. The presented line plots correspond to the white dashed lines shown in the maps.

6.5 Summary

The results show larger mean channel-wise B_1^+ magnitudes and larger mean B_1^+ phase gradients in AP direction for 10.5 T compared to 7 T, investigating non-angulated elements (D2,D3,D6,D7) at the exhale respiratory state inside the ROI.
Comparing the mean $\Delta\varphi$ within the ROI, larger phase changes and larger mean gradients in AP direction of $\Delta\varphi$ are observed for non-angulated posterior elements, compared to non-agulated anterior elements, for both 7 T and 10.5 T.

The simulated data illustrates larger exhale CV values and larger ΔCV values for 10.5 T compared to 7 T. Quantitatively, the maximum obsreved CV(R1) is 21.7%/42.7% for 7 T/10.5 T using static pTx. The largest observed ΔCV is 35.8%/44.1% for 7 T/10.5 T using 4kT points, with CV(R1) below 10%.
Additionally, increasing the number of kT points decreases CV(R1) and increases the respiration-induced changes ΔCV and Δmean(FA).
Besides, an increase of 13% of the maximum $\Delta \mathrm{psSAR}_{10\mathrm{g}}(\vec{u}_{\mathrm{SCM}})$ (for all regularisation parameters and starting sets of phase vectors) and an increase by 25% of $\Delta \mathrm{psSAR}_{10\mathrm{g}}(u_{\mathrm{PCM}}^{\max})$ (for 8-channel setup) is observed from 7 T to 10.5 T.

For in-vivo measurements and XCAT body model simulations, respiration-induced relative differences of the SOM $|B_1^+|$, within the ROI, are larger for 10.5 T compared to 7 T. The maximum $\frac{|B_1^+(\mathrm{R4})|-|B_1^+(\mathrm{R1})|}{|B_1^+(\mathrm{R1})|}$ is 18%/69% for simulations and 15%/25% for measurements at 7 T/10.5 T. Additionally, the channel-wise phase of an inner posterior element varies faster at 10.5 T compared to 7 T. This is quantified by the gradients along the line plots for the exhale respiratory states. The simulations show a phase gradient of -3.0/-5.8 $\frac{\circ}{\mathrm{mm}}$ and the measurements show a phase gradient of 2.3/3.3 $\frac{\circ}{\mathrm{mm}}$ for 7 T/10.5 T.
Please note that different subjects were measured at the two different field strengths due to the scanners being located at different sites. Additionally, the measured subjects are not identical to the simulated model.

Chapter

7 Discussion and Outlook

The purpose of this work was to investigate the safety relevance of respiratory motion for UHF body MRI. Using a simulative approach, the impact of respiration-induced changes on the B_1^+ field and SAR was estimated. First of all, the used coil models were validated by comparing measured and simulated phantom B_1^+ maps. Power limits, which were applicable to the coil setup used for in-vivo measurements, were determined. Second, the impact of respiration-induced changes on B_1^+ and SAR were discussed for 7 T. A final question addressed in this thesis was the behavior of respiration-induced changes for increased field strength such as 10.5 T.

7.1 Coil validation

Prior to investigations of respiration-induced changes, a qualitative validation and quantitative analysis of the simulated coil design was performed by comparing MR scanner measurements and simulations of B_1^+ maps. For single-channel B_1^+ validation at 7 T, additional H-field probe measurements were performed.

A quantitative agreement of channel-wise simulated and measured B_1^+ magnitude maps of the loop was achieved by adjusting ohmic losses for each individual loop element in the simulations. For a single channel, the resonance peak was measured, and the line width was determined. From the line width, the ohmic losses, including material losses, soldering losses, and lumped element losses, were calculated and implemented into the simulation.

For a single dipole channel, a qualitative agreement of simulated and measured B_1^+ magnitude maps was achieved, while quantitative differences were observed. An implementation of the dipole losses emerged to be highly challenging.

Adding local ohmic resistors in series to the simulated port did not account for complex dipole losses. Possible explanation is the spatially varying current density over the dipole length. Additionally, the skin effect distributed over the full dipole length was not accounted for by using ideal PEC material with infinite small thicknesses. To account for locally varying current density and the skin effect, a location-dependent loss implementation is possibly needed. In addition, the coaxial cable of the loop element is located parallel to the dipole arm, as shown in fig. 3.1.1, for the 7 T setup, which adds coupling, and it turned out to be more difficult to implement losses for the dipole element compared to the loop element.

For a better understanding of these effects, additional measurements were performed in [80], showing a strong coupling of loop and dipole located in the same module. The cable positioning of the two channels had an impact on the scattering matrix and also slightly on the B_1^+ distribution. To mitigate these effects, circulators were incorporated in the H-field probe measurements to ensure a 50 Ω source as a transmit channel, absorbing the reflected power of the transmit channels. Additionally, in single-channel MR scanner measurements, cable traps were employed to reduce the impact of cable positioning on the B_1^+ distribution. The impact of the cable positioning on the B_1^+ distribution was reduced, this way, but not completely eliminated. Further investigations may include fine adjustments of the lattice balun capacitors and inductivities and implementing cable traps in all modules. The loop coaxial cable could be included in the simulations to obtain a better representation of the measured setup. This might reduce the differences observed in the channel-wise dipole B_1^+ distribution between simulation and measurement.

Considering a setup with eight modules, several additional challenges were encountered compared to the investigations of a single channel. Despite substantial efforts to use the same coil array positioning for measurements and simulations differences in the B_1^+ magnitude have been observed between measured and simulated data for the eight loop elements, while a good agreement between simulated and measured B_1^+ magnitude was achieved for a single channel-wise setup. The coil module angle and the distance between coil module and phantom was fixed by by using styrofoam blocks.

For the dipole elements, a good agreement was achieved for the B_1^+ magnitude of the 8-channel setup, while larger simulated B_1^+ magnitude values have been observed for a single channel-wise setup compared to the measured B_1^+ magnitudes.

Both element types exhibit a similar trend: the simulated B_1^+ magnitudes surpass (loops) or align with (dipoles) the measured B_1^+ magnitudes when transitioning from a single channel-wise setup to an 8-channel setup.

The setup using 8 loop channels showed surprisingly a larger measured $|B_1^+|$ compared to the simulated $|B_1^+|$. A possible explanation is that the assumed losses for the single-loop channel validation are too high for the 8-channel setup. Losses were not applied to the dipole elements, yet the losses could decrease from the single-channel setup to the 8-channel setup, possibly explaining the decreased differences between measurement and simulation when switching from a single-channel setup to an 8-channel setup.

For single-channel measurements, the cable routing was performed carefully without any overlap of the loop and dipole cables. This was not possible for 8-channel measurements, where, in total, 16 cables (8 dipoles, 8 loops) needed to be routed. Strong coupling via the coaxial cables may lead to decreased losses in the elements since the coupling of the coil array is stronger than that of a single module. S-matrix measurements have revealed high coupling via the coaxial cables and cable position-dependent coupling for all 16 channels, which are not shown in this paper. Slight differences in losses of each element are in addition likely due to manual soldering of capacitors and inductors.

Additionally, dielectric properties, such as electric conductivity and relative permittivity, of the PVP phantom were expected to have an impact on the magnitude of the B_1^+. Tentatively, simulations with no losses for the 'L' elements and decreased electric conductivity and relative permittivity of the phantom material have been performed and showed a higher $|B_1^+|$ for a setup using eight modules. A decrease in a similar range of the electric conductivity and relative permittivity of the PVP solution was observed in measurements over time of the open body phantom (fig. 3.3.1 C). The non-decreased dielectric properties used for initial simulations were measured in the same month as the B_1^+ measurements were performed. Additional simulations with further decreased electric conductivity down to 0.44 S/m indicated a trend of increased B_1^+ magnitude with decreased electric conductivity.

For 10.5 T , a good qualitative agreement was achieved for low FA regions using a single dipole channel. In this region, the wave-propagation of the short 10.5 T wavelength possibly explains the observed wave-like structure in the $|B_1^+|$ measured and simulated maps and line plot. For high flip angle regions, the GRE-based measurement sequence might be biased by saturation effects, as the FA is close to the Ernst angle. For the given T_1 and TR values, the Ernst angle is below 30 °. Close to the Ernst angle, the transversal magnetization is saturated, maximizing the MR signal. For flip angles larger than the Ernst angle, the transversal magnetisation even decreases [107].

The quantitative difference between the measured and simulated B_1^+ magnitude maps of a cp-shim vector mode using all 16 transmit channels might be explained by not implementing losses for the dipole elements. In addition, the coil positioning might be another source for deviations since at 7 T, a more accurate positioning had been possible as compared to 10.5 T.

For the 10.5 T coil array, all measured S-matrix values are below -10.0 dB [66], which indicates less coupling compared to the 7 T coil array setup (S-Matrix values up to -4.47 dB). At 10.5 T each module contains only a single dipole element. No intra-module coupling can occur compared to the 7 T coil array, where loop and dipole elements are placed in one module, and coupling between the coaxial cable of the loop element and the dipole arm is observed.

After qualitatively validating the simulated coil model by comparing measurements and simulations of phantom B_1^+ maps, power limits applying to the coil model for in-vivo measurements at 7 T were calculated.

The calculated maximum applicable power is safe without considering any losses occurring between the MR table coil plug and the coil channel. The calculated maximum applicable power for the 7 T 16ch Tx/Rx body array was rounded down: 8 W for the loop channels and 16 W for the dipole channels.

The power is applied at the MR table coil plug, and the measured -1.7dB losses between the MR table coil plug and the Tx/Rx switch box were used as a safety factor. This safety margin is large enough to account for changes introduced by respiratory motion using the power-controlled mode investigated in this thesis. For three different target organs, the changes in the possible applicable allowed power are below the safety factor.

The performed safety assessment enabled in-vivo measurements to validate the observed simulated respiration-induced B_1^+ changes with this specific coil setup.

7.2 Respiration dependent simulation setup

This thesis presented a novel analysis of respiration-induced changes in EM fields in the context of body imaging in UHF MRI.

The XCAT model enables investigation of the effects of specific movements, such as chest and diaphragm motion, during the respiratory cycle. The model has previously been

employed in various MR applications [70, 108, 109], PET MR [110] and originally for CT applications [67, 69]. To the best of my knowledge, it is the first time that respiration-resolved XCAT models are used for EM-field simulations of MRI.
The impact of changes in dielectric parameters, such as 45% decrease in the lung electric conductivity and 56% decrease in the lung relative permittivity during inhalation, as well as the impact of body deformation during respiration, on FA and $\mathrm{SAR}_{10\mathrm{g}}$ distributions, was investigated.

The implementation of different dielectric properties into the simulated body models of different respiratory states has an impact on the B_1^+ phase inside the ROI of a single coil channel. Additional simulations where the lung dielectric parameters during inhalation were held constant showed almost no phase differences between the exhale and inhale respiratory state (fig. A.3.6). For anterior modules, the impact of body deformation during respiration adds respiration-induced phase changes, independent of changes in the dielectric properties. The channel-wise B_1^+ amplitude is not impacted by the differences in the dielectric properties.

Further parameters, such as cardiac motion, heart lesions, and inter-subject variability, could be assessed by the XCAT software but were not examined in this thesis.

A smaller impact of cardiac motion on B_1^+ and $\mathrm{psSAR}_{10\mathrm{g}}$ would be expected compared to respiratory motion. During the cardiac cycle, no distance changes between the body and coil modules will occur, which is an important parameter for respiration-induced changes. The heart volume is smaller compared to the lung volume. Therefore, even if different dielectric properties in the heart account for different cardiac states, the wave propagates only for a shorter distance through the heart tissue compared to the lung. Additionally, the heart volume changes during the cardiac cycle are smaller compared to the lung volume changes during the respiratory cycle.

Respiration-independent inter-subject specific absorption rate changes yielded a $\mathrm{psSAR}_{10\mathrm{g}}$ scaling factor of 1.8 [17] between different body models for prostate imaging at 7 T. Therefore, an interesting aspect would be to study the combined impact of respiratory motion and multiple body models. This could be done by investigating the 54 respiration-dependent different adult body models provided by XCAT [68, 111] or by using the segmentation of measurements to obtain respiration state resolved models with different anatomy that can be measured and simulated [17, 112].

Not only do respiration-induced changes in the body model impact B_1^+ and SAR, but respiration-induced distance changes between the body model and the coil modules are also expected to induce large changes in B_1^+ and SAR. Therefore, two coil setups were investigated, implying different distance changes between the body model and the coil modules during the respiratory cycle.

In summary, performing the safety assessment on the exhale respiratory state, the 'Moving' setup needs lower safety factors compared to the 'Fixed' setup. In the 'Moving' setup the coil front modules moves along with respiration, ensuring a constant minimum distance between the chest and the elements. This setup is typically used by the centers [18, 113–115]. Respiration-induced distance changes between anterior and posterior modules impacted B_1^+ and $\text{psSAR}_{10\text{g}}$ of the 'Moving' coil setup. This induced phase changes, leading to signal voids in the image during inhalation, which were not observed during exhalation in in-vivo measurements with 2-spokes [13]. Whereas for the 'Fixed' setups, the coil is spatially fixed at one position, with a varying minimum distance between the chest and the elements and this setup is used for special acquisitions such as whole-body MR angiography [116] or the design of patient-friendly setups [117]. The 'Fixed' setup had large distance changes between chest and anterior modules during inhalation. To obtain a good comparison between 'Moving' and 'Fixed' setups, the R4 (inhale) respiratory state had the exact same coil position for both setups.

A power limit calculation on the exhale respiratory state possibly implies a limit violation for the inhale respiratory state, for the 'Fixed'/'Moving' coil setup by a maximum factor of 2.5/1.3 (7 T). Therefore, respiration-induced distance changes between the chest and the anterior modules of 14 mm using the 'Fixed' coil setup, led to $\text{psSAR}_{10\text{g}}$ changes in the same range as 10 mm right left head movement, which showed a $\text{psSAR}_{10\text{g}}$ increase by a factor of 2.4 [29].

It could be assumed that (i) the impact of the respiration-induced changes in the distance between the body model and the coil module on $\Delta\text{psSAR}_{10\text{g}}$, was larger compared to (ii) distance changes between anterior and posterior modules, (iii) the impact of body deformation and (iv) the impact of respiration-induced changes in the dielectric properties.

(i) The large impact of the respiration-induced changes in the distance between the body model and the coil module on $\Delta\text{psSAR}_{10\text{g}}$ imply larger respiration-induced changes for the 'Fixed' setup compared to the 'Moving' setup and higher $\Delta\text{psSAR}_{10\text{g}}$ for anterior located $\text{psSAR}_{10\text{g}}$ values compared to those located posterior in the 'Fixed' setup. For a 'Fixed' setup, it was, in most cases, a conservative approach and thus favorable to calculate the power limits on $\mathrm{SAR_{10g}}$ maps of the inhale respiratory state, as the body model experienced stronger E and B fields when it was closer to the coil element.

(ii) Distance changes between anterior and posterior modules as well as (iii) body deformation possibly dominated respiration-induced changes in anterior-located $\mathrm{psSAR_{10g}}$ values for the 'Moving' setup and had a comparable impact on $\Delta\mathrm{psSAR_{10g}}$ as (iv) the impact of respiration-induced changes in the dielectric properties. Respiration-induced changes in the dielectric properties possibly dominated respiration-induced changes in posterior-located $\mathrm{psSAR_{10g}}$ values for the 'Fixed' and 'Moving' setup, as most of the lung volume is closer to the posterior modules compared to the anterior modules.

7.3 Respiration-induced FA changes

So far, the respiration-induced changes in the simulated setup have been discussed. This section will discuss the qualitatively and quantitatively observed respiration-induced B_1^+ changes for channel-wise results, B_1^+ changes for static pTx, FA changes for dynamic pTx and the comparison of respiration-induced B_1^+ changes in simulations and in-vivo measurements at 7 T and 10.5 T.

Investigation of channel-wise B_1^+ maps is a necessary step to understand the origin of respiration-induced FA pattern and value changes in FA maps of static and dynamic parallel transmissions (pTx). Changes in the phase and magnitude of individual channel-wise B_1^+ maps lead to changes in the interference pattern of multiple transmission channels during pTx.

When comparing the differences observed in B_1^+ magnitudes for different field strengths, it should be noted that they are not only due to wavelength-dependent dielectric properties but also due to different geometric coil setups.

Increasing B_0 from 7 T to 10.5 T leads in the shown XCAT model setup to 23% higher mean $|B_1^+|$ values inside the ROI, for the exhale respiratory state. This is in the range of the 27% increased power efficiency observed in the phantom study [22] at a depth of 4 cm. The power efficiency stated in [22] corresponds to the B_1^+ magnitude, normalized to the forward power, shown in this work. The slightly different coil setup for both field strengths using the XCAT model led to different input power for the same forward power and will be discussed in the following. Phantom simulations with a single module and the same

dielectric properties for 7 T and 10.5 T, similar to those shown in [22], were performed in addition (not shown in this thesis).
In those phantom simulations, $|B_1^+|$ increase of 29% is observed from 7 T to 10.5 T at a depth of 4 cm to the phantom boundary. Performing those simulations, a strong variation in the input power (36% XCAT, 56% phantom of the forward power) for the 7 T coil array dipole channels was observed, which affects B_1^+ directly. In the shown B_1^+ magnitude maps, $|B_1^+|$ is normalized to the forward power for 7 T and 10.5 T. The forward power is a known value in measurements and is used for normalizing measured B_1^+ maps. For 10.5 T, this strong change in the input power is not observed (80% XCAT, 76% phantom of forward power). The 7 T coil array validation process showed strong coupling for this coil setup with a non-ideal matching of the lattice balun, possibly explaining the different input-power for the different setups, contributing to differences in the B_1^+ magnitude observed between 7 T and 10.5 T.
In addition to the discussed differences of the B_1^+ magnitudes comparing 7 T and 10.5 T, the shorter wavelength for 10.5 T compared to 7 T implies stronger B_1^+ phase gradients for 10.5 T.

Respiration-induced $|B_1^+|$ changes are expected due to an increasing distance between the coil module and the ROI during inhalation, which also affects the B_1^+ phase within the ROI. In addition, the phase is impacted by respiration-induced changes in the dielectric properties of the lung.

Channel-wise respiration-induced changes at 7 T in phase (max: -61°) and amplitude (29%) are in accordance with channel-wise respiration-induced changes observed by Schmitter et al.[13] (phase: 55°, amplitude: 30%).
The changes in the lung dielectric parameters during inhalation induce phase changes. Additional simulations where the lung dielectric parameters during inhalation were held constant showed almost no phase differences between the exhale and inhale respiratory state (fig. A.3.6). This finding explains the observed larger mean $\Delta\varphi$ values for non-angulated posterior elements, compared to non-agulated anterior elements, for both field strengths 7 T and 10.5 T. The EM-wave passes more lung volume between the posterior elements and the ROI compared to the lung volume passed between the anterior elements and the ROI.
The shorter wavelength for 10.5 T compared to 7 T implies stronger phase gradients in AP direction: $\frac{\partial}{\partial x_{AP}}\varphi(\mathrm{R1}, 7\,\mathrm{T}) < \frac{\partial}{\partial x_{AP}}\varphi(\mathrm{R1}, 10.5\,\mathrm{T})$. The phase at higher B_0 is therefore more sensitive to spatial displacements of the body model, which might be the reason for the

observed higher respiration-induced spatially varying phase $\frac{\partial}{\partial x_{AP}}\Delta\varphi(7\,\mathrm{T}) < \frac{\partial}{\partial x_{AP}}\Delta\varphi(10.5\,\mathrm{T})$.

The interference of channel-wise respiration-induced changes is anticipated when combining multiple channels using pTx pulses.
Already 10 years ago, Schmitter et al. [13] demonstrated by measurements the impact of respiratory motion on the excitation profile for UHF MRI experimentally, using dynamic pTx.

At 7 T the wavelength is short enough that respiration has an impact on the FA pattern of the pTx pulse. The discussed respiration-induced B_1^+ changes in single channels were caused by distance changes between the transmitting element and the ROI, which changes the B_1^+ phase and magnitude and additionally by changes in dielectric parameters. For multiple channels, the effects seen in single channels interfere with possibly larger respiration-induced FA changes compared to the channel-wise observed respiration-induced B_1^+ change. This thesis confirmed for the first time the experimental finding of respiration-induced changes in the FA by simulations.

Respiration-induced changes of 24% in the B_1^+ magnitude were observed in a 7 T cardiac study [25] that used static pTx with an efficient shim. In this thesis, relative respiration-induced CV changes of up to 19.8% were observed for a similar coil setup ('Moving', 7 T, 'D') using static pTx with a homogeneous shim.
Investigating different setups, the findings indicated that CV changes strongly depend on the coil setup, element type, and shimmed respiratory state for static pTx using 1000 different starting phase vectors. The value of $\min(B_1^+)$ is an important parameter for enhancing MRI, as very low $\min(B_1^+)$ results in MR signal dropouts. The observed local respiration-induced changes in $\min(B_1^+)$ strongly depend on the individual RF pulse solution of the optimization. The respiration-induced B_1^+ magnitude changes observed for static pTx pulses were larger compared to single channel-wise respiration-induced changes, possibly resulting from constructive and destructive interference of respiration-induced changes among multiple channels. Extending the work to RF coil arrays with a greater number of channels may yield even larger respiration-induced B_1^+ changes.
For optimizations on the 'exhale' respiratory state only or on both respiratory states, 'exhale and inhale' simultaneously smaller respiration-induced changes in the CV and $\min(B_1^+)$ were observed compared to optimizing on 'inhale' only. Reducing the respiratory motion from deep breathing to shallow breathing reduced respiration-induced B_1^+ changes. This is in accordance with [15]. Optimizing the RF pulse on both respiratory states or on

the exhale respiratory state is advisable, although the inhale state may be more comfortable during breath-hold.

The results indicate that respiration-induced changes were strongly impacted by the applied RF pulses. Increasing the number of kT points allows decreasing the CV value of B_1^+ for a given respiratory state for the same RF power, by increasing the degree of freedom in the FA optimization process. However, in-vivo measurements showed that a higher number of kT points were more susceptible to respiration-induced changes [13, 26], possibly due to case-specific optimizations, which were susceptible to slight body changes induced by respiration. This thesis also qualitatively observed a similar phenomenon in the simulated maps. Quantitatively this thesis demonstrated a slightly higher range of CV values considering inhale and exhale (2%-38%) compared to [26] (4%-22%). It should be noted that different coil arrays were used and the reporting of the best solution for multiple body shapes by [26], while this thesis reports all solutions from 200 starting sets for a single body model.

Going to higher field strength, the stronger phase gradient observed for single-channel B_1^+ phases at 10.5 T compared to 7 T, suggests higher respiration-induced changes using static or dynamic pTx.

The benefits of higher SNR with increasing field strength came at the cost of a stronger interference pattern resulting in lower FA uniformity and larger CV values. Concluding, to achieve similar homogeneity for 7 T and 10.5 T , using the same RF power, an increase in the number of kT points is needed for 10.5 T . Also, increased respiration-induced FA changes have been shown in this work with increasing field strength. The smaller wavelength at higher fields induced stronger phase variation [118]. Those spatially faster varying phases were more sensitive to intra-subject changes inducing phase perturbations.

In summary, optimization of the RF pulse on B_1^+ maps of both respiratory states is advisable and becomes increasingly important with rising field strength and when moving from static pTx to dynamic pTx.

7.4 Qualitative comparison of respiration-induced B_1^+ changes in simulation and measurement at 7 T and 10.5 T

Despite the use of two different volunteers for measurements at 7 T and 10.5 T and in addition, a different body model used for simulations, qualitative agreement between simulated and measured respiration-dependent SOM and single channel-wise phase B_1^+ maps were obtained.

This qualitative agreement increases the confidence in the simulated respiration-dependent observations. Further studies, including the utilization of multiple volunteers that are consistent at both 7 T and 10.5 T and the subsequent segmentation of measured data, could improve the comparability of measured and simulated data.

7.5 Respiration-induced SAR changes

In the context of previously observed respiration-induced FA changes, it was expected that changes in local SAR can occur due to respiration, considering the coupling of electric and magnetic fields as described by Maxwell's equations. The E-field cannot be measured directly. However, thermometry measurements allow indirect measurement of the $\mathrm{SAR}_{10\mathrm{g}}$ within phantoms [66]. Despite this, MR thermometry in the human body presents challenges such as perfusion of blood, which changes the temperature and the large amount of required power. Therefore, EM simulations become relevant to calculate local $\mathrm{SAR}_{10\mathrm{g}}$ for safety assessment.

EM simulations and the calculation of spatial SAR distributions are presently the only practical possibilities to confirm the safety compliance of a setup. At low field strengths ($B_0 < 7,\mathrm{T}$), a near-field approximation employing a quasi-static field is applied, and high SAR values are observed close to the coil array elements [119]. In contrast, for high field strengths ($B_0 \geq 7\,\mathrm{T}$), far-field effects, considering an electromagnetic wave, become relevant in linking electric and magnetic fields [1]. Consequently, local $\mathrm{SAR}_{10\mathrm{g}}$ hot spots were observed [120].

So far, only body models in a single respiratory state have been simulated [27, 28]. The impact of respiration on the electric field and, thus, on the safety-relevant SAR has not been investigated.

As expected, in this work, it was, in fact, observed that respiration-induced motion impacts the location and the values of psSAR_{10g}. Maximum respiration-induced psSAR_{10g} changes up to a factor of 2.5 have been observed (7 T, 'Fixed' coil setup). The exact scaling factor strongly depended on the coil setup (discussed in 7.2) and the used shim vector. The changes in the FA maps induced by respiration strongly depended on the applied RF pulses. Additionally, an impact of the RF pulses was expected on the respiration-induced SAR_{10g} changes. In dependence on the RF pulse, mainly four observations were made: First, RF pulses, which lead to no respiration-induced psSAR_{10g} changes exist. Second, different RF pulses possibly imply different psSAR_{10g} locations. Anterior psSAR_{10g} locations, posterior psSAR_{10g} locations and changes of the psSAR_{10g} location from anterior to posterior during respiration were observed. Third, RF pulses inducing strong psSAR_{10g} value changes have been observed. And fourth, there was no correlation between respiration-induced changes in the FA and the psSAR_{10g}. RF pulses with high respiration-induced CV changes can have low respiration-induced psSAR_{10g} changes, and vice versa. Therefore, even for small respiration-induced FA-changes, the 10 s SAR limit can be exceeded if the power limits are calculated e.g. on the exhale respiratory state, while performing a breath-hold scan during the inhale respiratory state. Breath-hold scans are used, for example, for fast cardiac imaging, which uses preparation pulses often close to the SAR limit [121]. A respiratory cycle typically lasts 5 s, therefore, during free breathing, the 10 s SAR limit is averaged over 2 respiratory cycles and location changes of the psSAR_{10g} during respiration could potentially average the psSAR_{10g} values.

To analyze the impact of respiration-induced psSAR_{10g} changes on safety assessments, two different control modes were investigated. The online local 'SAR-controlled mode' SCM and the precalculated 'power-controlled mode' PCM.

The SCM is utilized at many sites for pTX at UHF, both in the head [92–95] and body [91, 95, 96]. This control mode measures phases and amplitudes of static or dynamic pTx pulses to calculate the psSAR_{10g} values on the fly. The psSAR_{10g} calculation was based on VOP matrices, which are a reduced set of Q-matrices. The channel-wise RF pulses were scaled to stay below the IEC upper SAR limit of 20W/kg. If any safety factor were neglected (which is not the case in actual measurements) and the VOP models were based on a single respiratory state, a possible violation of the IEC limit up to a factor 2.5/1.3 could occur for a 'Fixed'/'Moving' coil setup. Possibly even higher respiration-induced psSAR_{10g} changes could be observed since only a subset of 10^6 random shim vectors has been considered. Meanwhile, in [10], it was shown that this number is no longer sufficient to fully explore the excitation vector space for a pTx coil with eight or more channels. However, not all of those shim vectors are realistically applied shim vectors to attain a desired B_1^+ distribution. For the simulation setup described here, respiration-induced psSAR$_{10g}$ changes of static and dynamic pTx were covered by a safety factor of 1.14 for the 'Moving' setup.

The PCM is another method used for SAR limitation [10, 13, 97–99]. It allows to utilize a pre-calculated power limit per channel independent of the RF pulse phase, derived from the upper psSAR$_{10g}$ value of a simulated model. This eliminates the need for on-the-fly shim vector and VOP model-dependent psSAR$_{10g}$ computations, as during the scan, only the maximum applied amplitude per channel will be tracked, independent of the phase. However, the PCM power limits are necessarily more conservative than those of the SCM. The mean amplitude scaling factor between amplitudes allowed by the PCM and the SCM was 1.3 for phase shimming and a 'Moving' setup. Nevertheless, this work demonstrated that PCM is less susceptible to intra-subject changes as respiration, and previous research suggests that it is also less vulnerable to inter-subject [10] changes compared to the SCM.

The local SAR increases with field strength using similar transmit performance for 7 T and 10.5 T [22]. This is due to increased phase variations, which possibly lead also to the slightly increased respiration-induced SAR changes from 7 T to 10.5 T. Small increases in the respiration-induced psSAR$_{10g}$ changes were expected as also inter-subject-induced psSAR$_{10g}$ changes showed small differences between 7 T and 11.7 T [122]. Further increasing the field strength to 11.7 T or 14 T could lead to possibly further increases of respiration-induced psSAR$_{10g}$ changes.

7.6 Impact of breathing pattern and element type on respiration-induced B_1^+ and psSAR$_{10g}$ changes using static pTx at 7 T

The strong impact of changes in distance between coil array and body has been illustrated by the large respiration induced B_1^+ changes for the 'Fixed' setup where the minimum distance between coil array and body changes by up to 14 mm, in contrast to a constant minimum distance for the 'Moving' setup. For the 'Fixed' and the 'Moving' setup, a conventional breathing pattern was investigated, combining abdominal breathing and chest breathing. In the next step abdominal breathing and chest breathing were investigated separately.

For chest breathing the same coil displacement as for the 'Moving' setup with conventional breathing was considered, therefore similar respiration-induced changes in B_1^+ and $\text{psSAR}_{10\text{g}}$ were expected and observed. For abdominal breathing, no chest movement is observed and the coil stays rigid at one position, equal to the exhale state of the 'Moving' setup for conventional breathing. The main differences between the inhale and exhale respiratory states are the downshifting of the heart and other organs and the change in dielectric properties. Accordingly, smaller respiration-induced B_1^+ changes were expected and observed for the abdominal breathing setup compared to the chest breathing and conventional breathing with the 'Moving' coil setup. The respiration-induced $\text{psSAR}_{10\text{g}}$ changes are less affected by the breathing pattern compared to respiration-induced B_1^+ changes.

Different coil elements, such as loops, dipoles or the combination of loops and dipoles generate different B_1- and E-field patterns. Therefore, different respiration-induced changes in dependence of the used element type could be expected.

In general, larger respiration-induced changes are observed for the combined setup using dipole and loop channels, compared to dipoles only, the respiration-induced changes of both element types possibly interfere constructively. Additionally, B_1^+ optimizations using 16 channels (dipoles and loops) have more degrees of freedom, compared to B_1^+ optimizations using 8 channels (dipoles or loop), leading to possible RF pulse solutions tailored to one specific case. Small modifications in the body model may then result in large changes in the B_1^+ maps.

Only small differences in $\Delta\text{psSAR}_{10\text{g}}$ are observed. The $\text{psSAR}_{10\text{g}}$ is close to the surface of the body. Therefore, respiration-induced changes of $\text{psSAR}_{10\text{g}}$ are most prone to changes in the distance between the coil array and the body, the field distribution did not make a large impact on the respiration-induced changes. Please note that the element type makes an impact on the absolute $\text{psSAR}_{10\text{g}}$ value per 1 W input power.

In conclusion, changes in the breathing pattern during data acquisition impact the FA pattern, therefore, an unchanged, constant breathing motion during one scan is important. The impact of breathing type and element type on the respiration-induced FA and $\text{psSAR}_{10\text{g}}$changes is much smaller compared to the impact of the coil setup ('Moving' or 'Fixed').

7.7 Impact of the respiration on the S-Matrix

The MR scanner's directional couplers measure the S-Matrix, enabling respiration gating without any increase in measurement time, additional hardware, or sequence design [102].

The Scattering matrix (S-matrix) is related to the forward and reflected power of the coil array channels. The coupling between different coil elements, as well as the power reflected by each element, depend on the loading of these elements. Changes, for example, due to respiratory motion, induce changes in the reflected power in the RF coil channels and thus the S-Matrix [102]. This thesis confirms the respiration dependence of the S-Matrix, shown by Buikmann et al. for 2T measurements and Hess et al. at 7 T measurements, for 7 T EM field simulations.

Larger respiration-induced S-Matrix changes are observed and expected for the 'Fixed' coil setup compared to the 'Moving' coil setup, using conventional breathing for both setups. The distance changes between coil array modules and the body strongly impact the load of the coil, and hence the S-Matrix.

An additional interesting consideration is the determination of the breathing pattern using the S-matrix. In [31], we observed different results between chest and abdominal breathing for the posterior elements, while conventional and chest breathing showed only small differences. It is necessary to note that these particular results are subject to the limitation that different dielectric properties of the lung material between the inhale and exhale respiratory states were not included.

7.8 Limitations and outlook

The investigated respiration-induced B_1^+ and psSAR_{10g} changes are limited to a single coil model for each field strength. Differences between respiration-induced changes between dipole elements, loop elements and dipole & loop combination indicate the relevance of different coil models, especially for respiration-induced FA changes.

Coil types as body coils behind the bore liner [91] and hence far away from the body surface will likely show a different behavior than the investigated body coil arrays placed directly on the body. It is expected that, smaller respiration-induced psSAR_{10g} changes are observed because the respiration-induced distance changes between the coil module and the body model relative to the total distance between the coil module and the body model are smaller compared to the presented 'Fixed' setup. Detailed investigations are necessary to assess the impact of respiration on B_1^+.

Furthermore, while different coil positions were shown for the safety assessment at 7 T without considering respiration, the impact of respiration-induced B_1^+ and $\mathrm{psSAR}_{10\mathrm{g}}$ changes were only investigated for a cardiac coil array position. Future work may investigate the respiratory effects of shifted coil positions towards the feet, as used for investigating the liver and prostate. These setups likely experience less respiration-induced changes due to less coil motion in this region and a larger distance to the lung tissue. Because of the increased distance between the lung tissue and the coil array, it is likely that changes in the dielectric properties of lung tissue during respiration have less impact on respiration-induced B_1^+ and $\mathrm{psSAR}_{10\mathrm{g}}$ changes, specifically in prostate imaging compared to cardiac imaging.

The investigated respiration-induced changes in B_1^+ and $\mathrm{psSAR}_{10\mathrm{g}}$ are limited to a single body model. It is worthwhile to note that a different study [17] presented inter-subject specific absorption rate changes by a factor of 1.8 independent of respiration for prostate imaging at 7 T. Therefore, it may be interesting to examine a number of respiration-resolved body models and not only incorporate different human body models in the context of VOP calculations, but also to consider the inhalation and exhalation states in these multiple body models. Meanwhile, XCAT provides 54 respiration-dependent adult body models [68, 111]. Alternatively, segmentation of measured images could be used to obtain models with different anatomy that can be measured and simulated [17, 112].

The RF pulse optimization was limited to homogeneous shimming, while other optimizations, such as aligning the averaged phases to obtain constructive interference (efficient shim), are for example, used for respiration navigator scans [123]. Initial investigations of efficient shim vectors showed CV changes slightly smaller but in a similar order of magnitude compared to the homogeneous shim vectors. The data is not shown in this work.

An interesting extension of this work would be investigating respiration-induced $\mathrm{psSAR}_{10\mathrm{g}}$ changes in respiration-robust and universal pulses. Despite small respiration-induced FA changes for those pulses, the respiration-induced $\mathrm{psSAR}_{10\mathrm{g}}$ changes are not necessarily small.

To achieve comparable results from measurements and simulations at 7 T, the importance of individual adjustment of the lumped elements in the lattice balun was pointed out in this work. While this was not the main focus of this thesis, the used coil could be improved by further adjustments of the lattice balun, implementation of cable traps, investigations of additional element losses, and it might be advantageous to include the coaxial cables in the simulations.

Investigating the respiration-induced changes using multiple coil models, coil types, coil positions, and a larger number of body models featuring different anatomical shapes and both genders offers a useful continuance of the presented work.

Chapter

8 Conclusion

For the first time, simulations have confirmed respiration-induced B_1^+ changes, which have previously been demonstrated by measurements.
Optimization of the FA inside the human heart should take respiration into account, particularly in dynamic pTx. To avoid this effect, FA optimizations could be performed by including multiple respiratory states, which becomes increasingly important with rising field strength.

In conclusion, this work demonstrates that depending on the setup and field strength, the impact of respiration-induced $\text{psSAR}_{10\text{g}}$ should possibly be included in safety assessments during UHF cardiac imaging. It should be noted that especially breath-hold scans are crucial, e.g if power limits were calculated on exhale $\text{SAR}_{10\text{g}}$ matrices, while performing a breath-hold scan during inhale. Nevertheless, often data acquisition is performed under free breathing, as the scan time exceeds the time duration of possible breath-holds, the observed averaging over the $\text{psSAR}_{10\text{g}}$ values with the varying location of the $\text{psSAR}_{10\text{g}}$ is advantageous.
When using a 'Fixed' setup at 7 T, conducting a safety assessment of the inhale respiratory state would result in a more conservative and favorable approach for most RF pulses. For the 'Moving' setup using the XCAT body model, a safety factor of 1.35 would cover the observed changes in $\text{psSAR}_{10\text{g}}$ induced by respiration, regardless of the state used for safety assessment. Additionally, inter-subject changes require a safety factor of up to 1.8 [17] for 7 T prostate imaging. Therefore, it may be beneficial to utilize multiple respiration-dependent body models, in addition to multiple body models with different body shapes for SAR calculations, or add additional safety factors, depending on the coil setup and field strength.

Bibliography

[1] M. E. Ladd, P. Bachert, M. Meyerspeer, E. Moser, A. M. Nagel, D. G. Norris, S. Schmitter, O. Speck, S. Straub, and M. Zaiss, "Pros and cons of ultra-high-field MRI/MRS for human application," *Progress in Nuclear Magnetic Resonance Spectroscopy*, vol. 109, pp. 1–50, 2018.

[2] D. G. Norris, "High Field Human Imaging," *Journal of Magnetic Resonance Imaging*, vol. 18, no. 5, pp. 519–529, 2003.

[3] F. Padormo, A. Beqiri, J. V. Hajnal, and S. J. Malik, "Parallel transmission for ultrahigh-field imaging," *NMR in Biomedicine*, vol. 29, no. 9, pp. 1145–1161, 2016.

[4] A. Raaijmakers and B. Steensma, "Local sar assessment for multi- transmit systems: A study on the peak local SAR value as a function of magnetic field strength," in *Saftey and Biological Effects in MRI*, 2021, ch. 13.

[5] IEEE/IEC, "62704-1:2017 Determining the peak spatial-average specific absorption rate (SAR) in the human body from wireless communications devices, 30 MHz to 6 GHz - Part 1: General requirements for using the finite difference time-domain (FDTD) method for," Tech. Rep., 2017. [Online]. Available: https://webstore.iec.ch/publication/34411

[6] FDA, "Submission of Premarket Notifications for Magnetic Resonance Diagnostic Devices," Rockville, MD, 2016. [Online]. Available: https://www.fda.gov/regulatory-information/search-fda-guidance-documents/submission-premarket-notifications-magnetic-resonance-diagnostic-devices

[7] T. M. Fiedler, M. E. Ladd, and A. K. Bitz, "SAR Simulations & Safety," *NeuroImage*, vol. 168, no. March 2017, pp. 33–58, 2018.

[8] F. Seifert, G. Wübbeler, S. Junge, B. Ittermann, and H. Rinneberg, "Patient safety concept for multichannel transmit coils," *Journal of Magnetic Resonance Imaging*, vol. 26, no. 5, pp. 1315–1321, 2007.

[9] A. Massire, M. A. Cloos, M. Luong, A. Amadon, A. Vignaud, C. J. Wiggins, and N. Boulant, “Thermal simulations in the human head for high field MRI using parallel transmission,” *Journal of Magnetic Resonance Imaging*, vol. 35, no. 6, pp. 1312–1321, 2012.

[10] J. Petzold, S. Schmitter, B. Silemek, L. Winter, O. Speck, B. Itterman, and F. Seifert, “Investigation of alternative RF power limit control methods for 0.5 T, 1.5 T, and 3 T parallel transmission cardiac imaging: a simulation study,” *Magnetic Resonance in Medicine*, in press.

[11] R. Pohmann, O. Speck, and K. Scheffler, “Signal-to-noise ratio and MR tissue parameters in human brain imaging at 3, 7, and 9.4 tesla using current receive coil arrays,” *Magnetic Resonance in Medicine*, vol. 75, no. 2, pp. 801–809, 2016.

[12] S. Schmitter, L. Delabarre, X. Wu, A. Greiser, D. Wang, E. J. Auerbach, J. T. Vaughan, K. Uğurbil, and P. F. Van De Moortele, “Cardiac imaging at 7 tesla: Single- and two-spoke radiofrequency pulse design with 16-channel parallel excitation,” *Magnetic Resonance in Medicine*, vol. 70, no. 5, pp. 1210–1219, 2013.

[13] S. Schmitter, X. Wu, K. Uğurbil, and P.-F. Van de Moortele, “Design of parallel transmission radiofrequency pulses robust against respiration in cardiac MRI at 7 Tesla,” *Magnetic Resonance in Medicine*, vol. 74, no. 5, pp. 1291–1305, 2015.

[14] M. A. Cloos, N. Boulant, M. Luong, G. Ferrand, E. Giacomini, D. Le Bihan, and A. Amadon, “KT-points: Short three-dimensional tailored RF pulses for flip-angle homogenization over an extended volume,” *Magnetic Resonance in Medicine*, vol. 67, no. 1, pp. 72–80, 2012.

[15] C. S. Aigner, S. Dietrich, and S. Schmitter, “Three-dimensional static and dynamic parallel transmission of the human heart at 7 T,” *NMR in Biomedicine*, vol. 34, no. 3, pp. 1–15, 2021.

[16] C. S. Aigner, S. Dietrich, T. Schaeffter, and S. Schmitter, “Calibration-free pTx of the human heart at 7T via 3D universal pulses,” *Magnetic Resonance in Medicine*, vol. 87, no. 1, pp. 70–84, 2022.

[17] E. F. Meliadò, C. A. van den Berg, P. R. Luijten, and A. J. Raaijmakers, “Intersubject specific absorption rate variability analysis through construction of 23 realistic body models for prostate imaging at 7T,” *Magnetic Resonance in Medicine*, vol. 81, no. 3, pp. 2106–2119, 2019.

[18] A. Sadeghi-Tarakameh, G. Adriany, G. J. Metzger, R. L. Lagore, S. Jungst, L. DelaBarre, P. F. Van de Moortele, K. Ugurbil, E. Atalar, and Y. Eryaman, "Improving radiofrequency power and specific absorption rate management with bumped transmit elements in ultra-high field MRI," *Magnetic Resonance in Medicine*, vol. 84, no. 6, pp. 3485–3493, 2020.

[19] H. Serrai, S. Buch, O. Oran, and R. S. Menon, "Using variable-rate selective excitation (VERSE) radiofrequency pulses to reduce power deposition in pulsed arterial spin labeling sequence at 7 Tesla," *Magnetic Resonance in Medicine*, vol. 83, no. 2, pp. 645–652, 2020.

[20] S. Schmitter, M. Bock, S. Johst, E. J. Auerbach, K. Uğurbil, and P. F. Van De Moortele, "Contrast enhancement in TOF cerebral angiography at 7 T using saturation and MT pulses under SAR constraints: Impact of verse and sparse pulses," *Magnetic Resonance in Medicine*, vol. 68, no. 1, pp. 188–197, 2012.

[21] O. Kraff, A. Fischer, A. M. Nagel, C. Mönninghoff, and M. E. Ladd, "MRI at 7 Tesla and above: Demonstrated and potential capabilities," *Journal of Magnetic Resonance Imaging*, vol. 41, no. 1, pp. 13–33, 2015.

[22] M. A. Ertürk, X. Wu, Y. Eryaman, P. F. Van de Moortele, E. J. Auerbach, R. L. Lagore, L. DelaBarre, J. T. Vaughan, K. Uğurbil, G. Adriany, and G. J. Metzger, "Toward imaging the body at 10.5 tesla," *Magnetic Resonance in Medicine*, vol. 77, no. 1, pp. 434–443, 2017.

[23] F. Padormo and D. J. Larkman, "Assessing and Correcting Respiration Induced Variation of B1 in the Liver," in *Proc. Intl. Soc. Mag. Reson. Med.*, vol. 17, 2009, p. 754.

[24] K. Nehrke and P. Börnert, "Free-Breathing Abdominal B1 Mapping at 3T Using the DREAM Approach," *Proc. Intl. Soc. Mag. Reson. Med.*, vol. 20, p. 3356, 2012.

[25] S. Dietrich, C. S. Aigner, C. Kolbitsch, J. Mayer, J. Ludwig, S. Schmidt, T. Schaeffter, and S. Schmitter, "3D Free-breathing multichannel absolute Mapping in the human body at 7T," *Magnetic Resonance in Medicine*, vol. 85, no. 5, pp. 2552–2567, 2021.

[26] C. S. Aigner, S. Dietrich, and S. Schmitter, "Respiration induced B1+ changes and their impact on universal and tailored 3D kT-point parallel transmission pulses for 7T cardiac imaging," *Magnetic Resonance in Medicine*, 2022.

[27] A. Christ, W. Kainz, E. G. Hahn, K. Honegger, M. Zefferer, E. Neufeld, W. Rascher, R. Janka, W. Bautz, J. Chen, B. Kiefer, P. Schmitt, H. P. Hollenbach, J. Shen, M. Oberle, D. Szczerba, A. Kam, J. W. Guag, and N. Kuster, "The Virtual Family - Development of surface-based anatomical models of two adults and two children for dosimetric simulations," *Physics in Medicine and Biology*, vol. 55, no. 2, 2010.

[28] B. R. Steensma, E. F. Meliadò, P. Luijten, D. W. J. Klomp, C. A. T. Berg, and A. J. E. Raaijmakers, "SAR and temperature distributions in a database of realistic human models for 7 T cardiac imaging," *NMR in Biomedicine*, vol. 34, no. 7, pp. 1–14, jul 2021.

[29] E. Kopanoglu, C. M. Deniz, M. A. Erturk, and R. G. Wise, "Specific absorption rate implications of within-scan patient head motion for ultra-high field MRI," *Magnetic Resonance in Medicine*, vol. 84, no. 5, pp. 2724–2738, 2020.

[30] N. Schön, J. Petzold, S. Schmitter, F. Seifert, C. S. Aigner, G. J. Metzger, and B. Ittermann, "Impact of respiration on B1+ field and SAR distribution at 7 T using a novel EM simulation setup," *Proc. Intl. Soc. Mag. Reson. Med.*, no. 1120, 2020.

[31] N. Schoen, F. Seifert, G. J. Metzger, B. Ittermann, and S. Schmitter, "Investigation of respiration-induced changes of the scattering matrix by EM simulations and a breathing body model," *Proc. Intl. Soc. Mag. Reson. Med.*, no. 3342, 2021.

[32] N. Schoen, F. Seifert, J. Petzold, G. J. Metzger, O. Speck, B. Ittermann, and S. Schmitter, "The impact of respiratory motion on electromagnetic fields and specific absorption rate in cardiac imaging at 7T," *Magnetic Resonance in Medicine*, vol. 88, no. 6, pp. 2645–2661, 2022.

[33] N. Schoen, F. Seifert, G. J. Metzger, O. Speck, B. Ittermann, and S. Schmitter, "The safety relevance of respiration-induced EM field variations in cardiac imaging at 7T and 10.5T," in *DS- ISMRM Jahrestagung*, 2023.

[34] M. d' Arsonval, "Dispositifs pour la mesure des courants altematifs a toutes frequences." *Computes Rendus Seances et Memoires de la Societe de Biologie*, vol. 3, pp. 450–451, 1896.

[35] T. F. Budinger, "MR safety: Past, present, and future from a historical perspective," *Magnetic Resonance Imaging Clinics of North America*, vol. 6, no. 4, pp. 701–714, 1998.

[36] P. Mansfield and A. A. Maudsley, "Medical imaging by NMR," *The British Journal of Radiology*, vol. 50, no. 591, pp. 188–194, mar 1977. [Online]. Available: http://www.birpublications.org/doi/10.1259/0007-1285-50-591-188

[37] P. Mansfield, I. L. Pykett, P. G. Morris, and R. E. Coupland, "Human whole body line-scan imaging by NMR," *The British Journal of Radiology*, vol. 51, no. 611, pp. 921–922, 1978.

[38] R. Damadian, M. Goldsmith, and L. Minkoff, "Field focusing n.m.r. (FONAR) and the formation of chemical images in man," *Philosophical Transactions of the Royal Society of London. B, Biological Sciences*, vol. 289, no. 1037, pp. 489–500, 1980.

[39] F. G. Shellock, *Magnetic Resonance Procedures Health Effects and Safety*, 1st ed. CRC Press, 2000.

[40] R. W. Brown, Y.-C. N. Cheng, E. M. Haacke, M. R. Thompson, and R. Venkatesan, *Magnetic Resonance Imaging: Physical Principles and Sequence Design*. Chichester, UK: John Wiley & Sons Ltd, 1999.

[41] United States Food and Drug Administration, "FDA clears first 7T magnetic resonance imaging device." [Online]. Available: https://www.fda.gov/news-events/press-announcements/fda-clears-first-7t-magnetic-resonance-imaging-device

[42] K. Kose, "Physical and technical aspects of human magnetic resonance imaging: present status and 50 years historical review," *Advances in Physics: X*, vol. 6, no. 1, 2021.

[43] M. Vlaardingerbroek and J. den Boer, *Magnetic Resonance Imaging Theory and Practice*, 3rd ed., 1996.

[44] A. Abragam, *The Principles of Nuclear Magnetism*, 1983.

[45] C. P. Slichter, *Principles of Magnetic Resonance*, 1990.

[46] F. Bloch, W. W. Hansen, and M. Packard, "Nuclear Induction," *Physical Review*, vol. 69, no. 3-4, pp. 127–127, 1946.

[47] D. I. Hoult, "The principle of reciprocity in signal strength calculations - A mathematical guide," *Concepts in Magnetic Resonance*, vol. 12, no. 4, pp. 173–187, 2000.

[48] S. Trattnig, W. Bogner, S. Gruber, P. Szomolanyi, V. Juras, S. Robinson, Š. Zbýň, and S. Haneder, "Clinical applications at ultrahigh field (7 T). Where does it make the difference?" *NMR in Biomedicine*, vol. 29, no. 9, pp. 1316–1334, 2016.

[49] O. Kraff and H. H. Quick, "7T: Physics, safety, and potential clinical applications," *Journal of Magnetic Resonance Imaging*, vol. 46, no. 6, pp. 1573–1589, 2017.

[50] J. H. F. Van Gemert, W. Brink, A. Webb, and R. Remis, "An Efficient Methodology for the Analysis of Dielectric Shimming Materials in Magnetic Resonance Imaging," *IEEE Transactions on Medical Imaging*, vol. 36, no. 2, pp. 666–673, 2017.

[51] D. G. Norris, "Adiabatic radiofrequency pulse forms in biomedical nuclear magnetic resonance," *Concepts in Magnetic Resonance*, vol. 14, no. 2, pp. 89–101, 2002.

[52] T. S. Ibrahim, R. Lee, B. A. Baertlein, A. Kangarlu, and P. M. L. Robitaille, "Application of finite difference time domain method for the design of birdcage RF head coils using multi-port excitations," *Magnetic Resonance Imaging*, vol. 18, no. 6, pp. 733–742, 2000.

[53] D. I. Hoult and D. Phil, "Sensitivity and power deposition in a high-field imaging experiment," *Journal of Magnetic Resonance Imaging*, vol. 12, no. 1, pp. 46–67, 2000.

[54] Y. Zhu, "Parallel Excitation with an Array of Transmit Coils," *Magnetic Resonance in Medicine*, vol. 51, no. 4, pp. 775–784, 2004.

[55] U. Katscher, P. Börnert, C. Leussler, and J. S. Van den Brink, "Transmit SENSE," *Magnetic Resonance in Medicine*, vol. 49, no. 1, pp. 144–150, 2003.

[56] J. B. Schneider, "Understanding the Finite-Difference Time-Domain Method," 2021.

[57] "REMCOM SAR for MRI." [Online]. Available: https://de.remcom.com/articles-and-papers/computation-of-fields-and-sar-for-mri-with-fdtd-software

[58] R. Rumpf, "Electromagnetic Analysis Using Finite-Difference Time-Domain." [Online]. Available: https://empossible.net/academics/emp5304/

[59] S. Gedney, "An anisotropic perfectly matched layer-absorbing medium for the truncation of FDTD lattices," *IEEE Transactions on Antennas and Propagation*, vol. 44, no. 12, pp. 1630–1639, 1996.

[60] R. Kumar and A. Sharma, “Absorbing boundary condition (ABC) and perfectly matched layer (PML) in numerical beam propagation: a comparison,” *Optical and Quantum Electronics*, vol. 51, no. 2, pp. 1–13, 2019.

[61] Python Software Foundation, “Python.” [Online]. Available: http://www.python.org

[62] U. Zanovello, F. Seifert, O. Bottauscio, L. Winter, L. Zilberti, and B. Ittermann, “CoSimPy: An open-source python library for MRI radiofrequency Coil EM/Circuit Cosimulation,” *Computer Methods and Programs in Biomedicine*, vol. 216, p. 106684, 2022.

[63] O. Kraff and H. H. Quick, “Radiofrequency Coils for 7 Tesla MRI,” *Topics in Magnetic Resonance Imaging*, vol. 28, no. 3, pp. 145–158, 2019.

[64] A. J. Raaijmakers, M. Italiaander, I. J. Voogt, P. R. Luijten, J. M. Hoogduin, D. W. Klomp, and C. A. Van Den Berg, “The fractionated dipole antenna: A new antenna for body imaging at 7 Tesla,” *Magnetic Resonance in Medicine*, vol. 75, no. 3, pp. 1366–1374, 2016.

[65] M. A. Ertürk, A. J. Raaijmakers, G. Adriany, K. Uğurbil, and G. J. Metzger, “A 16-channel combined loop-dipole transceiver array for 7Tesla body MRI,” *Magnetic Resonance in Medicine*, vol. 77, no. 2, pp. 884–894, 2017.

[66] S. Schmidt, M. A. Ertürk, X. He, T. Haluptzok, Y. Eryaman, and G. J. Metzger, “Improved 1 H body imaging at 10.5 T: Validation and VOP -enabled imaging in vivo with a 16-channel transceiver dipole array,” *Magnetic Resonance in Medicine*, pp. 1–17, sep 2023.

[67] W. P. Segars, G. Sturgeon, S. Mendonca, J. Grimes, and B. M. W. Tsui, “4D XCAT phantom for multimodality imaging research,” *Medical Physics*, vol. 37, pp. 4902–4915, 2010.

[68] W. P. Segars, J. Bond, J. Frush, S. Hon, C. Eckersley, C. H. Williams, J. Feng, D. J. Tward, J. T. Ratnanather, M. I. Miller, D. Frush, and E. Samei, “Population of anatomically variable 4D XCAT adult phantoms for imaging research and optimization,” *Medical Physics*, vol. 40, no. 4, pp. 1–11, 2013.

[69] W. P. Segars, B. M. Tsui, J. Cai, F. F. Yin, G. S. Fung, and E. Samei, “Application of the 4-D XCAT Phantoms in Biomedical Imaging and beyond,” *IEEE Transactions on Medical Imaging*, vol. 37, no. 3, pp. 680–692, 2018.

[70] C. Paganelli, P. Summers, C. Gianoli, M. Bellomi, G. Baroni, and M. Riboldi, "A tool for validating MRI-guided strategies: a digital breathing CT/MRI phantom of the abdominal site," *Medical and Biological Engineering and Computing*, vol. 55, no. 11, pp. 2001–2014, 2017.

[71] Duke.edu, "XCAT Program." [Online]. Available: https://cvit.duke.edu/resource/xcat-phantom-program/

[72] Itis Foundation, "Dielectric Properties." [Online]. Available: https://itis.swiss/virtual-population/tissue-properties/database/dielectric-properties/

[73] S. A. Szermer, "Development of an MR Phantom Setup for the Validation of Phase Contrast Velocity Imaging," Master Eng., Beuth Hochschule für Technik Berlin, 2019.

[74] B. Hargreaves, "Rapid gradient-echo imaging," *Journal of Magnetic Resonance Imaging*, vol. 36, no. 6, pp. 1300–1313, 2012.

[75] V. L. Yarnykh, "Actual flip-angle imaging in the pulsed steady state: A method for rapid three-dimensional mapping of the transmitted radiofrequency field," *Magnetic Resonance in Medicine*, vol. 57, no. 1, pp. 192–200, 2007.

[76] L. Winter, B. Silemek, J. Petzold, H. Pfeiffer, W. Hoffmann, F. Seifert, and B. Ittermann, "Parallel transmission medical implant safety testbed: Real-time mitigation of RF induced tip heating using time-domain E-field sensors," *Magnetic Resonance in Medicine*, vol. 84, no. 6, pp. 3468–3484, 2020.

[77] S. Kuehn, F. Bomholt, N. Chavannes, and N. Kuster, "Active optical sensor for electromagnetic field measurements in time and frequency domains," *EuCAP 2010 - The 4th European Conference on Antennas and Propagation*, pp. 1–2, 2010.

[78] Speag, "TDS Standalone Remote Unit." [Online]. Available: https://speag.swiss/products/tds/tds-sni/remote-unit-standalone/

[79] T. Klepsch, T. D. Lindel, W. Hoffmann, H. Botterweck, B. Ittermann, and F. Seifert, "Calibration of fibre-optic RF E/H-field probes using a magnetic resonance (MR) compatible TEM cell and dedicated MR measurement techniques," *Biomedical Engineering / Biomedizinische Technik*, vol. 57, pp. 119–122, aug 2012.

[80] P. L. Wagner, "Validation of RF-field mapping methods at a 7T ultrahigh-field MR scanner," Master Eng., Technische Universität Berlin, 2023.

[81] F. Padormo, A. Beqiri, J. V. Hajnal, and S. J. Malik, “Parallel transmission for ultrahigh-field imaging,” *NMR in Biomedicine*, vol. 29, no. 9, pp. 1145–1161, 2016.

[82] S. Schmitter, X. Wu, G. Adriany, E. J. Auerbach, K. Uğurbil, and P. F. Van De Moortele, “Cerebral TOF angiography at 7T: Impact of B1+ shimming with a 16-channel transceiver array,” *Magnetic Resonance in Medicine*, vol. 71, no. 3, pp. 966–977, 2014.

[83] Z. Cao, X. Yan, and W. A. Grissom, “Array-compressed parallel transmit pulse design,” *Magnetic Resonance in Medicine*, vol. 76, no. 4, pp. 1158–1169, 2016.

[84] W. A. Grissom, M. M. Khalighi, L. I. Sacolick, B. K. Rutt, and M. W. Vogel, “Small-tip-angle spokes pulse design using interleaved greedy and local optimization methods,” *Magnetic Resonance in Medicine*, vol. 68, no. 5, pp. 1553–1562, 2012.

[85] H. W. Engl and W. Grever, “Using the L-curve for determining optimal regularization parameters,” *Numerische Mathematik*, vol. 69, no. 1, pp. 25–31, nov 1994. [Online]. Available: http://link.springer.com/10.1007/s002110050078

[86] I. Graesslin, H. Homann, S. Biederer, P. Börnert, K. Nehrke, P. Vernickel, G. Mens, P. Harvey, and U. Katscher, “A specific absorption rate prediction concept for parallel transmission MR,” *Magnetic Resonance in Medicine*, vol. 68, no. 5, pp. 1664–1674, 2012.

[87] G. Eichfelder and M. Gebhardt, “Local specific absorption rate control for parallel transmission by virtual observation points,” *Magnetic Resonance in Medicine*, vol. 66, no. 5, pp. 1468–1476, 2011.

[88] S. Orzada, T. M. Fiedler, A. K. Bitz, M. E. Ladd, and H. H. Quick, “Local SAR compression with overestimation control to reduce maximum relative SAR overestimation and improve multi-channel RF array performance,” *Magnetic Resonance Materials in Physics, Biology and Medicine*, vol. 34, no. 1, pp. 153–163, 2021.

[89] M. C. Restivo, “Assessment and Monitoring of RF Safety for Ultra-High Field MRI,” PhD thesis, Utrecht University, 2017.

[90] R. L. Mcintosh and V. Anderson, “SAR versus VAR, and the size and shape that provide the most appropriate RF exposure metric in the range of 0.5-6GHz,” *Bioelectromagnetics*, vol. 32, no. 4, pp. 312–321, 2011.

[91] T. M. Fiedler, S. Orzada, M. Flöser, S. H. G. Rietsch, H. H. Quick, M. E. Ladd, and A. K. Bitz, “Performance analysis of integrated RF microstrip transmit antenna arrays with high channel count for body imaging at 7 T,” *NMR in Biomedicine*, vol. 34, no. 7, pp. 1–18, jul 2021.

[92] J. Herrler, P. Liebig, R. Gumbrecht, D. Ritter, S. Schmitter, A. Maier, M. Schmidt, M. Uder, A. Doerfler, and A. M. Nagel, “Fast online-customized (FOCUS) parallel transmission pulses: A combination of universal pulses and individual optimization,” *Magnetic Resonance in Medicine*, vol. 85, no. 6, pp. 3140–3153, 2021.

[93] V. Gras, A. Vignaud, A. Amadon, D. Le Bihan, and N. Boulant, “Universal pulses: A new concept for calibration-free parallel transmission,” *Magnetic Resonance in Medicine*, vol. 77, no. 2, pp. 635–643, 2017.

[94] J. Hoffmann, A. Henning, I. A. Giapitzakis, K. Scheffler, G. Shajan, R. Pohmann, and N. I. Avdievich, “Safety testing and operational procedures for self-developed radiofrequency coils,” *NMR in Biomedicine*, vol. 29, no. 9, pp. 1131–1144, 2016.

[95] S. Orzada, T. M. Fiedler, H. H. Quick, and M. E. Ladd, “Post-processing algorithms for specific absorption rate compression,” *Magnetic Resonance in Medicine*, vol. 86, no. 5, pp. 2853–2861, 2021.

[96] I. Graesslin, P. Vernickel, P. Börnert, K. Nehrke, G. Mens, P. Harvey, and U. Katscher, “Comprehensive RF safety concept for parallel transmission MR,” *Magnetic Resonance in Medicine*, vol. 74, no. 2, pp. 589–598, 2015.

[97] G. J. Metzger, P. F. Van De Moortele, C. Akgun, C. J. Snyder, S. Moeller, J. Strupp, P. Andersen, D. Shrivastava, T. Vaughan, K. Ugurbil, and G. Adriany, “Performance of external and internal coil configurations for prostate investigations at 7 T,” *Magnetic Resonance in Medicine*, vol. 64, no. 6, pp. 1625–1639, 2010.

[98] F. Seifert, A. Cassara, G. Weidemann, and B. Ittermann, “Reliable and robust RF safety assessment of transmit array coils at ultrahigh fields,” *Proc. Intl. Soc. Mag. Reson. Med.*, no. 4891, 2014.

[99] E. F. Meliadò, A. Sbrizzi, C. A. van den Berg, P. R. Luijten, and A. J. Raaijmakers, “Real-time assessment of potential peak local specific absorption rate value without phase monitoring: Trigonometric maximization method for worst-case local specific absorption rate determination,” *Magnetic Resonance in Medicine*, vol. 85, no. 6, pp. 3420–3433, 2021.

[100] J. Petzold, B. Ittermann, and S. Frank, "Robustness of pTx safety concepts to varying subjects and subject positions," *Proc. Intl. Soc. Mag. Reson. Med.*, no. 2488, 2021.

[101] D. Buikman, T. Helzel, and P. Röschmann, "The rf coil as a sensitive motion detector for magnetic resonance imaging," *Magnetic Resonance Imaging*, vol. 6, no. 3, pp. 281–289, 1988.

[102] A. T. Hess, E. M. Tunnicliffe, C. T. Rodgers, and M. D. Robson, "Diaphragm position can be accurately estimated from the scattering of a parallel transmit RF coil at 7 T," *Magnetic Resonance in Medicine*, vol. 79, no. 4, pp. 2164–2169, 2018.

[103] P. Russer, *Electromagnetics, Microwave Circuit, And Antenna Design for Communications Engineering*, 2nd ed. Artech House, 2006.

[104] J. Malmivuo and R. Plonsey, *Bioelectromagnetism: Principles and Applications of Bioelectric and Biomagnetic Fields*, 1st ed. Oxford University Press, 1995.

[105] N. Schoen, F. Seifert, G. J. Metzger, O. Speck, B. Ittermann, and S. Schmitter, "Respiratory motion affects peak spatial SAR value and location – impact on safety supervision for 7T cardiac imaging," *Proc. Intl. Soc. Mag. Reson. Med.*, no. 2547, 2022.

[106] N. Schoen, "The impact of the field strength on respiratory induced EM fields and SAR variations in kT-point optimized cardiac imaging at UHF," *Magnetic Resonance in Medicine (to be submitted)*, 2024.

[107] R. R. Ernst and W. A. Anderson, "Application of Fourier transform spectroscopy to magnetic resonance," *Review of Scientific Instruments*, vol. 37, no. 1, pp. 93–102, 1966.

[108] S.-H. Lee, J.-S. Barg, S.-J. Yeo, and S.-K. Lee, " High-Resolution Numerical Simulation of Respiration-Induced Dynamic B 0 Shift in the Head in High-Field MRI ," *Investigative Magnetic Resonance Imaging*, vol. 23, no. 1, p. 38, 2019.

[109] N. Lowther, S. Ipsen, S. Marsh, O. Blanck, and P. Keall, "Investigation of the XCAT phantom as a validation tool in cardiac MRI tracking algorithms," *Physica Medica*, vol. 45, pp. 44–51, 2018.

[110] J. Mayer, R. Brown, K. Thielemans, E. Ovtchinnikov, E. Pasca, D. Atkinson, A. Gillman, P. Marsden, M. Ippoliti, M. Makowski, T. Schaeffter, and C. Kolbitsch,

"Flexible numerical simulation framework for dynamic PET-MR data," *Physics in Medicine and Biology*, vol. 65, no. 14, 2020.

[111] Duke.edu, "XCAT Anatomy Models." [Online]. Available: https://cvit.duke.edu/resource/xcat-anatomy-files/

[112] M. De Greef, O. Ipek, A. J. Raaijmakers, J. Crezee, and C. A. Van Den Berg, "Specific absorption rate intersubject variability in 7T parallel transmit MRI of the head," *Magnetic Resonance in Medicine*, vol. 69, no. 5, pp. 1476–1485, 2013.

[113] B. Steensma, P. F. van de Moortele, A. Ertürk, A. Grant, G. Adriany, P. Luijten, D. Klomp, N. van den Berg, G. Metzger, and A. Raaijmakers, "Introduction of the snake antenna array: Geometry optimization of a sinusoidal dipole antenna for 10.5T body imaging with lower peak SAR," *Magnetic Resonance in Medicine*, vol. 84, no. 5, pp. 2885–2896, 2020.

[114] G. Solomakha, C. van Leeuwen, A. Raaijmakers, C. Simovski, A. Popugaev, R. Abdeddaim, I. Melchakova, and S. Glybovski, "The dual-mode dipole: A new array element for 7T body imaging with reduced SAR," *Magnetic Resonance in Medicine*, vol. 81, no. 2, pp. 1459–1469, 2019.

[115] S. H. Rietsch, S. Orzada, S. Maderwald, S. Brunheim, B. W. Philips, T. W. Scheenen, M. E. Ladd, and H. H. Quick, "7T ultra-high field body MR imaging with an 8-channel transmit/32-channel receive radiofrequency coil array," *Medical Physics*, vol. 45, no. 7, pp. 2978–2990, 2018.

[116] S. B. Fain, F. J. Browning, J. A. Polzin, J. Du, Y. Zhou, W. F. Block, T. M. Grist, and C. A. Mistretta, "Floating table isotropic projection (FLIPR) acquisition: A time-resolved 3D method for extended field-of-view MRI during continuous table motion," *Magnetic Resonance in Medicine*, vol. 52, no. 5, pp. 1093–1102, 2004.

[117] J. Paška, M. A. Cloos, and G. C. Wiggins, "A rigid, stand-off hybrid dipole, and birdcage coil array for 7 T body imaging," *Magnetic Resonance in Medicine*, vol. 80, no. 2, pp. 822–832, aug 2018. [Online]. Available: http://doi.wiley.com/10.1002/mrm.27048

[118] L. Winter and T. Niendorf, "Electrodynamics and radiofrequency antenna concepts for human magnetic resonance at 23.5 T (1 GHz) and beyond," *Magnetic Resonance Materials in Physics, Biology and Medicine*, vol. 29, no. 3, pp. 641–656, 2016.

[119] Z. Wang, J. C. Lin, W. Mao, W. Liu, M. B. Smith, and C. M. Collins, "SAR and temperature: Simulations and comparison to regulatory limits for MRI," *Journal of Magnetic Resonance Imaging*, vol. 26, no. 2, pp. 437–441, 2007.

[120] S. Wolf, D. Diehl, M. Gebhardt, J. Mallow, and O. Speck, "SAR simulations for high-field MRI: How much detail, effort, and accuracy is needed?" *Magnetic Resonance in Medicine*, vol. 69, no. 4, pp. 1157–1168, 2013.

[121] J. W. Van Oorschot, F. Visser, A. L. Eikendal, E. J. P. Vonken, P. R. Luijten, S. A. Chamuleau, T. Leiner, and J. J. Zwanenburg, "Single Breath-Hold T1ρ-Mapping of the Heart for Endogenous Assessment of Myocardial Fibrosis," *Investigative Radiology*, vol. 51, no. 8, pp. 505–512, 2016.

[122] V. Gras, E. Chazel, N. Boulant, A. Amadon, and M. Luong, "Workflow proposal to test SAR virtual observation points with convex optimization: application to intersubject variability at 11.7T MRI," *Proc. Intl. Soc. Mag. Reson. Med.*, no. 2688, 2023.

[123] S. Schmitter, S. Schnell, K. Uğurbil, M. Markl, and P. F. Van de Moortele, "Towards high-resolution 4D flow MRI in the human aorta using kt-GRAPPA and B1+ shimming at 7T," *Journal of Magnetic Resonance Imaging*, vol. 44, no. 2, pp. 486–499, 2016.

List of Figures

List of Tables

Abbreviations and symbols

Abbreviation	Description
ABC	absorbing boundary conditions
AFI	actual flip angle
AP	anterior posterior direction
cp	circular polarized
CNR	contrast to noise ratio
D	dipole
EM	electromagnetic
FA	flip angle
FDA	food and drug administration
FDTD	finite difference time domain
FOV	field of view
FWHM	full width half maximum
GRE	gradient echo
HF	head-feet direction
IEC	international electrotechnical commission
L	loop
LD	loop and dipole
max	maximum
min	minimum
MIP	maximum intensity projection
MR	magnetic resonance
MRI	magnetic resonance imaging
RMSE	root mean squared error
PCM	power-controlled mode
psSAR	peak spatial SAR
pTx	parallel transmission
PVP	polyvinylpyrrolidone

PML	perfectly matched layer
UPML	uniaxial perfectly matched layers
Ri	respiratory state, ranging from R1-exhale to R4-inhale, R5 has an increased inhalation depth
ROI	region of interest
ROI_1	heart ROI in single transversal slice
ROI_3	heart ROI in three transversal slices spaced 20 mm apart
ROI_H	heart ROI in 28 transversal slices spaced a 4 mm apart
ROI_{SA3}	heart ROI in three slices along short-axis view, spaced 20 mm apart
RF	radio frequency
RMS	root mean square
RMSE	root mean squared error
S-matrix	scattering matrix
SAR	specific absorption rate
SCM	SAR-controlled mode
SNR	signal-to-noise ratio
SOM	sum of magnitude
std	standard deviation
TEM	transverse electromagnetic
UHF	ultra high field
Tx	transmit
TX/RX	transmit receive
VOP	virtual observation points
β	gradient echo excitation pulse

Symbol	**Unit**	**Description**
$a(x)$	1	absorption function
b	1	regularisation parameter for dynamic pTx
$\vec{B}$	T	magnetic flux density (B-field)
$\vec{B_0}$	T	static magnetic field strength, flux density
$\vec{B_1}$	$\frac{\mu T}{\sqrt{kW}}$	magnetic RF field induced by applied RF pulse with Larmorfrequency with x, y and z component
B_1^+	$\frac{\mu T}{\sqrt{kW}}$	transmit B_1 field, rotating in the direction of the spins, normalized on 1 kW forward power

$B^+_{1,i}$	$\frac{\mu T}{\sqrt{kW}}$	B_1^+ field of element i, normalized on 1 kW forward power
B^-_1	$\frac{\mu T}{\sqrt{kW}}$	receive B_1 field, rotating in the opposite direction of the spins, normalized on 1 kW forward power
C	F	capacitor
c_{SCM}	1	scaling factor used to calculate $\vec{u}_{SCM}$
c_0	$\frac{m}{s}$	speed of light in vacuum
CV	%	coefficient of variation
$\vec{D}$	$\frac{C}{m^2}$	displacement current
d_c	mm	chest displacement
d_d	mm	diaphragm displacement
dt_{kT}	s	pulse duration of kT-point pulse
$\vec{E}$	$\frac{V}{m}$	electric field (E-field)
f_0	$\frac{1}{s}$	resonance frequency
$\vec{H}$	$\frac{A}{m}$	magnetic field (H-field)
$\vec{\tilde{H}}$	$\frac{A}{m}$	normalized H-field by η_0
$\vec{J}$	$\frac{A}{m^2}$	current density
$\vec{J}_i$	$\frac{1}{m^2}$	current densities per unit input current at the element i
m	g	mass
M_0	$\frac{A}{m}$	macroscopic net magnetisation
M_{xy}	$\frac{A}{m}$	transversal magnetisation
M_z	$\frac{A}{m}$	longitudinal magnetisation
N_{el}	1	number of elements
P	W	power
P^{max}_{fwd}	W	maximum allowed upper forward power to stay below IEC 60601-2-33 first-level controlled mode trunk SAR limit
$\mathcal{P}$	$\frac{C}{m^2}$	polarization of the medium
p_i	V	RF pulse of element i
$p(t)$	V	RF pulse of all elements
$psSAR_{10g}$	$\frac{W}{kg}$	psSAR averaged over 10g
Q	1	Q-factor
$\underline{Q}$	$\frac{W}{kg}$	Q-Matrix
$\underline{Q}_{10g}$	$\frac{W}{kg}$	Q-Matrix averaged over 10g
$\vec{r}$	m	location vector
$\vec{r}_{center}$	m	location vector to center of the heart

R	Ω	resistance
R_L	Ω	ohmic losses in loop element
$\mathcal{S}$	1	signal
$\mathcal{S}_1$	1	signal of surrounding material
$\mathcal{S}_2$	1	signal of small structures
$\mathcal{S}_0$	1	signal for 0V preparation pulse voltage applied
s_i	$\frac{\mu T}{V}$	spatial sensitivity of element i, normalized on 1 V forward voltage
$\vec{S}$	1	S-matrix
$\vec{S}_0$	1	temporally invariant part of S-matrix
$\Delta\underline{S}_{motion}$	1	respiration dependent S-matrix part
SAR_{10g}	$\frac{W}{kg}$	SAR averaged over 10g
t	s	time
t_s	s	sampling time period
T_1	s	longitudinal (spin-lattice) relaxation time
T_2^*	s	transversal (spin-spin) relaxation time
TR_1, TR_2	s	delay times in AFI between two RF pulses
TR	s	repetition time
U	V	voltage
$\vec{u}$	1	complex shim vector
$\vec{u}_{kTi}$	1	complex shim vector of kT pulse i
$\vec{u}_{\eta}^{meas}$	1	efficient shim vector, determined at measured data
u_i	1	amplitude applied to element i
$\vec{u}_{SCM}$	1	amplitude scaled by SCM
$\vec{u}_{PCM}$	1	amplitude scaled by PCM
$\vec{u}_{PCM}^{max}$	1	maximum allowed amplitude using PCM
v_{fwd}	V	forward voltage
v_{ret}	V	return voltage
V	m^3	volume
V_{fwd}	V	forward voltage matrix
V_{ret}	V	return voltage matrix
V_{voxel}	m^3	voxel volume
$wbSAR_{10g}$	$\frac{W}{kg}$	whole body SAR averaged over 10g
w_i	1	complex weight
x_{abc1}	m	position of beginning of ABC layer
x_{abc2}	m	position of end of ABC layer

Z	Ω	impedance
Z_0	Ω	characteristic impedance
Z_{ij}	Ω	impedance at element i when power is applied at element j
$Z1, Z2, Z3$	Ω	impedances of T-Type lumped element circuit for co-simulations
α	$^\circ$	flip angle achieved by preparation pulse applied for τ =1 ms with different voltages U
α_{rot}	$^\circ$	rotation angle of coil modules
$\delta\varphi$	$^\circ$	phase variation
$\Delta CV, \Delta min(\|B_1^+\|)$, $\Delta mean(\|B_1^+\|), \Delta\varphi$	$\%, \frac{\mu T}{\sqrt{kW}}, \frac{\mu T}{\sqrt{kW}}, ^\circ$	absolute respiration induced changes during inhalation of $CV, min(\|B_1^+\|), mean(\|B_1^+\|), \varphi$
$\Delta psSAR_{10g}$	$\%$	relative respiration induced changes during inhalation of $psSAR_{10g}$
Δt	s	time steps for FDTD derivatives
$\Delta t_{\alpha\beta}$	s	time between preparation pulse and readout pulse
$\frac{\partial}{\partial \vec{r}_{AP}}$	1	gradient along AP direction
$\mathcal{E}$	1	effective permittivity tensor
ε	1	effective permittivity
ε_r	1	relative permittivity
ε_0	$\frac{1F}{m}$	permittivity of free space
γ	$\frac{MHz}{T}$	gyromagnetic ratio
$\mathcal{M}$	$\frac{N}{A^2}$	magnetic permeability tensor
μ	$\frac{N}{A^2}$	magnetic permeability of a medium
μ_0	$\frac{N}{A^2}$	magnetic permeability in free space
η_0	Ω	free space impedance
η	1	efficiency
$\bar{\eta}$	1	efficiency averaged over ROI
ρ	$\frac{C}{m^3}$	charge density
φ_i	$^\circ$	phase applied at element i
σ	$\frac{S}{m}$	electric conductivity
τ	s	RF pulse duration
ω_0	$\frac{1}{s}$	Larmor frequency
χ	1	magnetic susceptibility

$\mathbb{1}$	1	Identity matrix

Appendix

A.1 Coil validation and calculation of power limits

A.1.1 absolute B_1^+ mapping- preparation pulse method

To calculate $|B_1^+|$ at a certain voxel the $|B_1^+|$ for a 90° FA ($B_1^+(\alpha_{90^\circ})$ and the used power to obtain this FA (P_{90°) needs to be calculated.

$$B_1^+ = \frac{B_1^+(\alpha_{90^\circ})}{\sqrt{P_{90^\circ}}} \tag{A.1.1}$$

The FA is described by:

$$FA = \gamma \cdot |B_1^+| \cdot \tau \tag{A.1.2}$$

with γ the gyromagnetic ratio and τ the preparation pulse length. Inserting 90 ° as the desired FA, $\gamma = 42.577\frac{MHz}{T} \cdot 2\pi$ and $\tau = 1\,ms$:

$$90^\circ = \frac{\pi}{2} = 42.577\frac{MHz}{T} \cdot 2\pi \cdot |B_1^+(\alpha_{90^\circ})| \cdot 1 \cdot 10^{-3} s \tag{A.1.3}$$

$$\Rightarrow |B_1^+(\alpha_{90^\circ})| = \frac{1}{42.577 \cdot 4 \cdot 10^3} T \tag{A.1.4}$$

P_{90° is calculated by:

$$P_{90^\circ} = U_{90^\circ}^2 \cdot \frac{N_{el}}{R} \tag{A.1.5}$$

with N_{el} as the number of elements and R the resistance. Using eq. (3.4) and fig. 3.3.3, for a FA of 90° the normalized signal $\frac{S}{S_0} = 0$, and the voltage U_{90° is determined by determining the zero point in fig. 3.3.3B.

A.1.2 Figures

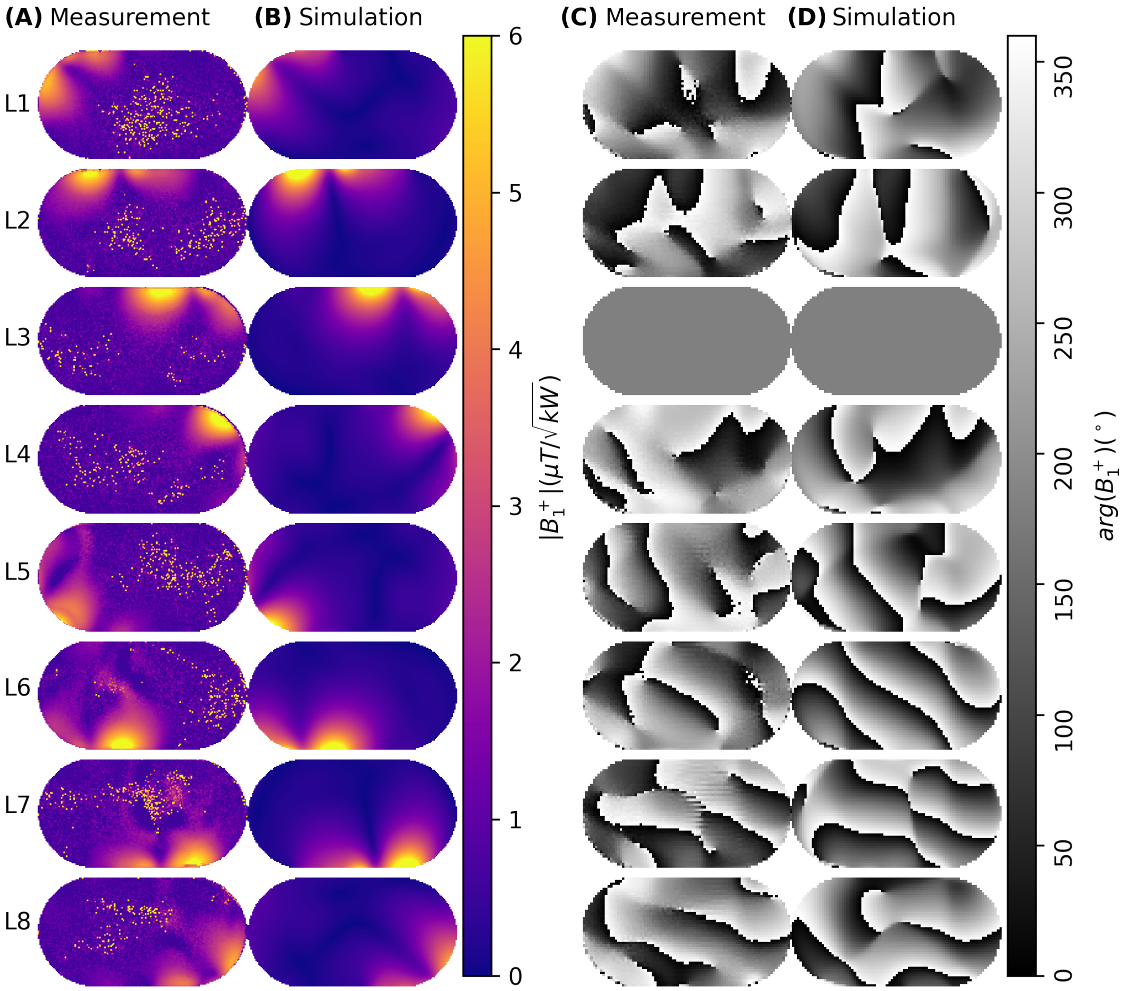

Figure A.1.1: Eight 'L' elements, phantom B_1^+ data: Compare absolute B_1^+ maps (A-B) and phase B_1^+ maps (C-D) for measurements (A,C) and simulations (B,D). The measured $|B_1^+|$ data in (A) is acquired with the preparation pulse method and the measured phase data in(C) is acquired with a GRE sequence.

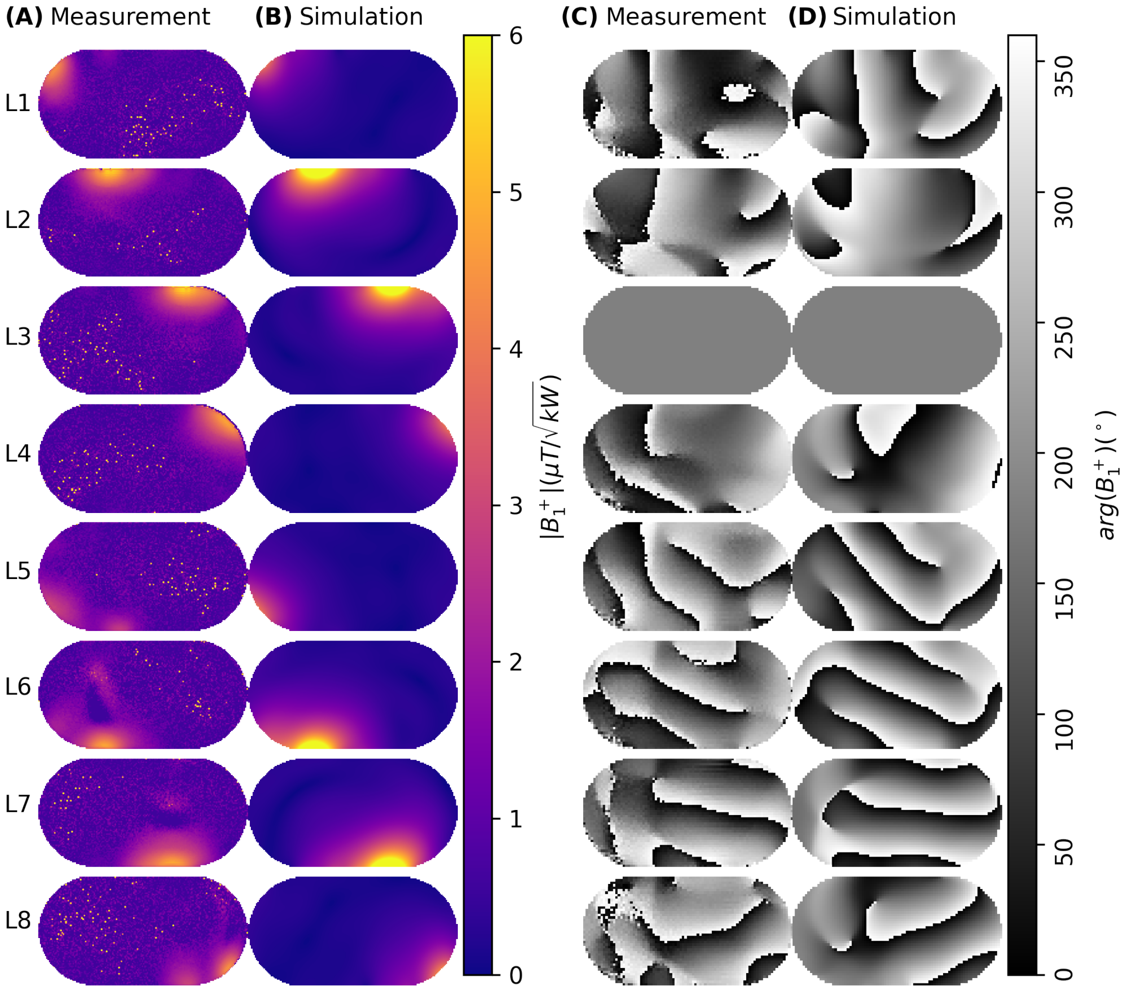

Figure A.1.2: Eight 'D' elements, phantom B_1^+ data: Compare absolute B_1^+ maps (A-B) and phase B_1^+ maps (C-D) for measurements (A,C) and simulations (B,D). The measured $|B_1^+|$ data in (A) is acquired with the preparation pulse method and the measured phase data in(C) is acquired with a GRE sequence.

A.2 The Impact of respiratory motion on EM-fields in FDTD simulation

A.2.1 Figures

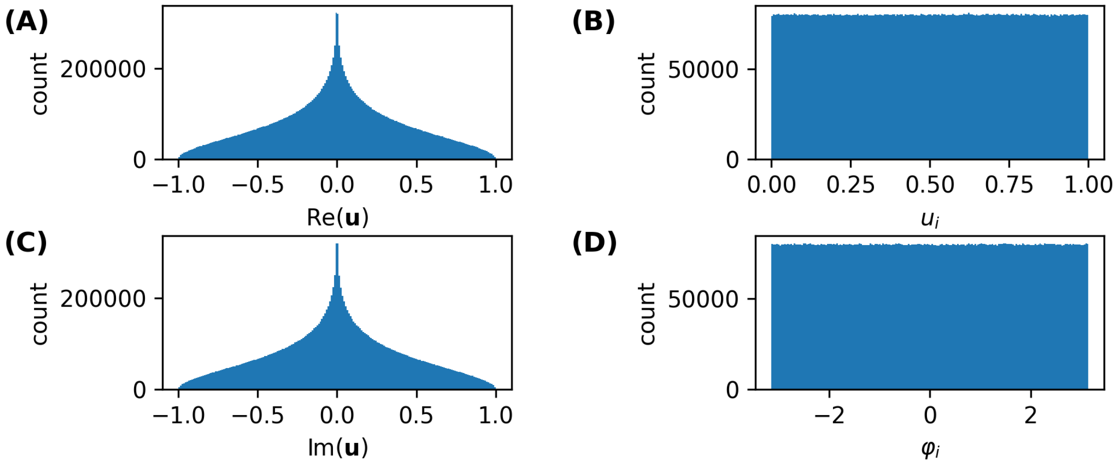

Figure A.2.1: This plot illustrates the distribution of the real part (A), the imaginary part (B), the absolute values (C), and the phases (D) of a set of 10^6 random amplitude and phase shim vectors. The amplitude and phase values are generated using the Python function numpy.random.uniform(). Please note that this plot does not account for the scaling factors c_{SCM} or c_{PCM}

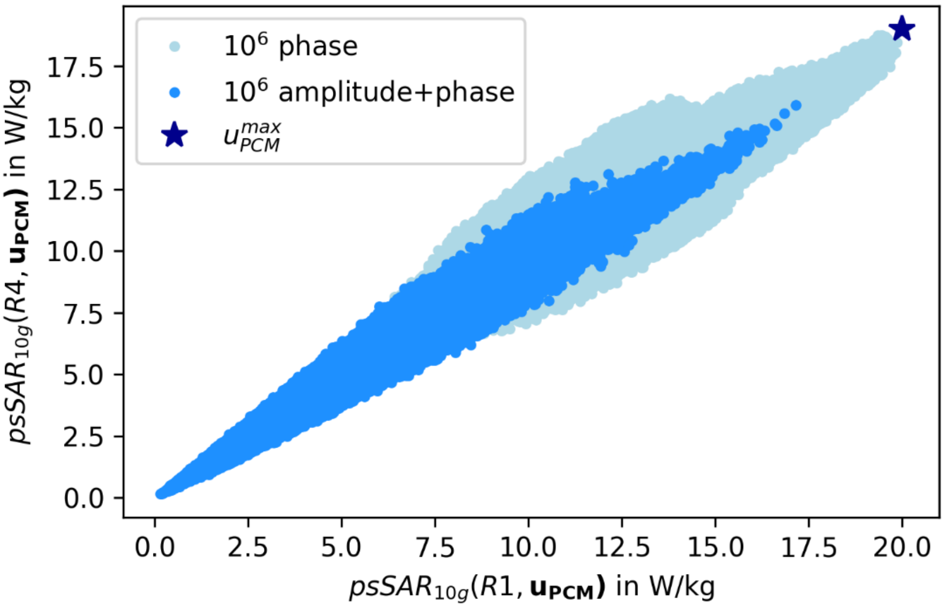

Figure A.2.2: This plot depicts the $psSAR_{10g}(R_4, \boldsymbol{u}_{PCM})$ in dependence of $psSAR_{10g}(R_1, \boldsymbol{u}_{PCM})$ to demonstrate a broad coverage of the psSAR by the selected 10^6 phase shim vectors and 10^6 amplitude and phase shim vectors which have $psSAR_{10g}$ values below the power-controlled upper SAR boundary $\boldsymbol{u}_{PCM}^{max}$. The 'Moving' coil setup with dipole channels and conventional breathing was used. For phase-only variations, the 10^6 test shim vectors are sufficient to 'find' the theoretical PCM maximum (star symbol), indicating that this 8-dimensional excitation-vector space is sufficiently explored. For the 16-dimensional space of phase-and-magnitude variations, the theoretical PCM maximum is not achieved.

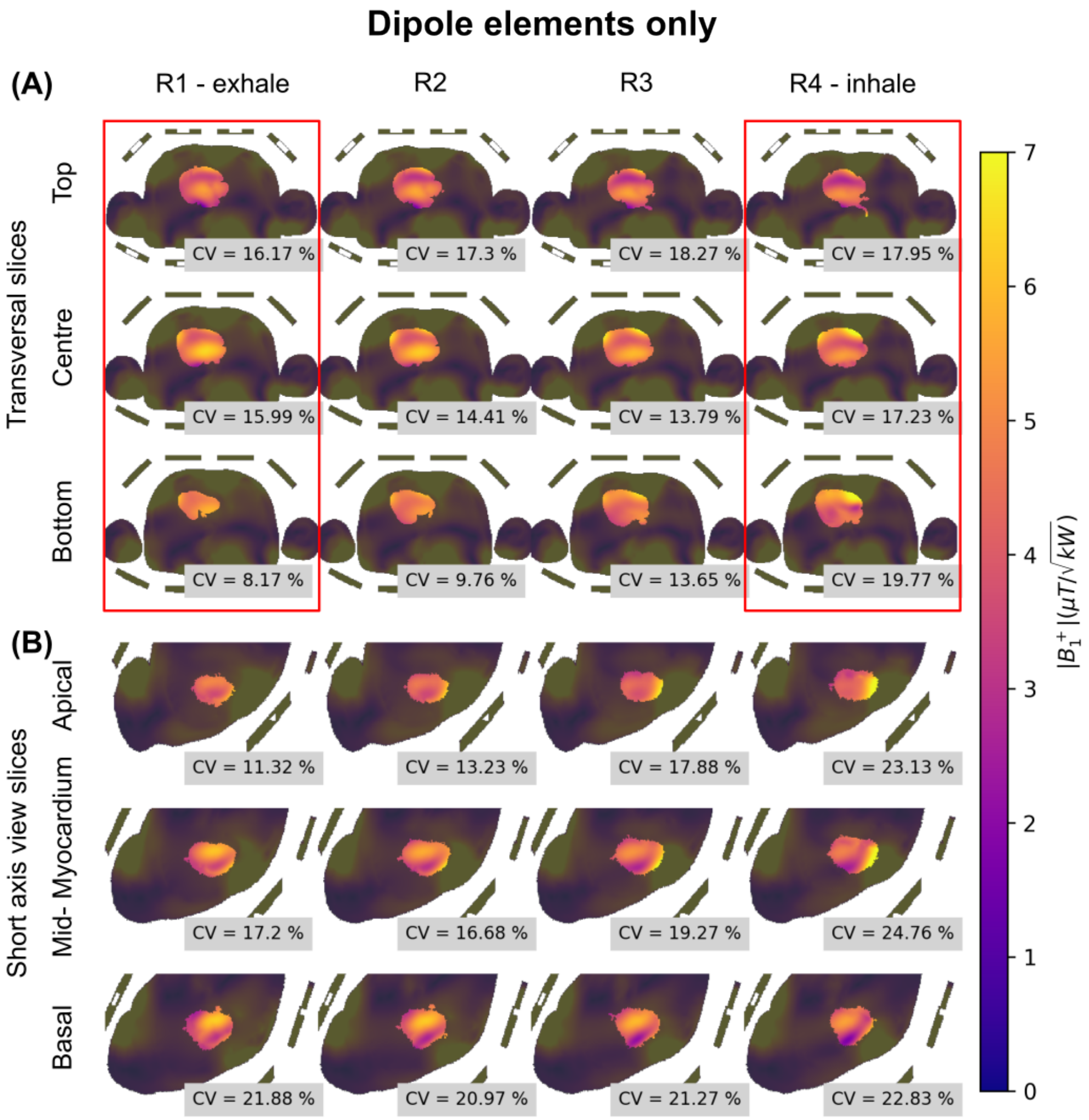

Figure A.2.3: B_1^+ maps of a homogenous shim vector: are shown for transversal slices with 20 mm distance covering the full heart (A) and short axis view slices with 20 mm distance (B). The shim vector was optimized for the ’Fixed’ setup with dipole elements only on the exhale and inhale respiratory state for three transversal slices ROI_3 (6 maps marked by the red boxes). The four columns show B_1^+ maps for the respiratory states R1 to R4. The observed CV values are smaller for the transversal slices (8.17%-19.77%) compared to the short axis view slices (11.32-24.76%). This and signal dropouts, for example in the basal slice of R4, illustrate that a static shim is not substantially to optimize a 3D volume. Possibly dynamic pTx as kT-points enable a better 3D optimization. In the gray boxes the CV for the corresponding slices is documented.

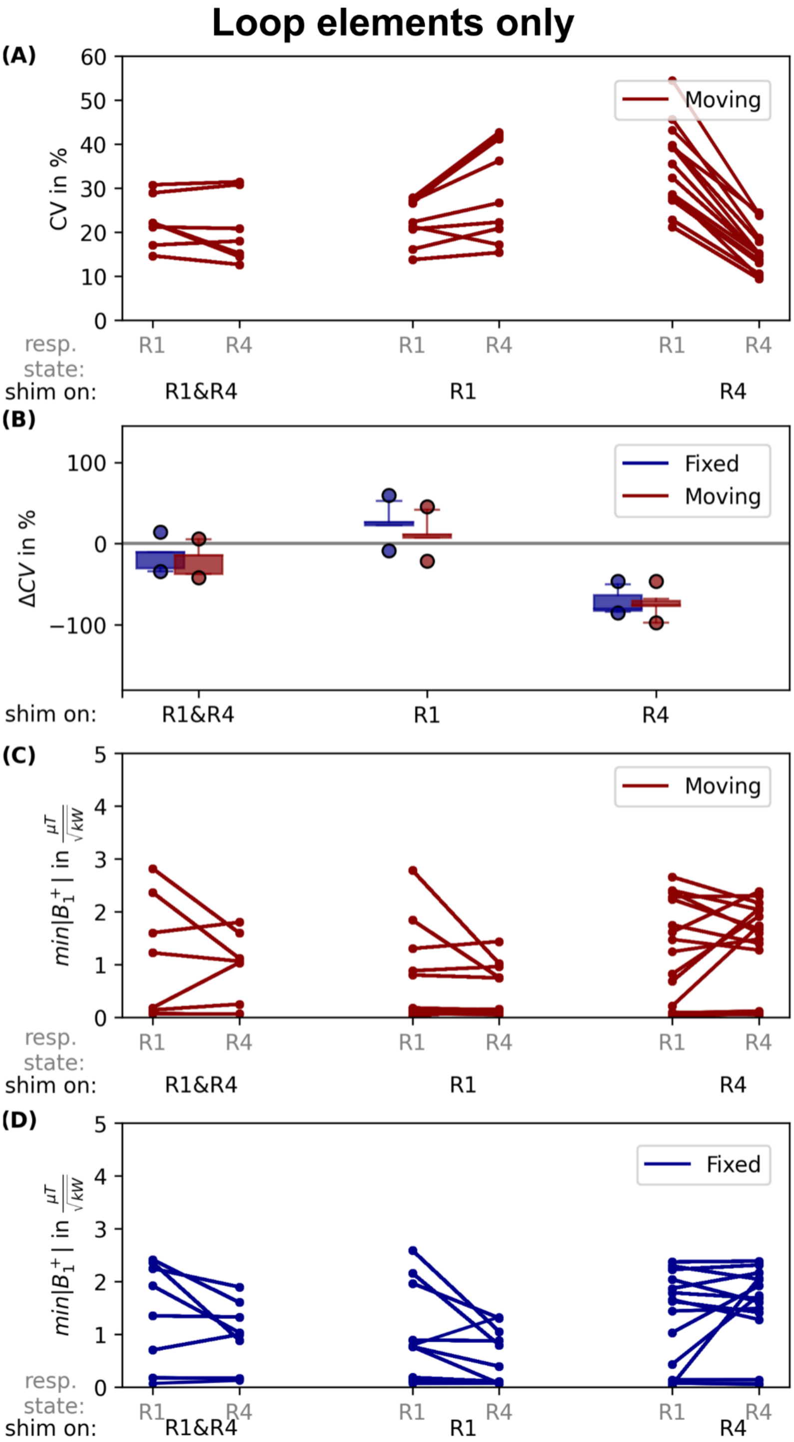

Figure A.2.4: Respiration-induced B_1^+ changes - coil setup and shimmed breathing state: A set of 1000 starting phase shim vectors was used to optimize the B_1^+ homogeneity for a ’Fixed’ and ’Moving’ coil setup using the loop channels only. Multiple initial phase vectors for the optimization can result in the same optimized shim vector. The optimization was performed on the ’exhale and inhale’ state simultaneously (R1&R4 - left column), ’exhale only’ (R1 - centre column) and ’inhale only’ (R4 - right column). For this setup the CV values (A), the ΔCV values (B) and the $min(|B_1^+|)$ (C&D) are evaluated. The CV values are only shown for the ’Moving’ setup, while all other values are shown for ’Moving’ and ’Fixed’. The optimization on R1&R4 shows the smallest respiration-induced CV and min B_1^+ changes.

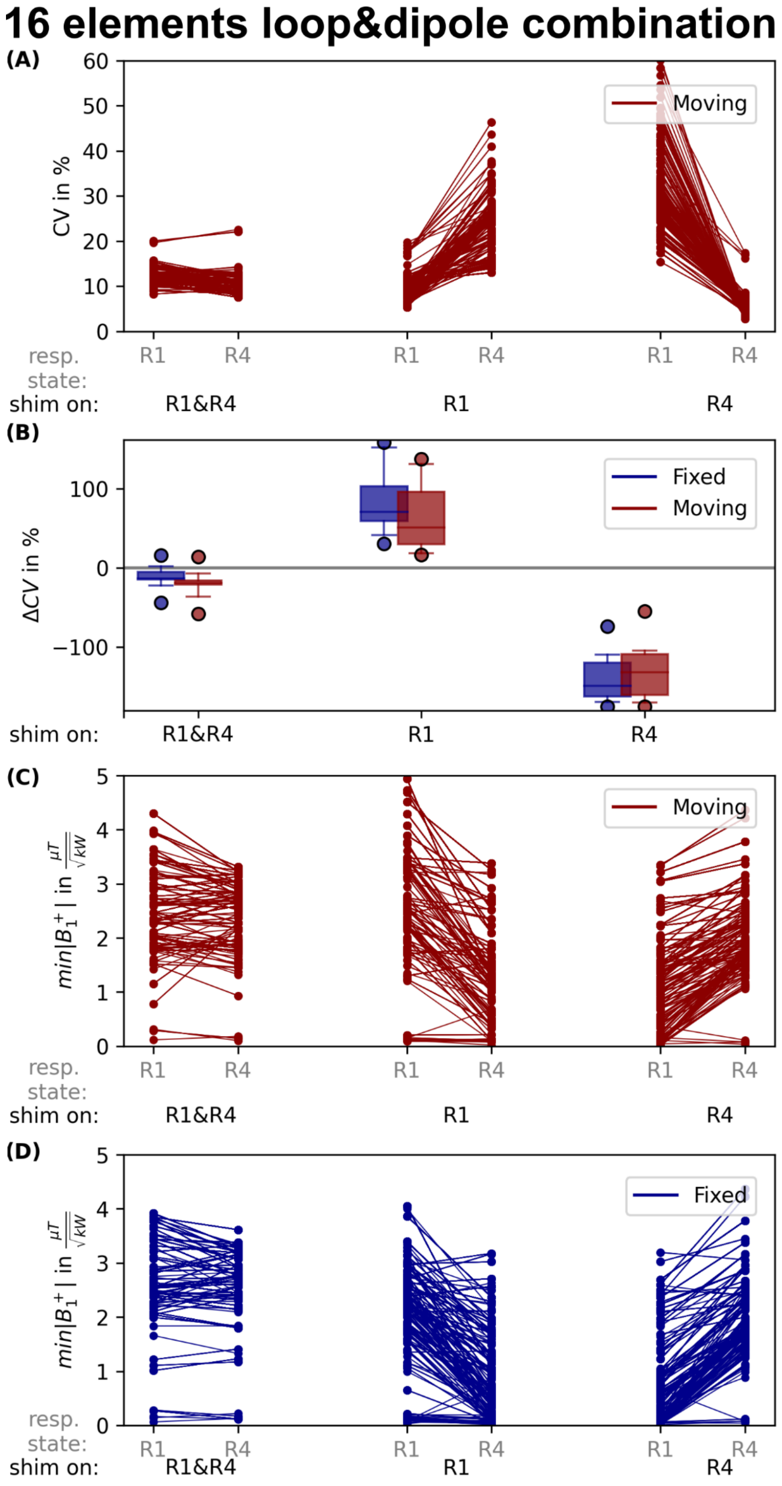

Figure A.2.5: B_1^+ changes - coil setup and shimmed breathing state: A set of 1000 starting phase shim vectors was used to optimize the B_1^+ homogeneity for a ’Fixed’ and ’Moving’ coil setup using the loop and dipole channels. Multiple initial phase vectors for the optimization can result in the same optimized shim vector. The optimization was performed on the ’exhale and inhale’ state simultaneously (R1&R4 - left column), ’exhale only’ (R1 - centre column) and ’inhale only’ (R4 - right column). For this setup the CV values (A), the ΔCV values (B) and the $min(|B_1^+|)$ (C&D) are evaluated. The CV values are only shown for the ’Moving’ setup, while all other values are shown for ’Moving’ and ’Fixed’. The optimization on R1&R4 shows the smallest respiration-induced CV and min B_1^+ changes.

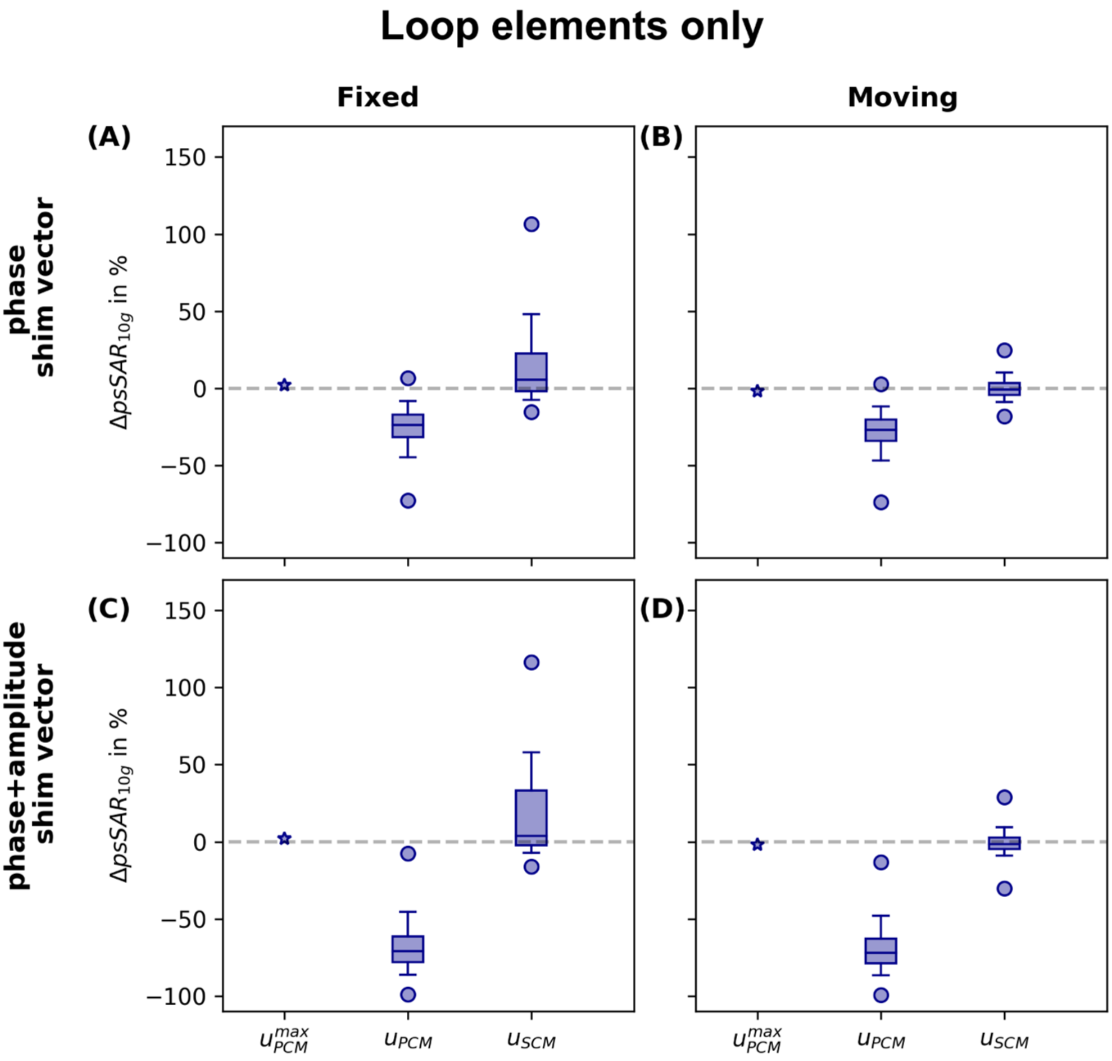

Figure A.2.6: Respiration-induced $psSAR_{10g}$ changes - coil setup and control mode: The respiration-induced $psSAR_{10g}$ changes are compared for a set of 10^6 random phase shim vectors (top row) and 10^6 amplitude and phase shim vectors (bottom row) applied to the VOP sets of simulations including only the loop elements. To ensure compliance with the IEC limit during the exhale state, the shim vectors $\boldsymbol{u}$ are scaled for the different control modes ($\boldsymbol{u}_{SCM}, \boldsymbol{u}_{PCM}$). In addition the upper amplitude (u_{PCM}^{max}) is calculated to obtain an amplitude limit for the shim vectors with $psSAR_{10g}(R1)$ below the IEC limit. This shim vectors and the upper amplitudes are applied to the inhale state and the resulting respiration-induced changes of the $psSAR_{10g}$ between inhale and exhale are evaluated. The respiration-induced changes are calculated for both 'Fixed' (left column) and 'Moving' (right column) setups. The box-plots display whiskers representing the 5th and 95th percentiles, boxes marking the first and third quartiles with the median value, and circles indicating the extrema.

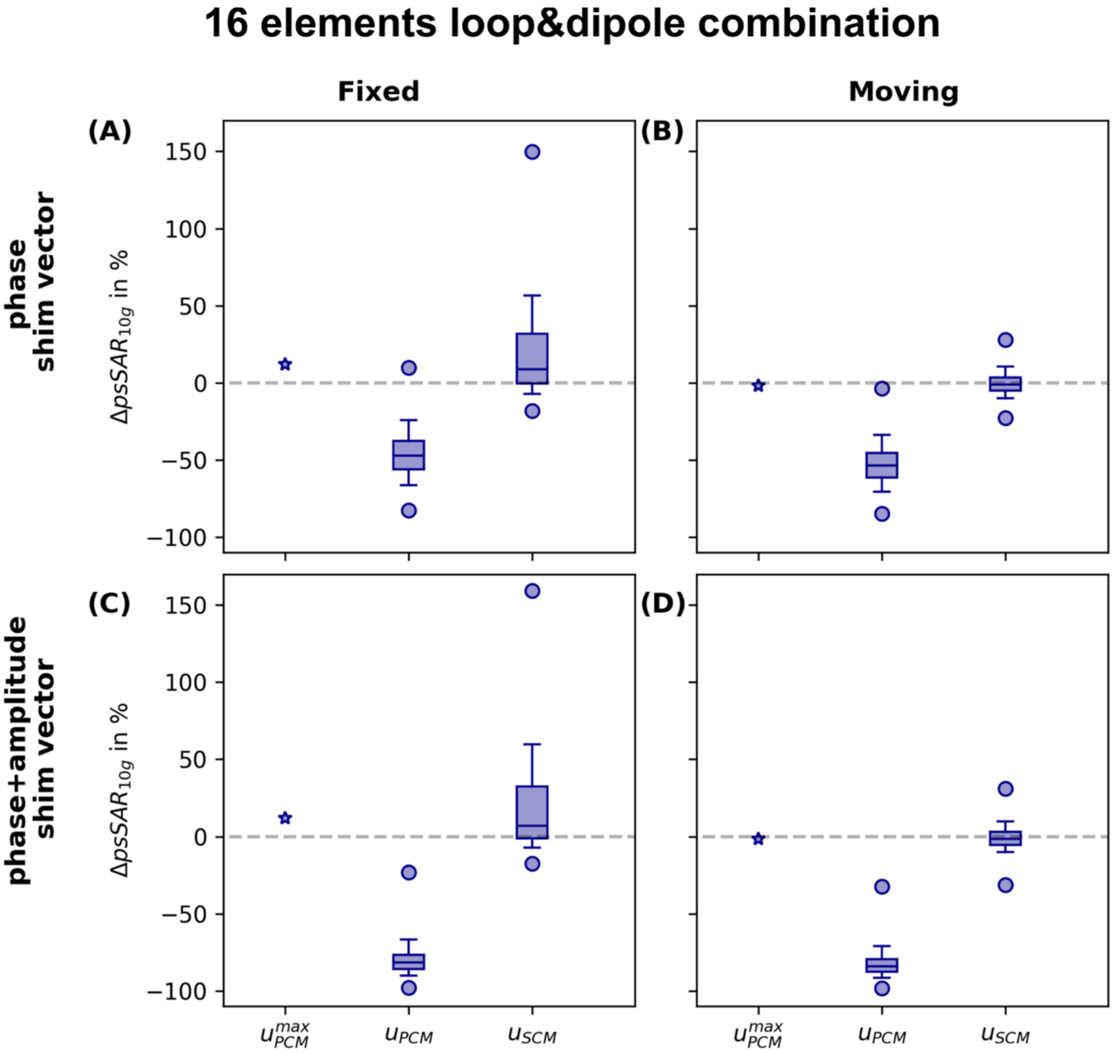

Figure A.2.7: Respiration-induced $psSAR_{10g}$ changes - coil setup and control mode: The respiration induced $psSAR_{10g}$ changes are compared for a set of 10^6 random phase shim vectors (top row) and 10^6 amplitude and phase shim vectors (bottom row) applied to the VOP sets of simulations including loop and dipole elements. To ensure compliance with the IEC limit during the exhale state, the shim vectors $\boldsymbol{u}$ are scaled for the different control modes ($\boldsymbol{u}_{SCM}, \boldsymbol{u}_{PCM}$). In addition the upper amplitude (u_{PCM}^{max}) is calculated to obtain an amplitude limit for the shim vectors with $psSAR_{10g}(R1)$ below the IEC limit. This shim vectors and the upper amplitudes are applied to the inhale state and the resulting respiration-induced changes of the $psSAR_{10g}$ between inhale and exhale are evaluated. The respiration-induced changes are calculated for both 'Fixed' (left column) and 'Moving' (right column) setups. The box-plots display whiskers representing the 5th and 95th percentiles, boxes marking the first and third quartiles with the median value, and circles indicating the extrema.

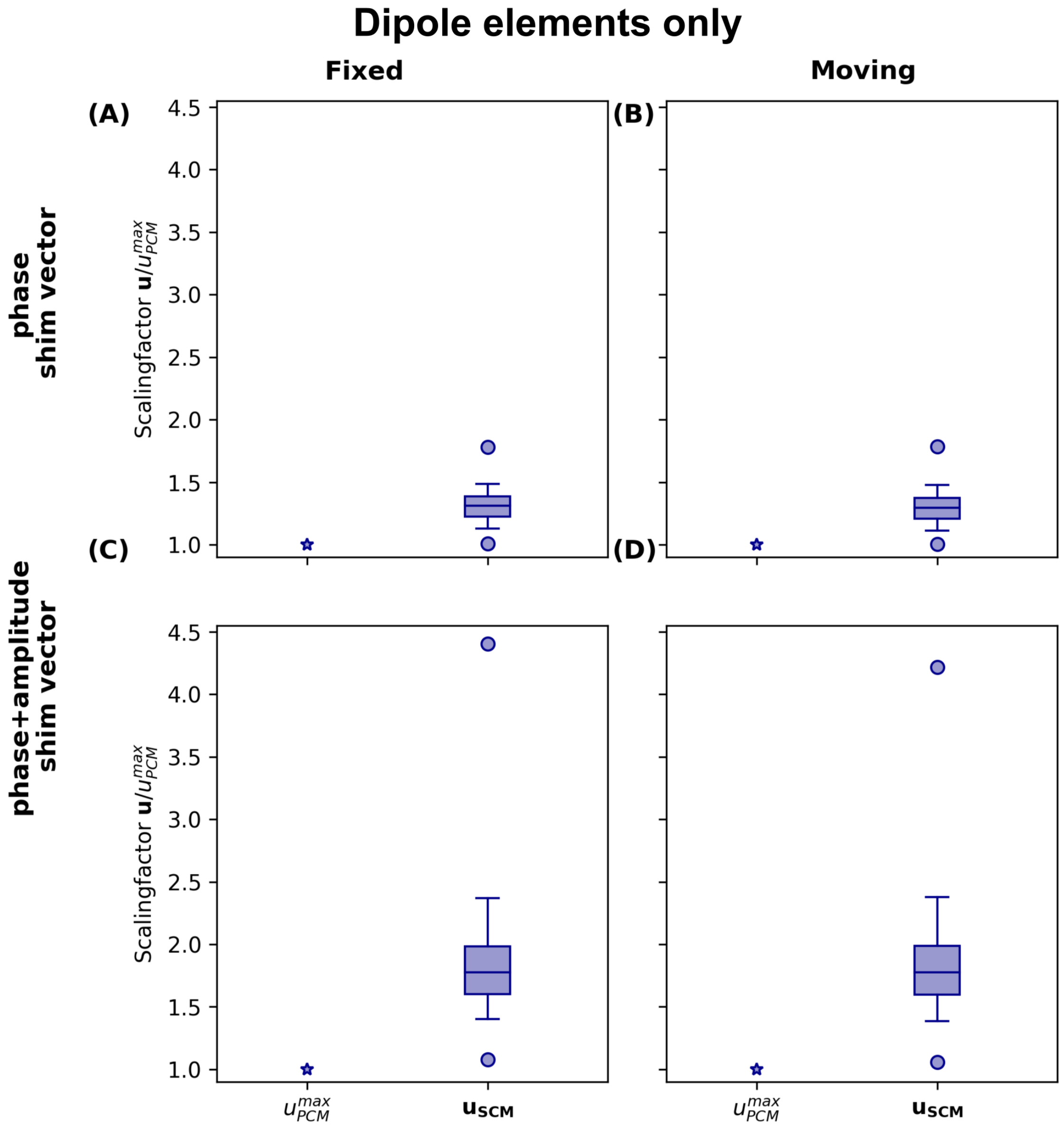

Figure A.2.8: Amplitude scaling factor: The scaling factor $\mathbf{u}/u_{PCM}^{max}$ illustrates the applicable amplitudes normalized on the power-controlled mode maximum amplitude. The amplitudes are in compliance to the IEC limit for the exhale state ($psSAR_{10g} < 20W/kg$) This is done for 10^6 random phase shim vectors (top row) and 10^6 random amplitude and phase shim vectors (bottom row). The left column shows the results for the 'Fixed' setup and the right column for the 'Moving' setup. The box-plots display whiskers representing the 5th and 95th percentiles, boxes marking the first and third quartiles with the median value, and circles indicating the extrema

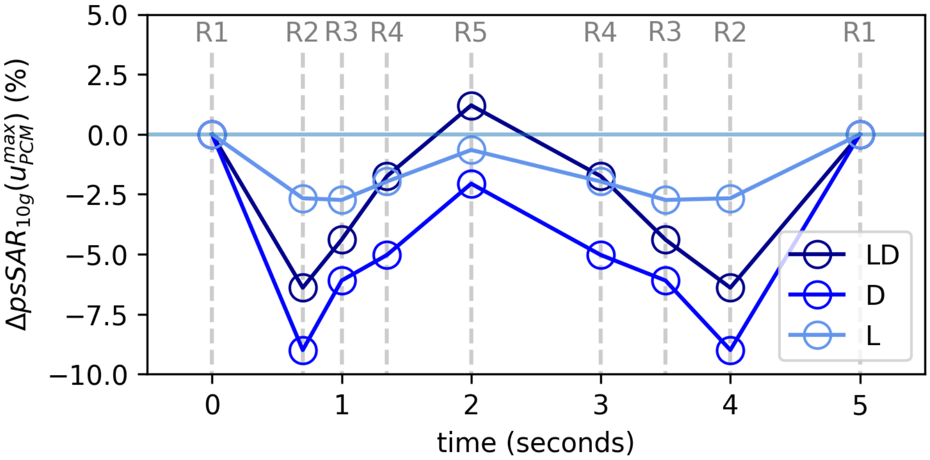

Figure A.2.9: Respiration-induced changes of $psSAR_{10g}$ for the power controlled mode upper boundary: The respiration-induced changes of the $psSAR_{10g}$ with respect to the exhale (R1) respiratory state are shown for the maximum amplitude of the power controlled mode (u_{max}^{PCM}). The Data is shown for the combination of loop and dipole channels (dark blue), dipole channels only (blue) and loop channels only (light blue).

A.3 The impact of the field strength on respiration-induced EM field changes

A.3.1 Tables

Element	mean$\vert B_1^+(R1)\vert$ / $\left(\frac{\mu T}{\sqrt{kW}}\right)$		$\Delta mean\vert B_1^+\vert$ / $\left(\frac{\mu T}{\sqrt{kW}}\right)$		min $\vert B_1^+(R1)\vert$ / $\left(\frac{\mu T}{\sqrt{kW}}\right)$		$\Delta min\vert B_1^+\vert$ / $\left(\frac{\mu T}{\sqrt{kW}}\right)$	
	7 T	10.5 T	7 T	10.5 T	7 T	10.5 T	7 T	10.5 T
D1	1.4	3.2	-0.12	0.28	0.44	0.01	-0.02	0.17
D2	3.3	5.2	-0.55	-0.84	1.1	1.09	-0.04	-0.2
D3	2.6	3.3	-0.64	-0.55	0.78	0.39	-0.32	-0.33
D4	0.7	1.7	-0.21	-0.19	0.23	0.06	-0.14	-0.12
D5	0.6	0.7	0.03	0.08	0.23	0.02	0.03	0.24
D6	1.1	1.6	-0.11	-0.04	0.42	0.37	0.06	0.07
D7	0.7	0.8	0.09	0.42	0.23	0.19	0.12	0.04
D8	0.3	0.3	-0.03	0.01	0.08	0.0	-0.04	0.0

Table A.3.1: Element wise B_1^+ for 7 T and 10.5 T. The mean and min $|B_1^+|$ within the ROI are given for the exhale (R1) respiratory state. Additionally, the corresponding respiration induced changes are listed.

Element	$\varphi(R1, \boldsymbol{r}_{center})$ / °		$\Delta\varphi(\boldsymbol{r}_{center}$ / °	
	7 T	10.5 T	7 T	10.5 T
D1	-95.3	-9.0	-28.1	-30.6
D2	148.9	-156.0	1.3	-0.2
D3	125.1	179.5	-1.9	-5.4
D4	-150.1	15.2	-63.3	-57.7
D5	141.9	-4.9	-62.8	-101.4
D6	106.0	-107.7	-60.4	-84.2
D7	134.4	-71.17	-57.1	-79.4
D8	-68.0	136.1	-87.0	-99.6

Table A.3.2: Channel-wise B_1^+ for 7 T and 10.5 T. The phase at the exhale (R1) respiratory state and the respiration induced phase changes are given at a central location in the heart.

Element	mean $\left(\frac{\partial}{\partial r_{AP}}\varphi(R1,x)\right)$ / °/mm		mean$\Delta\varphi(x)$ / °/mm		mean $\left(\frac{\partial}{\partial r_{AP}}\Delta\varphi(x)\right)$ / °/mm	
	7 T	10.5 T	7 T	10.5 T	7 T	10.5 T
D1	1.4	3.4	-32.4	-41.3	-0.3	-0.9
D2	2.7	4.1	-7.8	-6.6	-0.4	-0.5
D3	2.6	4.2	-11.5	-6.1	-0.4	-0.3
D4	1.4	3.4	-50.7	-50.5	-0.3	-1.1
D5	-1.0	-2.6	-57.7	-98.6	-0.2	0.4
D6	-2.4	-3.9	-60.1	-95.0	0.3	0.7
D7	-2.5	-4.1	63.4	-89.0	0.6	0.9
D8	-2.2	1.7	-82.8	1.5	0.2	0.5

Table A.3.3: Channel-wise B_1^+ for 7 T and 10.5 T. The mean gradient of the phase at the exhale (R1) respiratory state, the mean respiration-induced phase changes and the mean gradient of the respiration-induced phase changes within the ROI in the central heart slice are given.

pTx	Key Values	7 T		10.5T	
		R1	R4	R1	R4
static	CV (%)	[18.5,21.7]	[18.7,23.6]	[35.0,42.7]	[29.6,47.0]
	CV(R4)-CV(R1) (%)	[0.2,1.9]		[-8.0,5.2]	
	mean(FA) / °	[10.0,10.0]	[8.7,9.0]	[10.0,10.0]	[8.3,9.7]
	mean(FA(R4))-mean(FA(R1)) / °	[-1.3,-1.0]		[-1.7,-0.3]	
dynamic, 2kT	CV (%)	[4.7,7.1]	[12.4,22.7]	[8.5,19.7]	[21.6,36.6]
	CV(R4)-CV(R1) / %	[5.2,18.0]		[13.1,24.7]	
	mean(FA) / °	[9.9,10.0]	[7.4,9.4]	[9.6,9.9]	[7.7,9.0]
	mean(FA(R4))-mean(FA(R1)) / °	[-2.5,-0.6]		[-2.2,-0.7]	
dynamic, 4kT	CV (%)	[2.3,3.6]	[13.7,38.2]	[5.1,15.1]	[25.9,49.6]
	CV(R4)-CV(R1) (%)	[10.5,35.8]		[13.4,44.1]	
	mean(FA) / °	[10.0,10.0]	[5.7,9.9]	[9.7,10.0]	[8.4,14.1]
	mean(FA(R4))-mean(FA(R1)) / °	[-4.3,-0.1]		[-1.6,4.2]	

Table A.3.4: Quantitative summary of FA key values for 200 starting phase sets, applied to a FA optimization for the 3D heart in the exhale (R1) respiratory state. For dynamic pTx, a fixed regularisation parameter was used for all 200 starting sets. The generated RF pulses are assessed both for R1 and R4. The data is shown in fig. 6.1.3.

Set	Key Values	**7 T**		10.5T	
		R1	R4	R1	R4
RF pulse 1 min(CV(R4) − CV(R1))	CV / %	7.15	12.35	8.48	21.57
	mean(FA) / a.u	9.9	8.8	9.9	8.9
	$\text{psSAR}_{10\text{g}}$ / (W/kg)	20.0	22.36	20.0	19.99
RF pulse 2 max(CV(R4)−CV(R1))	CV / %	4.67	22.7	8.45	33.19
	mean(FA) / a.u	10.0	7.4	9.9	7.7
	$\text{psSAR}_{10\text{g}}$ / (W/kg)	20.0	20.16	20.0	20.01
RF pulse 3 max($\text{psSAR}_{10\text{g}}$(R4))	CV / %	4.71	17.29	8.45	32.7
	Mmean(FA) / a.u	10.0	8.6	9.9	7.8
	$\text{psSAR}_{10\text{g}}$ / (W/kg)	20.0	22.03	20.0	24.94

Table A.3.5: Summary of the key values of example FA maps shown in fig. 6.3.1 for 3 different RF pulses at 7 T and 3 different RF pulses at 10.5 T. Please note the RF pulses for 7 T and 10.5 T are not the same. Dynamic pTx using 2kT points was used to optimize the FA in the 3D heart ROI for the exhale respiratory state using different starting settings. Transversal slices are shown in fig. 6.3.1. (RF pulse 1) shows the solution with min($CV(R4) - CV(R1)$) and (RF pulse 2) with $max(CV(R4) - CV(R1))$ of the 2kT point cases shown in figs. 6.1.3 and 6.1.4, while (RF pulse 3) is the solution with the largest $\text{psSAR}_{10\text{g}}(R4)$ of the 2kT point cases shown in fig. 6.2.1.

A.3.2 Figures

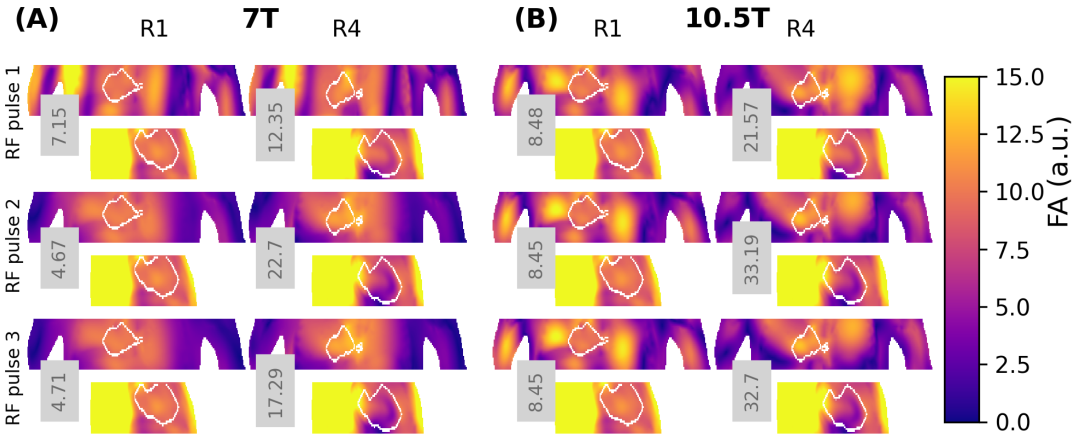

Figure A.3.1: Example FA maps in coronal and sagittal direction are shown for 3 different RF pulses at 7 T and 10.5 T. Dynamic pTx using 2kT points was used to optimize the FA in the 3D heart ROI for the exhale respiratory state using different starting settings. Transversal slices are shown in fig. 6.3.1. (RF pulse 1) shows the solution with $\min(CV(R4) - CV(R1))$ and (RF pulse 2) with $max(CV(R4) - CV(R1))$ of the 2kT point cases shown in figs. 6.1.3 and 6.1.4, while (RF pulse 3) is the solution with the largest $\mathrm{psSAR}_{10g}(R4)$ of the 2kT point cases shown in fig. 6.2.1. Inside the gray boxes the CV values for the entire 3D ROI is given, the corresponding mean(FA), and psSAR_{10g} are given in Supporting Information table A.3.5.

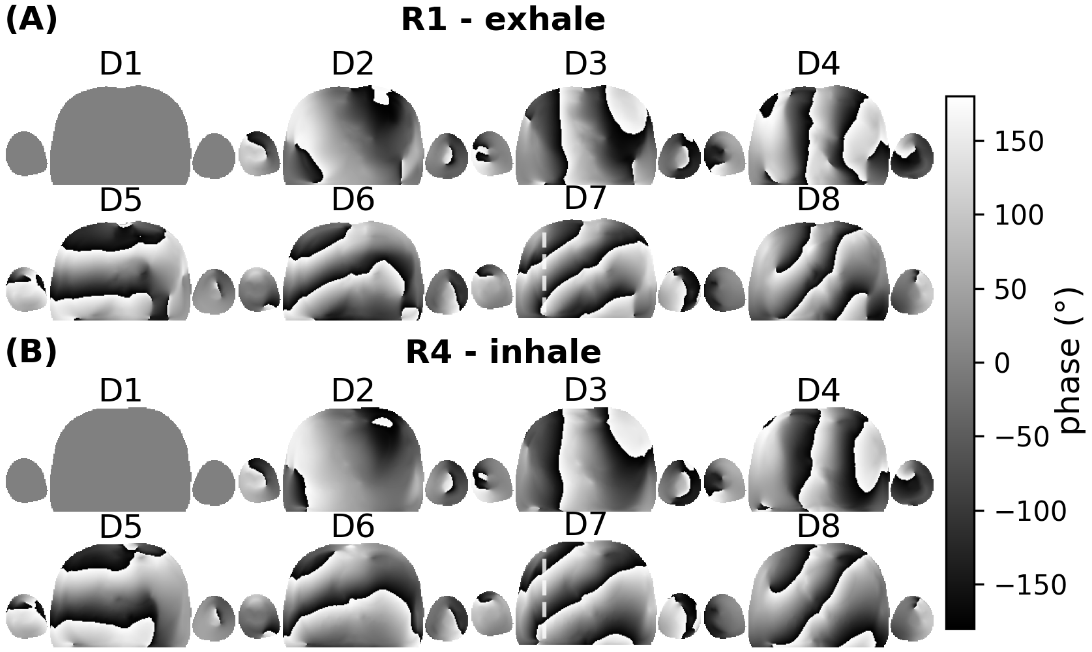

Figure A.3.2: B_1^+ phase maps of the simulated XCAT body model at 7 T for comparison with in-vivo measurements (Supporting Information fig. A.3.3): (A) inhale respiratory state and (B) exhale respiratory state phase maps for 8 'D' elements.

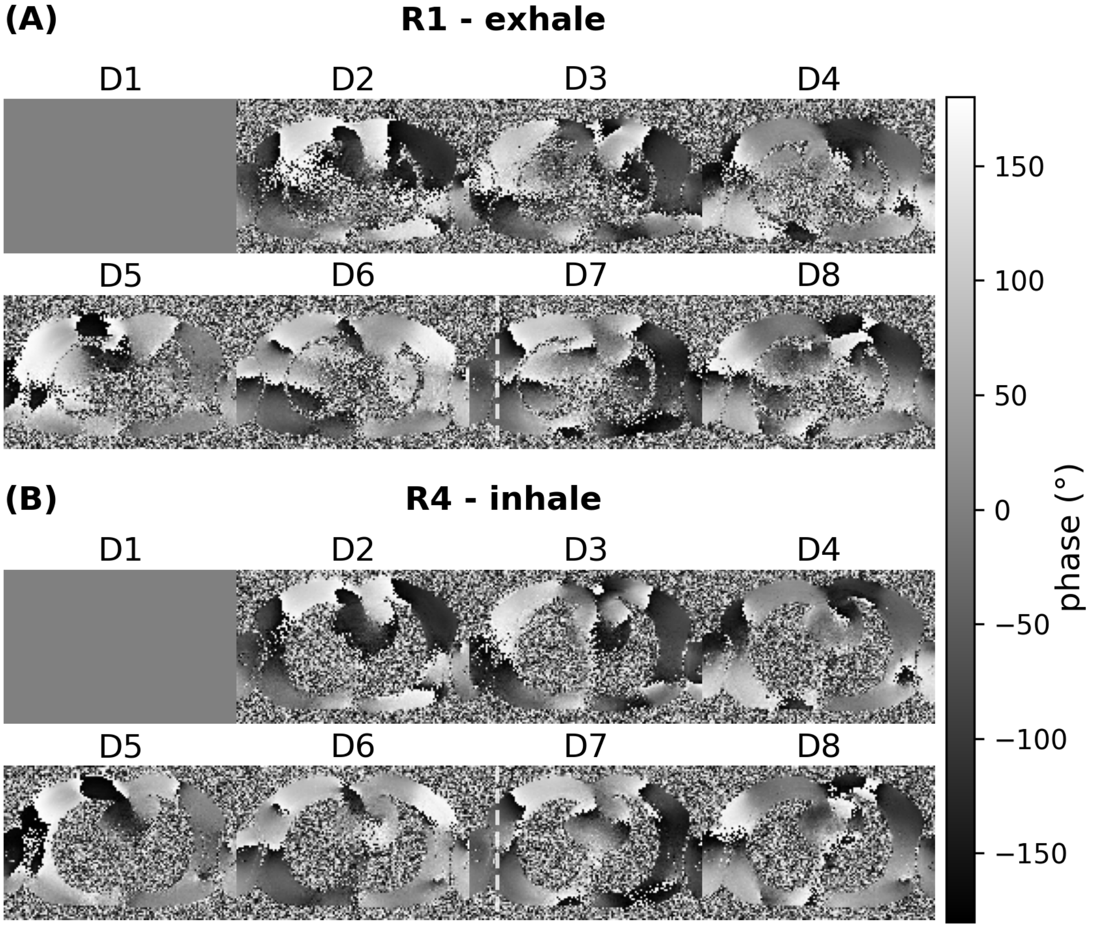

Figure A.3.3: In-vivo measurement of B_1^+ phase maps at 7 T for comparison with body model simulations (Supporting Information fig. A.3.2): (A) inhale respiratory state and (B) exhale respiratory state phase maps for 8 ’D’ elements.

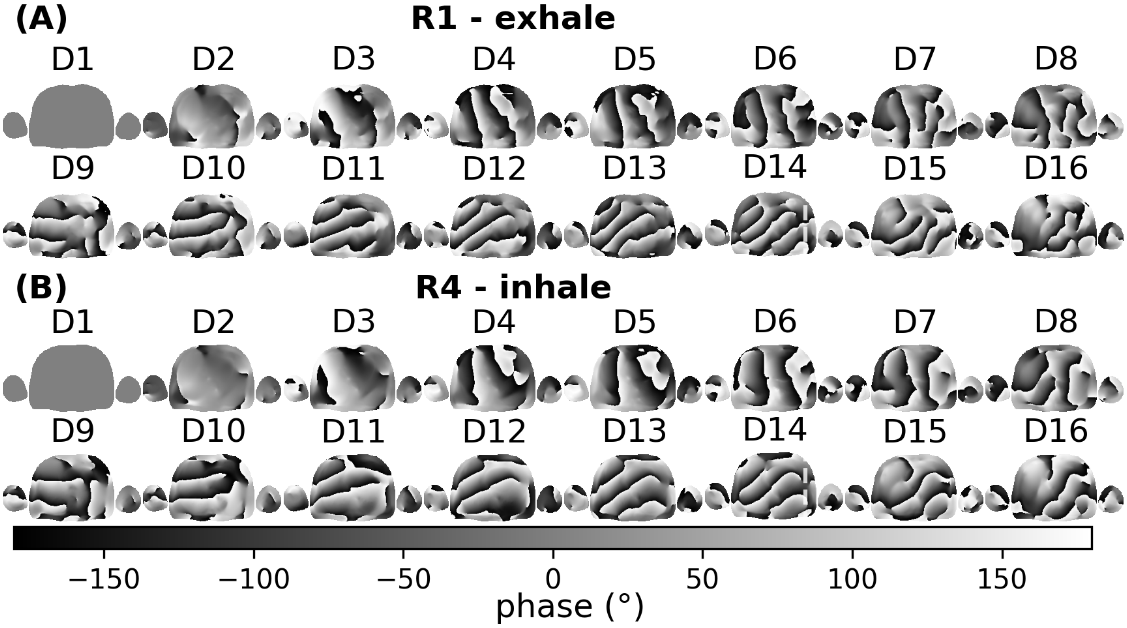

Figure A.3.4: B_1^+ phase maps of the simulated XCAT body model at 10.5 T for comparison with in-vivo measurements (Supporting Information fig. A.3.5): (A) inhale respiratory state and (B) exhale respiratory state phase maps for 16 ’D’ elements.

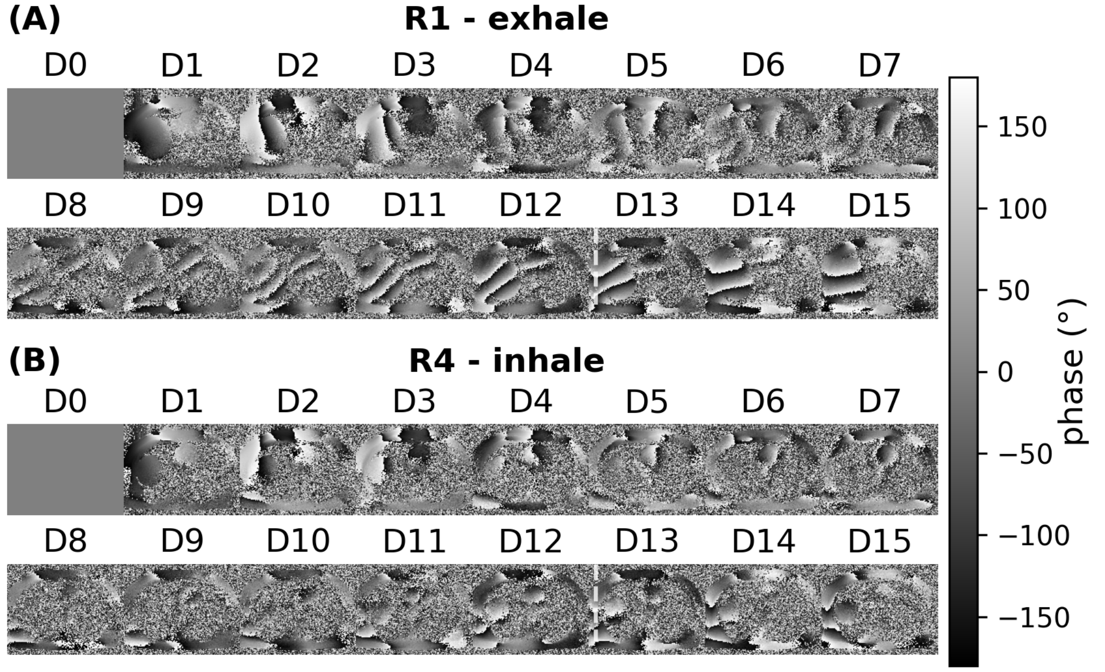

Figure A.3.5: In-vivo measurement of B_1^+ phase maps at 10.5 T for comparison with body model simulations (Supporting Information fig. A.3.4): (A) inhale respiratory state and (B) exhale respiratory state phase maps for 16 ’D’ elements.

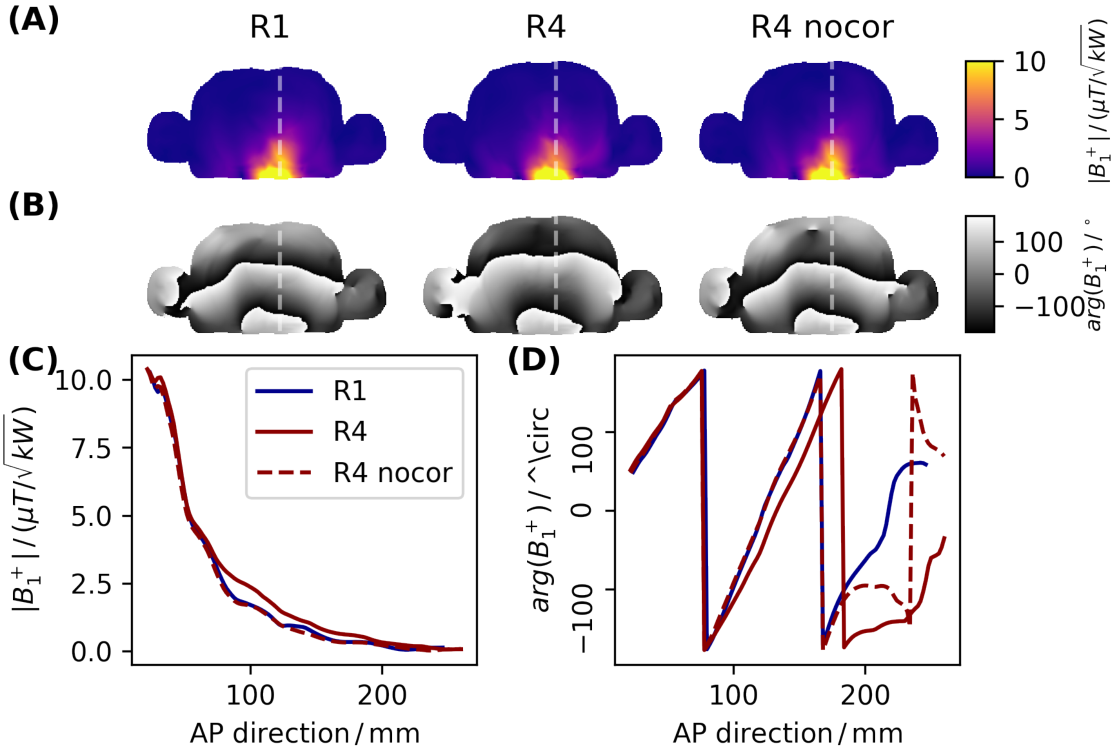

Figure A.3.6: Simulated impact of respiration-induced changes in the dielectric properties (σ, ε) on B_1^+ maps at 10.5 T. (A) shows the B_1^+ magnitude maps and (B) the B_1^+ phase maps for the exhale (R1), the inhale (R4) and the inhale with the same σ, ε as used for R1 , denoted as ’R4 no cor’.

Declaration of honour

I hereby declare that I prepared this thesis without impermissible help of third parties and that none other than the indicated tools have been used; all sources of information are clearly marked, including my own publications.
In particular I have not consciously:

- Fabricated data or rejected undesired results
- Misused statistical methods with the aim of drawing other conclusions than those warranted by the available data
- Plagiarised external data or publications
- Presented the results of other researchers in a distorted way

I am aware that violations of copyright may lead to injunction and damage claims of the author and also to prosecution by the law enforcement authorities.
I hereby agree that the thesis may be reviewed for plagiarism by mean of electronic data processing.
This work has not yet been submitted as a doctoral thesis in the same or a similar form in Germany or in any other country. It has not yet been published as a whole.

Magdeburg, ____________________

____

Natalie Schön